Wave Loads on a Submerged Intake Structure in the Surf Zone

Mark Hecimovich

Submitted under the supervision of
Dr. Ioan Nistor
Dr. Andrew Cornett

In partial fulfillment of the requirements for the degree of
Master of Applied Science in Civil Engineering

Department of Civil Engineering
University of Ottawa
March, 2013

Acknowledgments

I would like to thank my supervisors, Dr. Ioan Nistor and Dr. Andrew Cornett, for their tremendous help with this study. As my supervisor at the University of Ottawa, Dr. Nistor not only provided me with guidance and technical knowledge throughout my studies but also unconditional support through any challenge of the last 2 years. Dr. Nistor helped me with the work opportunity that made having this unique and exciting thesis topic possible. I am very grateful for Dr. Cornett allowing me use of testing facilities at the Canadian Hydraulics Centre to conduct wave experiments. While supervising the wave experiments portion of this study, Dr. Cornett provided invaluable insight in the areas of physical modelling and wave physics. When working on the analysis portion of this study, Dr. Cornett challenged my work and pushed me to become a better graduate student. This thesis project would not have been nearly as successful without the help from Dr. Nistor and Dr. Cornett. I would also like to acknowledge my former professor Dr. A. M. da Silva of Queens University for sparking my interest in the science of hydraulics and providing advice for pursuing graduate studies. Dr. da Silva recommended Dr. Nistor and the University of Ottawa has a terrific option for studying coastal engineering.

Many members of the staff at the Canadian Hydraulics Centre deserve my sincere gratitude for their help with this study. Thierry Faure worked closely with me on the design and execution of the model and provided valuable insight. Dan Pelletier was a tremendous help with instrumentation, data acquisition, and the GEDAP software. Scott Baker provided valuable advice and help with GEDAP as well. Without the help of the technical staff at CHC, I would never have been able to fabricate and construct the physical model. I am very grateful for all the help and assistance I received from the friendly staff at CHC.

Finally, I would like to thank my family for their constant support throughout the last 2 years. I would never have reached the point of submitting a master's thesis if not for the guidance and support of my parents over the years.

Abstract

Sea water intake structures submerged in the surf zone are used to provide water for cooling processes in large facilities such as power plants and refineries. Structures submerged in the surf zone are subject to large forces from breaking waves. To study these forces induced from realistic sea state conditions, a physical model of an intake structure submerged in the wave breaking zone was constructed and subjected to a wide spectrum of regular and irregular waves. The model structure was designed in a manner so force measurement could be isolated to separate components of the structure.

The data of peak forces on the structure was analyzed for correlations with varying irregular wave properties. Using the results of forcing on the structure from regular wave tests, drag and inertia coefficients for use in the Morison equation were determined for each separate component and configuration of the structure. These force coefficients were plotted against various wave properties to analyze correlations with wave conditions. Finally, the force coefficients for the structure were used with the Morison equation and current data from the experiments to successfully model forcing on the structure during irregular wave tests.

Table of Contents

List of Figures

List of Tables

List of Symbols

The following symbols are found throughout this paper:

α_P	Phillips alpha
Γ	Circulation
ε^2	Residual difference
π	Pi
ρ	Density (kg/m^3)
σ_U	Standard deviation of velocity (m/s)
ϕ	Velocity potential (m^2/s)
ω	Vorticity
A	Area (m^2)
C_D	Drag force coefficient
C_M	Inertial force coefficient
d	Depth (m)
D	Diameter (m)
$\frac{d}{L}$	Depth-to-wavelength ratio
$\frac{D}{L}$	Diameter-to-wavelength ratio
$\frac{du}{dt}$	Acceleration (m/s^2)
exp	Exponential
f	Frequency (Hz)
F_D	Drag force (kN)
F_I	Inertial force (kN)
f_P	Peak frequency (Hz)
f_V	Vortex shedding frequency (Hz)
g	Gravitational constant (9.81 m/s^2)
H	Wave height (m)
H_{m0}	Zero-moment wave height (m)
H_{MAX}	Maximum wave height (m)
H_O	Deep water wave height (m)
H_S	Significant wave height (m)

$\frac{H}{d}$	Wave height-to-water depth ratio
$\frac{H}{L}$	Wave height-to-wavelength ratio
KC	Keulegan-Carpenter number
L	Wavelength (m)
L_O	Deep water wavelength (m)
$\frac{L}{D}$	Centre-to-centre spacing ratio between 2 cylinders
MWL	Mean water level
$P(x)$	Probability function
Re	Reynolds number
S	Surface (m^2)
$S(x)$	Spectral energy density function
St	Strouhal number
t	Time (s)
T	Wave period (s)
T_P	Peak period (s)
u	Velocity in X direction (m/s)
U_M	Maximum amplitude of velocity (m/s)
v	Velocity in Y direction (m/s)
$\vec{v}$	Curl of velocity field
V	Volume (m^3)
w	Velocity in Z direction (m/s)
z	Distance from mean water level (MWL)

List of Abbreviations

The following abbreviations and acronyms are found throughout this paper:

AWA	Active Wave Absorption
CHC	Canadian Hydraulics Centre
FAST	Fatigue Aerodynamics Structures Turbulence
GEDAP	Generalized Experiment Control and Data Acquisition Package
JONSWAP	Joint North Sea Wave Project
LWF	Linear Wave Theory
LWT	Large Wave Flume
PVC	Polyvinyl Chloride pipe
MAX	Maximum value
MIN	Minimum value
MOJS	Morison, O'Brien, Johnson and Schaaf – Authors of the Morison equation
MWL	Mean Water Level
NDAC	Data Acquisition and Control Package
NRC	National Research Council of Canada (Ottawa)
SOF	Sinusoidally Oscillating Flow
STDEV	Standard Deviation
SWG	Segmented Wave Generator
VIV	Vortex Induced Vibration
VSD	Variance Spectral Density
ZCA	Zero Crossing Analysis

1.0 Introduction

Large facilities such as power plants and refineries located in coastal regions require sea water for cooling processes. Intake structures submerged in the surf zone are used to draw in cool sea water for these processes. Large breaking waves present in the surf zone can induce large forces on submerged structures. Estimating wave-induced forces and moments on these structures for design purposes is challenging, particularly when they are located in the surf zone. This is due to the non-linearity of the orbital velocities under breaking waves in shallow water, and the complexity of the interaction between the unsteady flow and the structure. It was proposed to conduct experiments on a physical model of a submerged intake structure to study forcing from passing waves. Typically, an intake structure features a vertical intake pipe and a horizontal velocity cap with cylindrical support posts. The velocity cap serves to prevent vortex formation and to protect local fish species (Larson and Dallas, 1975).

A large-scale (1:15) physical model study of waves shoaling and breaking in the vicinity of a submerged intake structure has been conducted to investigate the relationships between wave properties, water particle kinematics, and forcing on the structure. The results from peak forces on the structure were analyzed for correlations with various wave properties from wave tests. By designing the structure in a manner so that loads on separate components (central pipe, support posts, velocity cap) could be accurately measured, a method to predict wave-induced loads on the intake structure has been developed using the Morison equation, empirical force coefficients, and measured current velocities. The predictive model has been validated through comparison with force measurements in highly non-linear irregular waves. This study has provided valuable insight to the complex science of forces induced on submerged structures from large breaking waves that will allow for more economical and efficient structural design.

1.1 Novelty of Study

A structure submerged in the surf zone provides unique design challenges due to the complexity of the wave conditions and the relatively unknown physics of wave induced forcing. An intense review of the literature of wave forcing on submerged intake structures and other multiple cylinder configurations indicated that the experiments completed on an intake structure provide unique data and an opportunity for novel findings. There is no standard formula or model to accurately predict wave forcing on complex submerged bodies such as an intake structure. The turbulent, separated oscillatory flow fields induced from waves interacting with the structure create forcing that is difficult to predict.

Currently, there is little research on understanding force relationships and determining empirical force coefficients for these conditions (Sarpkaya, 2010).

Another unique aspect of these experiments is the realistic coastal environment simulated in the Large Wave Flume. Many experiments on wave forces use a U-tube apparatus (Sarpkaya, 1979) to create sinusoidal flow, simulating water particle kinematics from actual waves. The waves generated in this study were scaled replicas of realistic wave conditions with a range of heights, periods, and water levels to simulate different storms and tides. The bathymetry constructed in the flume allowed for wave conditions to be established in a deeper water offshore zone, and for wave transformation and breaking to occur naturally at the site of the structure. A mild sloping beach appropriately located behind the structure allowed for minor reflection of the wave energy.

The Morison equation (Morison et al., 1950) is commonly used to estimate drag and inertial forces on submerged cylinders due to waves. Many physical model studies have been conducted to investigate wave-induced forces on structures composed of multiple cylinders and determine appropriate force coefficients for use in the Morison equation (i.e. Zdravkovich, 1977, Sarpkaya, 1979), but few studies have considered intake structures under breaking waves conditions. Forcing on a single cylinder from breaking waves has been modelled using the Morison equation (Burrows et al., 1997), but this modelling not been successfully applied to a complex structure featuring multiple cylinders and plates. This study will be the first to attempt to use the Morison equation and empirical force coefficients to predict forcing from irregular waves on an intake structure. Currently there is limited understanding of the relationships between breaking waves and forces on multiple cylinders in close proximity, necessitating studies such as this one.

1.2 Objectives

Through review of available literature it became apparent that breaking wave forces on submerged structures consisting of cylinder and plate components was not well understood and no suitable predictive formula/models were available. This study proposed the following objectives:

- Provide an in-depth review of current research on the topic of wave induced forcing on submerged intake structures and multiple cylinder configurations
- Analyze the results of wave tests for correlations between irregular wave properties and peak horizontal and vertical forcing on intake structures

- Develop and test a wave force prediction model using the Morison equation and force coefficients determined empirically
- Provide insight into the relations between wave properties and forcing for improved prediction of the magnitude and cause of peak force events on submerged intake structures

1.3 Scope

When planning the scope of this study, similar experiments in published literature were consulted. Physical experiments involving submerged structures consisting of multiple cylinders almost exclusively focused on publishing force coefficient data for use with the Morison equation. This study determines force coefficient data for the intake structure in varying wave conditions from regular wave tests. Once determined, these force coefficients were used with the Morison equation to predict forcing on the submerged intake structure. Force results predicted using the Morison equation were analyzed and compared to results from irregular wave tests. An analysis of the peak forces in shallow water irregular waves was also conducted. The test plan for wave tests was selected to investigate a range of realistic wave conditions, including moderate and violent storm conditions, at different water levels.

1.4 Outline

The contents of the study have been presented in 6 sections:

Section 1 – Introduction: An introduction to the study is provided, including the novelty, scope and project objectives.

Section 2 – Literature Review: Background information on intake structures and a review of the science and mechanics involved with wave induced forcing on submerged structures. Relevant research in wave forcing on intake structures is examined from physical, analytical, and numerical models.

Section 3 – Physical Model: A description of the model is presented. The design of the model intake structure as well as the artificial bathymetry is detailed. The construction of the bathymetry, fabrication of the model structure, and the instrumentation used in the model are also detailed.

Section 4 – Experimental Methodology – The calibration of instrumentation and preparation for testing, test plan of wave experiments, and test methodology are presented.

Section 5 – Data Analysis – The methods and software used for collecting and processing data from experiments is discussed.

Section 6 – Results & Analysis – Results of peak forcing from irregular wave tests are discussed with varying wave properties. Regular wave force and current data is used to determine force coefficients for each component of the structure. The determined force coefficients are analyzed for correlations with changing wave properties. Finally, measured velocity data is used with empirical force coefficients and the Morison equation to predict forcing on the structure during irregular wave tests.

Section 7 – Conclusions and Recommendations – The findings discussed from each section of the results & analysis are consolidated for conclusions. Recommendations for future work are made.

Section 8 –Recommendations – Opportunities to improve future experiments of similar topics are presented and recommendations for future work are made.

2.0 Literature Review

A review of literature for similar studies and science relevant to this study was conducted to obtain a clear objective, understand the physical processes taking place in the model, and to create a thesis with novel and innovative results. A brief background on intake structures is presented, followed by a review of the fluid mechanics concerning forcing on submerged structures from turbulent flow. Through physical and numerical modelling, relationships can be established between wave properties, velocities and the resulting forces on submerged structures. Physical, analytical, and numerical models are reviewed for their relevance to this study and applicable methods. The review is concluded with the current state of this field of research and novelty of this study.

2.1 Submerged Intake Structures

A typical submerged water intake structure similar to the one modelled in this study is composed of a vertical intake pipe, horizontal velocity cap, and cylindrical support posts. This design was patented by Larson and Dallas in 1975 (Figure 2.1). Water is drawn down through the central pipe protruding above the mud-line to a buried pipe that conveys the flow to the onshore location, usually for cooling in a power station or processing plant. A velocity cap is placed above the pipe to prevent a vertical velocity gradient in the ambient flow down towards the pipe and prevent vortex formation. A vortex formed above the intake is harmful for vessels and local ecology, reduces flow into the pipe, and induces vibrations and cavitation in the structure.

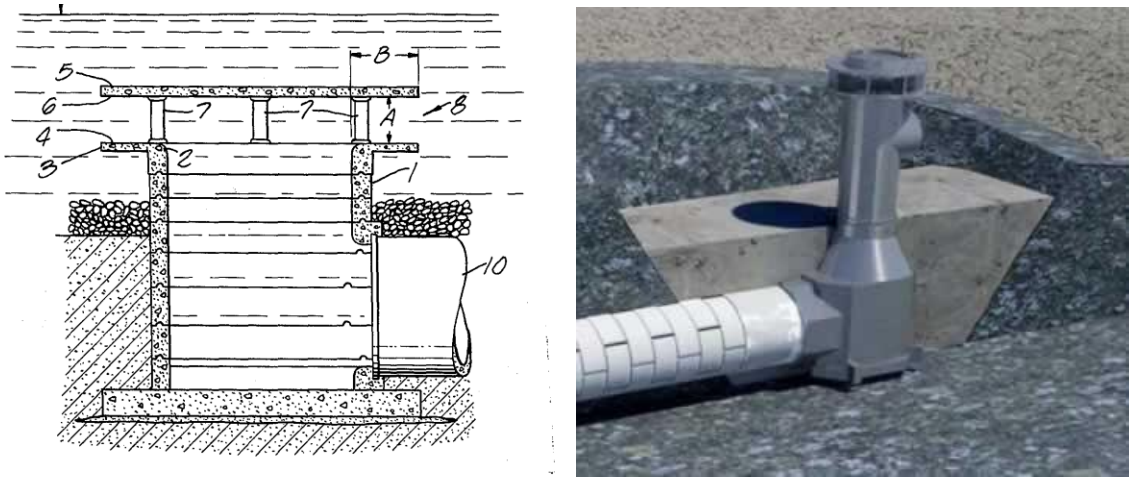

Figure 2.1: Diagram (left) of typical water intake structure from patent (Larson and Dallas, 1975), 3-D rendering (right)

Structures such as a capped intake structure can act as artificial reefs that attract fish. In modern design procedure, any structure that is built in an environment that will affect fish life needs to minimize impact on local species. A horizontal velocity cap placed at an appropriate height above the pipe will

create a uniform horizontal velocity profile between the pipe inlet and cap. This will allow fish species to sense the downward flow into the pipe as they approach the intake, and provide enough time to escape. Typically, an intake is designed so that a horizontal velocity profile in the flow exists such that the velocity does not vary more than 0.1 m/s between any 2 points underneath the cap (Larson and Dallas, 1975).

Sea water intake structures are typically built in shallow or transitional water depths. Placing the structures farther offshore will result in larger construction and material costs to cover the more difficult deep water construction and additional piping needed. However, the cooler water available at deeper depths is more desirable, as most sea water intakes are used in cooling processes. Deep water also provides more protection from forcing on the structure induced by passing waves. Considering all these factors, sea water intakes are often constructed in coastal zones where forcing from surface waves need to be considered in assessing ultimate limit state loadings during the design process.

2.2 Theoretical Background

Gravity waves propagating in a fluid generate oscillatory orbital velocities that can penetrate to considerable depths, and these oscillatory flows generate unsteady forcing on submerged structures. The turbulent flow from waves around a cylindrical member of an intake structure, such as a support post or the central pipe, is a very random process and there is no closure model for flow turbulence that satisfies the laws of fluid mechanics. When flow interacts with a submerged cylinder, the flow field is affected by flow separation, vortex formation and motion, turbulence, dynamic response on the structure, and structural and fluid-dynamical damping (Sarpkaya, 2010).

2.2.1 Navier-Stokes Equations

The motion of fluid particles in flow is described with a series of equations known as the Navier-Stokes equations, named after Claude-Louis Navier and George Gabriel Stokes. These time averaged equations have many uses in the study of fluid mechanics, and can be used to model fluid particle velocities in turbulent flow.

$$\frac{\partial u}{\partial t} + u\frac{\partial u}{\partial x} + v\frac{\partial u}{\partial y} + w\frac{\partial u}{\partial z} = X - \frac{1}{\rho}\frac{\partial \rho}{\partial x} + v\left[\frac{\partial^2 u}{\partial x^2} + \frac{\partial^2 u}{\partial y^2} + \frac{\partial^2 u}{\partial z^2}\right] \quad [2.1]$$

$$\frac{\partial v}{\partial t} + u\frac{\partial v}{\partial x} + v\frac{\partial v}{\partial y} + w\frac{\partial v}{\partial z} = Y - \frac{1}{\rho}\frac{\partial \rho}{\partial y} + v\left[\frac{\partial^2 v}{\partial x^2} + \frac{\partial^2 v}{\partial y^2} + \frac{\partial^2 v}{\partial z^2}\right] \quad [2.2]$$

$$\frac{\partial w}{\partial t} + u\frac{\partial w}{\partial x} + v\frac{\partial w}{\partial y} + w\frac{\partial w}{\partial z} = Z - \frac{1}{\rho}\frac{\partial \rho}{\partial z} + v\left[\frac{\partial^2 w}{\partial x^2} + \frac{\partial^2 w}{\partial y^2} + \frac{\partial^2 w}{\partial z^2}\right] \quad [2.3]$$

The velocity components in the x, y, z directions are represented by u, v, w respectively; X, Y, Z are the directional components of the body force per unit mass, and *p* is pressure. The term (∂_u/∂_t), (∂_v/∂_t), (∂_w/∂_t) is the substantive acceleration, representing local acceleration and convective acceleration of the fluid.

2.2.2 Rotational Flow

In reality, fluids studied are viscid and rotational with internal shear stresses. Rates of rotation of fluid particles (ω) about each axis (x, y, z) are given in this series of equations:

$$\omega_x = \frac{1}{2}\left(\frac{\partial \mathrm{w}}{\partial \mathrm{y}} - \frac{\partial \mathrm{v}}{\partial \mathrm{z}}\right), \qquad \omega_y = \frac{1}{2}\left(\frac{\partial \mathrm{u}}{\partial \mathrm{z}} - \frac{\partial \mathrm{w}}{\partial \mathrm{x}}\right), \qquad \omega_z = \frac{1}{2}\left(\frac{\partial \mathrm{v}}{\partial \mathrm{x}} - \frac{\partial \mathrm{u}}{\partial \mathrm{y}}\right) \quad [2.4]$$

Rotation is related to fluid circulation and vorticity, two other fundamental concepts for fluid mechanics. Circulation (Γ) is the line integral of the velocity vector around a surface (S) of a region of fluid. Circulation is calculated using the rates of rotation of the fluid:

$$\Gamma = \iint 2\omega_x dydz + \iint 2\omega_y dxdz + \iint 2\omega_z dxdy \quad [2.5]$$

In real fluids, vorticity occurs and may be created and destroyed as flow conditions change and encounter submerged objects. Vorticity is a value of how much fluid particles spin (or local rotation of fluid particles) as they propagate in flow. The internal shear forces within a fluid, possible only when the fluid has viscosity, dissipate vorticity. Vorticity (ω) may be defined as the derivative of the circulation divided by the area of the surface (S).

$$\omega = \frac{d\Gamma}{\mathrm{dA}} \quad [2.6]$$

Or in vector form, vorticity is defined as the curl of the velocity field:

$$\vec{\omega} = \vec{\nabla}\, x\, \vec{u} \quad [2.7]$$

A vortex is described as a spinning turbulent mass of fluid spiraling in flow. As fluid passes by a submerged cylinder, vortices are created on the lee side of the body, and detach periodically from alternating sides of the cylinder. This process is known as vortex shedding, and its characteristics are

dependent on the properties of the fluid, dimensions and characteristics of the body, and flow conditions. Cylinders sustain oscillatory lift (or transverse) forces from vortex shedding in the direction perpendicular to the flow. The characteristics and shedding frequency of the vortices has an effect on the induced forcing on a submerged body (Sarpkaya, 2010). Vortices shedding behind a cylinder in flow are visualized using hydrogen bubble technique in Figure 2.2.

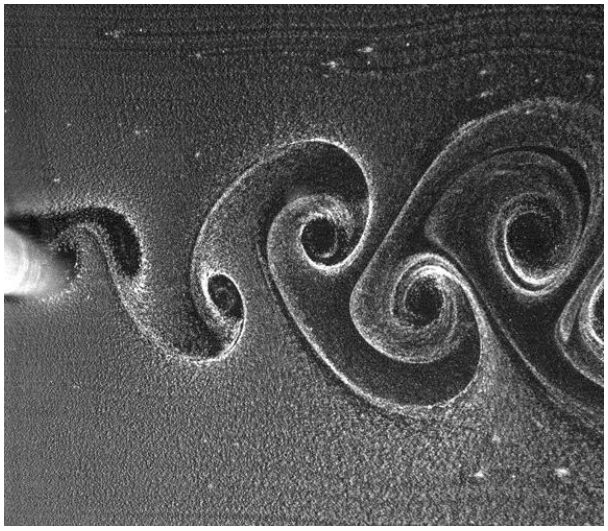

Figure 2.2: Karman Vortex street behind a circular cylinder (Kumar and Laughlin, 2012)

The image in Figure 2.2 displays the alternating nature of vortex shedding. The path of vortices propagating downstream of the cylinder is known as the von Karman Vortex street, or simply vortex street. Vortices and properties of the vortex street affect drag and lift forces on the cylinder they detach from as well as bluff bodies downstream. The dissipation of vortices in flow due to the viscosity and internal shear forces of the fluid is not well understood due to the turbulent nature of flows in which vortex shedding occurs. Previous studies have been conducted in order to quantify this dissipation in relation to the diameter of cylinder from which the vortices shed. Bloor and Gerrard (1966) found that a vortex that has propagated four diameters downstream from a circular cylinder still maintains 70% of its vorticity from its shedding point. With regards to circulation, Schmidt and Tilmann (1972) found that circulation is reduced by 50% as vortices travel from 5 to 12 diameter downstream positions.

2.2.3 Added Mass and Inertial Force

Structures submerged in coastal environments will be subjected to oscillatory turbulent flow as water particles are put in motion by the energy of passing surface waves. The term added mass, or added inertia, is used to describe the apparent (but not real) increase in mass of a body due to surrounding

fluid. Added mass represents the increase (or decrease) of the inertia of the fluid within the volume of fluid around the structure. It may also be described as the change in acceleration/deceleration of the fluid, or negative/positive inertia per unit mass of fluid. The quotient of force needed in addition to produce acceleration in the fluid divided by the acceleration of the submerged body will also describe the added mass (Sarpkaya, 2010). The effect of added mass in flow around a submerged body and the subsequent force on the body is referred to as the inertial force. The inertial force is directly related to the acceleration of the flow.

Instantaneous forces from flow on a body such as a cylinder are impossible to predict. Inertia impulsively imposed on a flow field around a body causes vortex shedding, fluctuating lift forces, and additional drag. Impulsive inertia applied to flow about a body depends on the character of the motion of the body. The concept is very complex, as flow put in motion is disturbed almost instantly by flow separation and vortex shedding. It is estimated that ideal inertia coefficients (C_M) in force calculations are accurate for the first second following the impulsive start of fluid motion (Sarpkaya, 2010). Coefficients used to represent inertial force (C_M) are at best an estimation of the added mass effect occurring during flow from wave action. Realistically, the effect of added mass changes over the entire wave cycle, making inertial force prediction using a constant coefficient impossible for an entire wave cycle. It should be noted as well that their respective effect on flow conditions cause the inertial force and drag forces to affect each other simultaneously.

2.2.4 Separated Unsteady Flow and Drag Force

As unsteady turbulent flow induced from surface waves passes around a submerged body, flow separation will occur. Flow separation is a condition that occurs when flow is sufficiently turbulent that it detaches from the fluid boundary layer around the body in the form of eddies and vortices (Figure 2.2) that pull on the body. The point of separation can occur anywhere along the diameter of the body and is dependent on the ambient flow conditions and Reynolds number (Figure 2.4). Form drag, or the drag force, is the force resulting from the separation of flow and the resulting change in pressure (Sarpkaya 2010). Calculation of drag force involves a drag coefficient (C_D). Similar to the inertia coefficient (C_M) discussed in the previous section, the true values for drag coefficients will vary during the entire wave cycle. For simplicity, values for force coefficients are averaged over a wave cycle. Drag coefficients for single cylinders are dependent upon the Reynolds number (Re) of the flow. There is a sudden drop in drag coefficient at very high Re values as the wake behind the cylinder becomes narrow and the cylinder experiences less force from vortices detaching (Figure 2.3). Previous studies on forces for submerged

cylinders conclude that the key to understanding drag and inertia forces is the understanding of the formation, properties, and behaviour of vortices (Sarpkaya 2010).

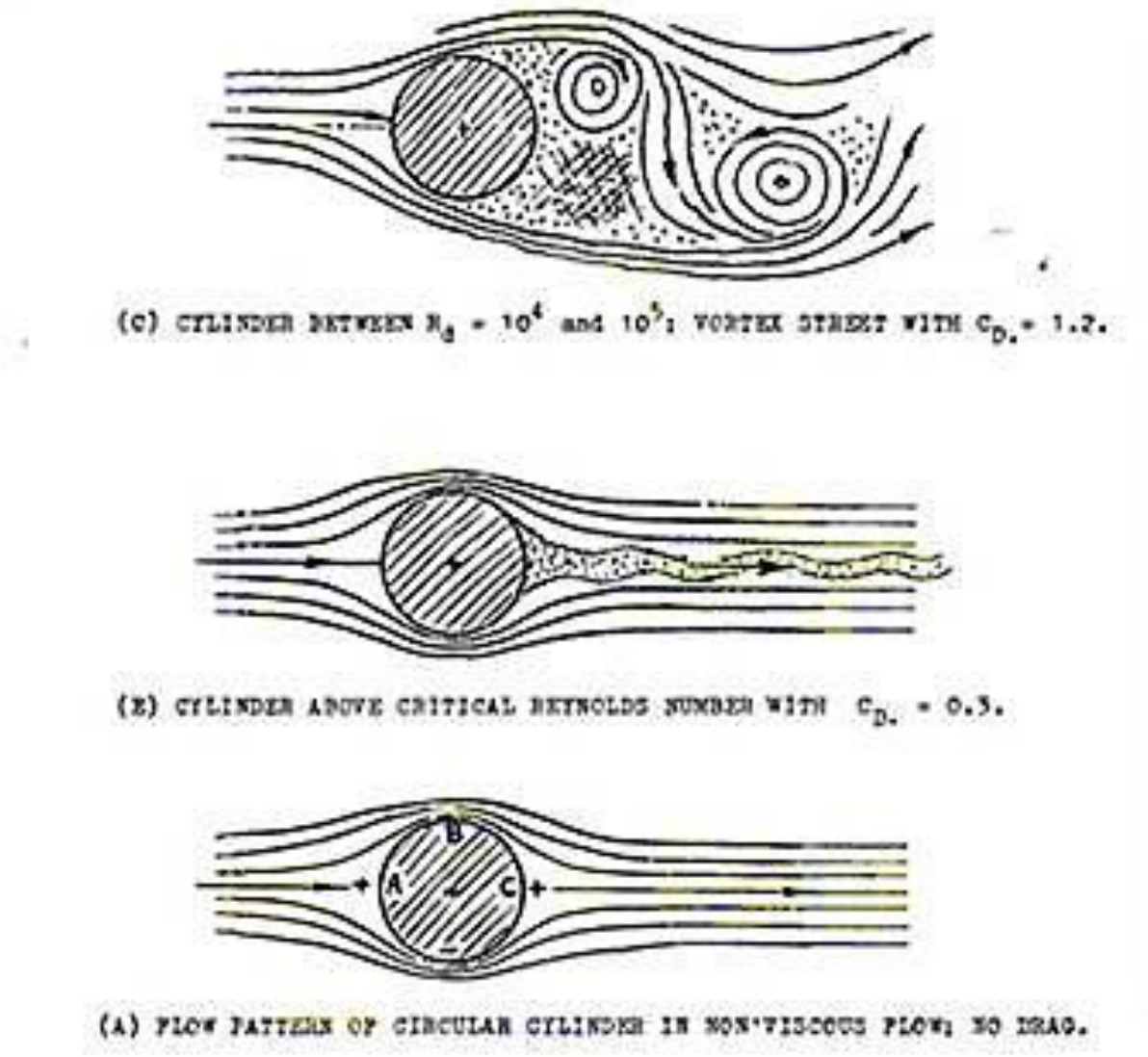

Figure 2.3: Variation of flow field and drag coefficients for cylinders with increasing Reynolds number (Hoerner 1965)

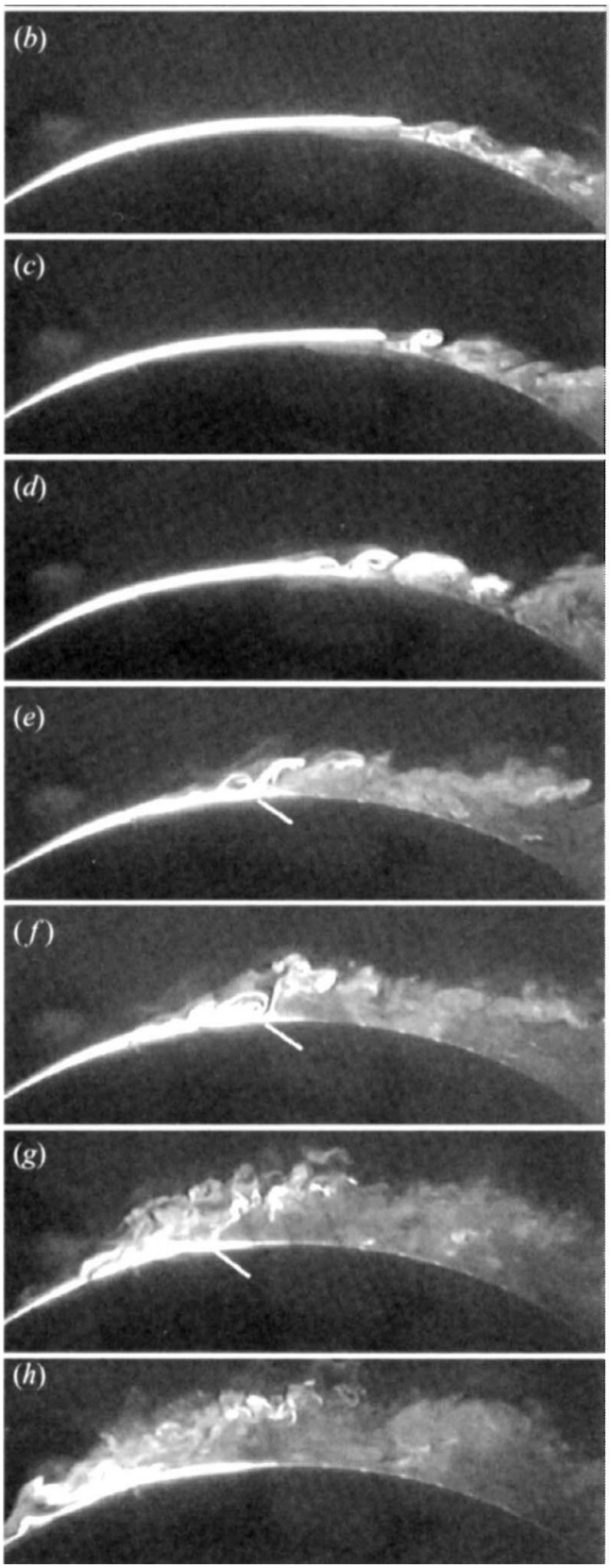

Figure 2.4: Varying locations of flow separation on a cylinder. White arrows indicate shear layer eruptions (Sarpkaya 2006b)

2.2.5 Sinusoidally Oscillatory Flow

In the science of wave induced forces, water particle motion and kinematics resulting from passing waves is often simplified as sinusoidally oscillatory flow. Sinusoidally oscillatory flow (SOF) is the back and forth movement of water particles, with displacement and velocity being represented mathematically with a sine wave. Many experiments utilize U-tanks that oscillate flow back and forth to simulate waves passing overhead. However, the orbital motions of fluid particles in real waves are more complex and can give rise to 3D effects (transverse and vertical flow) that are ignored when SOFs are used in an experiment.

An observation taken from experiments using SOFs to study forces on submerged cylinders that is applicable to this study is the reversal of wake produced when the flow direction reverses. It can be seen that flow separation points (Figure 2.4) undergo large migrations. Within one flow cycle, the boundary layer around the cylinder can change from laminar to turbulent. The flow conditions change with velocity, and therefore the Reynolds number varies over the cycle from subcritical to supercritical. Vortex shedding is affected by this and released vortices can be swept back against the cylinder (Sarpkaya 2010). Each scenario will have different vortices of different characteristics and levels of dissipation, making estimates of this effect very difficult to quantify. All these factors influence the forcing on the cylinder, particularly the drag force, over a wave cycle.

2.2.6 Transverse Forces and Strouhal Number

Transverse forces, also referred to as lift forces, are forces on the submerged body in the direction perpendicular to the flow direction. The main contributor to transverse forces in turbulent flows is the alternating nature of vortex shedding. As mentioned above, vortices formed in the boundary layer around the cylinder eventually grow and detach. The negative pressure of the vortex pulls on the cylinder and gives rise to the transverse force, and transverse pressure gradient. This is an oscillating effect, as vortices alternate shedding from opposite sides of the cylinder in the direction opposite from the last detached vortex (Figure 2.5).

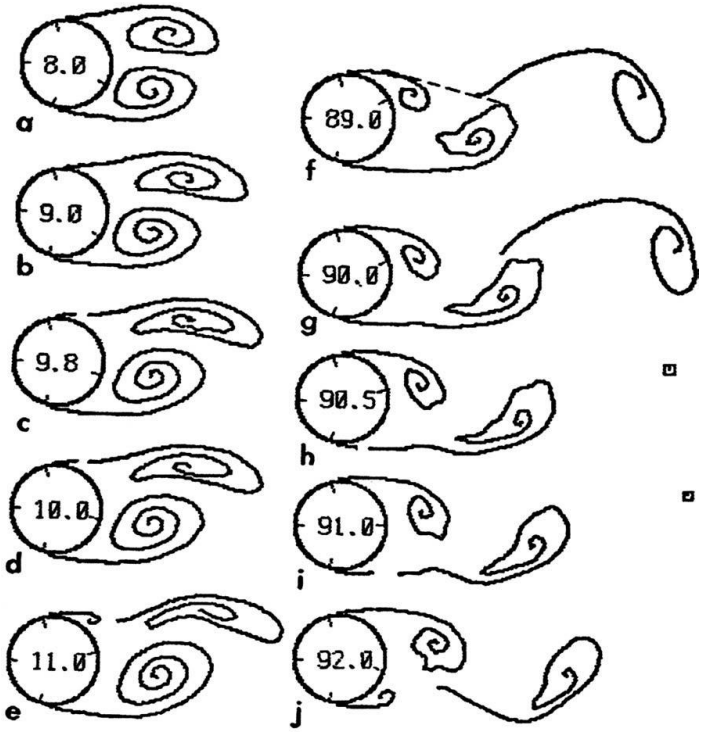

Figure 2.5: Progression of alternating vortex shedding (Sarpkaya and Shoaff, 1979b)

A significant aspect of transverse forcing is the frequency of oscillation of the force, stemming from the alternating vortex shedding. This frequency varies with the Reynolds number, amplitude of water particle velocity, geometry of the submerged body and with time over the wave cycle. The relationship between these factors and frequency of vortex shedding is the Strouhal number (St). Transverse forces often give rise to vortex-induced vibrations (VIVs). If the frequency of these forces and vibrations matches the natural frequency of the structure, it can lead to an unexpected amplification of forces. The calculation of the Strouhal number can be seen below, where f_V is the vortex shedding frequency, D is the diameter, and U_m is the velocity amplitude.

$$St = \frac{f_v D}{U_m} \qquad [2.8]$$

2.2.7 Water Particle Kinematics in Waves

Linear Wave Theory (LWF), or Airy Wave Theory, describes the characteristics of water particles kinematics and orbital trajectories induced by small-amplitude sinusoidal waves. This theory, developed by George Biddell Airy in the 19th century, employs principles used in the Navier-Stokes equations (fluid flow is inviscid, incompressible and irrotational). Linear wave theory provides simplified equations for water particle kinematics in deep, transitional, and shallow water conditions (Figure 2.6).

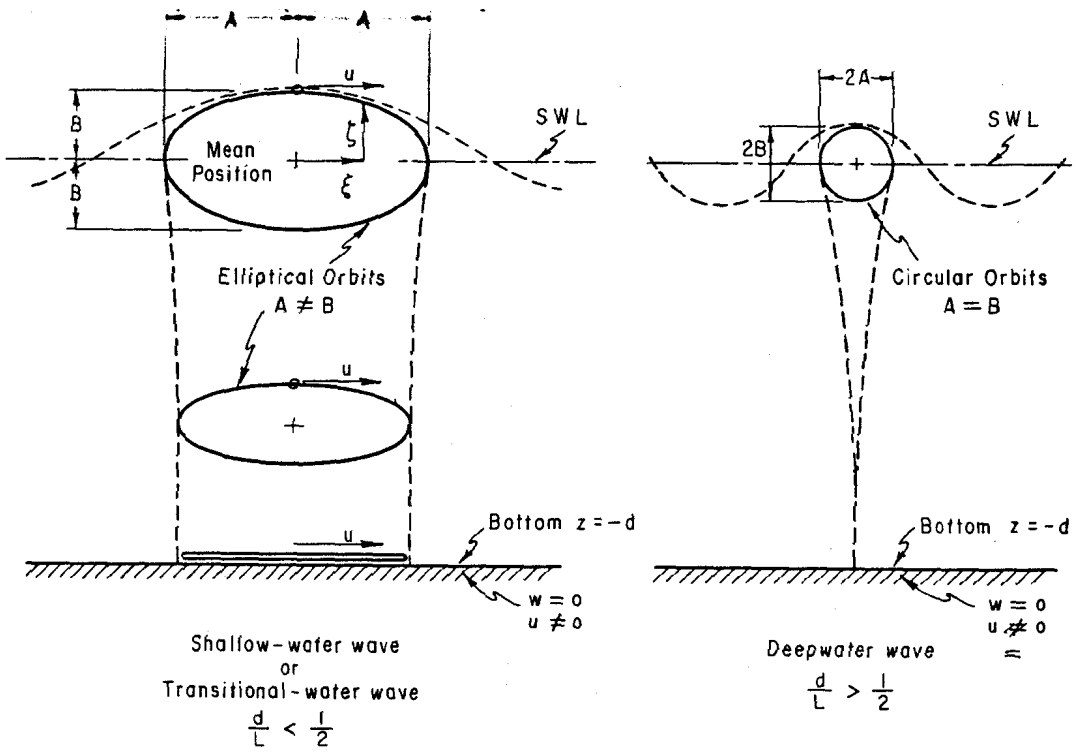

Figure 2.6: Water particle orbits with depth for shallow/transitional (left) and deep water waves (right) (CERC, 1984)

In shallow water conditions, water particle orbits are assumed to be flat, with particles oscillating back and forth as wave energy passes. The velocity of these particles is related to the wave height (H) and water depth (d):

$$u = \frac{H}{2}\sqrt{\frac{g}{d}}cos\theta \qquad [2.9]$$

When the water depth-to-wave length ratio (d/L) is less than 0.5 but greater than 0.04, the waves are classified as transitional. Water particles in transitional waves have an elliptical orbit (Figure 2.6), with a vertical component of orbital velocity. The linear horizontal (u) and vertical (w) component of orbital are written as:

$$u = \frac{H}{2}\left(\frac{gT}{L}\right)\frac{cosh\left[\frac{2\pi(z+d)}{L}\right]}{sinh\left[\frac{2\pi d}{L}\right]}sin\theta \qquad [2.10]$$

$$w = \frac{H}{2}\left(\frac{gT}{L}\right)\frac{sinh[\frac{2\pi(z+d)}{L}]}{sinh[\frac{2\pi d}{L}]}cos\theta \qquad [2.11]$$

Where T is the wave period, L is wave length, g is gravitational constant, and z is the distance from the still water level. The linear horizontal and vertical accelerations are:

$$\frac{du}{dt} = \frac{H}{2}\left(\frac{gT}{L}\right)^2 \frac{cosh\left[\frac{2\pi(z+d)}{L}\right]}{sinh\left[\frac{2\pi d}{L}\right]} cos\theta \quad [2.12]$$

$$\frac{dw}{dt} = -\frac{H}{2}\left(\frac{gT}{L}\right)^2 \frac{sinh[\frac{2\pi(z+d)}{L}]}{sinh[\frac{2\pi d}{L}]} sin\theta \quad [2.13]$$

Many analytical studies (Sarpkaya 1979) using formulae to predict linear wave forces on structures will use equations provided by LWF for the orbital velocity components, if velocity data from a current meter is not available. However, as large waves shoal in shallow water they become increasingly nonlinear. In these instances, Linear Wave Theory does not accurately predict water particle kinematics. Shallow water waves consist of long wave troughs and short, steep crests. Boussinesq (1872) described horizontal water particle velocity at the bed level (u_b) for shallow water waves over a horizontal bed using free surface deviation (η).

$$\frac{\partial \eta}{\partial t} + \frac{\partial}{\partial x}[(d+\eta)u_b] = \frac{1}{6}d^3\frac{\partial^3 u_b}{\partial x^3} \quad [2.14]$$

$$\frac{\partial u_b}{\partial t} + u_b\frac{\partial u_b}{\partial x} + g\frac{\partial \eta}{\partial t} = \frac{1}{2}d^2\frac{\partial^3 u_b}{\partial t \partial^2 x} \quad [2.15]$$

Water particle velocity below a wave crest can be estimated based on the known celerity of wave crest propagation in shallow water (c) (Kenyon and Sheres, 1990).

$$u \approx c\frac{H}{2d} = (gd)^{\frac{1}{2}}\frac{H}{2d} \quad [2.16]$$

2.2.8 Loading and Response of Cylinders in Waves

The force coefficients (C_M and C_D) associated with wave-induced forces on cylinders has been investigated and found to be related to the ratio of the amplitude of water particle displacement and the cylinder diameter (D) (Keulegan and Carpenter, 1956). This ratio is termed the Keulegan-Carpenter number (KC):

$$KC = \frac{U_m T}{D} \quad [2.17]$$

Where U_M is the amplitude of the horizontal component of the orbital velocity, and T is the period of oscillation. Wave loading on a submerged cylinder was investigated in a flume using both regular and irregular waves (in transitional wave conditions) with known KC values (Bullock et al. 1978). Their experiments for regular waves show for 8 < KC < 25 that the magnitudes of drag and inertia forces are similar. It is remarked that waves in the shallow and transitional zones show non-linearity in the forces, as the vortices shed during passage of a wave crest differ from the vortices during a wave trough (Zdravkovich, 1977). The KC number also can describe vortex evolution and the properties of the resulting vortex street (Figure 2.7).

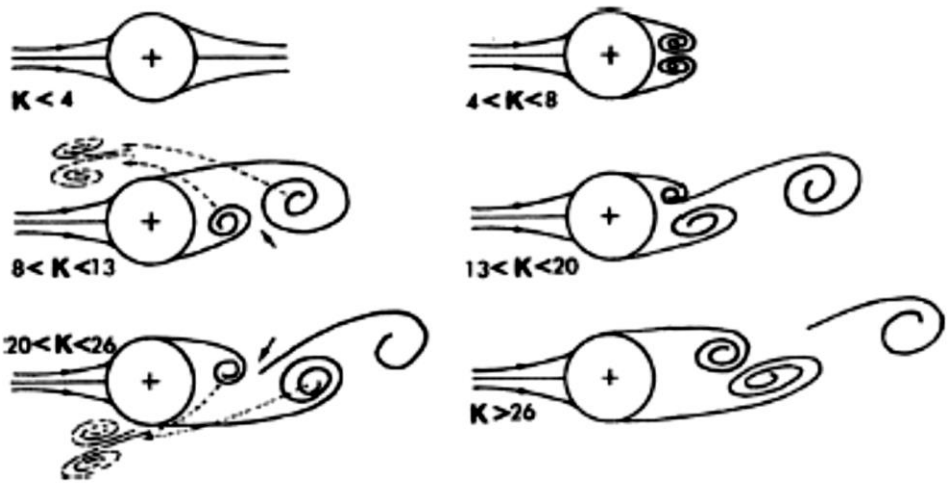

Figure 2.7: Diagram of vortex evolution about a submerged cylinder at various ranges of KC (Sarpkaya 2010)

The KC number is a valuable tool for understanding the changes in forces in different wave conditions. Using a suitable wave theory, the amplitude of horizontal velocity (U_M), can be estimated for any combination of wave height, period, wave length, and water depth. A study that investigates a large range of KC values will therefore cover a large range of wave conditions, or cylinder diameters.

2.3 Physical Models

Studies involving experiments on similar physical models were reviewed for experimental and analytical methods as well as relevant findings. Relevance was classified as models featuring wave induced forcing on a submerged cylinder, structures with multiple cylindrical components in close proximity (similar to the support posts and central pipe of an intake structure), and designs similar to an intake structure.

2.3.1 Non-breaking and Breaking Wave Loads on a Cooling Water Outfall

Mogridge and Jamieson (1978) tested a submerged cooling water outfall structure subjected to non-breaking and breaking wave loads. Experiments conducted at the National Research Council of Canada (NRC Ottawa) were used to quantify the loads an outfall structure would be subjected to, based on wave and meteorological data from the proposed construction location in the Bay of Fundy. The large diameter structure (approximately 8m diameter) is described as a capped cylinder with vents on the sides for flow to discharge (Figure 2.8). The mean water level at the proposed structure location was 8m. The model was built to a scale of 1:36 and subjected to both regular and irregular waves, resulting in non-breaking and breaking wave events.

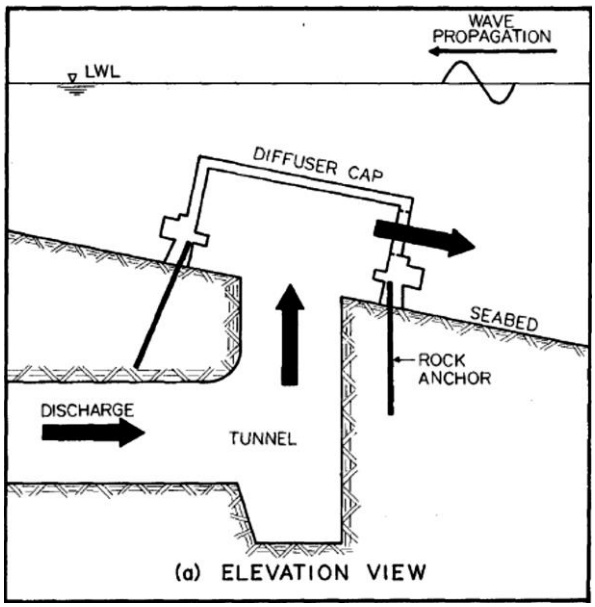

Figure 2.8: Diagram of capped water discharge structure tested at NRC (Mogridge and Jamieson, 1978)

Experiments on the model structure were performed in a wave flume at the NRC. The structure was fitted at its base with a semiconductor strain gauge force dynamometer to measure forces and overturning moments. Force results were compared between non-breaking and breaking wave loads, with separate comparisons between breaker types and wave steepness. Initial results showed that forces and moments are largest for waves tested in shallower water depths (Figure 2.9).

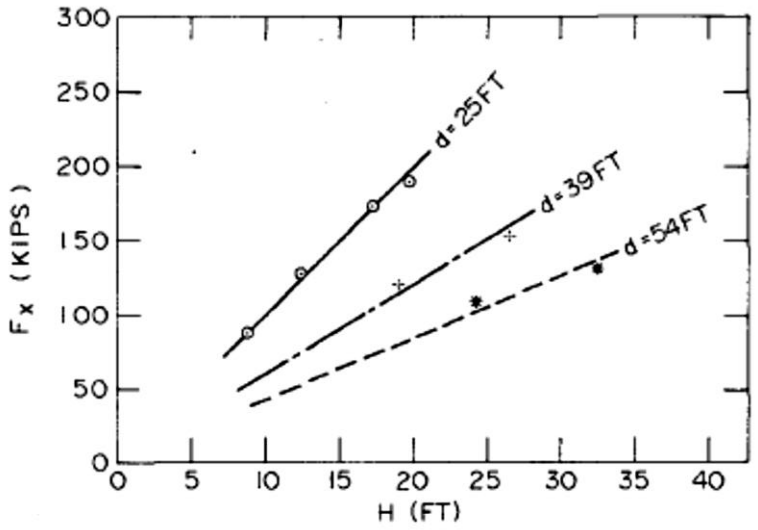

Figure 2.9: Non-breaking wave loads versus wave height for various depths (Mogridge and Jamieson, 1978)

Tests featuring regular waves were conducted to recreate a storm that had damaged the prototype structure in the region of interest. Measured forces were analyzed on a wave-to-wave basis, corresponding to the zero up-crossing wave heights. In this manner of analysis, wave period was not taken into account when analyzing forces from irregular waves. Scatter plots of force versus wave height showed much more scatter for irregular wave tests when compared to regular wave tests, due to a wider frequency range and the presence of both breaking and non-breaking waves in irregular wave tests. The variance in wave properties during irregular wave tests provided the maximum possible wave heights and steepness at the given depth. It was found that when the wave heights were not limited by water depth, interaction of wave frequencies produced groups of very high and steep waves that resulted in the largest loads on the structure. Wave loads plotted against instantaneous wave slope at the time of maximum loadings provided better correlations than plots of loads versus wave height.

Results for forces on the capped structure were compared to theoretical values for forces on a solid cylinder of similar dimensions. It was suggested that forces in the horizontal direction would be similar, with up to 25% +/- variance in force values. The theoretical results for overturning moment are suggested to be much larger, indicating that the perforated vents in the outfall structure have load reducing merits. Breaking wave loads were found to have a larger influence in the vertical (or Z direction) forces, with maximum loads always occurring in the upwards direction. This result was consistent with all breaker types. The authors concluded that a large variation in wave period only caused small variation in the loading on the structure, and that loads were more directly related to water depth and wave height.

2.3.2 Breaking Wave Forces on Slender Piles

Apelt and Piorwicz (1987) noted that forces and moments on cylinders in breaking waves are considerably larger than those that would be predicted by the Morison equation. To investigate the impact of breaking waves on a slender pile, a model was constructed consisting of a shallow water breaking zone, with waves generated in a deeper "offshore" zone. A slender aluminum cylinder fitted with force transducers was installed in the breaking zone. The bottom slope of the breaking zone was 1:15. Regular waves were used in the experiments, with varying steepness (H_O/L_O) and period (T). The aim of the investigation was to determine the statistical variation of force results with these varying parameters.

The results of the experiments indicated that force initially decreases as the depth-to-deep water wave height ratio (d/H_O) decreases, and then progresses at a consistent value. This would indicate as d/H_O increases, wave conditions around the structure eventually trend towards deep water conditions (Figure 2.10). The data was plotted separately by each deep water wave steepness values (H_O/L_O).

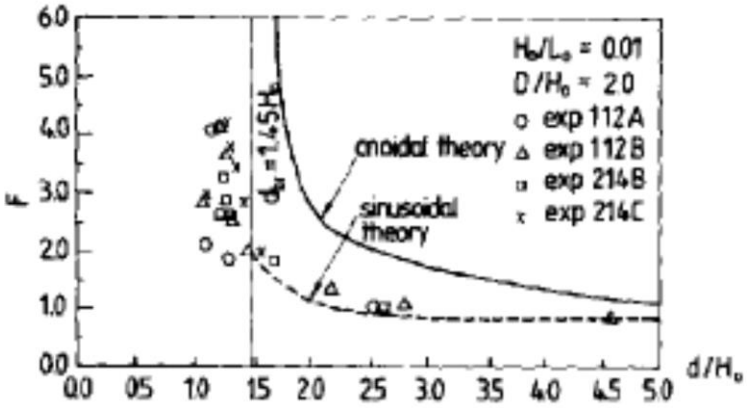

Figure 2.10: Example of force versus depth-to-wave height plot (Apelt and Piorwicz, 1987)

The authors plotted force results on probability paper in order to determine magnitudes of forces with 1% probability of exceedance. No correlation was found between varying wave steepness values. Forces of probability of 1% exceedance were plotted versus cylinder diameter-to-deep water wave height ratio to observe relative breaking wave force. The study concluded with determining that maximum wave force is related to bottom slope, relative cylinder diameter (D/H_O), and wave steepness (H_O/L_O).

2.3.3 Breaking Wave Forces on a Vertical Cylinder

Peak forces from irregular waves causing forces on an exposed vertical cylinder upon a shoal were investigated by Kyte and Tørum (1996) using a statistical approach to analyse peak forces. The cylinder

was placed upon an artificial shoal in a wave flume to simulate a realistic environment these structures are built in, and to induce wave breaking by limiting water depth. The experiments noted that large plunging breakers delivered the most force when striking the cylinder. The authors set to obtain the statistical variability of the wave impact force, as well as the variability due of the irregular waves. A Weibull distribution was plotted (Figure 2.11) using the probability equation [2.18] to extrapolate and determined the probability of certain force levels occurring.

$$P(F) = \exp(-\frac{F - F_o}{F_c})^{\gamma} \qquad [2.18]$$

The probability function uses measured force (F), location factor (F_O), scale factor (F_C), and shape factor (γ). Force measurements were placed in 0.5N bins, with data points selected from the upper end of each bin. Probability is plotted on a logarithmic scale to provide a straight line approximation in the data (Figure 2.11). This method was used to provide the "one per mille" wave force, or probability of 1 in 1000.

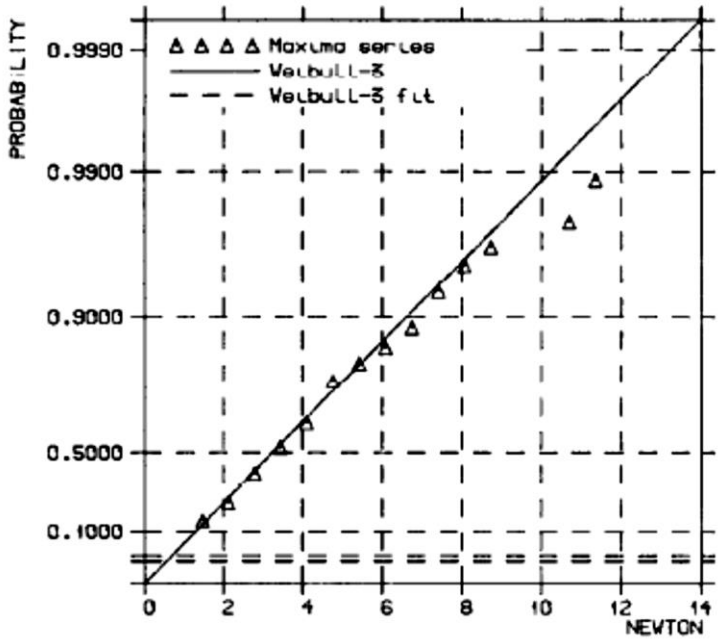

Figure 2.11: Weibull distribution of breaking wave forces (Kyte and Tørum, 1996)

2.3.4 Cylinder Groups in Breaking and Nonbreaking Waves

Physical experiments at the Coastal Research Centre (FZK) in Hannover were conducted by Sparboom et al. (2005) to record forces from waves acting on a group of slender piles. The aim of the study was to observe and quantify the influence of various pile spacing ratios and orientations in order to better

understand the effects that proximity of multiple cylinders of a structure has on forces from passing waves. Apelt and Piorwicz (1986) noted that maximum forces for multiple cylinders were of larger magnitude than for cylinders in isolation, for all configurations. Regular wave experiments were conducted in the large wave channel (GWK), with varying wave heights, periods, and steepness. A select few irregular waves were generated using a JONSWAP spectrum. The model was built at a large scale in order to mitigate scale effects.

The most notable increase in maximum wave force was for a configuration of 3 piles parallel to the wave crests, separated by 1-diameter spacing. The central pile in this configuration experienced a 60% maximum force increase during regular waves when compared to a single pile in isolation being exposed to the same wave conditions. Results of this configuration can be seen in Figure 2.12. There was an increase in force (approximately 20%) for the same geometrical configuration using 3-diameter spacing. These results contrast with previous studies on pile proximity (Zdravkovich, 1977), that found proximity effects are significantly reduced if distance between piles exceeds a 2.2-diameter spacing.

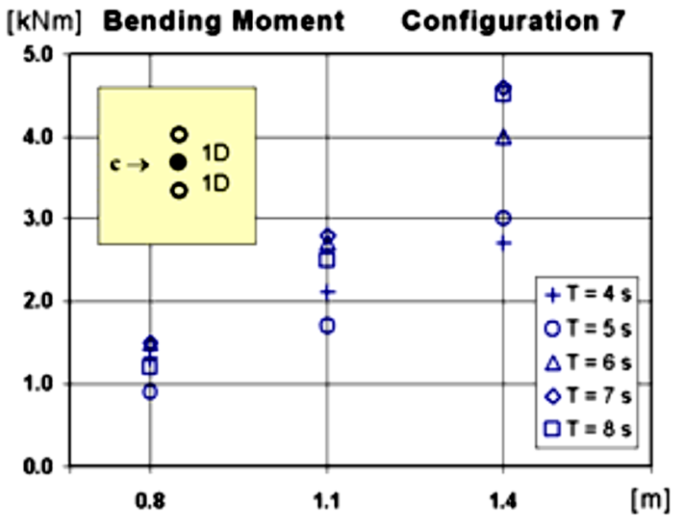

Figure 2.12: Increase in measured force with increase in wave height for various periods (Sparboom et al., 2005)

It was suspected that there may be an effect on maximum force for a central pile surrounded by other piles from sheltering, but this was not observed. All cases experienced an increase in force when compared to single cylinder configuration, which is consistent with similar experiments involving multiple cylinders. The authors conclude by stating that there are no reliable formulae for calculating wave forces for cylinders in close proximity while accounting for interference amplification effects, and that experimental work such as this study should be used as guidance for design.

2.3.5 Forces on Cylinder Array of Varying Spacing in Random Waves

To determine effects of inter-cylinder gap as well as angle of wave incidence on forces, physical experiments were carried out in a large wave flume on an array of 3 cylinders (Kudeih, Cornett, & Nistor, 2010). Forces from random waves were measured, with different significant wave heights (H_S) and peak periods (T_P), as well as a superimposed current. Each wave condition was repeated using variable spacing between cylinders as well as orientation of the array to simulate varying angles of wave incidence. The angle of wave incidence varied between 0^o (all 3 cylinders in-line perpendicular to the flow), 30^o, 60^o, and 90^o (all 3 cylinders in-line parallel to the flow). Maximum wave force experienced on an array of cylinders perpendicular with the flow direction is plotted (Figure 2.13) as a function of spacing.

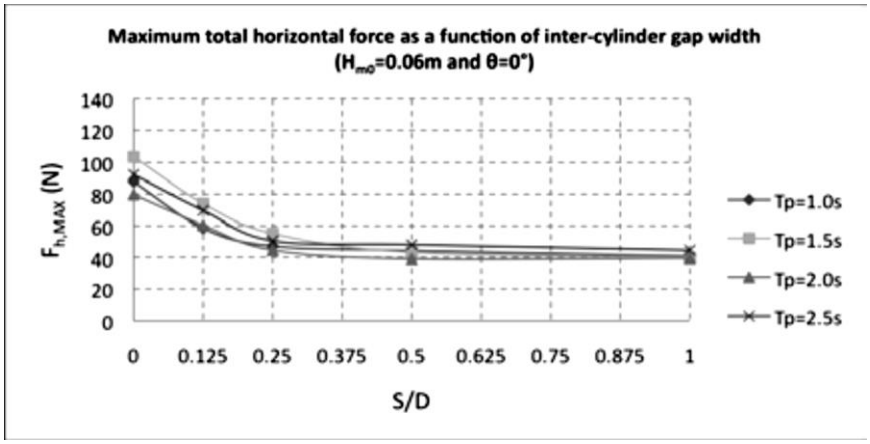

Figure 2.13: Maximum in-line forces with variable spacing and peak period for a transverse array of 3 cylinders (Kudeih, Cornett, & Nistor, 2010)

From Figure 2.13 it is clear that peak period of wave conditions had very little effect on maximum inline force the cylinder array was subjected to. Force decreased with spacing until S/D = 0.25, after which force remained constant. The spacing range in this experiment is very small compared to other experiments of this nature, with the maximum S/D (spacing-to-diameter) value of 1 much lower than the critical spacing of 3.5 determined by Zdravkovich (1977). These experiments did reaffirm however the amplification of wave forces when cylinders are placed in proximity, with force results for each test being consistently double than the force value for measured on a single cylinder.

2.4 Analytical Models

Studies that investigated wave forcing on submerged structures were reviewed for analytical methods and solutions. Common empirical formulae used in the topics of wave forcing were reviewed for use in the analysis portion on this study.

2.4.1 Morison Equation

Research and experiments by Morison et al. (1950) at the Fluid Mechanics Laboratory of the University of California (Berkley) were conducted for estimating wave forces on submerged piles. The result was the development of an empirical formula for wave forcing on submerged cylinders. The equation attempts to describe the force experienced by cylinders due to wave induced oscillatory kinematics. This equation became known as the Morison equation or MOJS equation, to include the names of the 4 researchers (Morison, O'Brien, Johnson, and Schaaf).

$$F = \rho\, C_M\, V \left(\frac{du}{dt}\right) + \frac{1}{2}\rho\, C_D\, A\, u|u| \qquad [2.19]$$

This formula predicts the total in-line force experienced by a cylinder in oscillatory flow. When the kinematics vary along the cylinder, the total force can be obtained by integrating the equation over the cylinder length. The 1st and 2nd terms represent the contributions due to inertial and drag forces, calculated from the horizontal component of water particle kinematics in waves. The inertia force, represented by the first term in the equation, is determined by the volume of the cylinder (V) and the flow acceleration (du/dt). Flow accelerating around a body gives rise to the fluid mechanics phenomenon of added mass, the accelerative force exerted on the mass of water displaced. This is accounted for with the inertia coefficient (C_M). The drag force component is composed of the area of the cylinder perpendicular to the flow direction (A) and the square of the velocity. Drag force depends on a drag coefficient (C_D). The inertia and drag coefficients vary with different structural geometry, orientation, and wave and flow conditions. Determining force coefficients and their relation to these factors is the objective of many studies on wave forcing on submerged structures. Varying inertia and drag coefficients allows for roughness of the cylinder, proximity effects, KC number, and Reynolds number effects to be accounted for.

There has been criticism of the Morison equation, claiming it to be a primitive and simple manner of solving an incredibly complex fluid dynamics problem (Sarpkaya 2010). There is no explicit way to include the effect of vortex shedding on the force, and particle kinematics in the direct vicinity of

submerged structures are hard to obtain accurately by either measurement using instrumentation or estimating the effect using a suitable wave theory (Burrows et al., 1997). Controlled laboratory conditions can produce accurate results for predicting force using the Morison equation, but field studies on wave forces show extensive scatter for force coefficients. This is due to the complexity of the sea state and the resulting effects on flow separation and vortex formation. In reality, wave loads are a function of wave properties, wave-induced kinematics, flow-structure interactions and structure responses, and are very difficult to predict with high accuracy.

The Morison equation remains the industry standard for design of submerged cylinders experiencing forces from passing waves and the vast majority of research in this field is conducted on force coefficient determination rather than development of new equations. All experiments or studies researching force coefficients mentioned in this review use some form of the Morison equation.

2.4.2 Methods for Fitting Force Coefficients

Inertia and drag coefficients used in the Morison equation for various wave conditions are determined by fitting the Morison equation to a force record from experiments of wave forcing on a submerged body. There are several methods used for fitting coefficients, with varying levels of accuracy.

Morison's Method

When Morison developed his formula for wave induced forcing on cylinders, drag and inertia coefficients were determined by isolating instances where either water particle velocity or acceleration was zero, and only one force term (and one unknown coefficient) composed the total force measured on the cylinder (Morison et al., 1950). These specific times in the wave record are observed by plotting water particle acceleration and velocity and comparing with the force record (Figure 2.14).

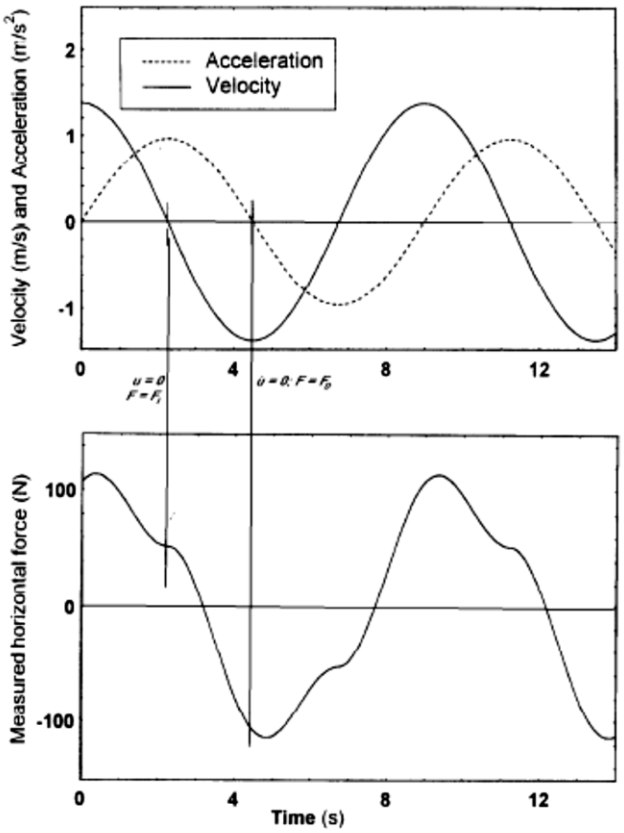

Figure 2.14: Water particle kinematics compared with force record (Morison et al., 1950)

Morison derived force coefficients for given wave conditions by claiming that when velocity is maximum and acceleration is zero, total force is equal to the drag force ($F_{t1} = F_D$). For the inertia term, coefficients were calculated when acceleration is maximum and velocity is zero ($F_{t2} = F_I$). Force coefficients can then be determined using the following equations:

$$C_D = \frac{2F}{\rho D * u|u|} \quad [2.20]$$

$$C_M = \frac{4F}{\pi \rho D^2 * \frac{du}{dt}} \quad [2.21]$$

This is a relatively simple method for determining force coefficient, but is not very accurate. Morison recognized this and attempted to reduce the amount of error by computing coefficients for many waves and averaging the results. This method ignores many data points that can be used to improve accuracy.

Least Squares Method

Previous studies for determining force coefficients for cylinders in regular and irregular waves have compared fitting techniques and noted that the method of least squares is more accurate than Morison's method for predicting peak forces induced from wave loading (Isaacson et al. 1991). The least squares fitting technique has the advantage of computing force coefficients for an entire time record. This method looks at Morison equation predicted forces as an approximation of the measured force and computes the linear coefficients. An example equation for this method can be seen below.

$$\varepsilon^2 = \frac{1}{N}\sum_{t=1}^{n}(F_{theory}\,(t, C_D, C_M) - F_{Experiment}(t))^2 \qquad [2.22]$$

The function is computed until the residual difference (ε^2) is minimized. This will return multiple solutions for C_D & C_M with lowest ε^2 value. A disadvantage of this method is often a minimized residual difference will provide coefficients that provide a close fit throughout the time record, but do not necessarily match the peaks in the forces well.

Force coefficients for a cylinder were evaluated for both regular and irregular waves by Burrows et al. (1997) using the method of least squares with successful results. The following equations were employed:

$$K_i = \frac{\sum_{i=1}^{n} F_o\,\dot{u}\sum_{i=1}^{n} u^4 - \sum_{i=1}^{n}\dot{u}\,u|u|\sum_{i=1}^{n} F_o\,u|u|}{\sum_{i=1}^{n}\dot{u}^2\sum_{i=1}^{n} u^4 - \sum_{i=1}^{n}\dot{u}\,u|u|\sum_{i=1}^{n}\dot{u}\,u|u|} \qquad [2.23]$$

$$K_d = \frac{\sum_{i=1}^{n} F_o\,\dot{u}\sum_{i=1}^{n}\dot{u}\,u|u| - \sum_{i=1}^{n}\dot{u}^2\sum_{i=1}^{n} F_o\,u|u|}{\sum_{i=1}^{n}\dot{u}\,u|u|\sum_{i=1}^{n}\dot{u}\,u|u| - \sum_{i=1}^{n}\dot{u}^2\sum_{i=1}^{n} u^4} \qquad [2.24]$$

Where F_O is the observed (experimental) force, u is water velocity, ů is water acceleration. K_i and K_d are terms that represent inertia and drag coefficients respectively, along with cylinder geometry. Davies et al. (1990) provides a simplified version of the above equations, assuming the time average term $\sum_{i=1}^{n}\dot{u}\,u|u|$ is theoretically zero:

$$K_i = \frac{\sum_{i=1}^{n} F_o\,\dot{u}}{\sum_{i=1}^{n}\dot{u}^2} \qquad [2.25]$$

$$K_d = \frac{\sum_{i=1}^{n} F_o\,u}{\sum_{i=1}^{n} u^2|u|} \qquad [2.26]$$

Least squares fitting has been applied successfully to evaluating forces on groups of cylinders as well (Hildebrandt et al. 2008). Different methods used in each experiment would ultimately yield different values for Morison coefficients. A certain amount of error is to be expected and investigating proven methods and deviations is the most efficient way to obtain the best fit.

Weighted Least Squares Method

When designing structures to be subjected to wave forces, the maximum loads carry higher importance. Using force coefficients that will predict peaks in force more accurately is addressed by using a weighted least squares method.

$$\varepsilon^2 = \frac{1}{N}\sum_{t=1}^{n}[F_{Experiment}(t) - F_{theory}\,(t, C_D, C_M)]^2 * [F_{Experiment}(t)]^2 \qquad [2.27]$$

This method for fitting puts additional emphasis on the experimental force term. A similar method to the one used by Burrows et al. (1997) was employed by Hur and Mizutani (2003) for a weighted least squares method. The authors wrote terms for each force and fitted with the weighted measured force (F_O):

$$f_D = \frac{1}{2}\rho * A * u|u| \qquad [2.28]$$

$$f_I = \rho * V * \mathring{u} \qquad [2.29]$$

$$C_D = \frac{\sum(F_o^3 * f_D)\sum(F_o^2 * f_I^2) - \sum(F_o^3 * f_I)\sum(F_o^2 * f_D * f_I)}{\sum(F_o^2 * f_D^2)\sum(F_o^2 * f_I^2) - \left[\sum(F_o^2 * f_D * f_I)\right]^2} \qquad [2.30]$$

$$C_M = \frac{\sum(F_o^3 * f_I)\sum(F_o^2 * f_D^2) - \sum(F_o^3 * f_D)\sum(F_o^2 * f_D * f_I)}{\sum(F_o^2 * f_D^2)\sum(F_o^2 * f_I^2) - \left[\sum(F_o^2 * f_D * f_I)\right]^2} \qquad [2.31]$$

A variation of weighted least squares was also used by Burrows et al. (1997), employing a Heaviside function to weight the peaks in force:

$$\varepsilon^2 = \sum_i H(|F_o| - T) * (F_o - F_e)^2 \qquad [2.32]$$

The Heaviside function operates such that H(x) = 0 for negative forces, and H(x) = 1 for positive. The term T represents a parameter for threshold force levels that can be adjusted to depend on the higher levels of force (Experimental force (F_O) and estimated force (F_e)). T is an integer number of standard

deviations of the force required to best fit the time series. The weighted least squares method is widely accepted as the most accurate method for fitting the Morison equation for purposes of obtaining force coefficient data for use in design. An extensive study by Wolfram and Naghipour (1999) concluded that out of 10 different methods of fitting the Morison equation to an experimental force record for purposes of determining force coefficients of the cylinder, weighted least squares provided the least amount of error.

Spectral Fitting Method

Force coefficients for a cylinder in irregular waves may be determined by using the energy density spectra of the force and current velocities. The Keulegan-Carpenter number (KC) of a wave-cylinder interaction is proportional to wave amplitude and thus the square root of the wave energy spectral density. This method assumes the random wave is considered as the sum of sinusoidal waves with one wave for each elemental frequency. It is also assumed that water particle velocity is a random Gaussian process with a mean of zero. Borgman (1967) utilized a method involving a cross-spectral analysis between force and current velocity energy density spectra with the following transfer function:

$$H_{uf}(\omega) = \frac{S_{uf}(\omega)}{S_u(\omega)} \qquad [2.33]$$

The water particle velocity spectrum was developed using a wave theory, which introduced some error. The drag force term, calculated using the square of the water particle velocity, is linearized as:

$$u|u| = u * \sigma_u \sqrt{\left(\frac{8}{\pi}\right)} \qquad [2.34]$$

The comparative analysis of force coefficient fitting techniques by Wolfram and Naghipour (1999) concluded that spectral fitting methods provide poor results when compared with experimental forces and the largest amount of scatter when coefficients are plotted with KC.

Wave-by-wave Analysis

Davies et al. (1990) proposed wave-by wave analysis techniques in order to obtain more data for drag and inertia force coefficients from their regular and irregular wave tests on fixed cylinders. Each wave was defined by the zero-upcrossing of the horizontal component of the water particle velocity time series corresponding to the waves tested. From each individual wave cycle, drag and inertia force coefficients can be fitted, and a KC value can be calculated corresponding to the specific wave. For

irregular waves, the KC number is calculated using a velocity determined in the following manner [2.35], rather than maximum horizontal velocity (DNV, 2011). Velocity (u) value used for determining the KC value is calculated using the standard deviation of the fluid velocity (σ_u).

$$u = \sqrt{2} * \sigma_u \quad [2.35]$$

2.4.3 Analysis of Force Coefficients

The majority of studies reviewed in the field of wave forcing on cylindrical structures focus on determining force coefficients with varying wave conditions and structural geometry. Agerschou and Edens (1965) used first and fifth order wave theories to determine force coefficients for a single submerged cylinder. The authors concluded with minimal scatter that for a single cylinder undergoing linear wave forcing in isolation that force coefficients of $C_M = 2$ and $C_D = 1.2$ may be used. In reality, these coefficient values will change according to factors such as proximity to other bodies, wave non-linearity and steepness of the waves. These factors affect the water particle kinematics, vorticity of the flow around the structure, and pressure distributions; which all affect the forcing and therefore the force coefficients for the structure. Studies and experiments have been conducted to observe the relationships between force coefficients for single and multiple cylinder structural configurations with varying wave and current properties.

Morison Force Coefficients for Application to Random Seas

Regular and irregular wave experiments on the Christchurch Bay Tower Compliant Cylinder were conducted to evaluate force coefficients for a single cylinder, represented by a surface piercing pile (Burrows et al., 1997). Using the least squares fitting method, force coefficients from all random wave tests were determined with a wave-by-wave analysis and plotted against the Keulegan-Carpenter number of the wave (Figure 2.15).

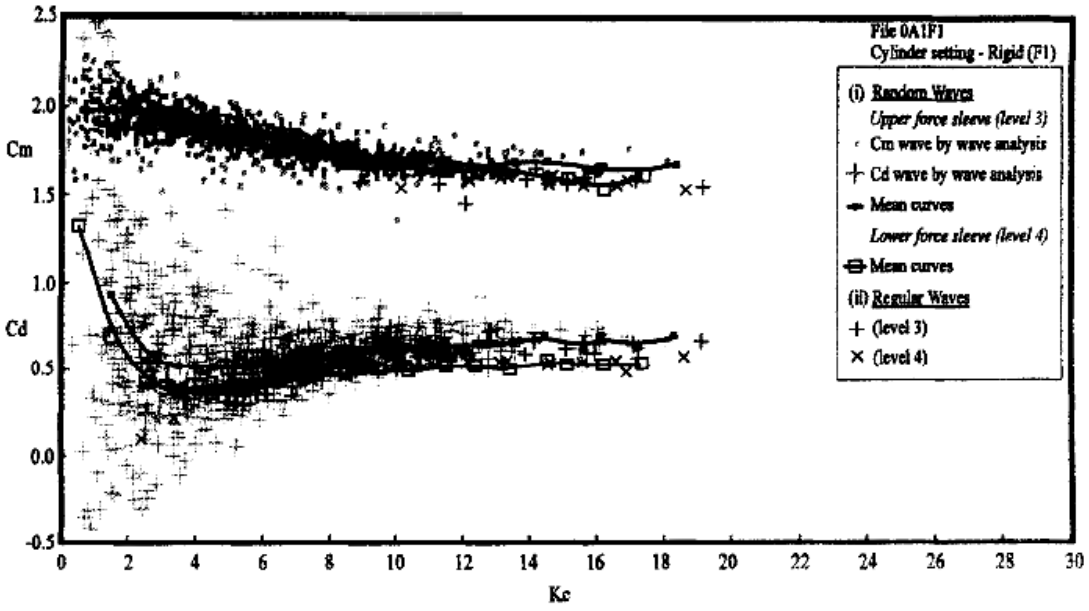

Figure 2.15: Force coefficients for a single cylinder in random waves (Burrows et al., 1997)

The force coefficients in Figure 2.15 are similar to the single cylinder values ($C_M = 2$, $C_D = 1.2$) determined by Agerschou and Edens (1965). Coefficients determined from regular wave tests show good agreement with coefficients from random waves. These results were used along with experimental velocity data to plot a Morison equation predicted force time series for comparison with measured force (Figure 2.16).

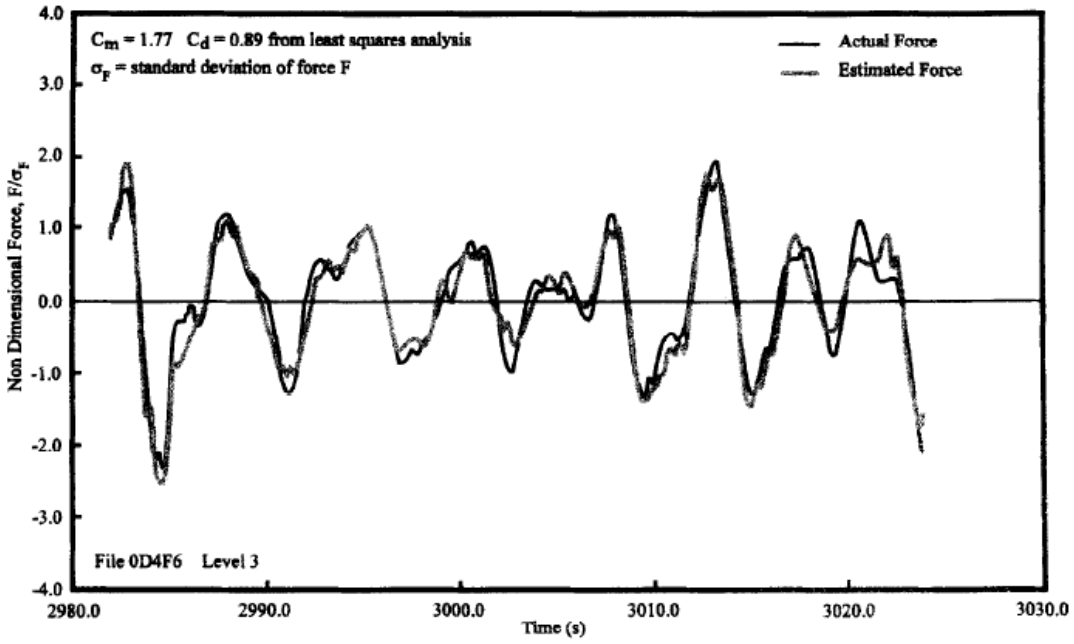

Figure 2.16: Experimental and Morison predicted horizontal in-line force on a single cylinder in random waves (Burrows et al., 1997)

Figure 2.16 shows that the Morison equation was able to predict forcing for a single cylinder in random waves with reasonable accuracy. The two series are in perfect phase; however the Morison equation fails to accurately predict the peak positive force in most waves. The authors concluded that force coefficient data from their study is applicable to any isolated cylinder in random waves, and that the least squares method is a favourable approach to analysis of force coefficients.

Breaking Wave Forces on a Vertical Cylinder

Goda (1973) derived an empirical equation for breaking wave forces on a vertical cylinder. As part of his studies on breaker types, Goda noted that the larger forces were experienced from plunging breaker waves due to larger water particle velocities induced by the wave breaking. Using regular waves, wave height was plotted versus horizontal force to determine the relationship. The author developed an equation for total force on a cylinder involving diameter (D), depth (d), maximum wave amplitude (η_{max}), deep water wave height (H_O), and force coefficient β_F. The force coefficient was fitted using scatter plots of wave height versus mean horizontal force, with a standard deviation provided for each coefficient value. This method applies to breaking wave forces on surface piercing cylinders, rather than fully submerged cylinders.

$$F = \beta_F \rho g D H_0 (d + \eta_{max}) \quad [2.36]$$

$$\eta_{max} = 0.75 H_0 \quad [2.37]$$

Proximity Effects on Drag Force between Two Circular Cylinders

Researchers in fluid dynamics have investigated changes in drag force coefficients (C_D) for multiple cylinders spaced closely in a flow field. The most significant findings from these experiments were published by Zdravkovich (1977) from his experiments with 2 cylinders in a wind tunnel. Zdravkovich investigated proximity effects, the changes to the flow field around a cylinder by the proximity of another cylinder, by testing variations of the spacing parameter L/D; where L is the centre to centre spacing between 2 cylinders of diameter D. Two arrangements were tested: Tandem (in-line with flow direction), and side-by-side (aligned perpendicular to flow direction).

In previous experiments it had been noted that two cylinders at close proximity produced changes in respective flow fields and created new patterns (Zdravkovich, 1977). Close proximity creates unexpected flow conditions that affect pressure distributions, changes in vortex shedding patterns, and affects drag forces. To illustrate these effects, Zdravkovich plotted the empirical interference drag coefficient (C_{Di}) vs. L/D. The interference drag coefficient is the difference between recorded drag coefficient for the

proximity affected cylinder, and the drag coefficient for the same cylinder in isolation. Figure 2.17 shows drag coefficients for the downstream cylinder in a tandem arrangement, and Figure 2.18 shows drag coefficients for a cylinder in a side-by-side arrangement.

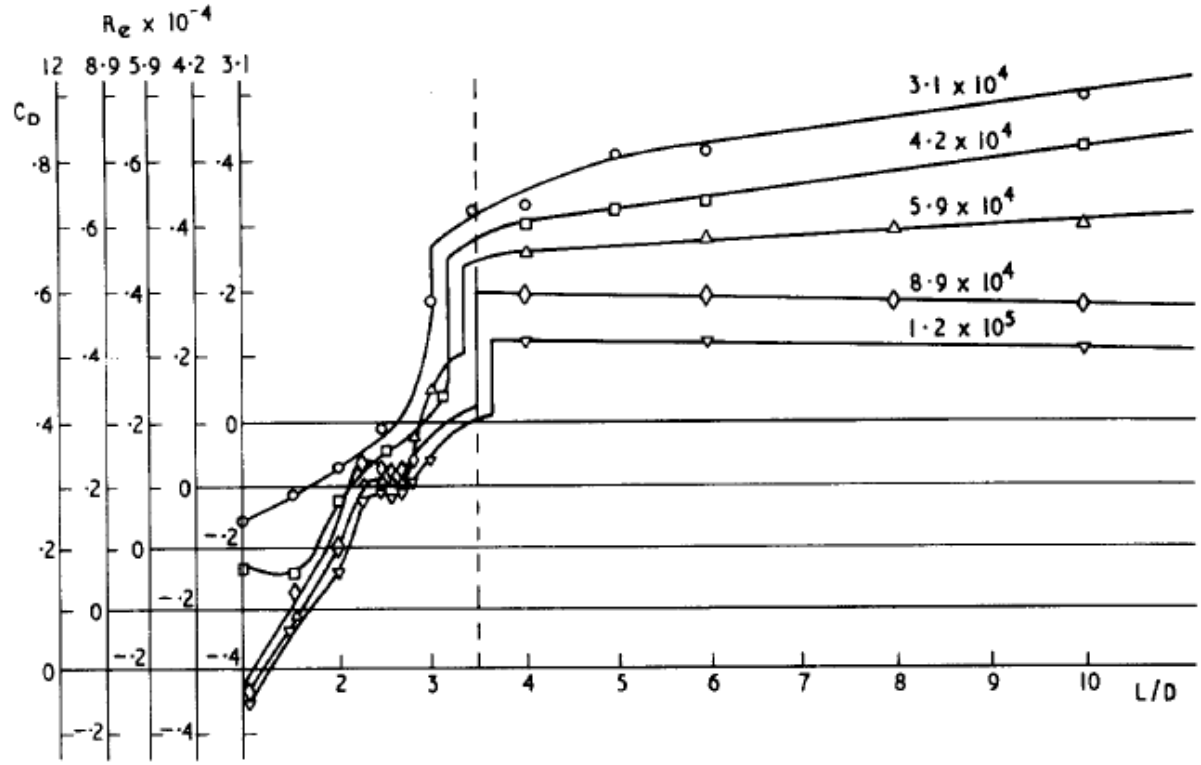

Figure 2.17: Effects of spacing on drag coefficient of downstream cylinder (Zdravkovich, 1977)

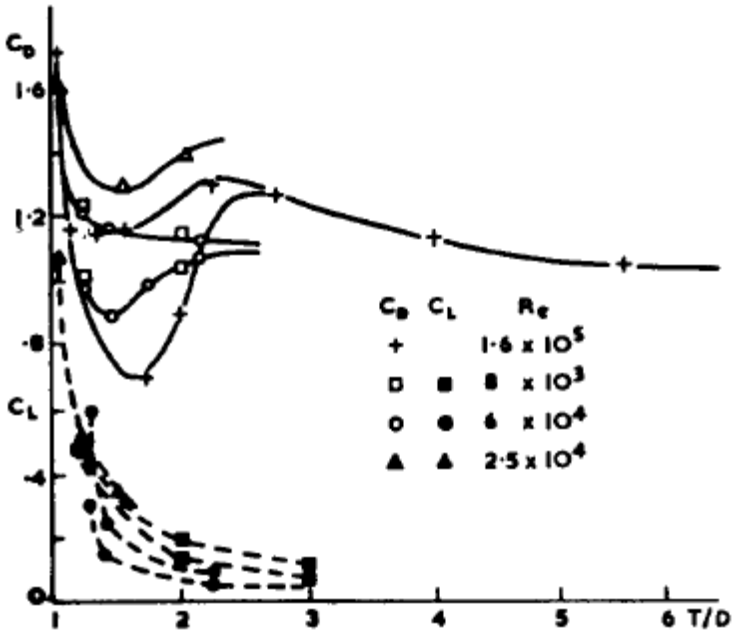

Figure 2.18: Effects of spacing on drag coefficients for side by side cylinders (Zdravkovich, 1977)

There are 2 notable discontinuities from these results. For the tandem arrangement, there is a large jump in downstream drag coefficients at spacing of 3.5 T/D, where T is the centre to centre spacing between 2 cylinders in the side-by-side configuration. Past this critical spacing it is concluded that proximity effects are drastically lowered. For the side by side arrangement, the discontinuity in the data occurs at 2.2 L/D, with cylinders behaving intermittently as an upstream or downstream cylinder in a tandem arrangement.

Circular Array of Cylinders with Central Pipe

The first experiments conducted to fit force coefficients for a circular array of cylinders were carried out by Sarpkaya (1979). The study attempted to quantify the change in force coefficients on cylinders in sinusoidally oscillating flows due to interference effects of nearby cylinders in a ring formation with a large central pipe cylinder. Proximity to other cylinders in a flow field has numerous and complex changes on hydrodynamic forces on a cylinder by effecting changes in pressure distribution, vortex shedding frequency, and dynamic response of cylinders in the array. Effects on force coefficients were quantified in terms of flow and structural parameters.

Previous experiments on tandem cylinders show proximity effects are noticeable when cylinders are in-line with flow for spacing to diameter ratio (L/D) of less than 3.5, and L/D less than 2.2 for side by arrangements (Zdravkovich, 1977). Tandem arrangements were shown to have a large effect on drag

forces, with interference effects from a nearby cylinder effecting vortex properties observed from a single cylinder in similar flow. In the case of in-line cylinders, reduction of the drag coefficient for the downstream cylinder is caused by shielding by the upstream body, as well as occurrence of earlier transition in the boundary layers around the cylinder due to enhanced approaching flow turbulence.

Sarpkaya's experiments involved a 15 tube array with 1 central pipe of larger diameter. The diameter of the outer tubes was changed once to obtain results for 2 different configurations. To fit the force coefficients with forces measured in the experiments, Sarpkaya employed the standard Morison equation with the diameters of all cylinders included summed. Kinematics for the water particle orbital velocities of the sinusoidally oscillating flow were calculated using linear wave theory (LWT):

$$F = -0.5L\rho C_D * \Sigma D_i * U_m^2|\cos(\omega t)|\cos(\omega t) + 0.25\pi L\rho C_M * \Sigma {D_i}^2 * U_M \omega \sin(\omega t) \quad [2.38]$$

Force coefficients were then fit to the data using Fourier averaging equations that included a term for velocity amplitude, which is a key component to the KC number. Force coefficients and the dominance of either inertia or drag forces are strongly related to the KC number (Sarpkaya & Tuter, 1974), reflecting a strong dependence on the interaction of the wakes shed from the outer tubes and central pipe.

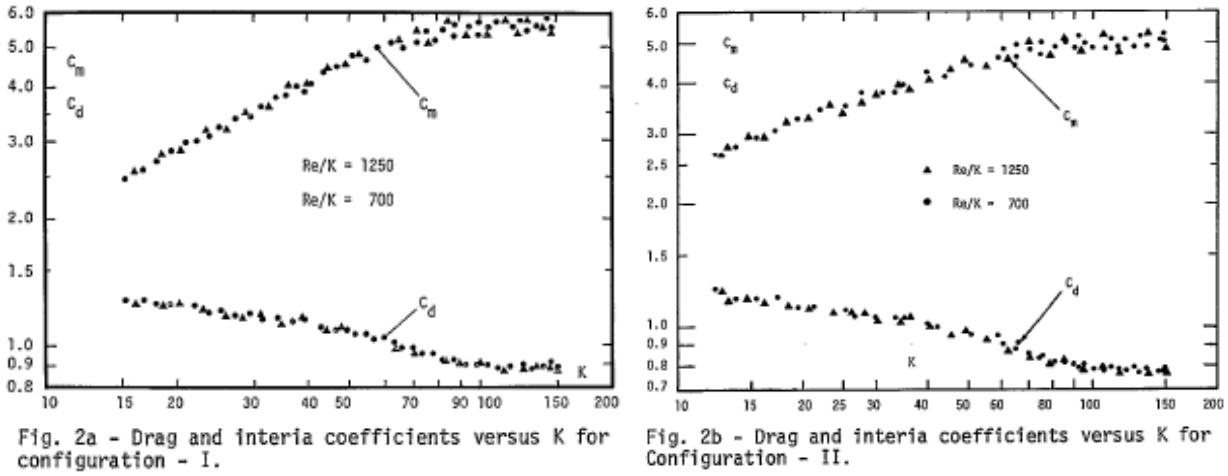

Fig. 2a - Drag and interia coefficients versus K for configuration - I.

Fig. 2b - Drag and interia coefficients versus K for Configuration - II.

Figure 2.19: Force coefficient data for 2 configurations of circular tube arrays with central pipe (Sarpkaya, 1979)

The inertia coefficients in Figure 2.19 are considerably larger than values predicted by potential theory and by experiments on isolated cylinders (Agerschou and Edens, 1965). This is due to the large fluid mass entrapped within the bundle of pipes. Drag coefficient values are lowered by the bundle effect, as noticed in previous experiments with multiple cylinders. The drag coefficient correlates negatively with the KC number. Smaller KC values, and therefore smaller in-line velocity amplitudes, lead to vortices

arriving at the 2nd cylinder weaker than at large KC values, which increase turbulence and wake interaction. The coefficients were found to not be strongly dependent on Reynolds number at relatively small values of KC.

Experiments involving structural configurations such as the one tested by Sarpkaya have a near infinite numbers of possible arrangements of two or more bodies and flow characteristics. Experiments are often conducted to serve a practical interest and to provide force coefficient data for a specific design. Further testing on cylinder proximity effects was done by changing the cylinder spacing more dramatically. Using a square array, it was observed that forcing from sinusoidally oscillating flow on cylinders with 2 diameter spacing was 60% larger for an array with 5 diameter spacing (Sarpkaya 1985), further evidence of the existence of critical spacing values affecting wave forces among arrays of cylinders.

Empirical Formulae for Energy Loss due to Flow Separation

Some studies have used a pressure based approach for estimating forces on piles due to waves, rather than using the Morison equation. Kakuno et al. (1996) used this approach for deriving empirical formulae for 2 square piles in close proximity, using the perturbation approach based on small amplitude and simple harmonic wave theory. The experiments were conducted using transitional waves. Using velocity potential theory, dynamic pressure exerted on the piles is defined as:

$$P = -\rho \frac{\partial \Phi}{\partial t} \qquad [2.39]$$

Where P is pressure, Φ is velocity potential, and ρ is fluid density. From linear potential theory, the velocity potential due to waves is defined as:

$$\Phi = \frac{gH}{2\omega} \frac{\cosh k(z+h)}{\cosh kh} \Phi e^{-i\omega t} \qquad [2.40]$$

Flow separation was solved numerically, using a discrete vortex method. The solution includes the wave properties and pile dimensions to provide an estimate of energy loss due to flow separation. Two separate expressions for velocity potential were needed for the front and back side of the pile array:

$$\Phi_{-} = e^{ikx} + \left[\frac{ikC'}{ikC'-1} + ikBM - (kB)^2 M^2\right] e^{-ikx}; \quad (x < 0) \qquad [2.41]$$

$$\Phi_{+} = \left[\frac{1}{1-ikC'} + ikBM - (kB)^2 M^2\right] e^{ikx}; \quad (x > 0) \qquad [2.42]$$

Where B is the half distance between 2 cylinders, and M is an expression accounting for the geometry of the configuration (M=S/4B). S is half of the cross-sectional area of the cylinder, and C' is a complex value blockage coefficient:

$$C' = C'_r + iC'_i \quad [2.43]$$

$$\frac{C'_i}{B} = \frac{|T|kH}{(\frac{9\pi}{4})(\frac{a}{B})^2 kB} * \frac{sinh^2 kh + 3}{sinh 2kh + 2kh} f \quad [2.44]$$

The real part of C' is dependant of the geometry of the cylinder and can be calculated from potential theory. The imaginary part above consists of terms for the half-width of the opening between cylinders (a), transmission coefficient (T), and an empirical coefficient (f = 1.5 for rectangular cylinders, 0.75 for circular). The formulae listed above provide a good fit when compared to experimental forces by accounting for energy lost to flow separation as waves pass by the cylinders. Similar to the Morison equation, an empirical coefficient needs to be derived to provide a more accurate description of measured force.

2.5 Numerical Models

Highly complex fluid mechanics processes that influence forcing from wave induced kinematics, such as flow separation, vorticity, and proximity effects on adjacent flow fields, are difficult to recreate using numerical models. For these reasons, physical models are still relied on for determining wave induced forcing on submerged structures. For bodies of simple geometry, such as a single submerged pile, numerical modelling has proven an effective method for predicting wave induced forces. Some numerical models have the capability of simulating nonlinear sea state conditions and subsequent water particle kinematics.

2.5.1 Numerical Models for Wave Forces on Offshore Structures

The National Renewable Energy Laboratory (NREL) has designed a numerical model for estimating irregular wave forces on cylindrical wind turbines. FAST (Fatigue, Aerodynamics, Structures and Turbulence) uses a linear irregular wave model and Morison's equation to compute forces from waves on offshore structures (Jonkman and Buhl, 2005). A flow chart of the computational procedure used in FAST can be seen below (Figure 2.20).

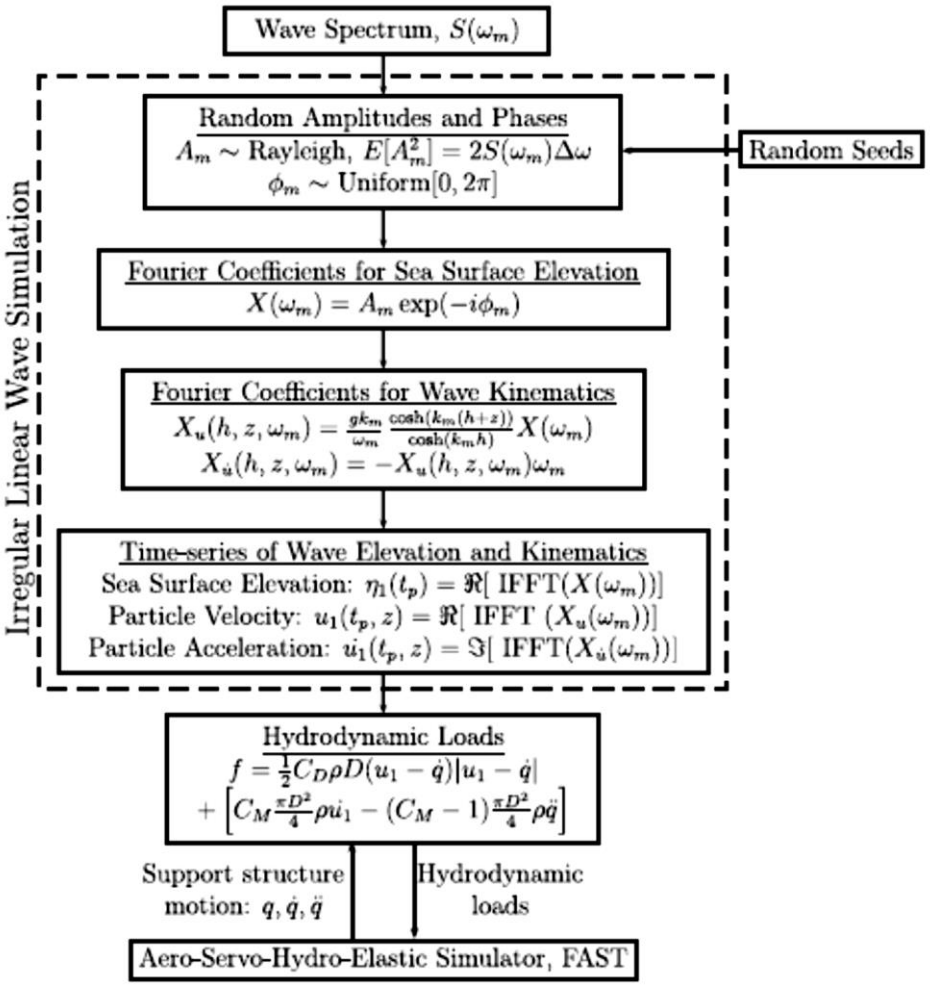

Figure 2.20: Flow chart for calculating wave loads on offshore wind turbines in FAST (Jonkman and Buhl, 2005)

Wind turbines and other large offshore structures are typically located in shallow waters. The waves in these regions tend to be nonlinear due to the effects of wave shoaling and breaking. The version of FAST referenced above is only programmed to estimate water elevations and water particle kinematics for linear waves. Agarwal and Manuel (2011) incorporated an irregular nonlinear model with FAST to better predict wave forces on cylindrical structures in intermediate and shallow water zones. The authors applied 2nd order transfer functions to water elevation and kinematics predictors in the FAST model in order to better simulate nonlinear waves. The results showed of their study showed that the nonlinear model was better able to predict extreme loads and long term response than the linear model.

Marino et al. (2011a) developed a fully nonlinear wave model that included breaking wave impact loading on offshore wind turbines, with an objective to innovate current models such as FAST by simulating extreme loading conditions. In order to generate a wave simulator that represented the

stochastic environment of the sea, a linear irregular sea state was generated by establishing a wave spectrum. Then, on critical sub-domains where large waves and high impact loads are expected to occur, a fully nonlinear solver for wave conditions is used. The nonlinear free surface is simulated using potential theory and a higher-order boundary element method (HOBEM) is used to discretize Laplace's equation. The result is a code that simulates overturning plunging breakers. The force calculation procedures used in the model depend on the wave conditions. If no breaking is occurring, a standard Morison equation is used. In the event of large plunging breakers, a wave impact force is computed. It was found that peak forces for nonlinear breaking waves can be up to 3 times higher than peak forces estimated using a standard linear wave approach.

2.5.2 Numerical Model for 2-D Detached Flow past Bluff Bodies

Lian (1988) used a numerical model to study two-dimensional separated flow around a plate in sinusoidally oscillating flow. The model assumes that the vorticity is concentrated in thin boundary layers around the body and in thin free shear layers. Potential flow was assumed outside these layers. A flat vertical plate was considered, with flow separation points assumed to be stationary at the sharp edges of the plate. The inline force was modelled, and the drag and inertia coefficients were determined. These force coefficients are plotted in Figure 2.21 with results from experiments by Keulegan and Carpenter (1956).

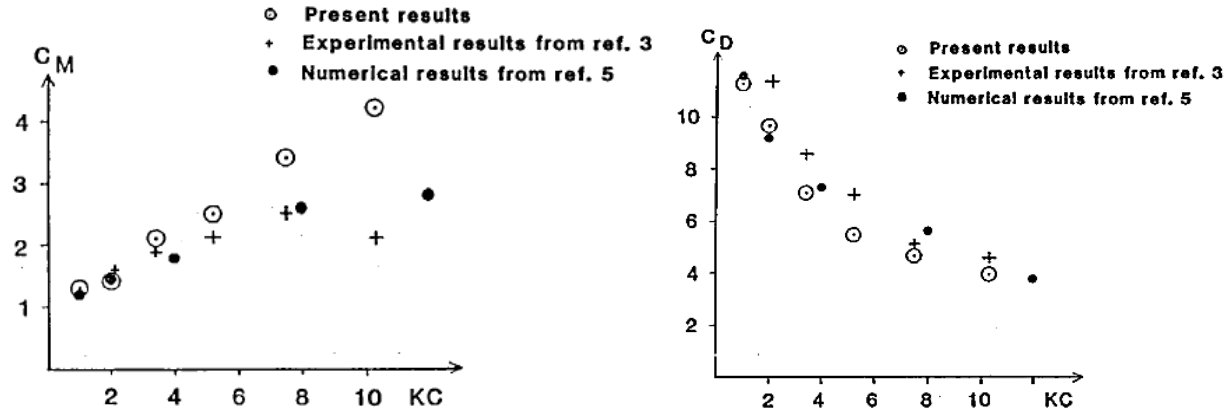

Figure 2.21: Numerical and Experimental results for force coefficients of a flat plate (Lian, 1988)

2.6 Discussion

The literature review on the topic of wave forces on submerged structures presented in this section provided insight for experimental methods and analysis techniques. The fluid mechanics behind wave induced forcing were investigated so that results of forces from wave testing could be analyzed for their relation to wave and current properties, and so that accurate conclusions could be drawn.

For predicting wave induced forcing on submerged structures, the Morison equation remains the standard method. There are criticisms of this equation. The Morison equation inadequately incorporates the complex physics of separated flows (Sarpkaya, 2010), and requires the input of water particle kinematics that often measured or predicted with significant error. However, a review of current literature showed that most research focuses on the derivation and analysis of force coefficients, and that efforts to develop a new equation for predicting wave forcing have proved largely unproductive (Burrows et al., 1997).

Some numerical models are able to predict wave induced forces on a single cylinder in isolation. There are models that replicate complicated sea states to model water particle kinematics for use in the Morison equation (Agarwal and Manuel, 2011), as well as methods that attempt to replicate separated flow and vorticity behind cylinders and plates (Lian, 1988). There are also criticisms of present day numerical methods. Sinusoidally oscillating separated flow is not accurately predicted using shear-layer discretization because there is still uncertainty in the location of separation points on a circular cylinder (Sarpkaya, 2010). There are currently no numerical models that accurately account for proximity effects between multiple cylinders in large breaking waves.

Current understanding of proximity effects on wave forcing involving multiple cylinders have been developed mainly through physical modelling (Zdravkovich, 1977) (Sarpkaya, 1979). These findings are important for design considerations, as unexpected force amplification can occur due to proximity effects depending on the geometry of a proposed structure. Through extensive review of current literature, it was determined that no formula or model exists for predicting wave induced forcing on multiple cylinders in proximity (Sparboom et al., 2005), necessitating physical experiments such as those of this study. There is no fluid-mechanically satisfying closure model for turbulence (Sarpkaya 2010), necessitating the use of physical models to further our understanding of wave-structure interactions.

3.0 Physical Model

Wave-induced forces on a submerged intake structure have been investigated through use of a physical model. In this section the model design and set up is described.

3.1 Description of Model

A physical model was built to replicate a submerged sea water intake structure located in a shallow water environment where various levels of irregular wave breaking would occur. To accomplish this, artificial bathymetry was constructed in a large wave flume so that the natural transformation of waves propagating from intermediate to shallow depths would be simulated automatically. The model intake structure was designed to be a scale replica of typical intake structures currently used in industry and was installed on the sloping bathymetry in front of a set of large glass windows. The model was outfitted with instruments to measure wave conditions, velocities, and the 6-axis forces acting on the model intake structure. The model was designed to simulate the wave transformation and breaking processes occurring in nature, accurately measure wave-induced forces acting on the submerged intake structure, while minimizing scale effects as much as possible.

3.1.1 Facilities

All experiments in this study were conducted at the Canadian Hydraulics Centre (CHC), a business unit of the National Research Council Canada (NRC), an organization in the Canadian federal government that focuses on research and development. The CHC conducts applied research and provides technical services in the fields of hydraulics, cold-regions technologies, and coastal engineering through extensive expertise in numerical and physical modelling.

3.1.2 Large Wave Flume

The Large Scale Wave Flume (LWF) at CHC is used for 2-dimensional experiments on coastal structures and processes, and is capable of large scale models and high Reynolds numbers in flow. The concrete flume is 97m long, 2m wide and 2.7m deep. The ability to conduct tests at large scale allows for reasonably accurate representations of wave breaking and turbulent flow. The flume is fitted with progressive porosity expanded-metal absorbers (metal beaches) at the end (Figure 3.1) to absorb and dissipate wave energy with less than 5% wave reflection (CHC, 2009).

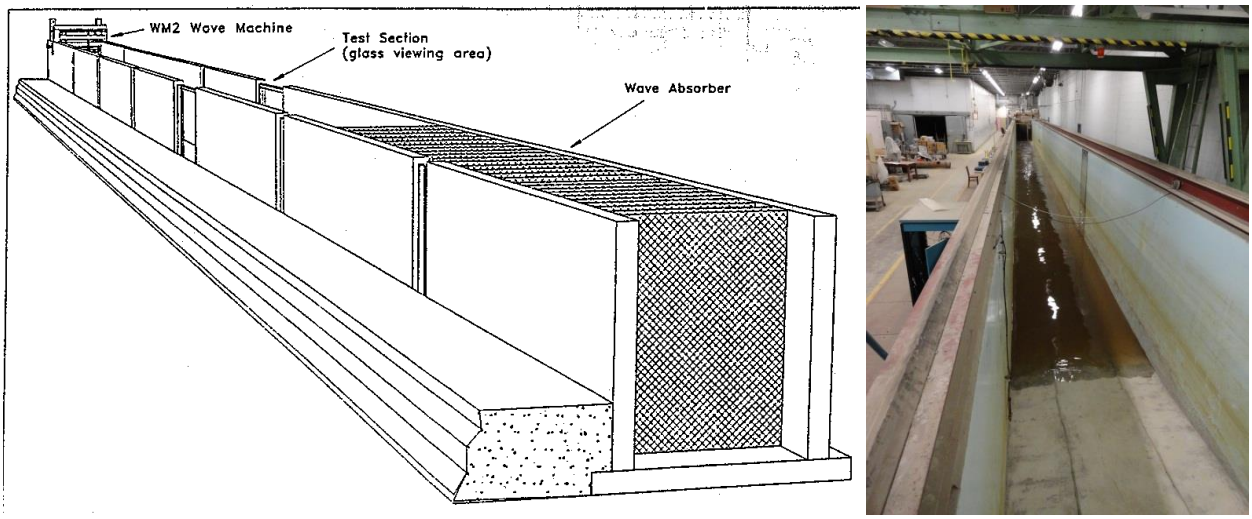

Figure 3.1: Drawing of Flume layout (left) from Davies (1992) and view down LWF towards wave maker (right)

Approximately 50m from the wave maker, or the half-way point of the flume, 5m of viewing windows were installed to provide side views and opportunity to film the experiments. The windows are made of thick glass panes fitted with a plexiglass outer layer, spanning the total height of the flume walls.

Figure 3.2: Observing a breaking wave through viewing windows

Water to the flume is supplied from a large head tank located in the 4th storey of CHC. Water is pumped up to the head tank from a sump using large pumps. Gravity is then used to provide water to the flume, through 2 pipes that fill each end of the flume simultaneously to ensure even water levels. This allows for the entire flume to be filled evenly in the likely event there is a structure or an artificial bathymetry constructed in the flume. Along each pipe supplying the flume is a valve that is used to drain water back to the sump.

3.1.3 Wave Generation

Waves are generated by a large wave paddle at the end of the flume capable of generating waves up to 1.1m in height. The wave generator is powered by 2 hydraulic actuators that allow for independent motion of the top and bottom of the wave paddle (Davies et al., 1992). This means that the waves can be generated in flapper mode, where the bottom of the paddle is fixed like a hinge, or by piston mode, where the bottom and top actuators move and the paddle remains vertical. The wave machine is sophisticated enough that a combination of paddle and piston mode is possible, with the entire paddle oscillating back and forth as well as flapping. In this study, the wave machine was operated in piston mode. The machine is controlled using a digital controller and specialized SWG software. To generate waves, the hydraulic actuators are programmed to follow a pre-compiled digital command signal specifying position as a function of time.

Figure 3.3: Wave maker at end of Large Wave Flume

The wave machine is equipped with a sophisticated active wave absorption (AWA) system that was not used in this study. This system allows reflected waves propagating back towards the wave paddle to be absorbed by the paddles movements. Incoming waves reflected from an installed structure or beaches are detected by a 5-probe array in the deep water section close to the wave machine. The wave machine senses water levels at the paddle and adjusts its movement to account for reflected waves and maintain the wave conditions in the flume specified by the test program. Reflection from the shallow sloped gravel beach used in this study is quite low, so the AWA system was not used.

3.2 Model design

3.2.1 Similitude

Similitude and scaling in a physical model is of critical importance when attempting to accurately represent processes occurring at the prototype scale. Proper similitude is defined as the condition when all inputs affecting reactions in the model are in proportion between prototype and model, or are too insignificant a factor to affect outcomes (Hughes, 1993). A common scaling parameter used in coastal engineering models is Froude scaling. A physical model conducted with Froude scaling stipulates that the Froude number of the flow at model scale is same as the Froude number at prototype scale. The Froude number quantifies the relative influence of inertial and gravitational forces on water particles.

$$\left(\frac{u}{\sqrt{gL}}\right)_m = F_m = F_p = \left(\frac{u}{\sqrt{gL}}\right)_p \qquad [3.1]$$

Froude similitude was used for experiments in this study since gravitational and inertial forces are dominant in comparison to viscous forces (Reynolds similitude). This study combines Froude similitude with a geometrical similitude, which implies geometric similarity between model and prototype. The geometric, or length, scale ratio for model-to-prototype in this study is 1:15. Table 3.1 below provides scale factors for several important quantities in the experiments. Since a Reynolds similitude was not used, the model scale Reynolds values are smaller than the full scale values, indicating that the flow is likely to be more turbulent at full scale. Another property that does not remain constant when using Froude scaling is surface tension. Surface tension effects are more important at smaller scales, and can affect wave breaking and air bubbles. All results from experiments in this study have been converted from model scale to full scale using the relationships shown in Table 3.1.

Table 3.1: Scaling relationships for physical model

Property	Scale Factor
Froude Number (Fr)	$N_{Fr} = 1$
Length (m)	$N_l = 15$
Time (s)	$N_t = \sqrt{N_l} = 3.87$
Mass (kg)	$N_m = N_l^3 = 3{,}375$
Velocity (m/s)	$N_v = \frac{N_l}{N_t} = 3.87$
Acceleration (m/s^2)	$N_a = \frac{N_l}{N_t^2} = 1$
Force (N)	$N_f = N_m * N_a = 3{,}375$
Reynolds Number (Re)	$N_{Re} = N_v * N_l = 58.05$
Surface Tension (N/m)	$N_\sigma = \frac{N_F}{N_l} = 225$
Fluid Density (kg/m^3)	$N_\rho = \frac{N_m}{N_l^3} = 1$

3.2.2 Intake Structure Design

The design of the model intake structure was based on typical submerged intake structures currently used in industry. The 3 key components identified to be consistently present in a commercial intake structure are the intake pipe, velocity cap, and posts that support the velocity cap. The model structure was designed with these 3 structural elements, in a manner as simple as possible to eliminate uncertainties in the distribution of force on different areas of the structure from passing waves. Using common commercial designs of submerged intake structures as a basis, the model structure was designed with horizontal circular velocity cap, 4 evenly spaced cylindrical pipe posts, and a central open inlet pipe. It is noted that inflow through the pipe was not simulated in this study. Similar intake structures used in industry often shut off flow through the pipes during large wave conditions. A base plate was designed to support the 4 posts and cap. This plate connects to the base plate of the central pipe, which supports the structure.

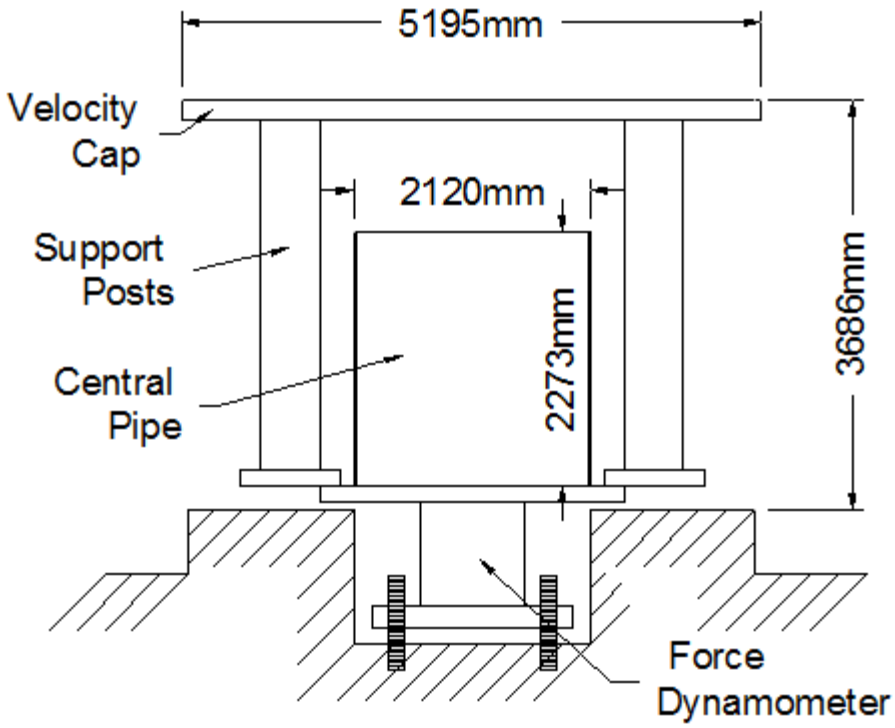

Figure 3.4: Drawing of model intake structure design

The velocity cap was made of ½"marine plywood, to maintain low weight and to prevent swelling and contortion of the material when submerged for long periods of time. The posts were made of 3/8" diameter aluminum tubing. Aluminum collars were welded to the top of the posts so that the cap could be screwed to the top of the posts. The base plate for the posts was made of aluminum to reduce weight while maintaining strength, and also so that the posts could be welded to the plate. The plate was pressure water cut in a cross shape (Figure 3.5) to reduce weight. The central pipe is cut from 5" PVC. The plate for the pipe was also ¼" PVC so that the pipe could be attached to the plate using PVC cement.

Figure 3.5: Pipe and posts aluminum base plate (left); Central pipe with PVS base plate (right)

Table 3.2: Dimensions of model intake structure in model and prototype scale

Structure Component	Model Scale (m)	Full Scale (m)
Cap diameter	0.357	5.195
Pipe diameter	0.141	2.12
Post diameter	0.035	0.524
Pipe height	0.138	2.273
Post height	0.206	3.09
Total structure height	0.247	3.686

To record forces from passing waves acting on the submerged intake structure, the model intake was mounted on a load cell or force dynamometer. The dynamometer was bolted to the bottom plate of the intake pipe so that any forces experienced by the velocity cap, posts, or central pipe would be transferred to the dynamometer. The dynamometer was levelled, its bottom surface fitted with a ½“ aluminum plate and bolted to the bottom of a shallow well cast into the concrete sea floor. The force dynamometer is described in more detail in the Description of Instrumentation section (3.4.2).

Figure 3.6: Images illustrating how the central pipe and ultimately the entire structure are supported by dynamometer

In an effort to quantify how much of the total force from passing waves acted on each of the separate structural components, the model structure was designed in a manner so that components of the structure could be separated from the central pipe and dynamometer, controlling which portions of the intake structure transferred force to the force dynamometer at the base. It is for this reason that 2 separate plates were used for the posts and for the central pipe. The first configuration of the structure to be tested was the entire structure resting on the force dynamometer so that forces on any component of the structure, in any direction, would be measured (Figure 3.7). This is known as configuration 1, or full structure.

CONFIGURATION 1

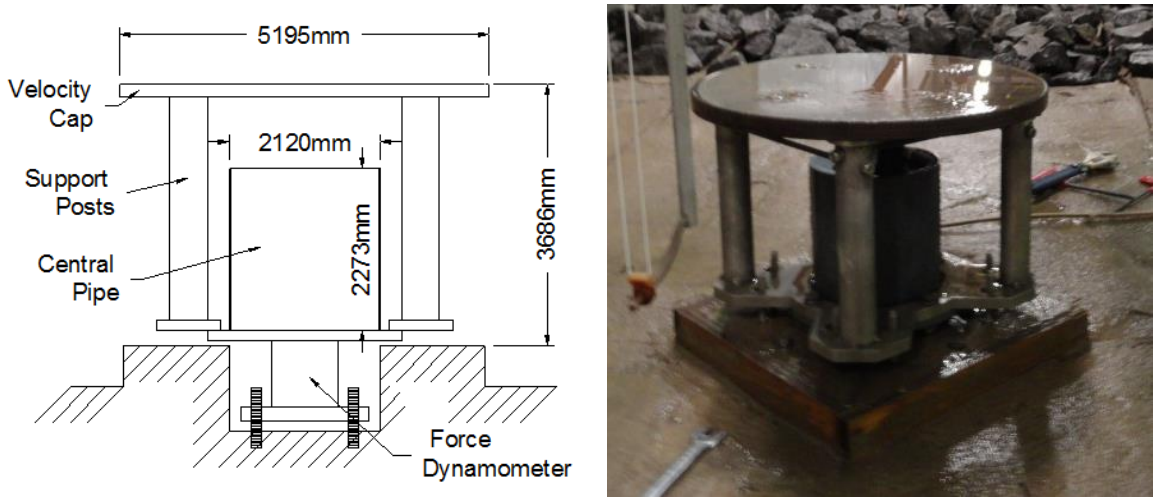

Figure 3.7: Full structure configuration

The next structural configuration would only measure forces on the central pipe. The surrounding frame, consisting of the 4 posts and the velocity cap, was needed to remain in place so that the same hydrodynamics in the vicinity of the structure would be replicated but with the experimental

hydrodynamic forces on the central pipe being isolated and recorded. The aluminum base plate which the frame rests on was unbolted from the PVC base plate of the central pipe. The aluminum plate was raised approximately 5 mm and secured to bolts anchored into the concrete pad on which the structure was located. This is known as configuration 2, or pipe only.

CONFIGURATION 2

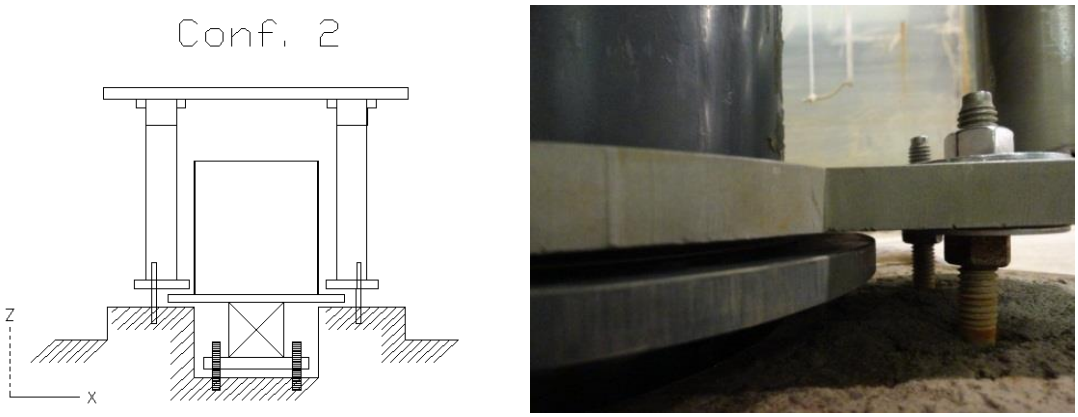

Figure 3.8: Pipe only structural configuration

The third structural configuration measures the forces on the central pipe and surrounding posts, excluding the forces measured on the velocity cap. To do this, the velocity cap was separated from the posts. To maintain the same hydrodynamics present under the full structure configuration, the presence of the cap was maintained by supporting the cap on 4 slender threaded rods anchored into the concrete pad. The aluminum base plate is bolted to the PVC base plate of the central pipe so that forces acting on the posts and central pipe are transferred the force sensor. This is configuration 3, or pipe and posts.

CONFIGURATION 3

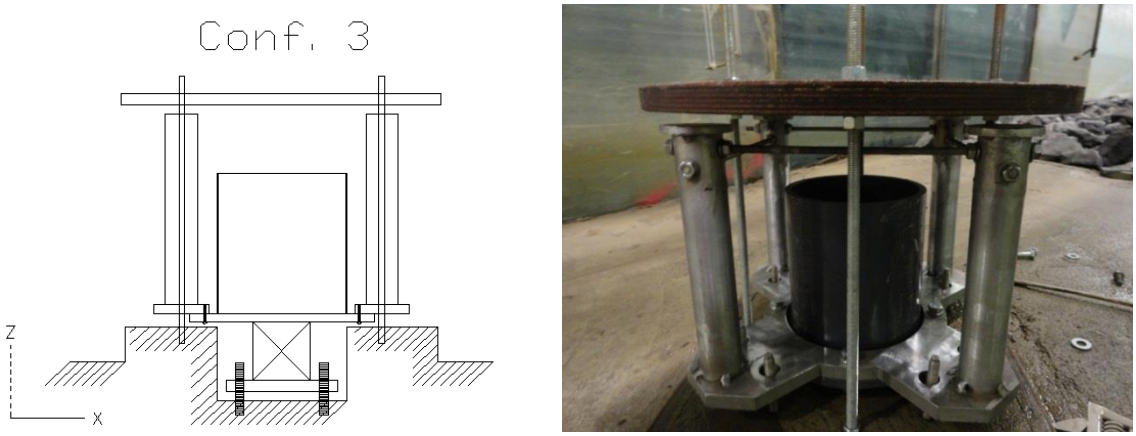

Figure 3.9: Pipe and posts configuration

3.2.3 Bathymetry Design

A rigid concrete bathymetry was constructed in the flume so that wave shoaling and wave breaking would be included in the model. The model structure was placed near the top of the sloping bathymetry so that the shallower water depth would induce wave transformation and wave breaking at the structure location (Figure 3.10). The end of the flume with the wave maker is considered the deep water "off-shore" zone. Approximately 49m from the wave maker the concrete bathymetry begins, rising at a 23% slope for 4.1 m at which point the slope of the bathymetry turns nearly flat (slope ≈ 4.6%). As the water depth decreases during this rise in the sea floor, propagating waves begin to transform into shallow water waves (H < L/2). As the waves shoal their wave lengths shorten and wave heights increase until the waves ultimately break. This is the shallow water zone in which the structure is located and wave breaking occurs. The structure is fixed to a diamond shaped concrete pad located in the shallow water zone at 57.3 m from the wave maker. Past this location, the concrete floor ceases and a large rock bed layer (average weight of 1.3 kg) begins for 5 m. A gentle sloped pea stone beach was selected for a beach to minimize wave reflections. The beach rises above the water level at a 10% slope.

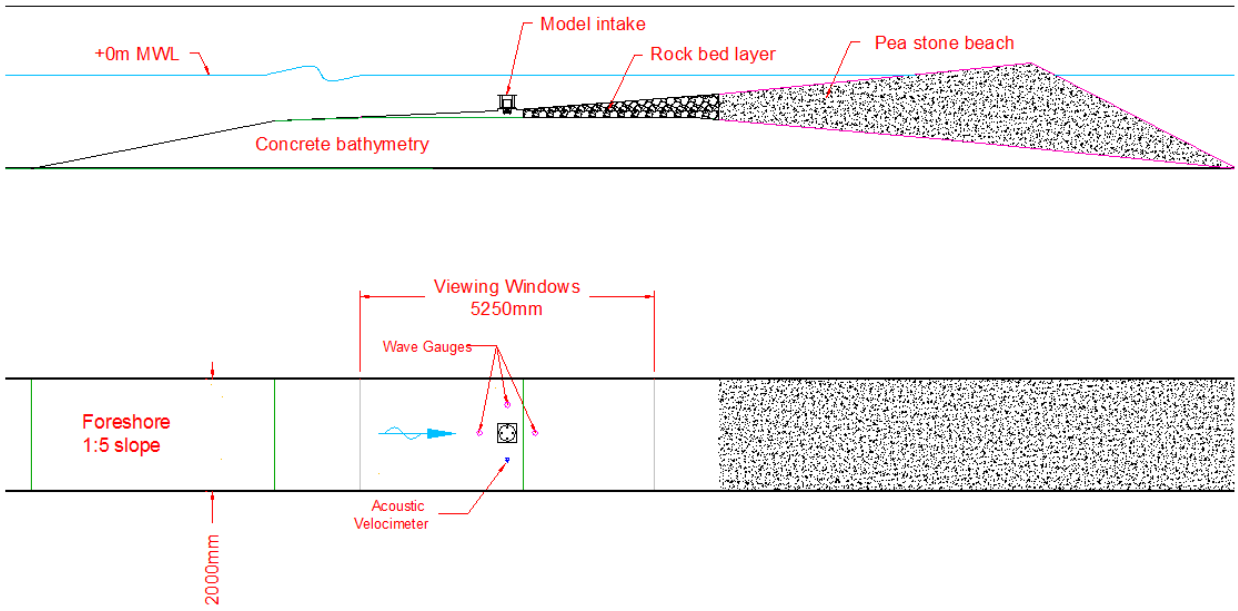

Figure 3.10: Elevation (a) and plan (b) view of artificial bathymetry in the large wave flume

3.2.4 Sign Convention

The horizontal (x-direction) forces on the structure are defined positive in the direction of wave propagation (Figure 3.11). The vertical forcing (z-direction) are defined positive upwards. The forcing in the transverse direction across the flume (y-direction) is positive in the direction into the page, following

the right hand rule. The origin of the co-ordinate system is located at the centre of the top plate of the force dynamometer. Moments are defined as forces creating rotation/bending around this point.

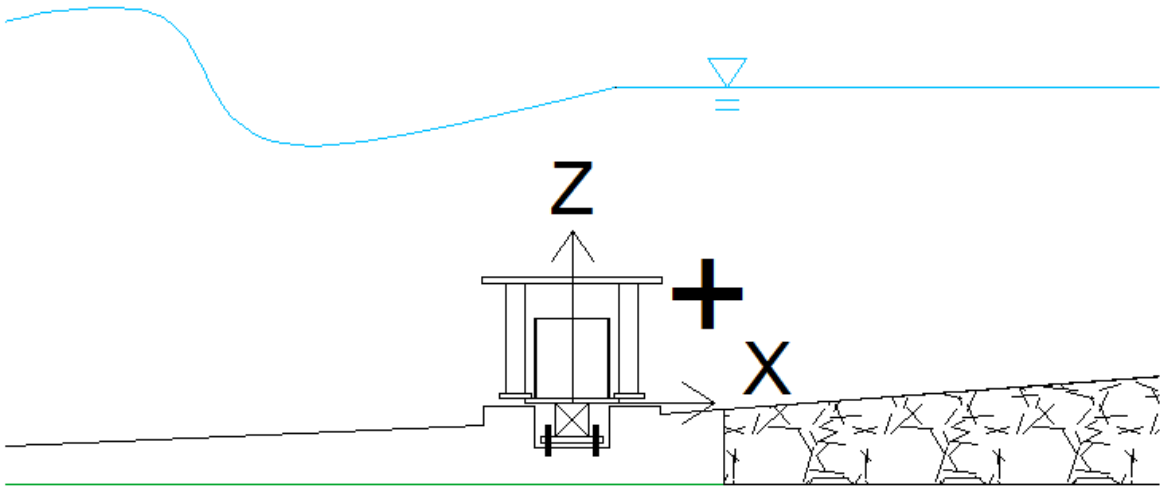

Figure 3.11: Sign convention for forcing on structure

3.3 Model setup

With the design of the bathymetry completed, construction of the concrete sea floor in the flume could begin. The bathymetry was designed as a 2-D profile to recreate the sea floor and water depth transitioning from a deep water offshore zone, to a shallow water wave breaking zone, and ultimately to a zero water depth pea stone gravel beach. The design used the pre-existing bathymetry in the flume, indicated by the flat line below the structure location and downward sloping line below the pea stone beach in Figures 3.10 & 3.11. A large portion of the pre-existing bathymetry in the foreshore area (transition between deep to shallow) was cut out to increase the slope. To build this steeper foreshore, the rising floor was created out gravel covered with 2" of poured concrete. The floor elevation was shaped by cutting Masonite boards to the shape of the sea floor profile and placing them on levelled pads on the existing flume floor. Two sets of Masonite boards were placed in parallel along the flume approximately 1m apart. The space between the boards and the wall of the flume were filled with pea stone gravel, with 2" left between the top of the boards and the gravel for concrete to be poured. A diamond shaped level concrete pad was built 57.3m from the wave board for the structure to be anchored to. A piece of PVC pipe was placed within the wooden formwork to create a well in which the force dynamometer would be anchored to (Figure 3.7).

Figure 3.12: Left: Formwork for bathymetry transitioning from deep to shallow water; Right: Gentle slope bathymetry formwork in shallow water zone with formwork for level pad at location of the structure

Once the Masonite boards were placed on level pads and filled with pea stone, concrete was poured on top to create the finished bathymetry. Concrete was brought into the flume and poured by crane and bucket technique. Once poured, the concrete was smoothed with a power trowel.

Figure 3.13: Pouring concrete through use of a crane and bucket (left); Troweling concrete on foreshore (right)

The Masonite boards extending behind the structure location were also filled with pea stone, but were covered with large stone instead of concrete (Figure 3.14). At the elevation of mean water level, the pea stone beach rises at a 10% slope. Behind the beach, the pea stone slopes down to the floor of the flume at the angle of repose of the pea stone. Several meters behind the pea stone beach is the steel beaches of the flume (Figure 3.15) that dissipate any wave energy transmitted past the pea stone beach.

Figure 3.14: Left: finished concrete bathymetry viewed from deep water zone; Right: large stone sea floor and pea stone beach

Figure 3.15: Finished bathymetry: concrete pad where structure will be fixed, large stone sea floor and pea stone beach

The model intake structure was placed on a shallow level concrete pad (Figure 3.16). A small well was cast in the middle of the pad to accomodate the force sensor. Anchor bolts (4) were drilled into the concrete in the bottom of the well to anchor the force sensor and ultimately the entire structure (Figure

3.7). Levelling nuts were used to level the force sensor in the well (Figure 3.16). A series of anchor bolts were drilled into the top of the pad to support the alimunum base plate and the velocity cap for testing of configurations 2 and 3 respectively.

Figure 3.16: Left: Concrete pad with anchor bolts; Right: Force dynamometer levelled and secured in well

Figure 3.17: Model structure installed on top of force dynamometer in concrete pad

3.4 Description of Instrumentation/Software

Instruments were installed in the model to measure wave elevations (in the offshore and shallow water zones), flow velocity near the intake structure, and hydrodynamic forces on the intake structure. CHC's real-time data acquisition and control package, NDAC, was used to acquire data from the various sensors deployed in the model.

3.4.1 Wave Gauges

Two sets of wave gauges were employed in this study. An array of 5 gauges was placed in the deep water zone near the wave maker. The gauges, or probes, were named WP1 – WP5, increasing in number in in the direction of wave propagation. Multiple gauges are used to enhance accuracy when establishing wave conditions; the offshore wave height was defined by averaging the wave height recorded at each gauge.

Figure 3.18: Array of 5 wave gauges in the deep water zone

Three wave gauges were placed near the location of the structure in the shallow water zone: One gauge 0.5 m in front of the structure, one beside the structure, and one 0.5 m behind the structure.

Figure 3.19: Set of 3 wave gauges in the shallow water zone at the structure location

The wave gauges used at CHC measure water surface elevation using an insulated copper wire connected to an electric circuit. The changes in the capacitance are detected between the wire and the surrounding water resulting from changes in the depth of submergence. The signal recorded is related to the percentage of the wire that is wetted. These wave gauges have proven to be very accurate with calibration errors of less than 0.5% over a 100 mm calibration range. This results in a measuring accuracy of ±0.5 mm at model scale, or ±7.5mm at prototype scale. An example of a portion of a wave record measured at the structure location from an irregular wave test can be seen in Figure 3.20. The data is recorded as a time series of water surface elevation. The data processing software at CHC uses this information to calculate wave properties.

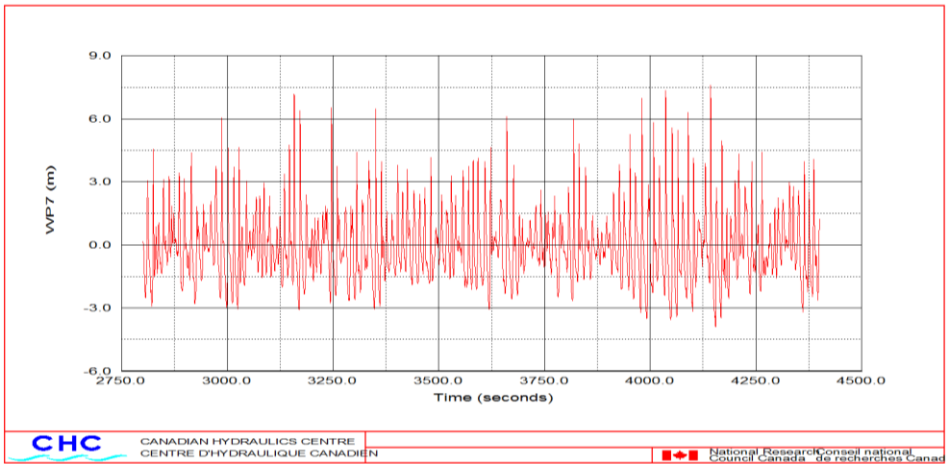

Figure 3.20: Plot of water elevation recorded at WP7 (structure location) during an irregular wave test

3.4.2 Force Dynamometer

A six-axis force sensor, model SP2.5D-6-2K manufactured by AMTI Corp. was used to record forces on the model intake structure during testing. The dynamometer is waterproof and able to withstand being completely submerged for long periods of time. The 6 axis refer to forces and moments in 3 dimensions (F_X, F_Y, F_Z, M_X, M_Y and M_Z). The load cell outputs 6 channels of data, one for each component of force and moment. The force transducer consists of a single cylindrical strain element. At either end is a 2.0" bolt-hole-circle, with strain gages placed on the outer diameter of the strain element and bridges together.

Figure 3.21: 6-axis force sensor used during testing on the model structure

3.4.3 Current Meter

The velocity of the wave induced currents at the depth and location of the structure were measured in 3 dimensions using the Nortek Vectrino high-resolution acoustic velocimeter (Figure 3.22). This current meter uses Doppler technology by bouncing sound waves at a frequency of 10 MHz off moving particles in the water. The Doppler-shift principle, the change in frequency or wavelength of the emitted wave by

the particles moving relative to the meter, is used to calculate current velocities in 3 dimensions. As long as the water isn't completely clear, this type of current meter allows for very precise measurements of water particle velocity. The Vectrino was placed approximately 50cm from the centre line of the structure, in the direction perpendicular to the length of the flume, to ensure no flow interference from the structure. The sign convention was the same as the force dynamometer, with positive x in the direction of wave propagation, positive z vertical upwards, and positive y in the transverse direction in accordance with the right hand rule.

Figure 3.22: The Vectrino acoustic velocimeter mounted to face the model intake structure

3.4.4 Data Acquisition System - NDAC

All data from the experiments was collected using NDAC, a real-time data acquisitions and control package developed by CHC. The analog voltage signals transmitted through these channels from the various instruments deployed in the model were converted into digital form using high accuracy 16-bit analog-to-digital converters for storage in a computer data file. The scale of the model was programed into NDAC at the beginning of the study and all data recorded was scaled accordingly. Once the data is in digital form, it can be analysed using GEDAP programs.

3.4.5 Data Analysis System - GEDAP

Once data from sensors has been collected, converted into digital form, and stored in a computer data file it can be analyzed. In this study the CHC's GEDAP (Generalized Experiment Control and Data Acquisition Package) analysis software was used. For data analysis in this study, GEDAP programs were used for data manipulation, frequency domain analysis, time domain analysis, and statistical analysis. GEDAP was originally developed at CHC for random wave generation and analysis, but has since been

used for other studies within the National Research Council of Canada as well as other laboratories worldwide.

3.4.6 Video

A video camera was mounted on a tripod to provide footage of the wave tests. The camera was placed outside the viewing glass to provide an elevation view of breaking wave profiles. Some tests were also filmed from an overhead angle to provide an alternate perspective.

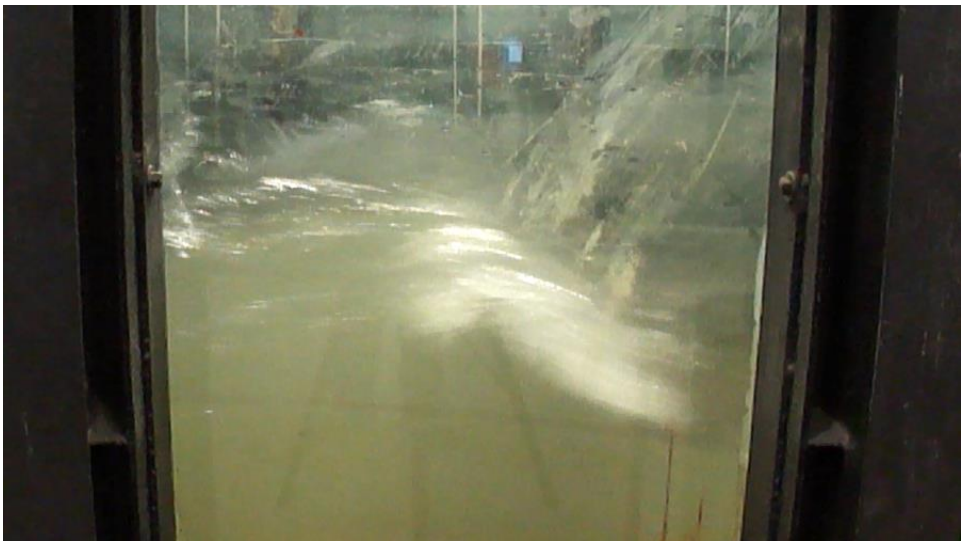

Figure 3.23: Freeze frame from filming of a regular wave test (side view). Reflection of tripod visible

Figure 3.24: Freeze frame from filming of an irregular wave test (top view)

4.0 Experimental Methodology

4.1 Instrument Calibration

No testing of the model started until known values used in calibration were successfully read by the data acquisition system. NDAC can also be used to re-zero sensor outputs in calm water before a test when conditions are still in the flume. The real-time water elevation readings from the wave gauges and force readings from the dynamometer were re-zeroed before each test to remove static offsets. Hence, subsequent readings with waves were made relative to these calm-water conditions.

4.1.1 Wave Gauge Calibration

The wave gauges were calibrated several times during the study. Calibration in the flume was done by leaving the wave gauges at fixed elevations, recording the water elevation value, then dropping the water in the flume a known level and recording the next value. A minimum of 4 water elevations were used during each calibration. If the readings from each individual wave gauge showed a linear decrease and an error of less than 0.5%, the gauges were considered to be successfully calibrated. All wave gauges were calibrated at the beginning of the study and re-calibrated at least once a week. The wave gauges were re-zeroed before each test once the water level was stable in the flume. Hence, the gauges measured changes in water level relative to this initial condition.

4.1.2 Force Dynamometer Calibration

The six-axis force dynamometer manufactured by AMTI Corporation is factory calibrated. This calibration was verified prior to testing by applying a known mass in the X, Y, and Z directions and observing the force recorded in NDAC. In the horizontal plane, a wire was attached to a bolt on top of the dynamometer, ran through a pulley with a known mass hanging vertically. For forces in the Z direction, a 20 kg weight was placed on top of the structure (Figure 4.1). The difference between the applied loads and the measured force was consistently less than 2%. There was little to no cross-talk between the 3 force channels.

Figure 4.1: Calibrating the force dynamometer in the Z direction

4.1.3 Dynamic Responses

The dynamic response of the model intake structure was investigated by applying impulsive loads (hammer taps) in all three orthogonal directions while recording the load cell outputs. It is important to understand the natural frequency of a structure being subjected to wave loads, as waves with the same frequency as the structure can cause force amplification, leading to inertial force values not accounted for in design and structural failure. Any vibration of the model intake gives rise to internal inertial forces that are recorded by the load cell, making it difficult to isolate the external forcing. The ability of the load cell to measure hydrodynamic forcing is limited to frequencies below the fundamental natural frequency of the structures dynamic response. The natural frequency in each direction is measured by plotting the force time series measured by NDAC and observing the oscillating decaying force values at the time of the hammer taps. The period of these oscillations is the natural frequency of the structure in the direction of the hammer tap.

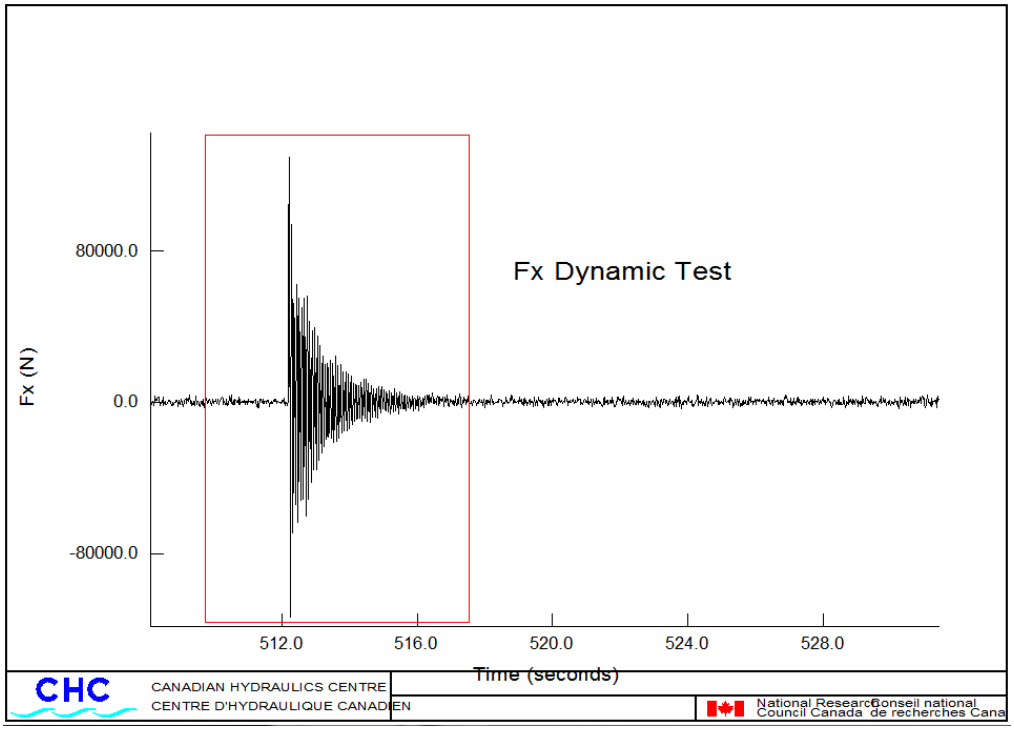

Figure 4.2: Force oscillation in the x direction due to hammer tap on full structure

Figure 4.2 shows the force time series following a hammer tap in the x direction (direction of wave propagation) on the full structure configuration. The natural frequency of the full structure in this direction may be calculated by counting the oscillations per second. The result is a natural frequency of 13.3 Hz (full scale) and 3.43 Hz (model scale) for the full structure (configuration 1) in the horizontal plane. All dynamic tests on each structure configuration and in each direction resulted in a natural frequency value greater than or equal to the natural frequency of the full structure in the x direction, making it the governing frequency. The system is able to reliably measure hydrodynamic forcing at frequencies below ~10 Hz, which is greater than the largest model scale natural frequency determined (3.43 Hz).

4.1.4 Current Meter Calibration

The software accompanying the Vectrino current meter featured auto-calibration abilities. Real time error and correlation readings were displayed during testing to ensure the current meter was functioning properly, but the internal calibration was not verified.

4.2 Wave Synthesis and Generation

4.2.1 Test Plan

To replicate realistic wave conditions within the flume, a test program featuring irregular waves was planned. Irregular, waves were defined by their peak period (T_p) and zero-moment wave height (H_{m0}). The zero-moment wave height is a characteristic value calculated from the energy density spectrum of an irregular wave record (see section 4.2.2). It is approximately equal to the significant wave height (H_S), the average of the largest 1/3 of recorded wave heights. The peak period (T_p), is the period for which the wave spectrum is maximized. In shallow water, the local water depth has a large impact on wave properties, so 3 water depths were planned representing low tide, mean water level (MWL), and high tide conditions in a realistic coastal environment. These conditions were calculated in full scale values as -2m MWL, 0m MWL, and +2m MWL respectively. Since the elevation of the bathymetry at the intake was set to -9.5m (full scale) the local water depths at the intake ranged from 7.5m at low tide to 11.5m at high tide (Figure 4.3). Nine different irregular sea states, with peak periods of 8, 11 and 14s and significant wave heights of 3, 4.5 and 6m were synthesized and generated at each water level. These wave conditions were created and set in the deep water zone and transform differently as the waves reach the shallow water zone and shoal. The wide range of water levels, significant wave heights, and peak periods were tested to ensure a broad spectrum of wave conditions, levels of wave breaking, and resultant forces on the intake structure. The duration for tests using irregular waves was 31 minutes in the model, or 2 hours full scale. This ensures a minimum of 500 unique waves per random wave test. At each water depth, a regular wave test was run using the 3 H_{m0} values for average wave height of the regular wave test. All regular wave tests used an average wave period of 11s. The entire test plan was executed for each structural configuration, beginning with configuration 3, and finishing with configuration 1. The structural configuration wasn't changed until all tests had been successfully executed on that configuration. The test plan is detained in Table 1 using full scale values.

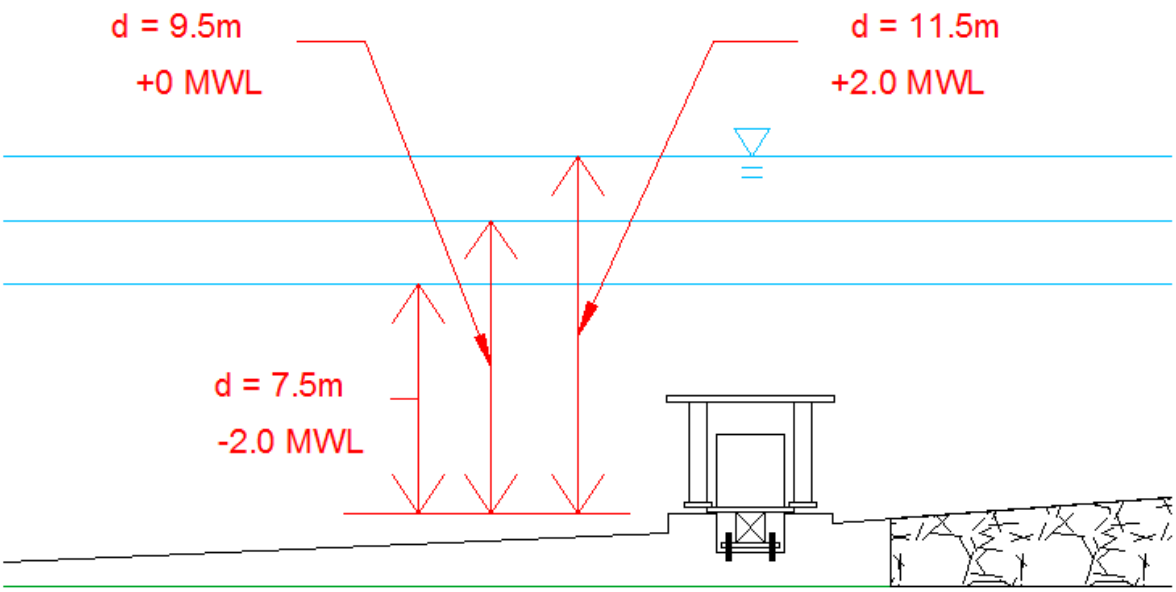

Figure 4.3: Three water levels used during experiments, with full scale depth at location of structure displayed

Table 4.1: Test program, featuring irregular and regular wave conditions

Drive Signal	Depth at intake (m)	Offshore H_{m0} (m)	T_p (s)	Type	Duration (min)
1	-2	3	8	Irregular	120
2	-2	3	11	Irregular	120
3	-2	3	14	Irregular	120
4	-2	3	11	Regular	19
5	-2	4.5	8	Irregular	120
6	-2	4.5	11	Irregular	120
7	-2	4.5	14	Irregular	120
8	-2	4.5	11	Regular	19
9	-2	6	8	Irregular	120
10	-2	6	11	Irregular	120
11	-2	6	14	Irregular	120
12	-2	6	11	Regular	19
13	0	3	8	Irregular	120
14	0	3	11	Irregular	120
15	0	3	14	Irregular	120
16	0	3	11	Regular	19
17	0	4.5	8	Irregular	120
18	0	4.5	11	Irregular	120
19	0	4.5	14	Irregular	120
20	0	4.5	11	Regular	19
21	0	6	8	Irregular	120
22	0	6	11	Irregular	120
23	0	6	14	Irregular	120
24	0	6	11	Regular	19
25	+2	3	8	Irregular	120
26	+2	3	11	Irregular	120
27	+2	3	14	Irregular	120
28	+2	3	11	Regular	19
29	+2	4.5	8	Irregular	120
30	+2	4.5	11	Irregular	120
31	+2	4.5	14	Irregular	120
32	+2	4.5	11	Regular	19
33	+2	6	8	Irregular	120
34	+2	6	11	Irregular	120
35	+2	6	14	Irregular	120
36	+2	6	11	Regular	19

4.2.2 Wave Synthesis

Once the desired wave conditions (water level, H_{m0}, T_p) to be tested were selected, drive signals were synthesized using GEDAP software. A drive signal is a time-history specifying how the wave maker should move in order to generate a particular wave train. First, the target wave spectra representing the desired wave conditions were created in GEDAP. JONSWAP (Joint North Sea Wave Project) wave spectra were used in this study for each random wave test to describe the distribution of wave energy with frequency. An example of a JONSWAP wave spectrum can be seen in Figure 4.4. The equations describing the JONSWAP spectrum are below.

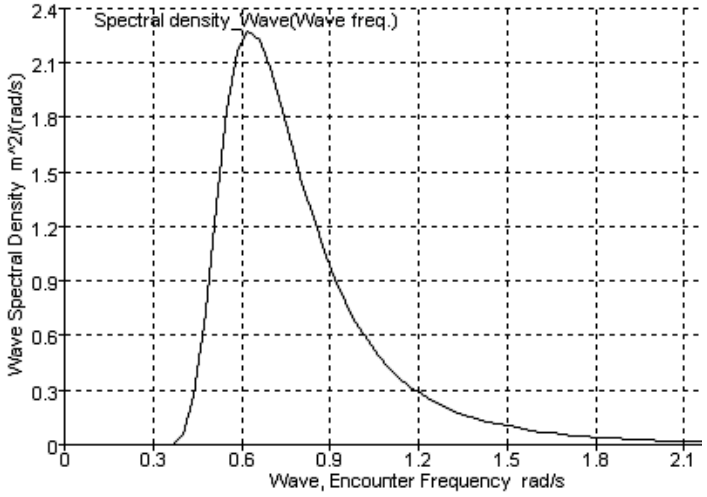

Figure 4.4: Example of a JONSWAP wave spectrum

$$S_{JONSWAP} = \frac{\alpha_p g^2}{(2\pi)^4 f^5} \exp\left[-\frac{5}{4}\left(\frac{f}{f_p}\right)^{-4}\right] \gamma^a \; ; \; a = \exp\left[-\frac{(f-f_p)^2}{2\sigma_J^2 f_p^2}\right], \; \sigma_J = \begin{cases} 0.07 \; for \; f \leq f_p \\ 0.09 \; for \; f > f_p \end{cases} \qquad [4.1]$$

In the above equations, f is the wave frequency, and f_p is the peak frequency (inverse of T_p). The JONSWAP constant ϒ is related to the kurtosis of the spectrum. The standard value of ϒ = 3.3 was used in calculating wave spectra to be used in this study. For Phillips alpha (α_P), a standard value of 0.0081 is used. The zero-moment wave height is considered to be approximately equal to the significant wave height (H_S), the average of the largest one third of wave heights in a random wave series. During wave synthesis, the target spectrum is derived from the significant wave height, H_{m0}, and the peak period, T_P.

$$H_S \approx H_{m0} = 4\sqrt{\int_0^\infty S_{JONSWAP}\, df} \qquad [4.2]$$

4.2.3 Wave Generation

The GEDAP program PARSPEC was used to create a JONSWAP wave spectrum using the above inputs and desired (H_{m0}) and (T_p) values. Next, the routine RWSYN was used to synthesize the target wave train from the JONSWAP spectrum. A complex transfer function is then used to take the desired wave train and synthesize command signals for the wave machine so that the waves are created in the flume. The final product is a pair of drive signals which can be used to control the wave maker. The program SWG is used to operate the wave maker, send drive signals that create the waves, and can be used to shut down the wave board if necessary.

The water level was adjusted by adding or draining water from the flume. The water level in the flume was measured and monitored by observing a measuring tape on a viewing window in the deep water zone. Water level readings from this tape correspond with the depth values for each test in Table 4.1. Once a drive signal was prepared, the correct water level was set in the flume, and all the sensors had been zeroed, the data acquisition system in NDAC is armed. This system was configured to begin recording data from all instrumentation in the model once wave generation begins. During testing, the collected data was converted into digital form and stored in a DAC file. Using GEDAP programs, this data file could be split into a series of files, one per channel, and analyzed using GEDAP programs or other software.

4.2.4 Wave Calibration

The initial command signals produced waves in the flume close to but not exactly the same as specified in the synthesis. The discrepancy between target waves and the waves generated in the flume was assessed by computing the zero-moment wave height for the wave records measured in the deep water zone. An average H_{m0} value was calculated by averaging the 5 H_{m0} values recorded from each of the offshore wave gauges. The percentage difference between the averaged measured and desired H_{m0} values was then applied as a multiplier to create a new drive signal, and the wave test is run again. The drive signal was considered to be well calibrated when the measured H_{m0} was within 3% of the desired value. For tests with regular waves, the same process was repeated using the average wave height (H_{ave}) instead of H_{m0}. Wave calibration was done for every irregular and regular wave test. All wave calibration tests occurred without the structure installed.

5.0 Data Analysis

Following the completion of each wave test, the measurements were analyzed to verify that the model and instrumentation systems were working properly. The wave and force time series were analyzed using GEDAP programs and procedures to statistically determining peak values and other useful statistics such as mean values, standard deviations, and maximum/minimum values. The results were checked for accuracy before the next test could begin.

5.1 Analysis Routines

The digital data files (DAC) containing information from all instrumentation used in the model were analyzed using GEDAP programs and procedures. The DAC file was split into separate channels containing time series data for each wave gauge, force component, and current direction. The start and end times were then truncated to remove data recorded before the waves had reached the model intake. The measurements were then transformed from model scale to full scale.

5.1.1 Force Data

Data from the 6 force channels (F_X, F_Y, F_Z, M_X, M_Y and M_Z) was first passed through a low pass filter using the routine FILTW to remove high frequency noise. A variance spectral density analysis was performed using the routine VSD (Variance Spectral Density) to compute force spectra, which revealed the distribution of force energy with frequency. A PEAKS analysis then identified local maxima and minima in the force time series as peak force values. The full time histories and the peaks were then analyzed by the statistic routine STAT1 to determine maximum/minimum values, average, and standard deviation. STAT5 was used to calculate probability distributions so that information such as the 95% largest force value could be obtained. The origin for measured Moments is the load cell at the base of the model intake structure (Figure 3.11).

5.1.2 Wave Data

The wave data was split into 2 groups: the 5 gauges located near the wave maker (referred to as offshore), and the 3 gauges at the location of the structure (referred to as structure location). The routine VSD was used to compute the wave spectra for each gauge. A zero-crossing analysis (ZCA) was performed on the wave records to define each individual wave and its respective properties such as wave height and period. Waves were defined in the time domain as zero down-crossing for this study. STAT5 was used again to calculate statistics and probability distributions for each measured wave record. Characteristic wave properties such as H_{m0} or T_p were defined for both the offshore and

structure locations by averaging the values for each group of gauges. Regular wave tests provided consistent waves and did not require a statistical analysis. Velocity and forces from regular wave tests were used to calculate force coefficients in the Results and Analysis (Section 6.2).

5.1.3 Velocity Data

Velocities were recorded in x, y, and z directions beside the structure, following the same sign notation for forces (Figure 3.11). The time histories were passed through a low pass filter using the routine FILTW to remove high frequency noise. The acceleration time histories were determined by taking the first derivative of the velocity data.

5.2 Quality Control

Once the GEDAP analysis procedure had run, the time series and energy spectra for both waves and forces were printed out for immediate observation of the results. This was necessary to ensure the test had been successful before the next wave test could begin. Figure 5.1 is an example of the analysis plot used in this study to view the wave data recorded in each test.

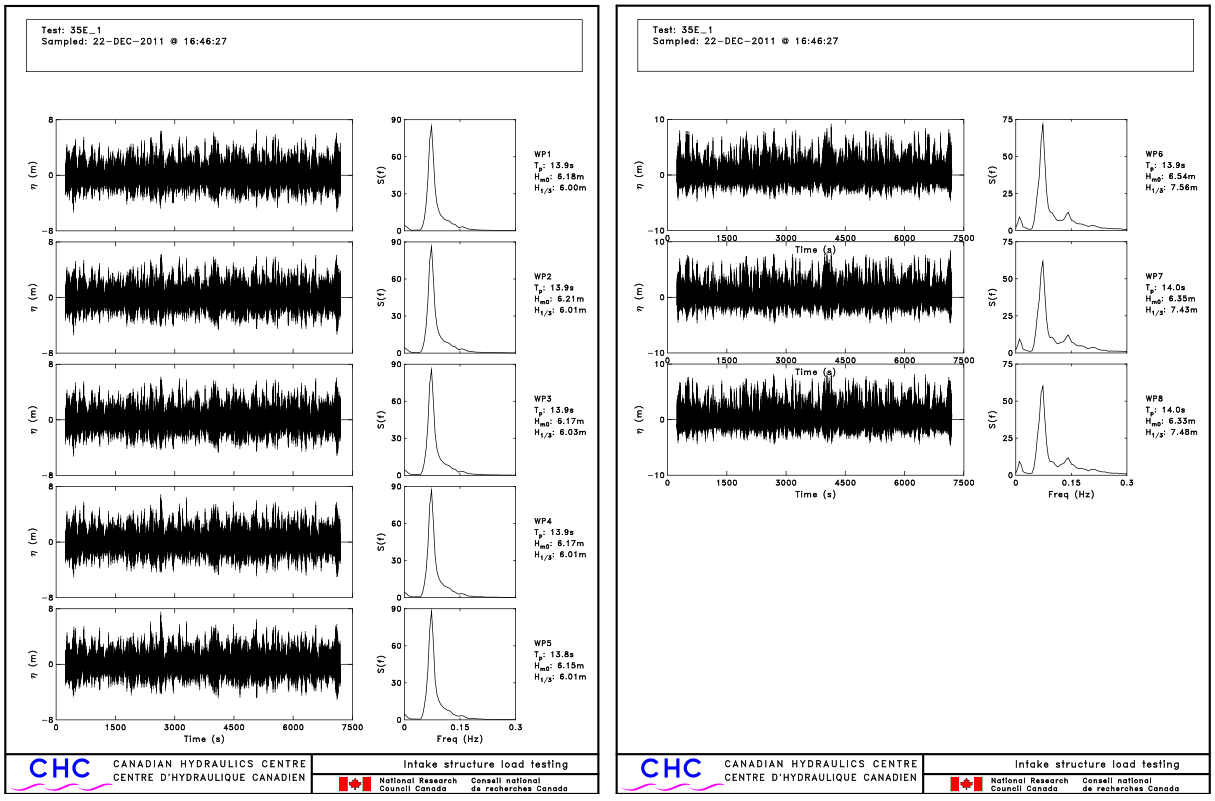

Figure 5.1: Water elevation time series for offshore wave gauges (left) and structure location gauges (right)

The above plots are created using GPLOT, a plotting package within the GEDAP system. These plots were reviewed after each test to ensure that all the gauges were functioning properly. If the measured H_{m0} value exceeded +/- 3% of the target value, a new drive signal was created and the test was conducted once more with the adjusted drive signal. Figure 5.2 shows the force data recorded in the same test.

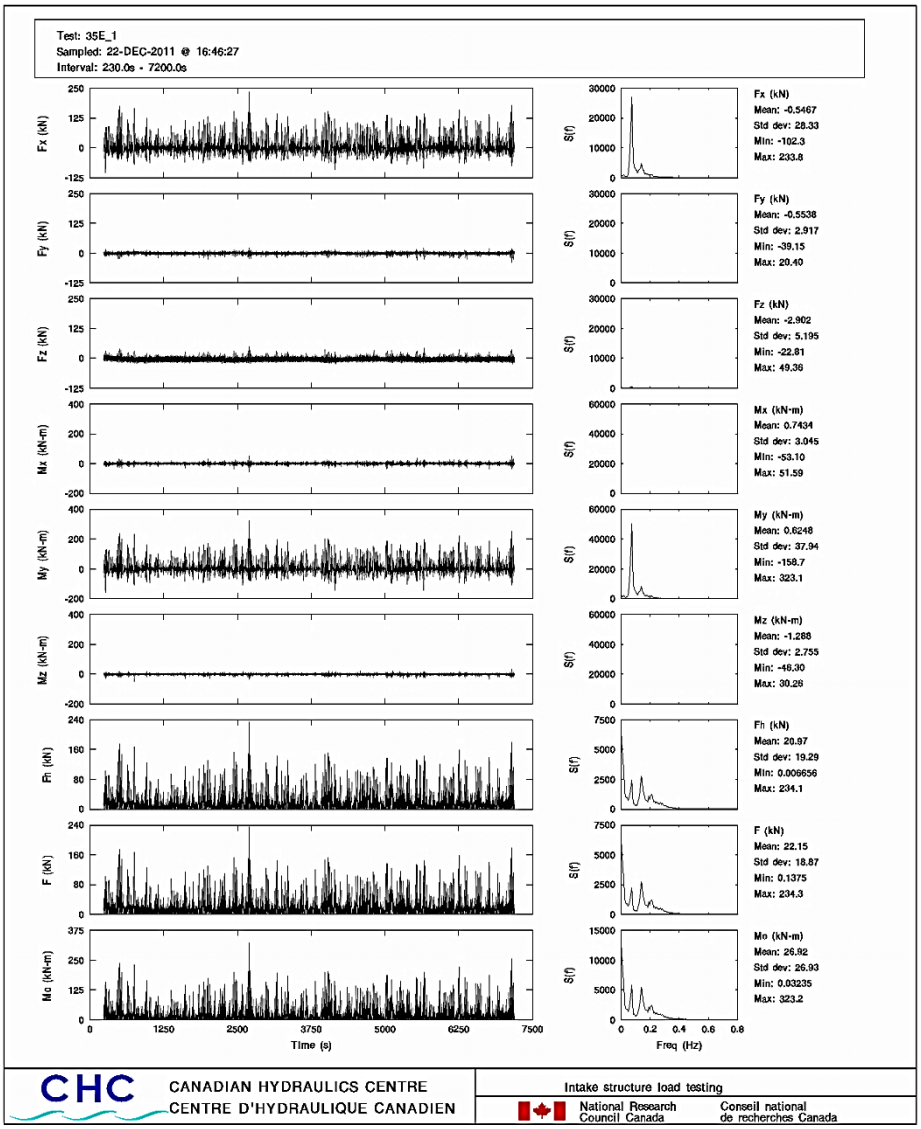

Figure 5.2: Time and frequency domain data for forces and moments on the structure during testing

In order of top to bottom, this Figure shows the time histories and spectra for: F_X, F_Y, F_Z, M_X, M_Y, M_Z, F_h (horizontal resultant), F (resultant of F_X, F_Y, and F_Z), and M_o (overturning moment). The horizontal and total resultant forces, as well as the overturning moment, were calculated using the routine Polar 2D. Polar 2D calculates the resultant of 2 vectors.

$$F_h = \sqrt{F_X^2 + F_Y^2} \quad [5.1]$$

$$F = \sqrt{F_h^2 + F_Z^2} \quad [5.2]$$

$$M_O = \sqrt{M_X^2 + M_Y^2} \quad [5.3]$$

The data was screened for errors such as trends in the data or unrealistic peak values. The current data recorded was observed in real-time during the experiments using the Vectrino software. The software provided error and correlation information to ensure the current meter was functioning properly.

5.2.1 Repeatability and variance of test results

Several wave tests were repeated up to 3 times to ensure there was repeatability of test results. All tests repeated provided similar wave and peak force results. Pictures from wave tests are presented in Figures 5.3 & 5.4.

Figure 5.3: Side view of wave test 17 (+0 MWL, H_{m0} = 4.5m, T_P = 8s) on full structure configuration

Figure 5.4: Top view of wave test 6 (-2 MWL, H_{m0} = 4.5m, T_P = 11s) on full structure configuration

6.0 Results & Analysis

6.1 Peak Force Analysis

For design purposes, the largest (or peak) forces of an irregular wave train are of significant interest. Forcing on the structure came from irregular waves for 3 different water levels, zero-moment wave heights (H_{m0}), and peak periods (T_p). These varying wave parameters were analyzed for their effects on peak forces recorded on the structure. Force results were also presented separately for each structural configuration tested in an effort to quantify the magnitude of forcing on each structural component in varying wave conditions. Finally, correlations are made between wave properties and peak force on the structure.

6.1.1 Effect of Zero-moment Wave Height

When reviewing literature on testing wave forcing on structures, it was noted that in-line wave force is strongly dependent on the wave height. Results from the irregular wave testing generate a wide spectrum of force values, with the largest forces being usually of highest interest. Therefore, the 95% largest force from each random wave test was plotted against the zero moment wave height H_{m0}, with various other wave properties factored in (such as wave period and water depth) to identify possible correlations. The 95% force is a statistically determined value that is used in the present comparison rather than the maximum recorded value due to large statistical variability in the theoretical maximum wave and force values from a random wave test. Using the 95% largest force also removes outliers and possible false readings in the data acquisition results from force sensors which would result in unrealistically large force values.

The 95% force is determined from peaks in the force data recordings. The analysis routine PEAKS in GEDAP is used to extract peak values, determined by local maxima and minima in a force time series. These values are then statistically distributed using STAT5, and a 95^{th} percentile value of total peak forces was determined. It is important to mention this, as a 95^{th} percentile value from an entire series would include all force values recorded and would be significantly lower. Using peak values, it was assumed each peak force value corresponded to local maxima or minima values in the corresponding water elevation time series, or wave record.

For most plots in this analysis, force results from all 3 structure configurations are included. When data is separated by tests on each structural configuration, the data is labelled by the components of structure transferring force to the dynamometer during wave tests. The 3 configurations tested are:

central pipe (configuration 2 - pipe), pipe and 4 surrounding posts (configuration 3 - pipe + posts), and the full structure including the velocity cap (configuration 1 - full). First, peak forces on each structural configuration were plotted versus the offshore H_{m0} value from each irregular wave test to observe trends (Figure 6.1).

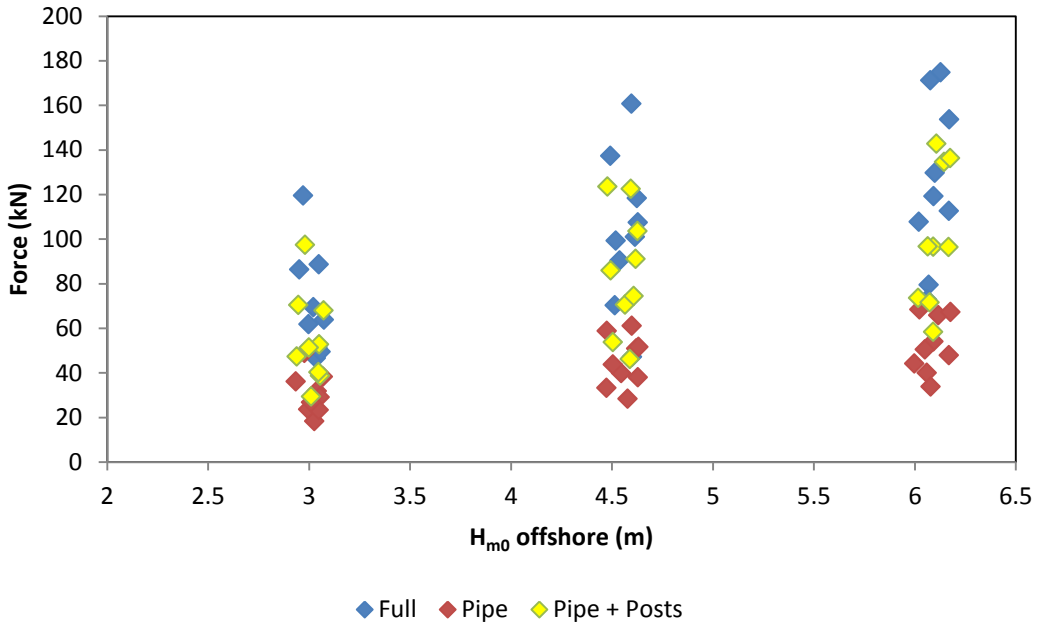

Figure 6.1: Peak forces versus offshore H_{m0} from irregular wave tests on 3 different structural configurations

The above plot of peak force in the horizontal direction versus offshore H_{m0} does not show much variability on the abscissa because only 3 variations of offshore H_{m0} were used in random wave tests, for each combination of 3 different peak periods and water levels. A linear upward trend can be seen for the forces as H_{m0} increases, but there is much scatter in the direction of the y-axis.

Due to different patterns of wave breaking between experimental tests (i.e., virtually no wave breaking for high-water level H_{m0} = 3m and excessive breaking for low-water level with H_{m0} = 6m), the H_{m0} values recorded at the structure location were considered. Results for H_{m0} of the wave gauges 0.5m in front, 0.5m behind, and beside the structure were averaged. The plot below shows 95% F_X force plotted versus the H_{m0} at the structure for each test.

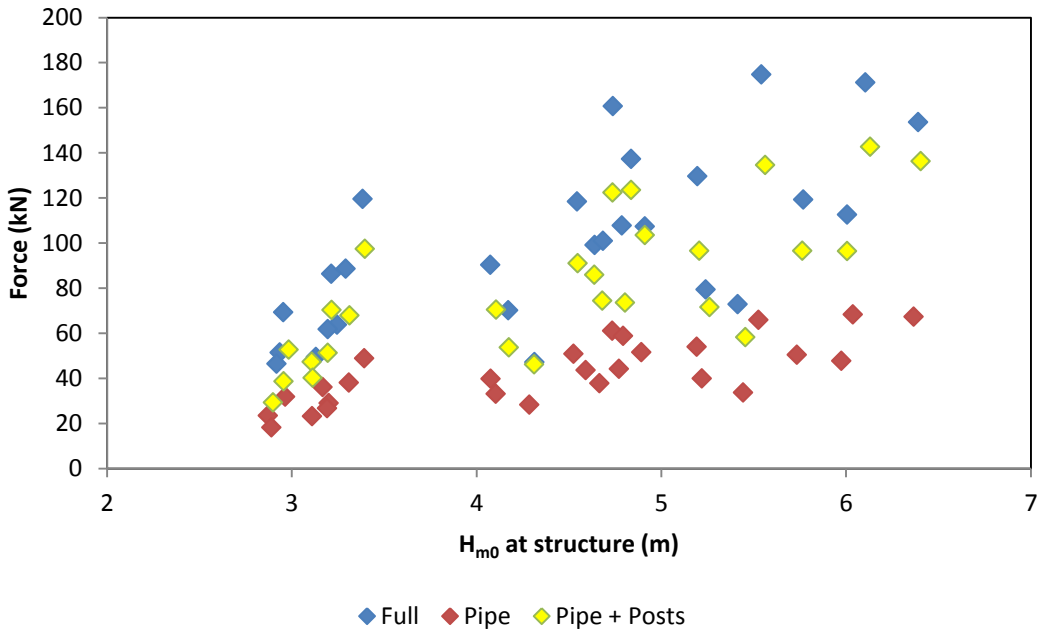

Figure 6.2: Peak forces versus H_{m0} recorded at the structure from irregular wave tests on 3 different structural configurations

Due to the varying levels of shoaling and wave breaking occurring as the irregular wave trains approach the shallow area of the structure the H_{m0} values recorded at the structure location have a larger variance. Again in Figure 6.2 the increase in 95% F_X is noted as H_{m0} increases. The magnitude of forcing on separate components of the structure is also noticeable in this Figure: the force on the pipe alone is less in magnitude than that recorded for the pipe and posts or for the total structure for every scenario of similar wave conditions, as one would expect. The above plot does include all 3 water levels (low water, mid water, and high water), which makes it unlikely to draw reasonable conclusions of the effect of H_{m0} on peak force in the Figure 3. In order to observe all the force data while accounting for water depth, the H_{m0} at the structure was divided by water depth at the structure (7.5m, 9.5m, 11.5m) used in each particular test to create normalized H_{m0} values that may be compared with each other. The results are plotted in Figure 4.

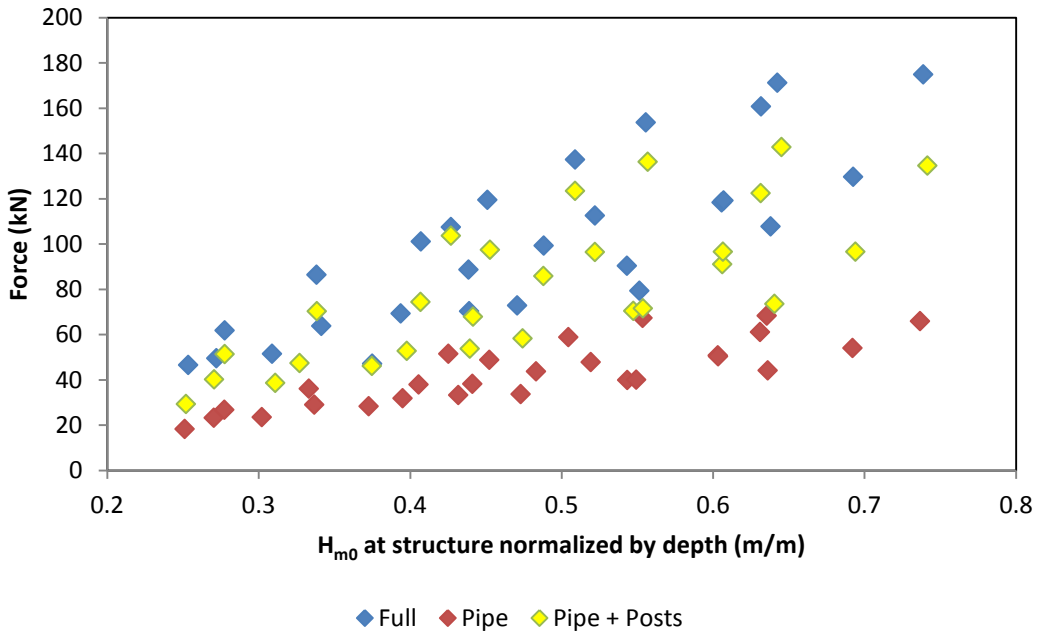

Figure 6.3: Peak forces versus the H_{m0} at the location of the structure normalized by depth from irregular wave tests

With H_{m0} normalized by water depth, a clear linear trend between peak force and H_{m0} is distinguishable. It is also noticeable that for the full structure (conf. 1) and pipe + posts (conf. 3), scatter in force values increases with H_{m0} while the force recorded on the pipe alone does not show as much scatter. Another observation from this plot is the linear relation of force with H_{m0} begins to become less steep at $H_{m0}/d \approx 0.7$ for all structural configurations. This is near the theoretical wave height-to-depth wave breaking criteria value of H/d = 0.78 (McCowan, 1894). This indicates that maximum forcing on a submerged structure in a wave breaking zone would result from highly nonlinear irregular wave trains with an H_{m0} value close to, but less than the theoretical breaking wave height for that particular water depth. The process is repeated using offshore H_{m0} values, normalized using the depth at the location of the structure. A similar pattern is observed.

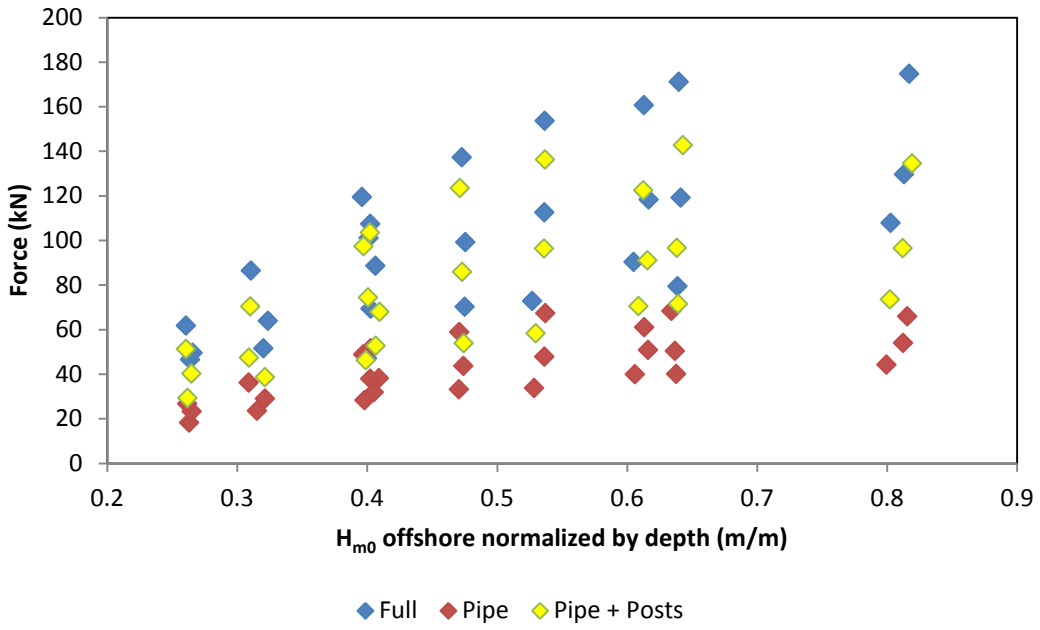

Figure 6.4: Peak forces versus the offshore H_{m0} normalized by the depth at the location of the structure

Again, a linear trend is observed between 95% force and H_{m0}/d. When using offshore H_{m0}, the wave heights are recorded before wave shoaling and breaking had occurred in the shallower region. The largest value on the abscissa represents tests where the offshore H_{m0} = 6m at the lowest water depth (water depth at prototype structure of 7.5m). Visual observations during these tests noted considerable breaking, with variance depending on the peak period of the waves. This demonstrates that offshore H_{m0}/d, while not describing wave conditions at the structure, may be used to estimate what magnitude of forcing a submerged structure may experience under breaking waves conditions. While there is a gap in the data between $H_{m0}/d \approx 0.65 - 0.82$, all data points in the range show that the upward trend is no longer linear and the force levels begin to level out at some point after $H_{m0}/d \approx 0.6$.

6.1.2 Effect of Water Level and Peak Period

The previous section focused on the effect of the zero moment wave height (H_{m0}) during each random wave test on 95% horizontal force (F_x). Next, the effects of water depth and peak period are plotted to observe trends. Rather than looking at all configurations, the full structure (configuration 1) force values were plotted against H_{m0}/d separately for each water level to observe if depth had a significant effect.

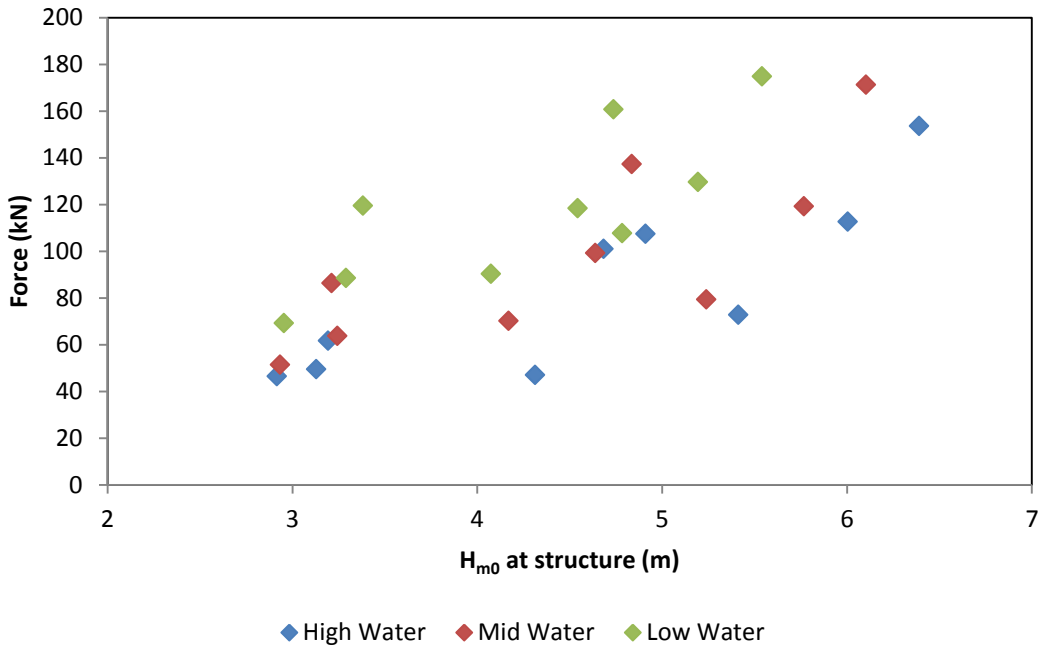

Figure 6.5: Peak forces from irregular wave tests for the full structure with various water depths

Looking at the peak forces on the full structure for various water levels, no significant impact from water depth is observed. Lower water conditions generated larger waves due to wave shoaling, and this condition is represented in plots featuring H_{m0}/d for the abscissa. The effect was similar for the pipe only and pipe + posts structural configurations.

Peak period (T_p), the inverse of the frequency value, is found on the abscissa, under the peak of the spectral density function of the irregular wave series (Figure 4.5). It was noted in the plot of peak forces versus offshore H_{m0}/d (Figure 6.4) that there are 3 separate lines in the scatter of data points for each configuration, and it was suspected that each line corresponds to the T_p value of the test. Peak force was plotted versus offshore H_{m0}/d with a separate series plotted for each group of tests using the specified T_p. Scatter plots were made separately for each structural configuration to avoid clutter and for easier visualization.

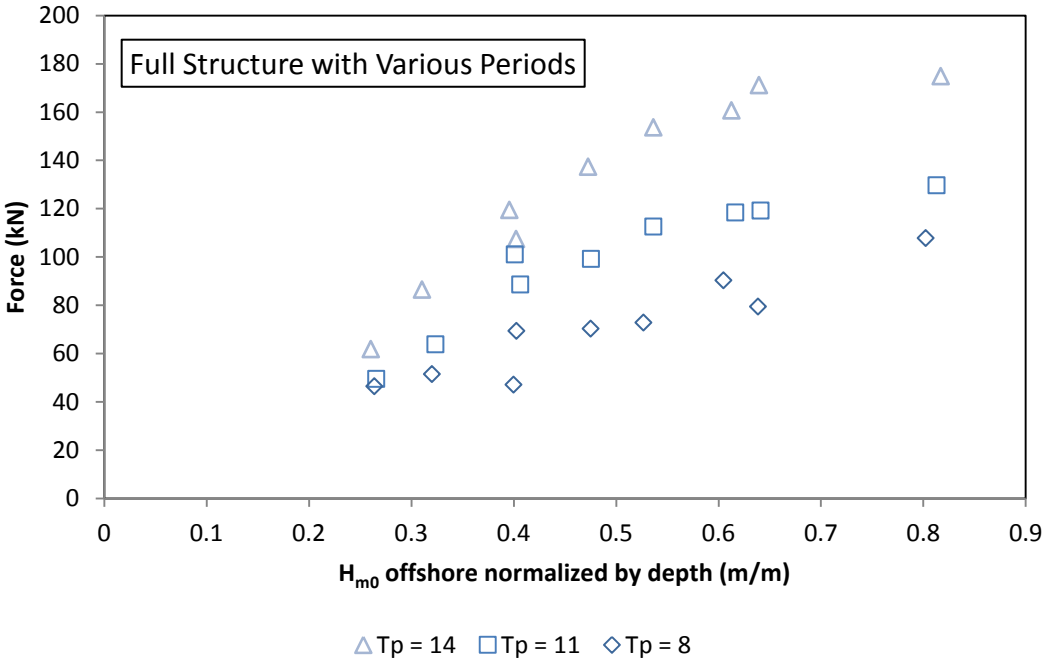

Figure 6.6: Maximum forces on the full structure for various peak wave periods

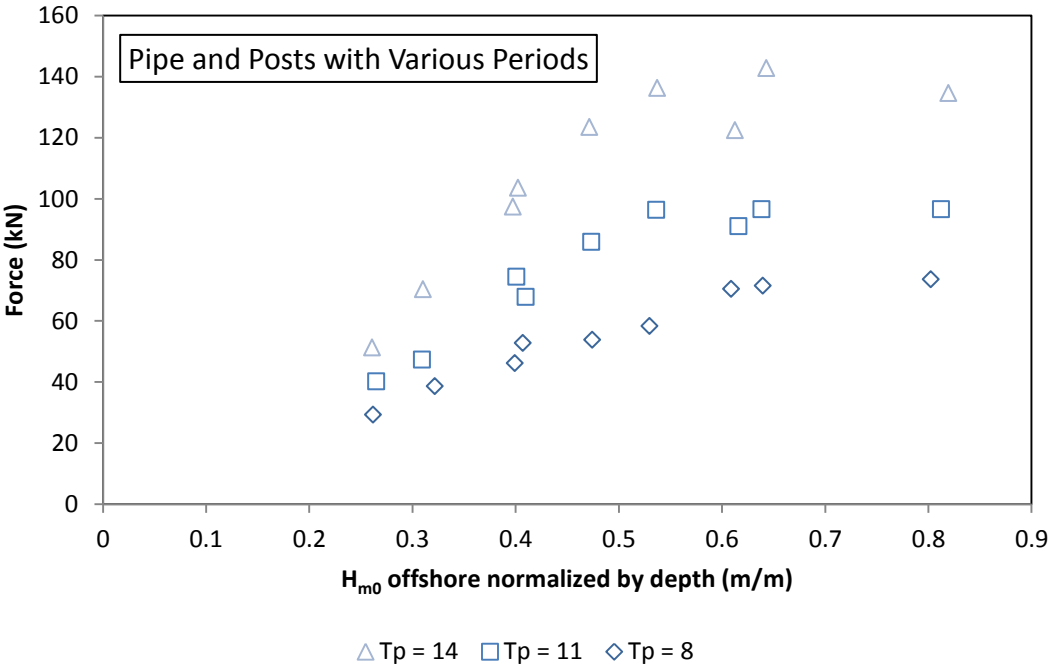

Figure 6.7: Maximum forces on the central pipe and 4 posts of the structure for various peak wave periods

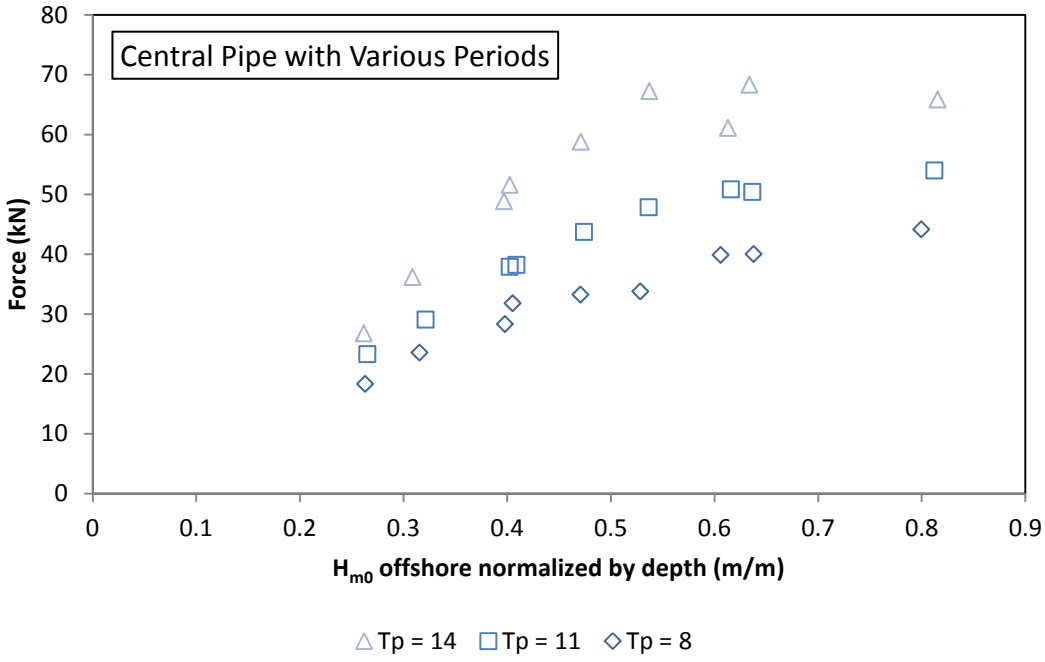

Figure 6.8: Maximum forces on the central pipe of the structure for various peak wave periods

Similar patterns are observed with respect to the peak (maximum) wave forces between varying wave periods in the plots of tests results from all structural configurations. The peak force values continue their upward trend with offshore H_{m0}/d, as well as levelling off around $H_{m0}/d \approx 0.65$ for each peak period and structural configuration. The differences in magnitude of force between $T_p = 8s$ and $T_p = 11s$, as well as between $T_p = 11s$ and $T_p = 14s$ at each value for H_{m0}/d seem to be fairly equal. This may indicate the relationship between force and peak period as H_{m0}/d increases would be linear, and that the slope of the trend line for peak force vs. H_{m0}/d increases with T_p. The peak force data was then plotted by period against H_{m0}/d, using the H_{m0} values recorded at the structure location. The results are plotted in Figures 6.9, 6.10 and 6.11

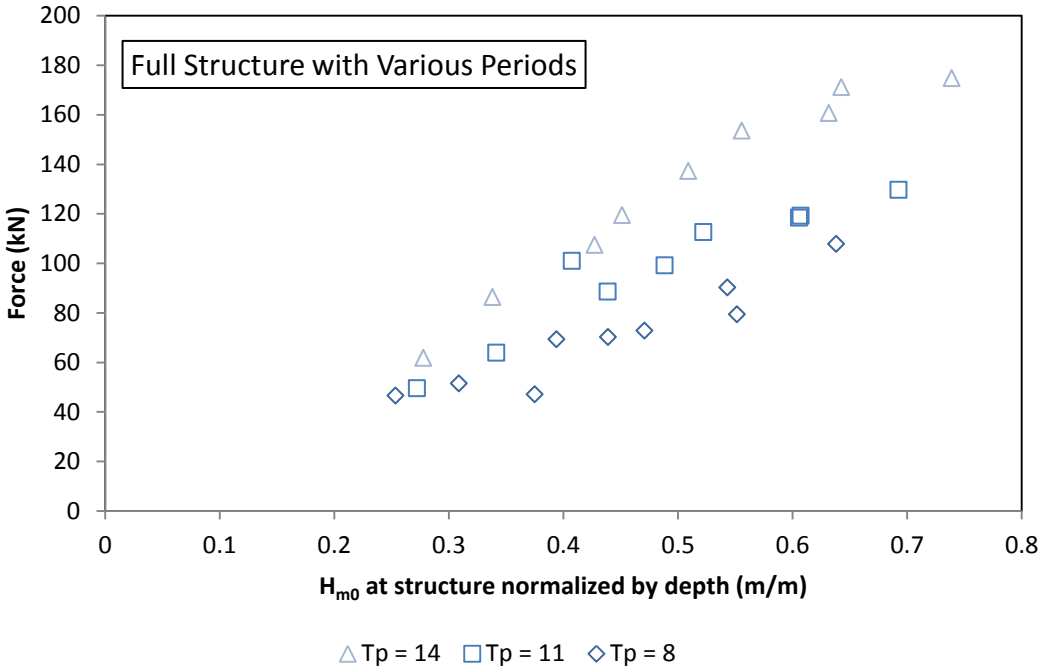

Figure 6.9: Maximum forces on the full structure for various peak wave periods

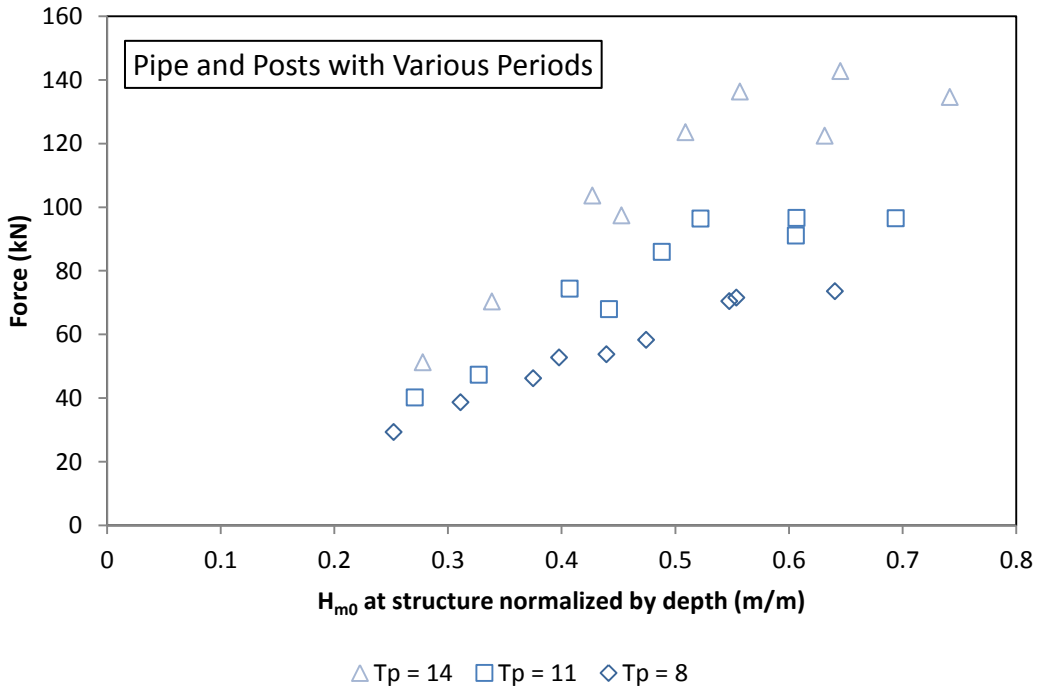

Figure 6.10: Maximum forces on the central pipe and 4 posts of the structure for various peak wave periods

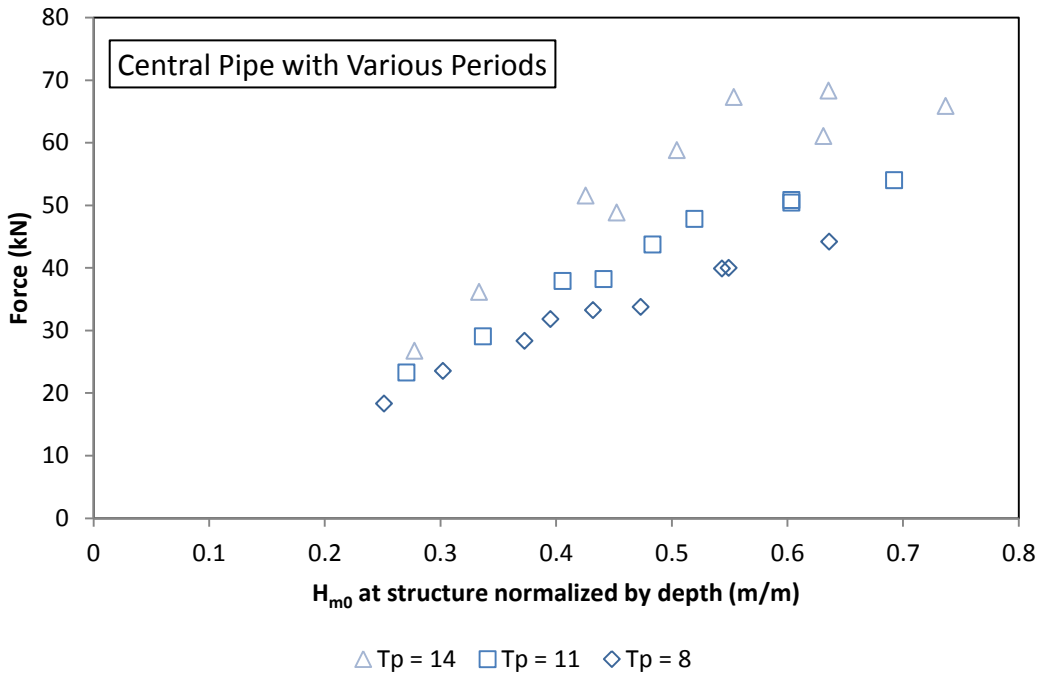

Figure 6.11: Maximum forces on the central pipe of the structure for various peak wave periods

Similar trends from Figures 6.6-6.8 are noticed in Figures 6.9-6.11. Peak force values for all structural configurations increase with H_{m0} values recorded at the structure location divided by water depth, with the rate of increase in the force values slowing as H_{m0}/d approaches 0.7. Due to the shallower water depths at the location of the structure versus the offshore zone, H_{m0}/d values at the structure larger than 0.8 were not possible during random wave tests. This was a result of the larger waves in those wave trains shoaling and breaking prior to hitting the structure, with much of the largest wave energy having dissipated from breaking. The peak in forces corresponding to an H_{m0}/d value of approximately 0.7 indicates that the largest wave events at the structure may occur during these random wave series. Maximum waves recorded from each random wave test were then compared with peak force to observe this relationship.

6.1.3 Maximum Wave Forces

It has been shown that correlations can be made between peak horizontal forces on the structure, zero moment wave height (H_{m0}), and peak period (T_p). Next, the largest waves recorded at the location of the structure were considered. It is known that horizontal forces exerted on the structure are directly related to the wave height. This was verified by comparing the wave record of the wave gauge directly

beside the structure from an irregular wave test with the record for forcing in the direction of wave propagation (F_X). A 100s sequence of this comparison is displayed in Figure 6.12.

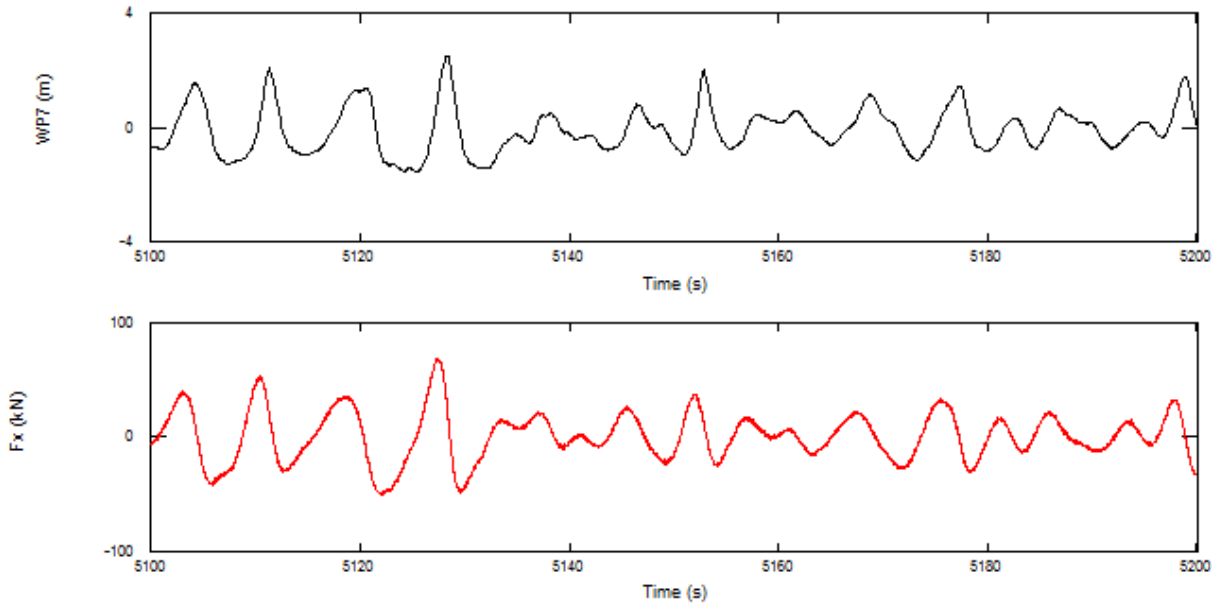

Figure 6.12: Wave record (top) with corresponding in-line force record (bottom)

The peaks in force occur slightly prior to the instant when the crest of the wave is recorded. This is due to a large component of the forcing resulting from the orbital acceleration of water particles. With this correlation between crest elevation and peak forcing, it was assumed that the largest force value recorded on the structure is generated by the largest wave occurring in a random wave series .The largest wave (H_{MAX}) was divided by depth and plotted versus 95% F_X in Fig. 6.13.

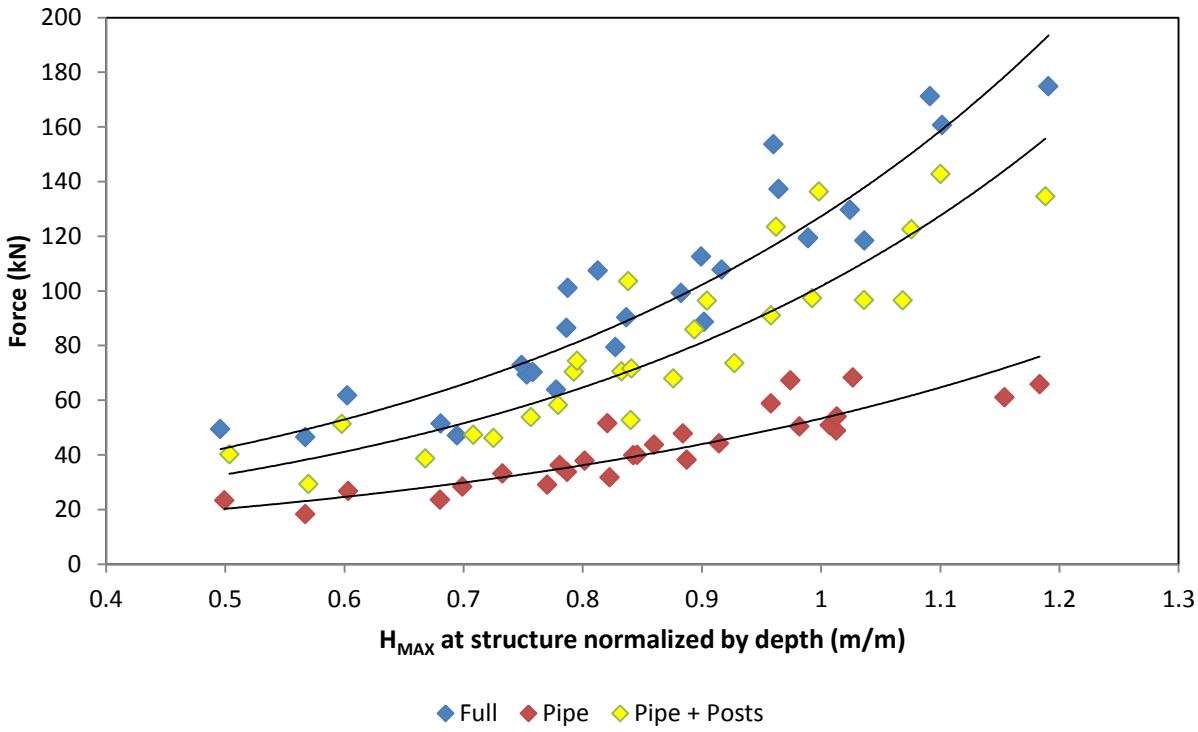

Figure 6.13: Peak forces versus the largest wave recorded at the structure during each test

An exponential correlation between peak force and H_{MAX}/d can be observed. The peak force increases at a greater rate versus H_{MAX}/d in Figure 6.12 than when plotted versus H_{m0}/d at the structure location, and with less scatter (Figure 6.13). It is interesting to note that the force values increase exponentially past $H_{MAX}/d >\approx 0.7$, or approximately to the theoretical wave height to depth ratio at which wave breaking is expected to occur. For these plots look at both offshore and structure location H_{m0}/d (Figures 6.3 & 6.4), the rate of increase in peak force begins to decrease as H_{m0}/d approaches 0.7. The trend in Figure 6.13 continues exponentially, suggesting that the largest forcing on the structure will occur at the largest possible H_{MAX}/d wave for the structure location, or the largest wave which is closest to breaking. In order to better understand the relationship between the peak force and the maximum wave height, the results were plotted separately by the peak period of the random wave series. Peak force results on the full structure only were plotted due to the amount of scatter present in Figure 6.13. The results are displayed below.

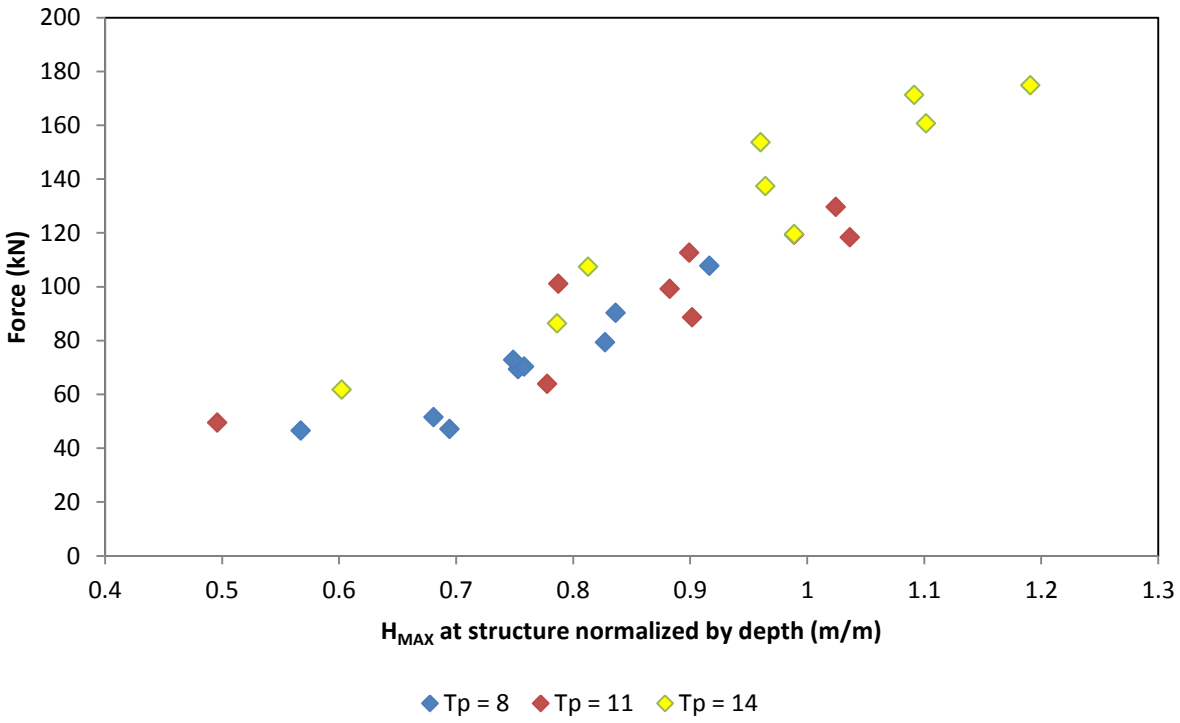

Figure 6.14: Peak force on full structure versus largest wave from each irregular wave series

There is some distinction between H_{MAX}/d values and peak forces between different peak periods (T_p) tested. Longer period waves have longer wave lengths and are less steep, therefore are capable of larger H_{MAX}/d values in the wave breaking zone. To normalize the results for wave length, the force values were divided by $g*(T_p)^2$, the value for deep water wave length according to Linear Wave Theory.

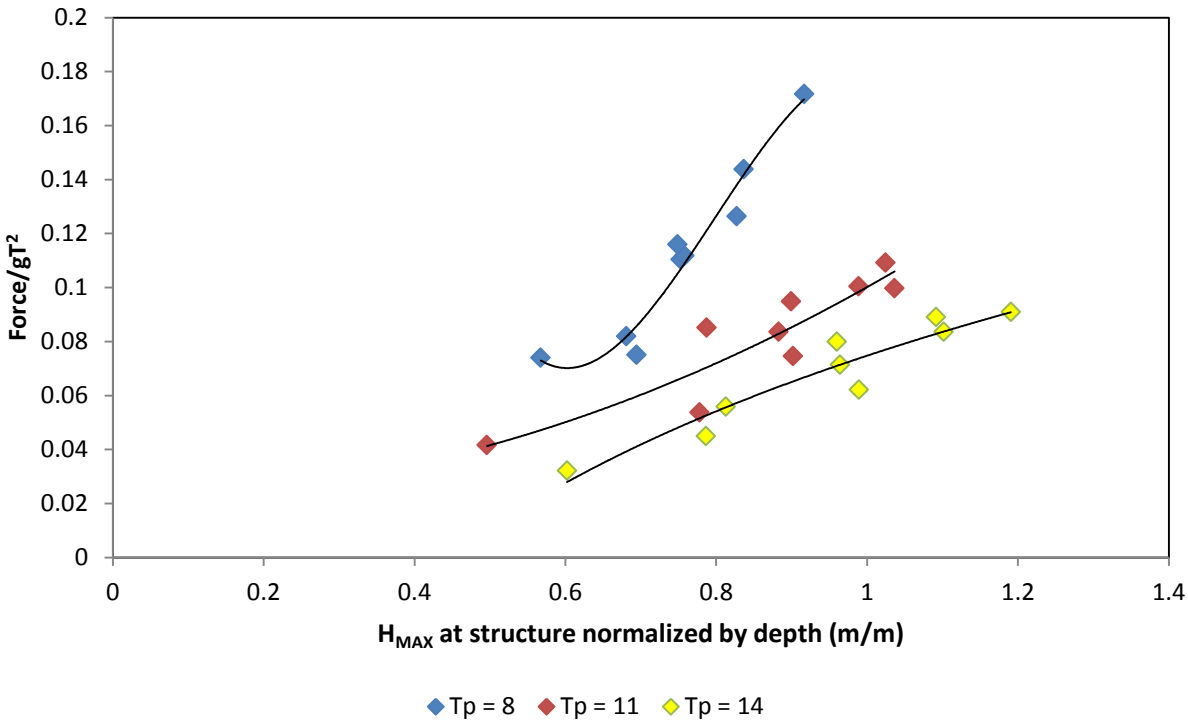

Figure 6.15: Peak force on full structure divided by wave length versus largest wave from each irregular wave series

There is a sharp increase in peak force values for maximum waves from random wave series with peak period of 8s when compared to the other 2 sets of random wave tests. This would indicate that maximum force is generated from the largest, steepest waves at the structure location. Shorter period limits how large can be in the shallow water zone the structure is located, so the maximum wave height is still the more important factor from random waves in determining what event will generate the largest force on the structure.

6.1.4 Negative Horizontal Forces

All peak horizontal force values used in analysis to this point have been positive forces, or in the direction of wave propagation. Figure 6.12 shows that peak force values are strongly related to maximum waves that are close to breaking, so it was determined that the maximum force in a random wave series would occur in the positive direction. The 95% largest negative forces (which occur during wave trough) values recorded on the full structure were plotted with the positive values of the same tests for comparison to see if a negative direction force event could potentially be the largest force on the structure (Figure 6.16). The results show that peak negative forces are significantly lower than peak

positive forces. The few occurrences of slightly larger negative forces deviate from the trend and are still lower than the largest positive force for the given offshore H_{m0}/d condition at the same peak period.

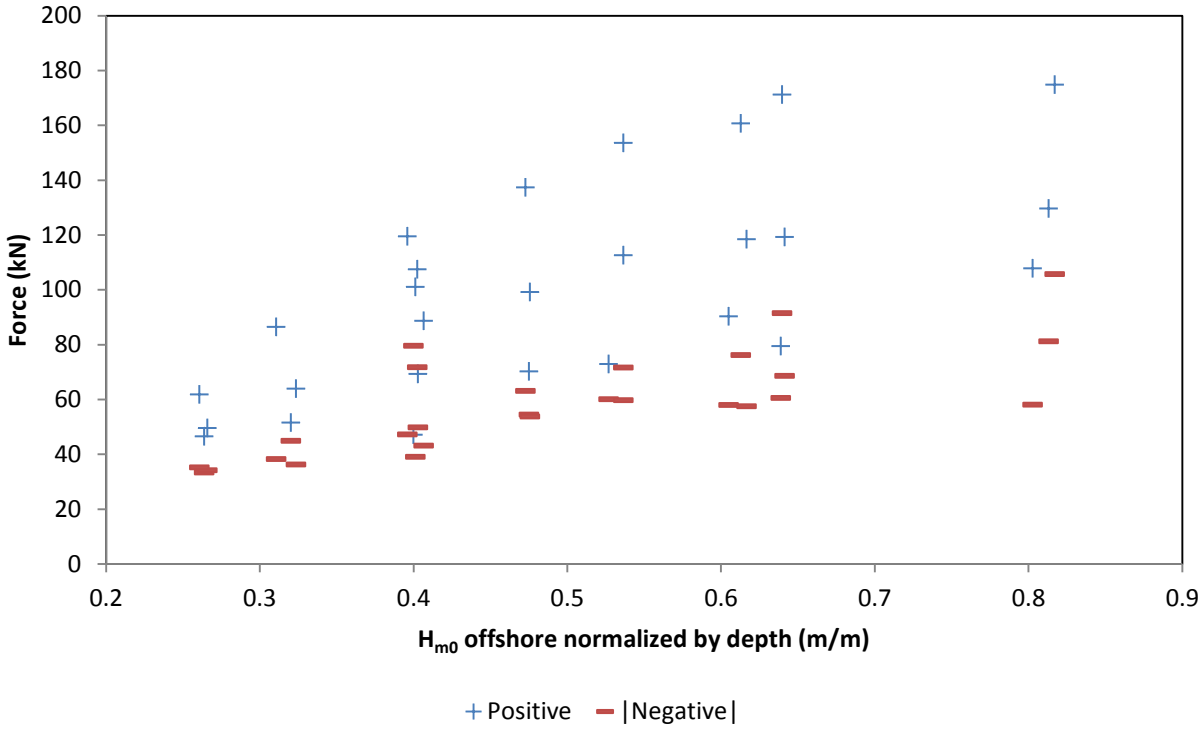

Figure 6.16: Peak negative forces compared with peak positive forces from irregular waves

6.1.5 Vertical Forces

The dynamometer on which the base of the structure was attached recorded also forces in the vertical, or Z-direction. The sign notation follows the right-hand rule in accordance with the notation of the in-line forces; forcing in the upward direction is positive, and negative in the downward direction. The central pipe and 4 posts are smooth cylinders with no horizontally protruding flanges or plates, so it was assumed they would contribute minimally toward vertical forces. Regardless, peak (95%) vertical force for all 3 structural configurations were plotted with a logarithmic Y axis in Figure 6.17 to show the magnitudes of peak vertical forces measured on all components of the structure.

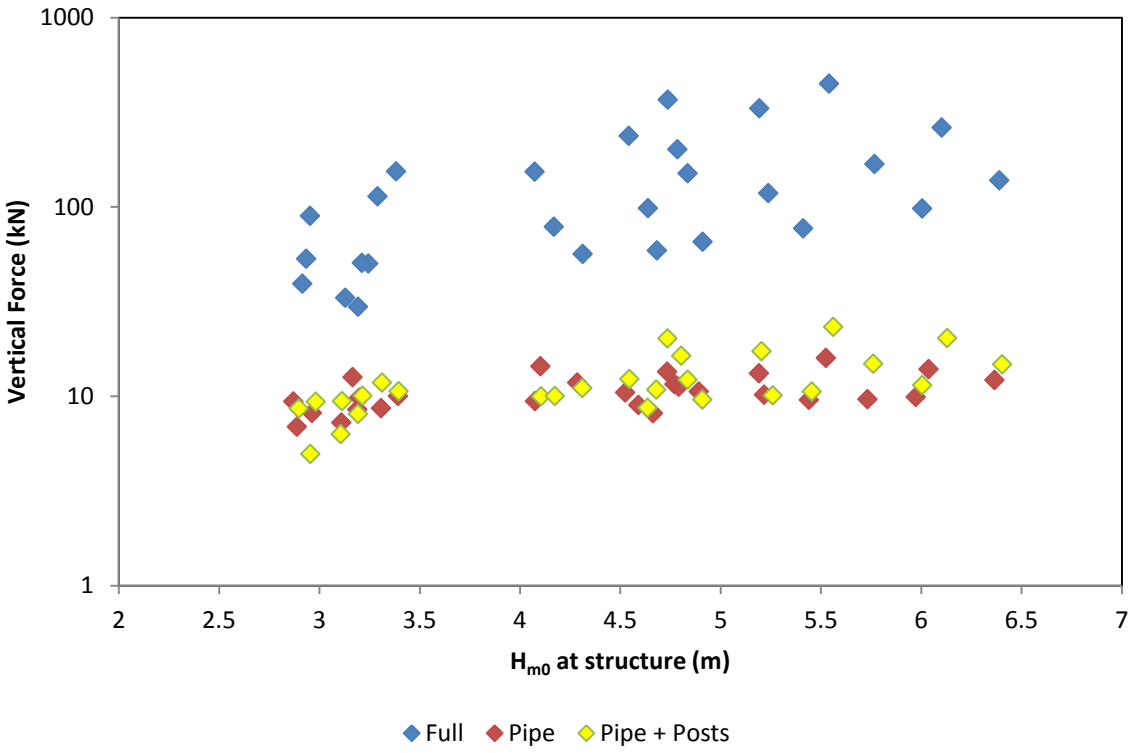

Figure 6.17: Peak vertical forces from tests on all 3 structural configurations

Immediately it can be observed that the peak vertical forces measured on the pipe and pipe + posts configurations are one order of magnitude less than the vertical forces on the full structure. This confirms the assumption that the vast majority of vertical force is measured from flow pushing up against the bottom of the cap as the wave crest passes the structure. The other interesting observation is that the pipe + post configuration peak vertical forces are not significantly larger than forces on the pipe alone and in a few cases were measured as less. The pipe + posts configuration includes the aluminum base plate which the posts are supported on. It was initially presumed that a lift force would be recorded from horizontal flow accelerating over this plate, but clearly this is negligible. The following analysis on vertical forces will therefore focus on results from tests on the full structure configuration only.

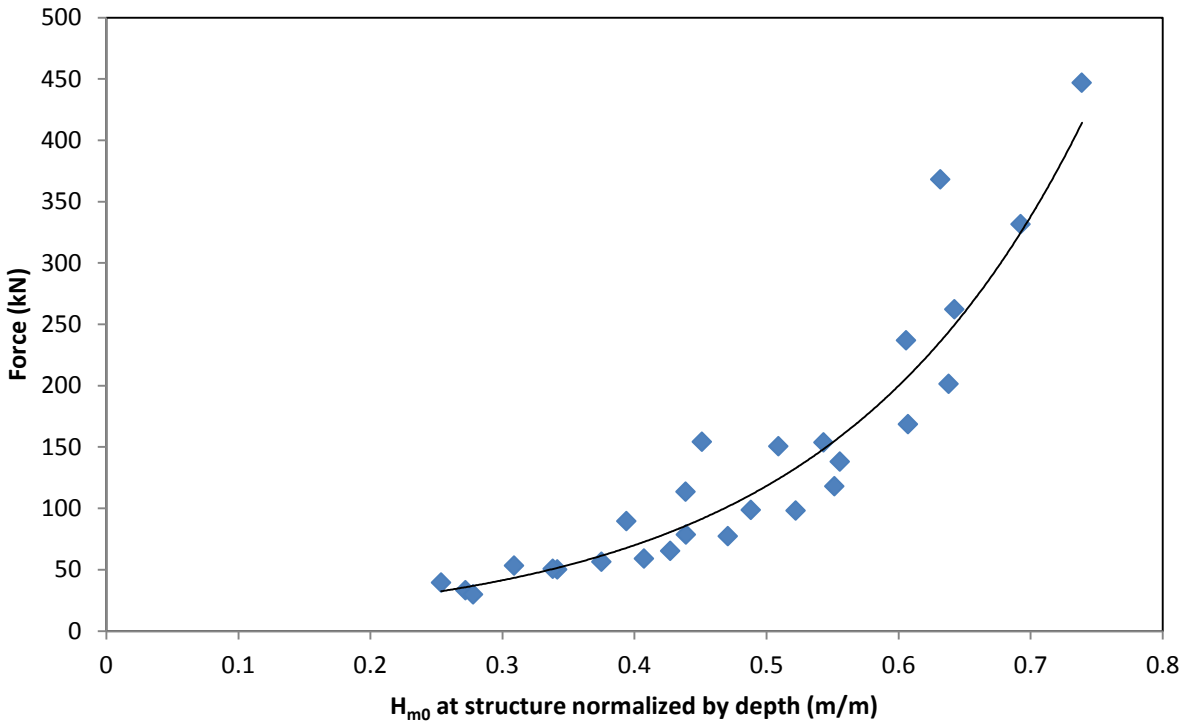

Figure 6.18: Peak vertical forces on full structure plotted versus H_{m0} normalized by water depth

The above graph shows an exponential increase in the vertical peak force when plotted against H_{m0} at structure normalized by depth. This is a different trend than for peak horizontal forces, which show a linear upward trend that begins to level off as H_{m0}/d approaches 0.8 (Figure 6.4). The data in the above plot was then separated by water level and peak period (T_p) to observe their respective effects on peak force (Figures 6.19 & 6.20). It is also worth noting that the peak vertical forces experienced by the velocity cap are significantly larger than the peak horizontal forces experienced by the central pipe and posts.

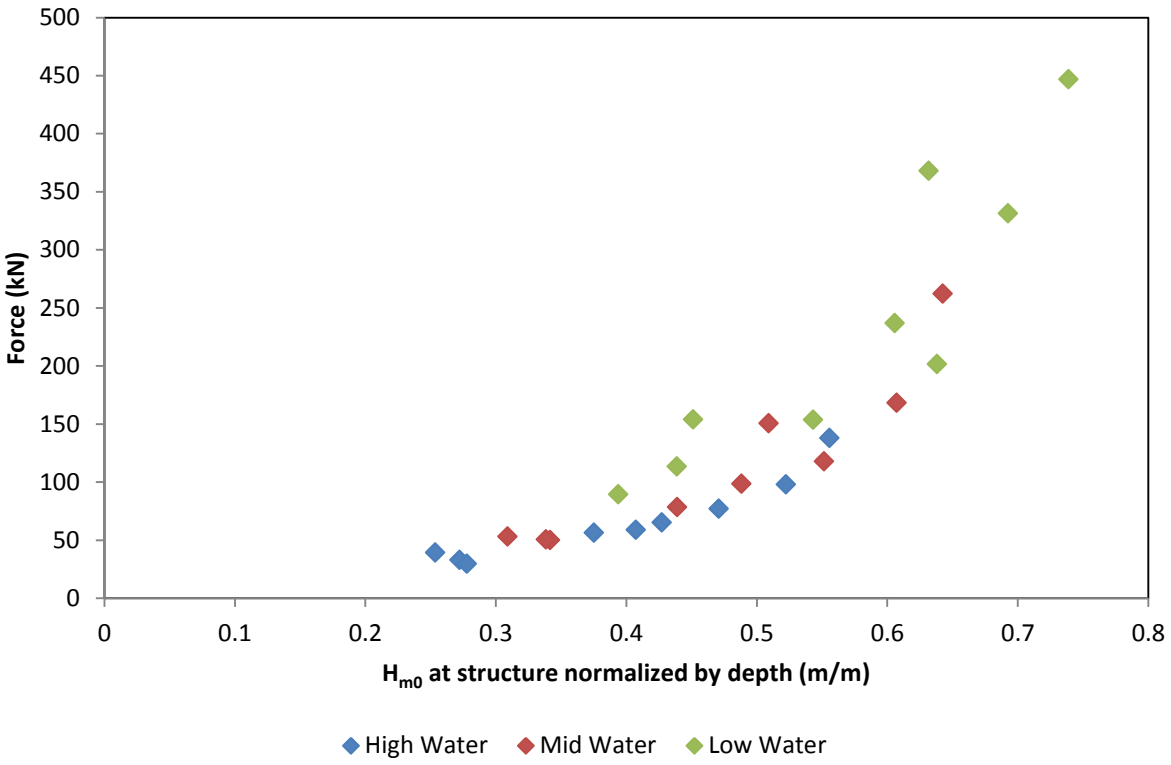

Figure 6.19: Peak vertical forces on full structure plotted separately by water depth

Figure 6.19 shows that wave conditions combined with lower water depths generate much larger vertical forces. High water level results in more depth at the structure, resulting in the cap being further away from the free surface. In intermediate wave conditions (waves transforming from deep to shallow water conditions according to H/L) such as those found at the structure location, the orbits of the water particles in waves become increasingly flatter and horizontal the further distance they are from the free surface (Figure 2.6). In the case of the low water conditions (shallower water depth at the structure), with the velocity cap of the structure closer to the free surface, more circular water particle orbits interact with the cap. The circular water particle orbits tend to have larger vertical components for both velocity and acceleration, generating thus larger forces acting on the cap. There is still much scatter along the line for peak vertical forces at low water level. The effect of peak period (T_p) was investigated.

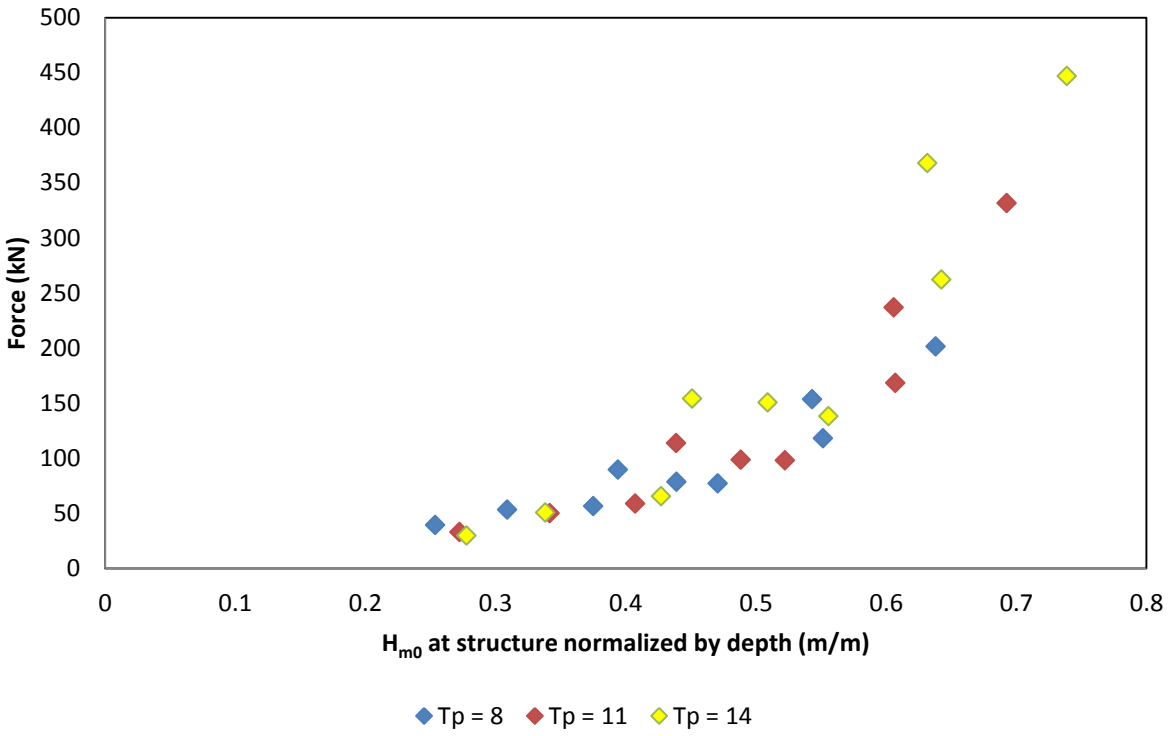

Figure 6.20: Peak vertical forces on full structure plotted separately by peak period

Peak vertical force increases with the peak period (T_p) of the irregular wave conditions, as noted previously with peak horizontal forces (Figures 6.9-6.11). In lower H_{m0}/d conditions, the peak period does not have a significant effect. The largest forces are recorded after $H_{m0}/d > 0.6$, where only 1 irregular wave test was tested, featuring a peak period of 8s has $H_{m0}/d > 0.6$. Most irregular wave tests with T_p = 8s feature shorter wave lengths that accompany shorter wave periods. The shorter wave length conditions resulted in steeper waves more likely to break and lose energy, with the largest waves in the random wave series breaking prior to reaching the structure location. This would indicate that the largest vertical forces are induced by the largest waves recorded at the structure, and they are more likely to occur during random wave conditions with high T_p values. The latter allow for longer and higher waves to shoal and break at the structure location. The maximum waves recorded at the structure were then analyzed with peak vertical forces (Figures 6.21).

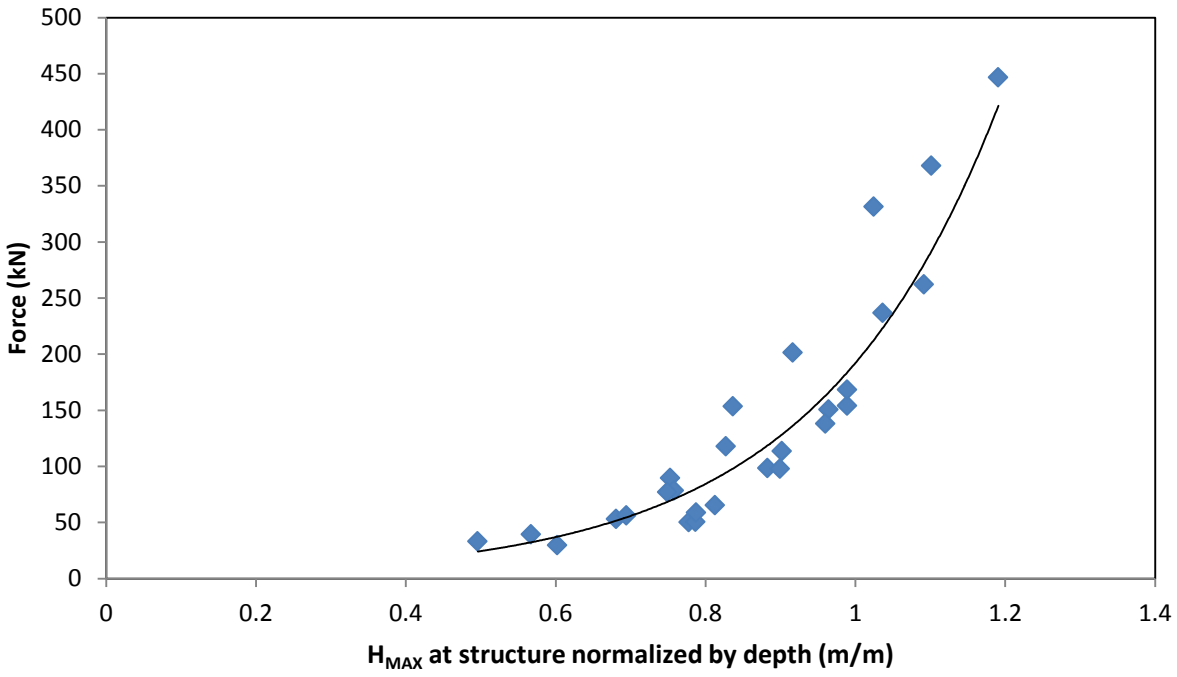

Figure 6.21: Peak vertical force on the full structure plotted against largest waves in irregular wave series

Figure 6.21 shows an exponential increase in peak force with H_{MAX}/d as Figure 6.13 showed for the horizontal forces with the same wave conditions. The largest vertical forces are also recorded at the highest possible H_{MAX}/d, which are large waves that have already shoaled and are in the process of breaking. There is still significant vertical scatter at some H_{MAX}/d values, and this is clarified in Figure 6.22 where the peak force values are plotted separately by peak period.

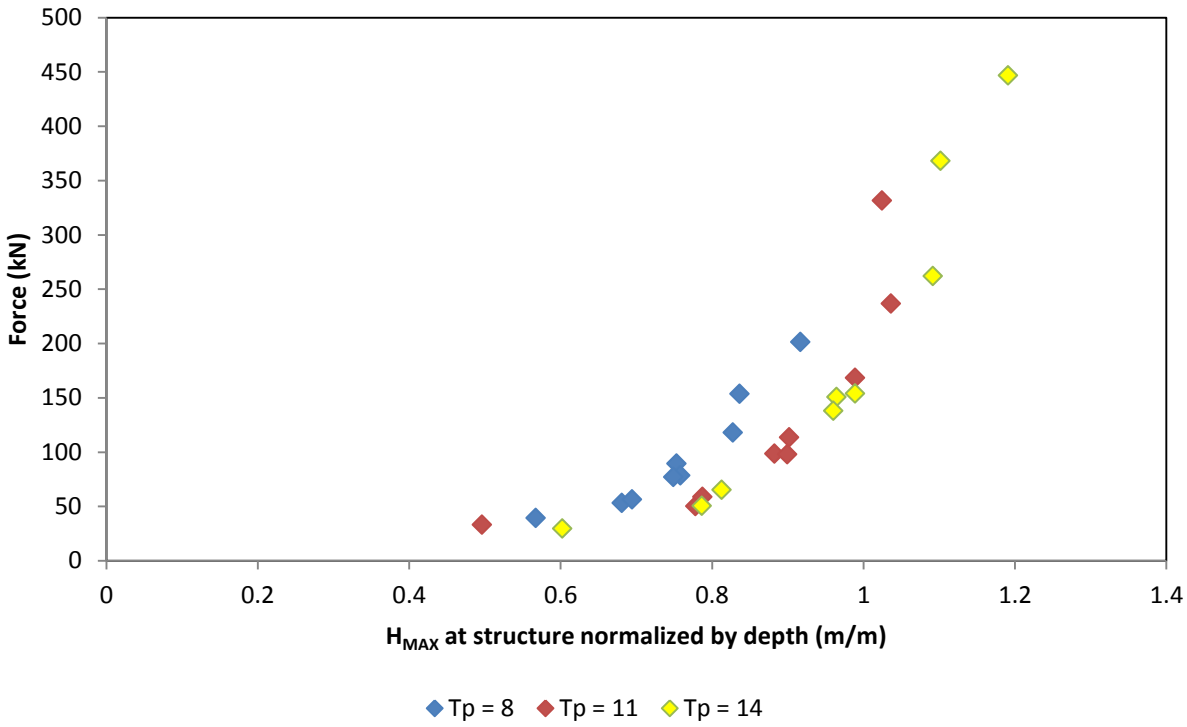

Figure 6.22: Peak vertical force plotted by peak period against largest waves in irregular wave series

There are a few interesting observations that can be drawn from Figure 6.22. Irregular wave conditions for T_p = 8s show a clear exponential trend that occurs at lower H_{MAX}/d values than for forcing from the T_p = 11s and T_p = 14s tests. This would indicate that peak period does not have a significant effect on peak vertical force, and that the random waves with a shorter peak period actually show larger vertical forces. The reason for that is that irregular wave trains with T_p = 8s shoaling along the progressively shallower bathymetry created in the flume have shorter wave lengths and cannot achieve the same maximum wave heights as waves with longer periods. The longer period tests feature significantly larger maximum height waves, and hence, larger peak vertical forces. It can be concluded that peak vertical force is exponentially related to wave height normalized by depth, and that increasing the peak period only increases likelihood of larger forces by allowing for larger waves to pass over the structure. In conditions that allow for short period large steep waves, larger peak vertical forces are generated. This is shown below in Figure 6.23, which is the same plotted data as Figure 6.22 above, with the force values divided by a factor representing the offshore wave length. The shorter period results are larger than the longer period results at any given H_{MAX}/d condition.

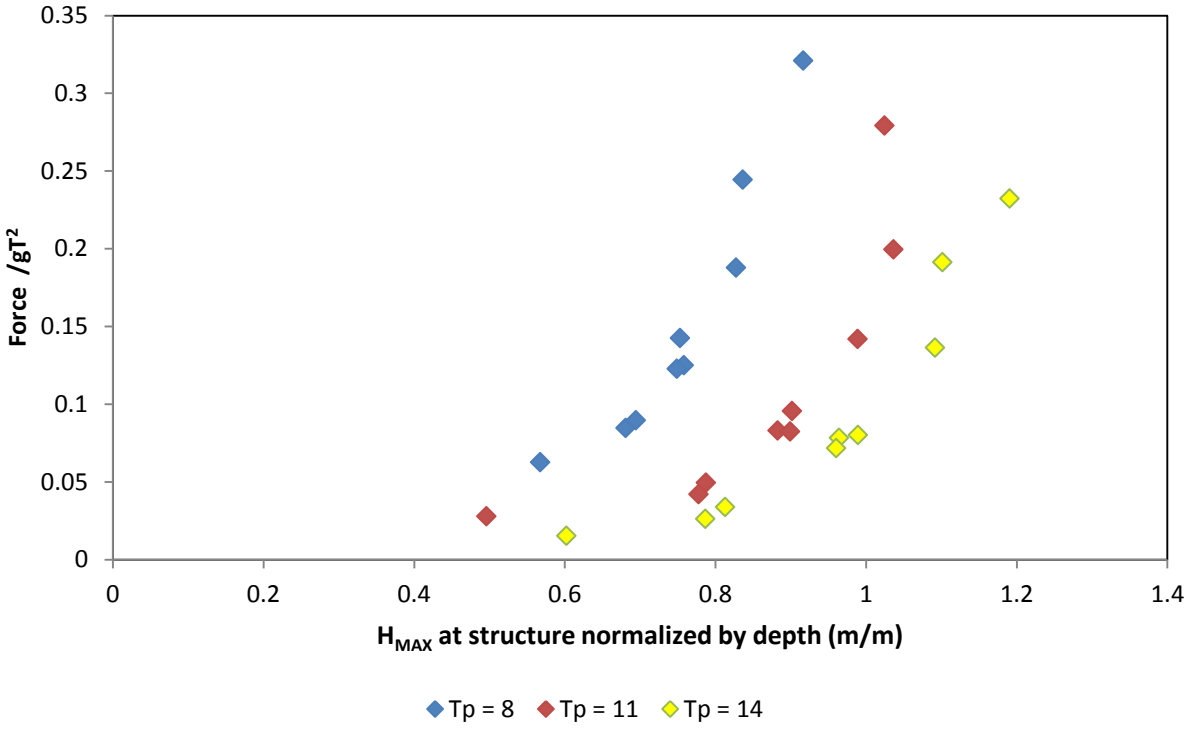

Figure 6.23: Vertical force normalized by offshore wave length versus depth normalized maximum waves

6.1.6 Forces on Separate Structural Components

It was further investigated whether forces on separate components of the structure could be accurately determined from the peak force data. From Figures 6.3 & 6.4 it can be seen that the magnitude of peak forces on the central pipe and posts is approximately double the magnitude of the peak forces on the central pipe. Peak forces on the support posts were estimated in equation 6.1 by subtracting the peak force values from tests on the central pipe only configuration from the force results for configuration 3 of each respective irregular wave test. The results were plotted below, first with all results and then separated by peak period.

$$F_{Posts} = F_{conf3} - F_{Pipe} \qquad [6.1]$$

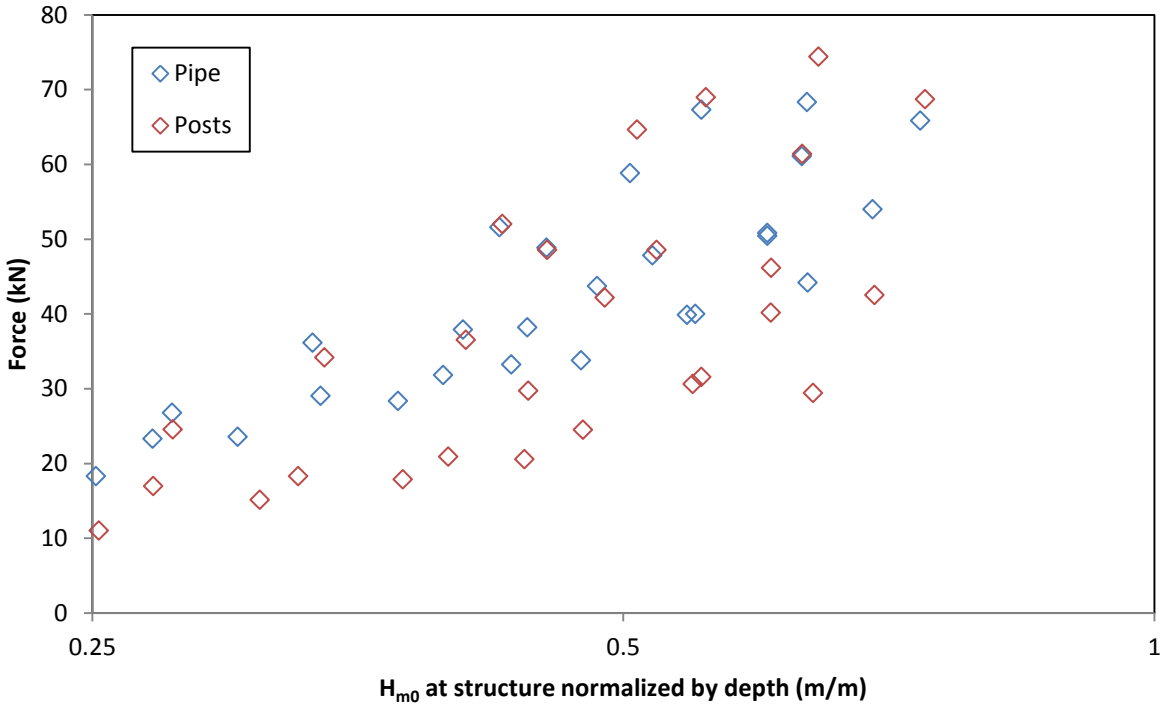

Figure 6.24: Peak forces recorded on central pipe and estimated on support posts

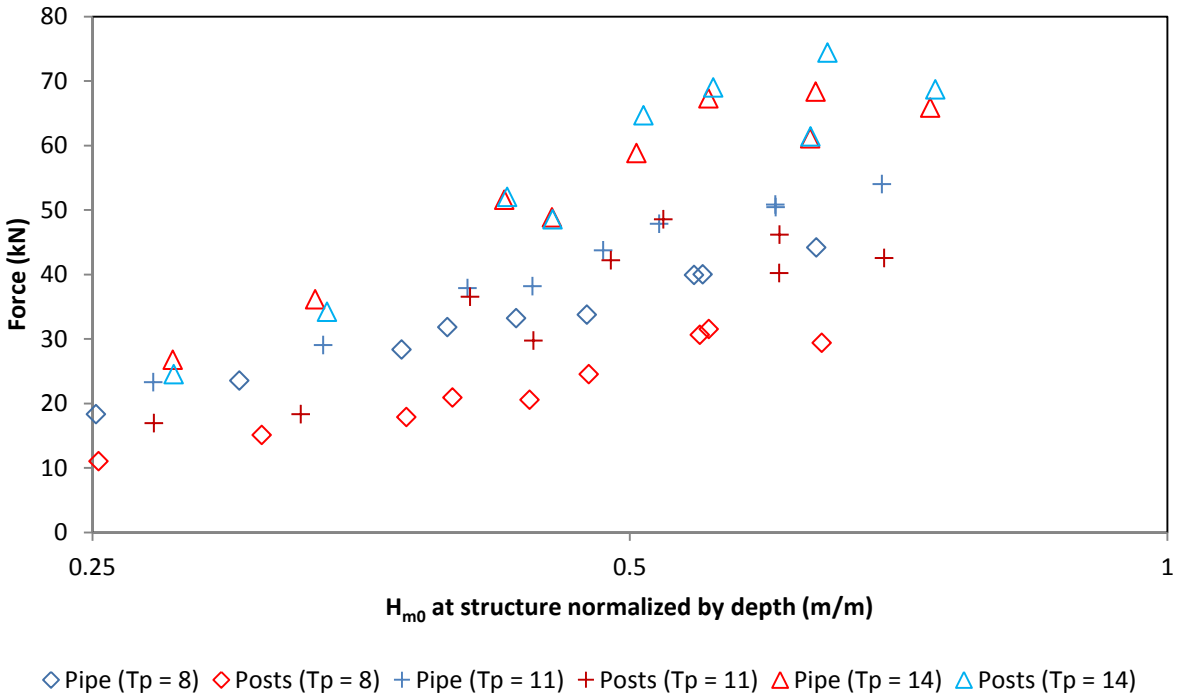

Figure 6.25: Peak forces recorded on central pipe and estimated on posts plotted separately by peak period

Figure 6.24 shows similar magnitude between peak forces measured on the central pipe and forces estimated on the 4 support posts. When comparing Figures 6.24 & 6.25, it can be seen that longer peak period values compose the upper portion of the scatter and shorter peak periods are found in the lower portion. For peak period of T_p = 14s, peak force values are very similar for H_{m0}/d. For peak periods of T_p = 8s and T_p = 11s, force results are either similar or larger for the pipe rather than the posts. The geometric properties of the central pipe and of the 4 combined posts are shown in Table 6.1.

Table 6.1: Geometric properties of the separate components of the structure

Component	Pipe	Post (x4)
Area normal to flow (m^2)	4.38	6.48
Volume (m^3)	7.27	2.66
Diameter (m)	2.12	0.52 (1 post)
Spacing ratio (L/D)	1.15	4.66

Since the magnitudes of peak forces are similar for the central pipe and 4 posts, it is suggested that area normal to the flow direction is more important to determining the magnitude of peak force on each component ($1.5A_{PIPE} \approx A_{POSTS}$; $V_{PIPE} > V_{POSTS}$). From the Morison equation, theoretically the volume of a cylinder affects inertia force (first term) and the area normal to the flow direction affects drag force (second term).

$$F_x = \rho \boldsymbol{C_M V} \left(\frac{du}{dt}\right) + \frac{1}{2} \rho \boldsymbol{C_D A} u|u| \qquad [6.2]$$

These results would indicate that peak forces from waves breaking at the structure are generally drag dominated. Drag or inertia force domination is typically determined by the Keulegan-Carpenter (KC) number for the flow and structure, but complicated water particle kinematics during large breaking waves making estimating this value unfeasible. Zdravkovich (1977) stated that inference effects between would lower the drag coefficient (and drag force) for spacing ratios less than or equal to L/D ≈ 3.5 for cylinders in line with flow and L/D ≈ 2 for cylinders arranged perpendicular to the flow direction. Using the spacing ratios in Table 6.1, it can be seen that the central pipe interferes and lowers the drag

coefficient for all 4 posts (either in-line with the flow or perpendicular), and that the posts have no interference effects with respect to drag forces on the pipe. Spacing is equal between pipe and posts in all 4 directions. These facts may be used to estimate force separately on each post and central pipe. Proportion of peak horizontal force on each structural component was compiled in histogram format. Peak force values used for the posts are the same values presented in Figure 6.24. Force values for the velocity cap in the horizontal directed were calculated in a similar manner as for the posts, by subtracting the 95% peak horizontal force on the pipe and posts configuration from the full structure configuration values. Results are plotted by peak period (T_p), in groups of offshore H_{m0} values arranged right to left of 3m, 4.5m, and 6m. Each of the 3 graphs represents a different water level.

$$F_{Cap} = F_{conf1} - F_{Conf3} \quad [6.3]$$

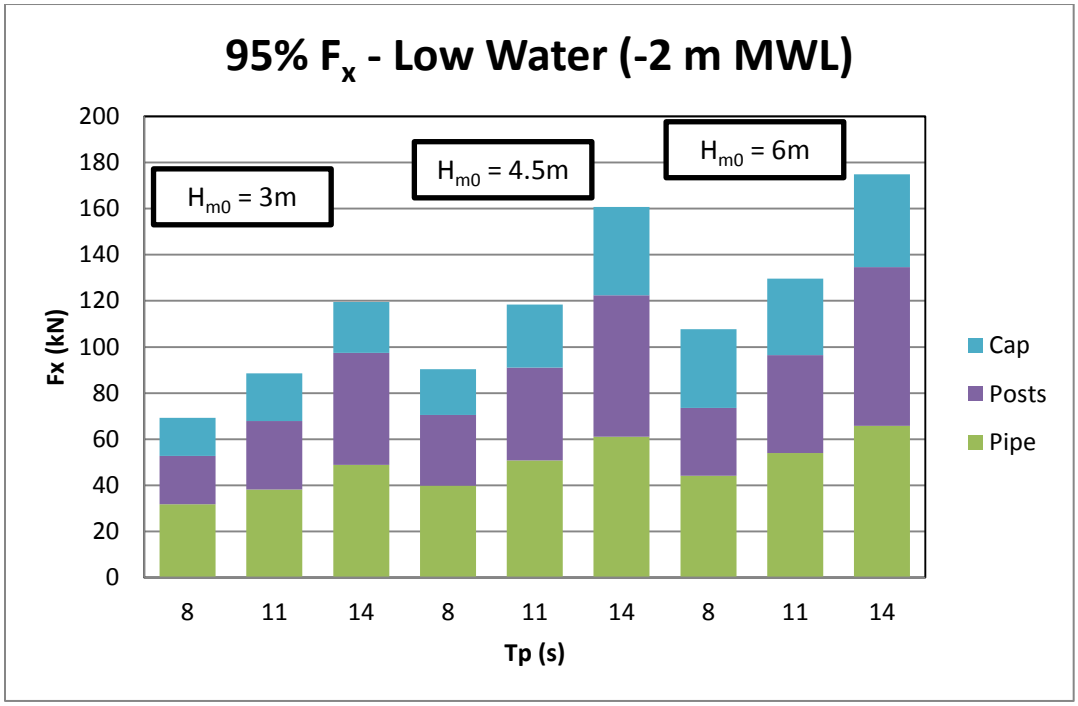

Figure 6.26: Proportion of peak horizontal force on each structural component in low water

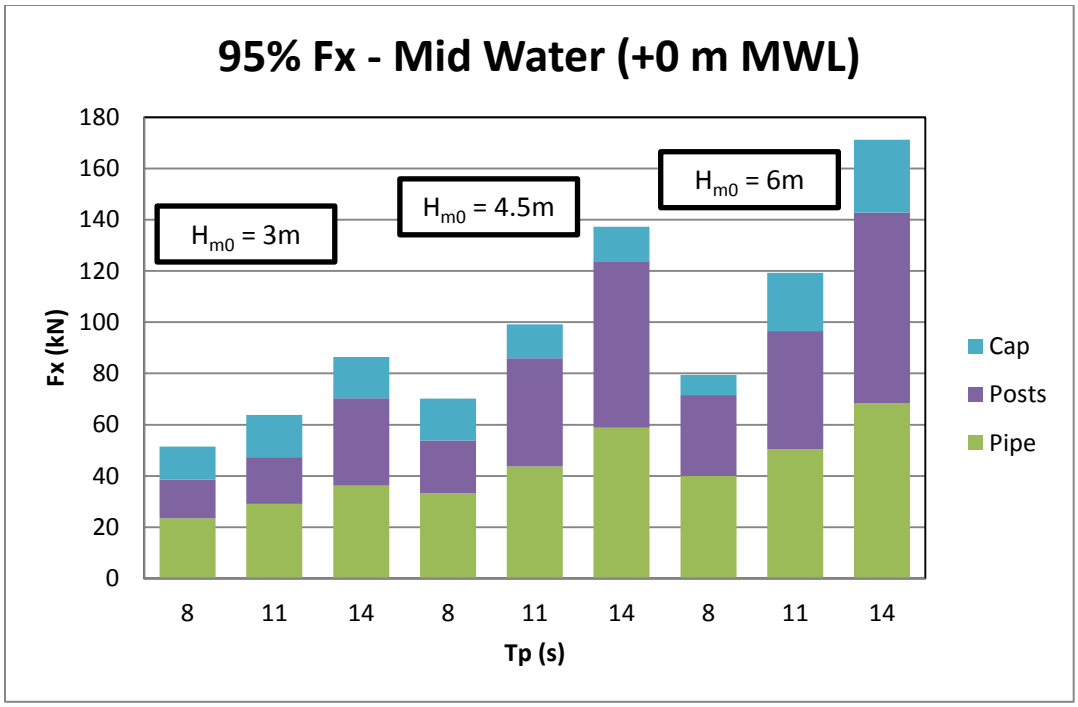

Figure 6.27: Proportion of peak horizontal force on each structural component in mid water

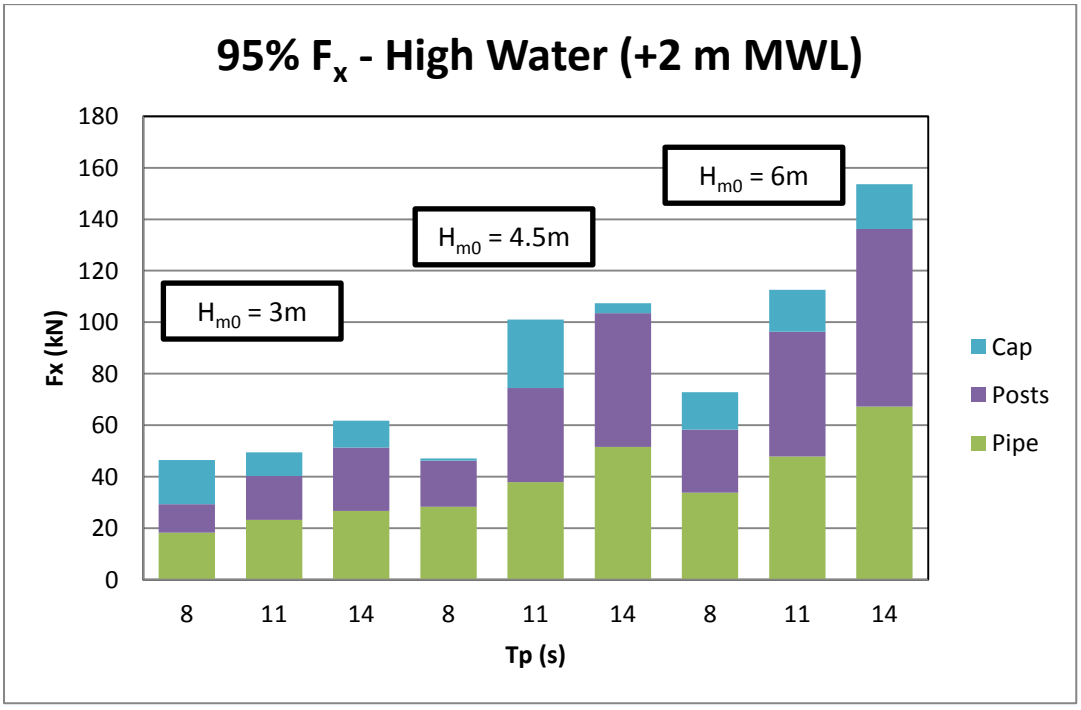

Figure 6.28: Proportion of peak horizontal force on each structural component in high water

Similarly to previous plots in this peak force analysis, the peak horizontal force in Figures 6.26-6.28 increases with the H_{m0} and T_p values within each group of irregular wave. In all wave conditions, the

magnitude of peak horizontal force on the central pipe and 4 support posts is very close, as seen in Figures 6.24 & 6.25. The value most affected by the changing wave conditions in the above histograms is the magnitude of peak horizontal forcing on the velocity cap. In low water conditions, the velocity cap contributes a large portion of the total horizontal force on the structure. In deep water conditions, the contribution is significantly less and, in some cases, almost zero. This is due to the changing shape of water particle orbits with depth in shallow water conditions (Figure 2.6). In deeper water, the orbit of the water particles at the depth of the velocity cap is relatively flat, with a small vertical velocity and acceleration component. Hence, the thin velocity cap does not experience much force from water particles moving in the horizontal direction. In shallower water, the cap is closer to the free surface. At this depth, water particle orbits are closer to a circular one, with a more pronounced vertical component of the velocity and acceleration. The water particles moving in these orbits from passing waves interact with the velocity cap, with a component of this measured force being horizontal.

6.1.7 Discussion on the Peak Force Analysis

From the presented results, a number of conclusions can be drawn, relating the properties of irregular waves and the induced peak forces on the submerged intake structure:

1. Peak horizontal force increases linearly with H_{m0}/d and peak period (T_P)

Figure 6.3 shows that peak force values recorded on the structure increase linearly until $H_{m0}/d \approx 0.66$, close to the theoretical wave height-to-depth for wave breaking value of 0.78. Graphs displaying the force values from Figure 3 again separately by structural configuration and peak period (Figures 6.9-6.11) show the trend continues for each peak period tested and for each structural configuration. There is little scatter or deviation from the trend in these plots, reinforcing the finding that peak in-line force on the submerged structured increases linearly with H_{m0}/d and with the peak period for an irregular wave series. It is assumed the most extreme wave conditions at the location of interest will induce the largest forcing on a submerged structure, but these results show normalized wave heights are a better indicator of the expected peak forces.

2. Largest waves at the structure location induce the largest magnitude forces

When looking closely at the wave and force records (Figure 6.12), a direct correlation between the wave height and the peak in-line force was observed. Figure 6.13 shows that maximum wave heights correlate well with peak in-line force for all structural configurations. The force values are larger for tests with maximum wave events of $H_{MAX}/d > 0.7$, when the waves begin to break. This plot shows that peak force

events recorded on the structure occurred when waves break at (or shortly after) the location of the structure. The larger the H_{MAX}/d value plotted, or the closer the largest wave of the series was to breaking, this resulted in a linear increase in the peak force values. Peak period was not seen to have a significant effect on the peak force magnitudes. These results would suggest that the largest potential force would come from the largest possible H_{MAX}/d at the location of interest.

3. Vertical and horizontal forces on the velocity cap are larger in low water conditions

Peak forces on the cap in both vertical and horizontal direction showed an exponential increase in magnitude for tests in low water conditions (-2.0 MWL, depth of 7.5m at the structure). Peak vertical forces on the cap also correlated well with the maximum waves recorded at the structure (Figure 6.18). It was noted that peak period does not have a significant effect on peak vertical forcing; rather than that, maximum waves with steep crests generate the largest vertical force. When vertical force was normalized for wave length (Figure 6.23), the steeper shorter period waves generated the largest normalized vertical force.

4. Forces on central pipe and post are of similar magnitude to each other

Peak forces measured on the central pipe compared to those estimated on the support posts are shown in Figures 6.24 & 6.25. It was observed that the peak force values for pipe and posts were of similar magnitudes at the same peak period for each value of H_{m0}/d (structure location H_{m0}). Table 6.1 show geometric properties of the 2 components of the structure, as well as the influence the central pipe has at reducing drag forces on the surrounding posts. The magnitude of drag and inertia forces was investigated further in the next section of analysis, which focuses on determining force coefficients for the structure for purposes of estimating forcing using the Morison equation.

6.2 Force Coefficient Fitting

To understand forcing from waves on the submerged bodies, the Morison equation is used to estimate forces using wave induced current velocities and acceleration values. As discussed in the Literature Review section, this equation contains inertial and drag force term, with an empirical coefficient. These inertia and drag coefficients vary according to wave conditions and the geometry of the structure. The following section proposes to determine drag and inertia force coefficients for the structure, including coefficients representing each structural configurations as well as each separate component, using the current and force data recorded from the regular wave tests conducted as part of this study.

6.2.1 Morison Equation and Coefficient Fitting

In this section, the force data on the structure from the regular wave tests will be analyzed to develop a model for predicting irregular wave forcing on the studied structure. The model will be using the Morison equation or MOJS, the acronym for 4 original researchers (Morison, O'Brien, Johnson, and Schaaf). This equation requires a coefficient for each force term, representing the drag and inertia forces on the structure.

$$F = \rho \boldsymbol{C_M} V \left(\frac{du}{dt}\right) + \frac{1}{2} \rho \boldsymbol{C_D} A\, u|u| \qquad [6.4]$$

Inertia and drag coefficients (C_M & C_D respectively) can be empirically determined by obtaining the experimental force time series from waves passing over the structure and fitting them to the Morison equation. The various methods for fitting this equation with 2 unknown coefficients to experimental force data have been detailed in the Analytical section of the Literature Review and include: Morison's method, Fourier averaging, least squares, weighted least squares, and cross-spectral analysis. A comparative analysis of the relative error between force coefficient analysis techniques was carried out by Wolfram and Naghipour (1999). They found that the weighted least squares method provided the best fit for experimental data when determining the force coefficients. For these reasons, the weighted least squares method was selected to conduct this analysis. The equations used for fitting are provided below.

$$f_D = \frac{1}{2} \rho\, A\, u\, |u| \qquad [6.5]$$

$$f_I = \rho\, V \left(\frac{du}{dt}\right) \qquad [6.6]$$

$$C_D = \frac{\sum(F_o^3\ f_D)\sum(F_o^2\ f_I^2) - \sum(F_o^3\ f_I)\sum(F_o^2\ f_D\ f_I)}{\sum(F_o^2\ f_D^2)\sum(F_o^2\ f_I^2) - \left[\sum(F_o^2\ f_D\ f_I)\right]^2} \quad [6.7]$$

$$C_M = \frac{\sum(F_o^3\ f_I)\sum(F_o^2\ f_D^2) - \sum(F_o^3\ f_D)\sum(F_o^2\ f_D\ f_I)}{\sum(F_o^2\ f_D^2)\sum(F_o^2\ f_I^2) - \left[\sum(F_o^2\ f_D\ f_I)\right]^2} \quad [6.8]$$

Where F_O is the observed, or experimental, force recorded during the regular wave tests. Drag and inertia force terms without coefficients are represented by f_D and f_I, respectively. All values used in this analysis represent full-scale conditions.

6.2.2 Keulegan-Carpenter Number

The relative importance of the inertia and drag forces to the total force depends on the Keulegan-Carpenter number: the ratio of the water particle orbit amplitude generated by a passing wave to the cylinder diameter (Keulegan and Carpenter, 1956).

$$KC = \frac{U_M T}{D} \quad [6.9]$$

Where A is the amplitude of horizontal displacement of the water particle, U_M is the maximum horizontal velocity of a water particle during the wave cycle, T is the period of the wave, and D is the cylinder diameter. The KC number of a wave-cylinder interaction is a common parameter used in the analysis of wave forces on cylinders and is used to represent a large spectrum of cylinder diameters and wave conditions. Table (6.2) below illustrates the importance of inertia and drag forces over a range of KC numbers.

Table 6.2: Drag and inertia dominance at different KC ranges

KC < 3	Inertia force dominant – drag may be ignored
3 < KC < 15	Drag force may be linearized
15 < KC < 45	Full Morison equation – nonlinear drag
KC > 45	Drag force can be dominant

Forcing on the central pipe and the support posts is affected by vortices shed off structural members due to the separated flow conditions present in the vicinity of the structure. Vortex formation and strength is related to the KC number of the flow. At large KC numbers, there is a high vortex shedding frequency compared to wave frequency and flow tends to behave more uniform. However, the intake

structure in these experiments has multiple cylinders in close proximity, so the parameters set in Table 6.2 may not apply; specifically when it comes to drag forces, which are significantly affected by proximity effects (Zdravkovich, 1977). Studies determining the force coefficients under various wave conditions plot their force versus the range of KC numbers used in the experiments to illustrate the correlation between flow conditions and the drag/inertia force. This method will be used in this study in analyzing of the force coefficients for the intake structure.

6.2.3 Effect of Reynolds number on Force Coefficients

The Keulegan-Carpenter number is the most common parameter used when analyzing force coefficient results, but many studies also look at the effects of varying the Reynolds number. Drag forces are affected by the vortices in turbulent flow. The properties of these vortices, as well as the frequency at which they're shed, are related to the Reynolds (Re) number. Reynolds number has also been noted to influence inertia coefficients for a cylinder. Rance (1969) investigated the effects of varying Reynolds numbers on force coefficients for a submerged cylinder, with turbulent flow ranging to Re = 6.0×10^5. The intent of this study was to test the validity of using physical models to test structures where forces will vary with Re, given that a typical physical model uses Froude scaling and that Re values in the model will be significantly smaller than at the prototype scale. Therefore, prototype scale forces have the potential to be different in magnitude comparing to the forces measured on a physical model. Results of the work by Rance did show that forces on a single cylinder partly dependant on the Re number. However, the author concluded that interference effects from multiple cylinders placed in proximity may negate this dependency, and that further work on this topic is required. The experiments by Sarpkaya (1979) on force coefficients for riser configurations featured a central pipe surrounded by a tube bundle tested at various Re. The results for force coefficients at different Re values were nearly identical for varying KC values (Figure 6.29), indicating no dependence between force coefficients and the Reynolds number.

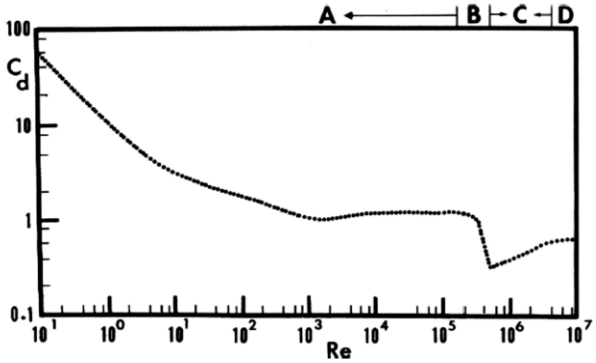

Figure 6.29: Drag coefficient values for a single cylinder as a function of Re (Schlichting, 1968)

6.2.4 Structure Classification

The standard method for estimating wave loads on slender cylinders is the Morison equation. Wave induced forces on wider cylinders that aren't classified as slender structure need to be analyzed for diffraction effects and cannot be analyzed using the Morison equation. Issacson (1979) showed that if the cylinder diameter divided by the wave length (D/L) was less than 0.2, diffraction effects may be ignored and the Morison equation could be accurately used. Issacson (1979) created a diagram illustrating which force analysis techniques should be used for a cylinder under varying wave conditions (Figure 6.30).

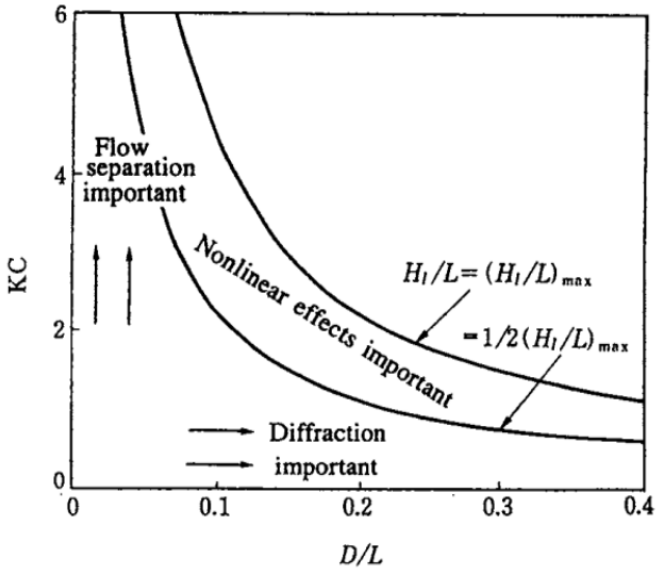

Figure 6.30: Wave force regimes (Isaacson, 1979)

The importance of diffraction is determined by the wave length (L) and the cylinder diameter (D). To determine if diffraction effects would warrant consideration in the analysis of horizontal forces from waves on the cylindrical members of the intake structure, all 9 possible regular wave lengths at the structure location were estimated using the Linear Wave Theory (Table 6.3).

Table 6.3: Wave lengths at the location of the structure from regular waves

Depth at structure (m)	Wave Length (m)		
	T = 8s	T = 11s	T = 14s
7.5	37.7	90.0	115.7
9.5	69.3	100.8	133.2
11.5	74.7	110.6	138.6

The largest diameter structural member, the central pipe, shows that D/L << 0.2 for any wave length at the structure location. Therefore, diffraction effects may be ignored for the present analysis and the Morison equation will be used to estimate wave induced forcing on the structure.

6.2.5 Central Pipe Force Coefficients

To investigate the relationships between force coefficients and varying wave and current conditions for the intake structure, wave kinematics and force data from the regular wave experiments were extracted using the GEDAP software, using very small time steps (approximately 0.3s). Forces on the central pipe were first analyzed by plotting a train of 5 waves and comparing it with the forces on the pipe predicted using the Morison equation, calculated and using current data.

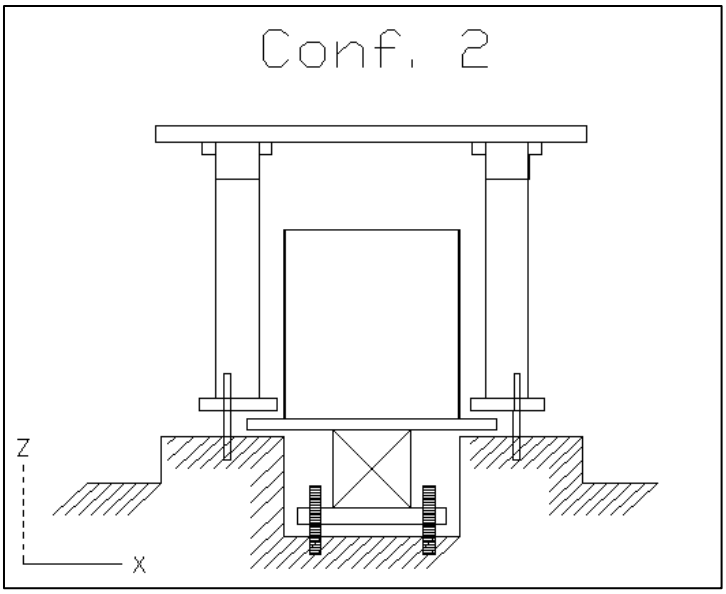

Figure 6.31: Configuration (2) for isolating forces measured on pipe while maintaining presence of posts and cap

Following standard methods for determining the force coefficients of submerged cylinders, the regular waves were first analyzed due to their uniform nature when compared to random waves. Regular wave tests were conducted similarly to the irregular waves: for 3 different water levels, with 3 different average wave heights, and all at a full scale period of 11s. The following is a summary of the procedure used to determine that force coefficients for test case 4 (Table 4.1): regular waves with an average full scale wave height of 3m, in 7.5m water depth (full scale). The time series recordings of the water particle velocities in 3 directions were measured and recorded using a Vectrino acoustic velocimeter.

Due to the errors observed in current meter readings under breaking wave conditions, current data sampled were filtered using a high end frequency cut-off of 0.2 Hz. The acceleration time series data for the current velocities were obtained by taking the first derivative of the velocity data using the DERIV function in GEDAP, short for derivative. The current kinematics for 5 wave cycles of test 4 is plotted in Figure 6.32. All regular wave cases tested are classified as transitional waves.

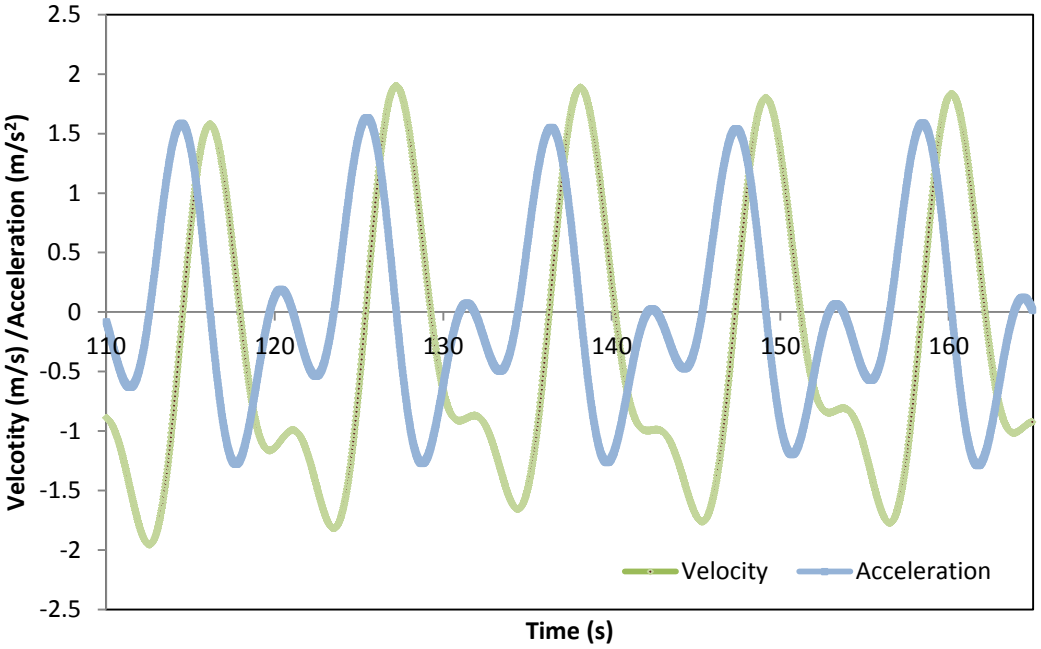

Figure 6.32: Kinematics of wave induced currents around structure in shallow water waves

Before force coefficients for each regular wave case were determined, the horizontal forces for test 4 were compared to the predicted forces using the Morison equation (Figure 6.33) using standard inertia and drag force coefficients (Cm = 2.0, Cd = 1.2) for wave induced forces on a single submerged cylinder without proximity effects (Agerschou and Edens, 1965). The force results are for a wave test 4 from Table 4.1 (-2 m MWL, H = 3 m).

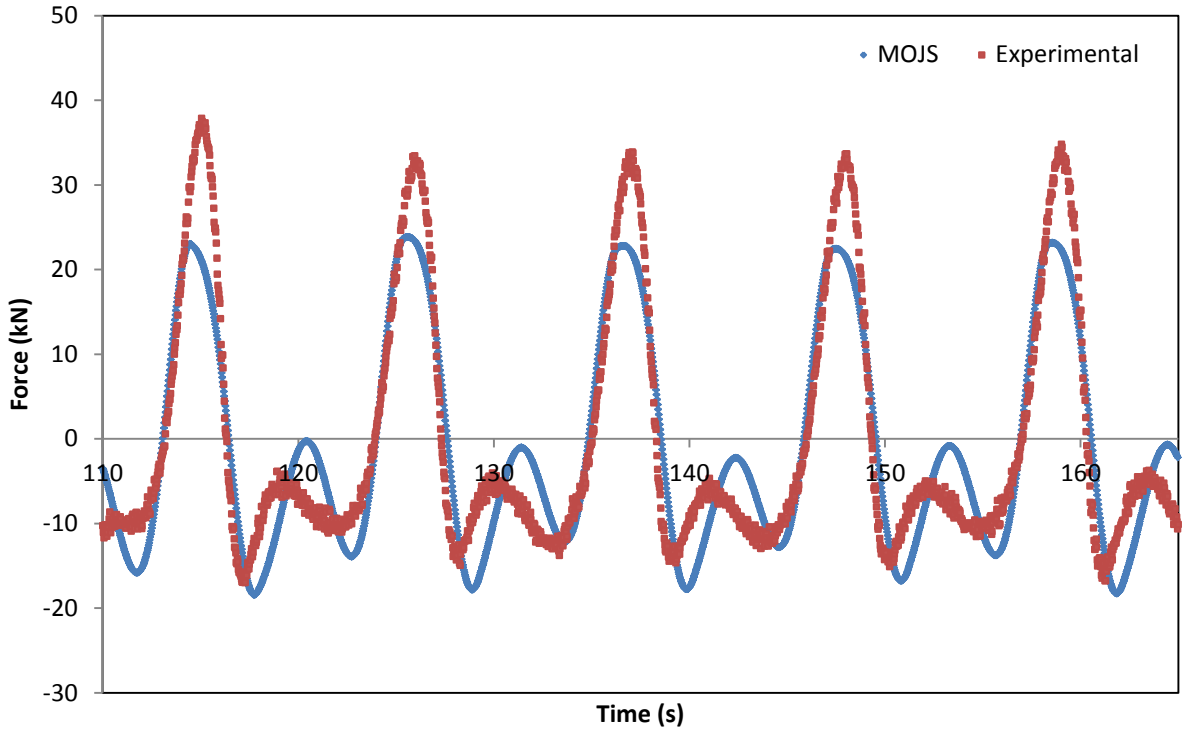

Figure 6.33: MOJS force compared to experimental forces on the central pipe using standard single cylinder coefficients (C_M = 2, C_D = 1.2) determined by Agerschou and Edens (1965)

The predicted forces by Morison equation (MOJS) provide a fairly good fit to the experimental force time series; however the peak force is underestimated. The current kinematics data (Figure 6.32) shows that at the time when peak force occurs, current velocity is low and the acceleration is high. Therefore, the inertia coefficient will have the largest impact on predicting peak forces. This agrees with past findings in the literature for studies employing arrays of cylinders. Predicted forces using MOJS were then re-plotted using coefficients fitted using the weighted least squares method outlined in the Morison equation section. The coefficients were determined by fitting the MOJS expression to a series of 10 regular waves. The fitted equation is plotted with the experimental forces in Figure 6.34. This is displayed again in Figure 6.35, with the inertial and drag force terms plotted separately to display phase and magnitude of each force.

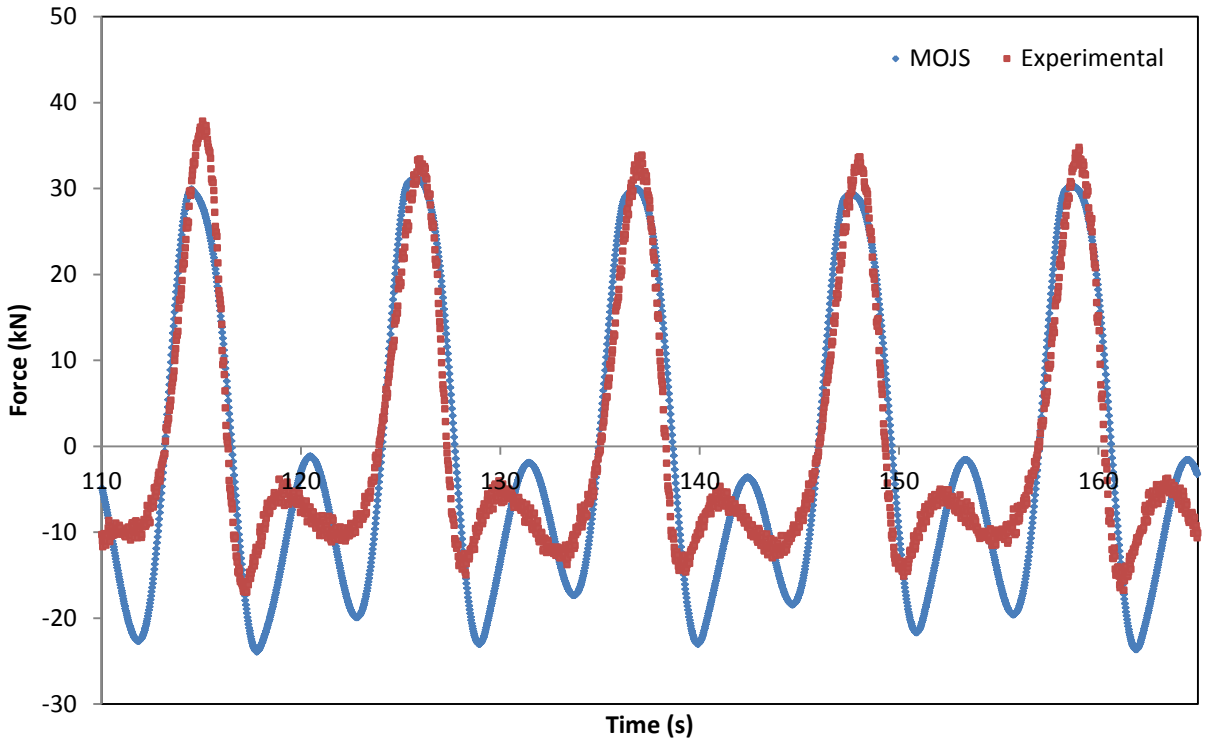

Figure 6.34: Morison (MOJS) equation fitted to peaks in force on central pipe using weighted least squares method; C_M = 2.60 and C_D = 1.93

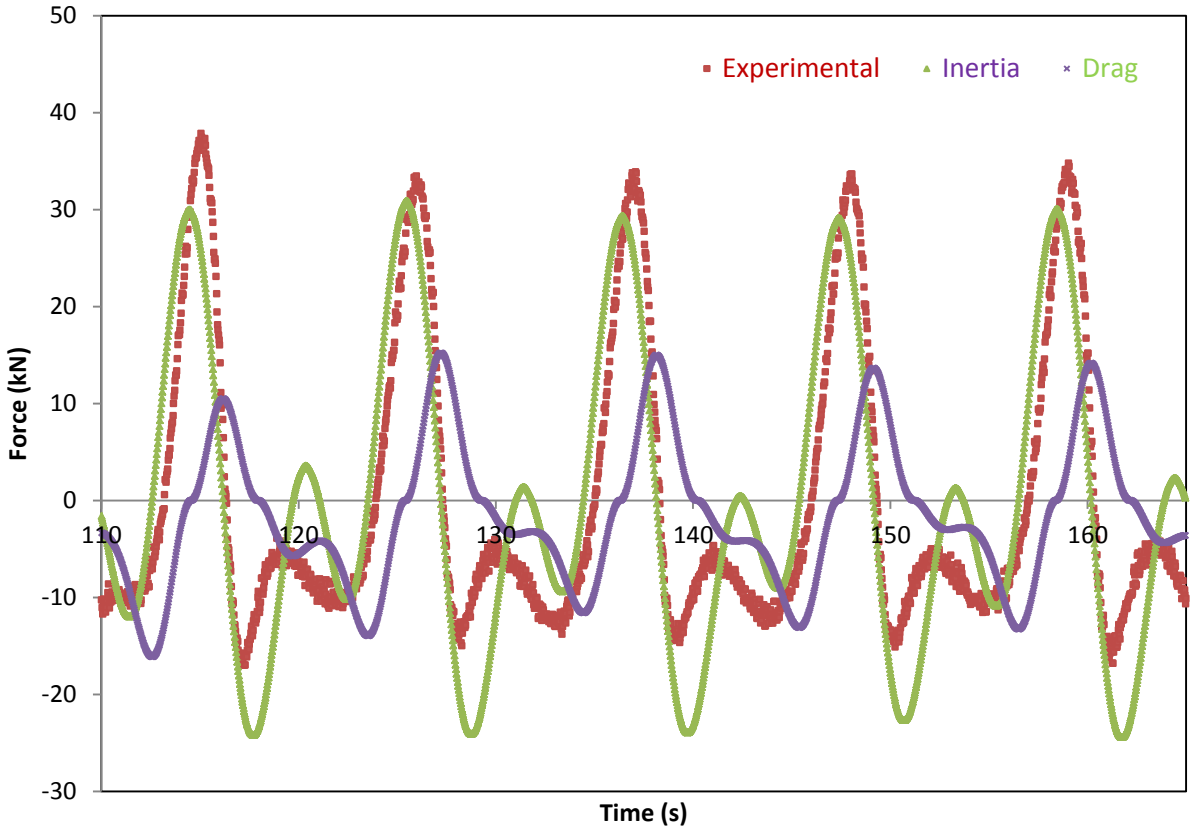

Figure 6.35: Inertia and drag force terms of MOJS equation plotted separately for forcing on central pipe

Drag and inertia coefficients vary over each wave cycle, so using one set of coefficients for the entire wave cycle will therefore not provide a perfect fit. When MOJS is fitted to the wave peaks in Figure 6.34, the predicted forcing in the negative direction is largely overestimated. This suggests that, during the wave trough, proximity effects between cylinders are minimized and standard single cylinder coefficients may be valid. Force coefficients can be fitted to adjust for extra turbulence and for separated flow conditions when wave the wave crest passes, but overestimate forcing for slower/less turbulent flow at wave trough. The same weighted least squares fitting method fit MOJS to peaks for test 4 was used for every other regular wave test and the correlations with the experimental forces were similar in the level of agreement. An example is shown in Figure 6.36 (test 28) for regular waves in water depth of 11.5m and an average wave height of 3m. A similar fit to test 4 is observed.

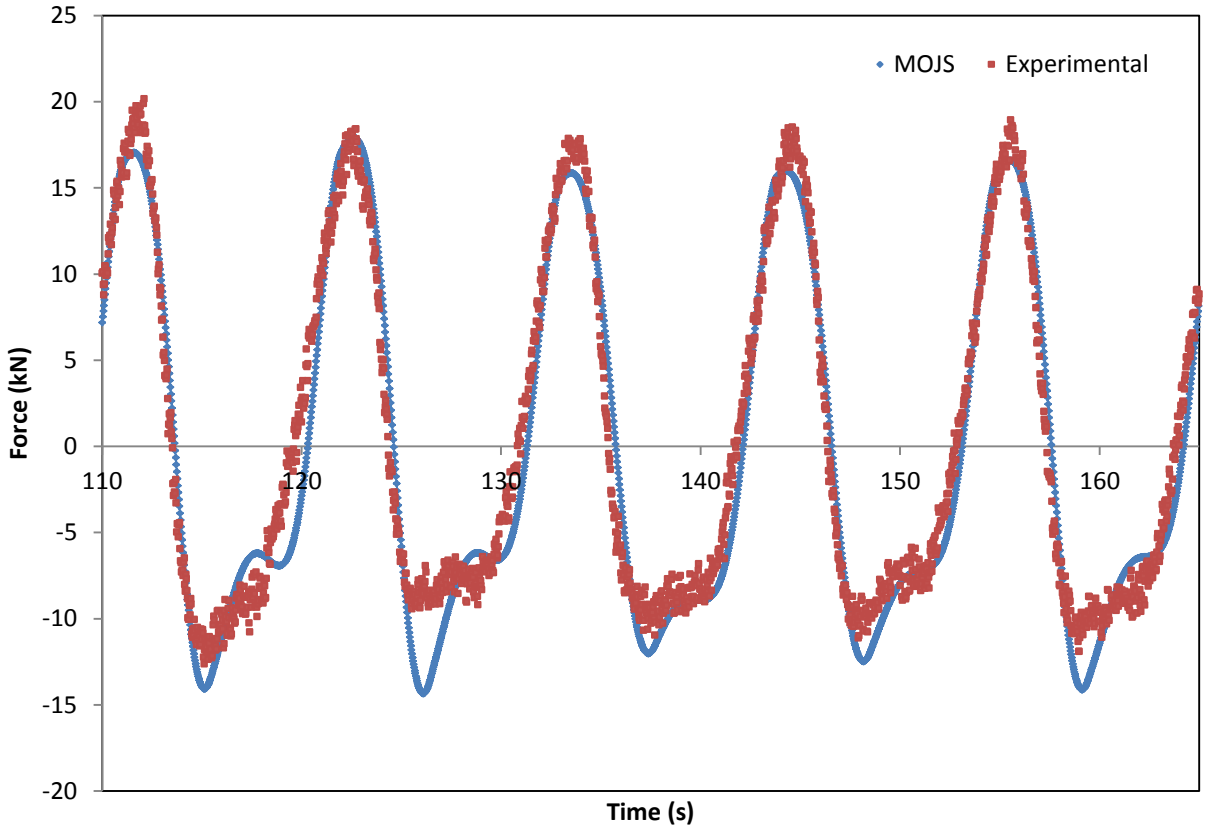

Figure 6.36: MOJS fitted to experimental forces for test 28 (H = 3m, d = 11.5m); C_M = 2.26 and C_D = 1.55

6.2.6 Support Posts Force Coefficients

Once force coefficients were determined for the central pipe for all regular wave tests, the process was then repeated for the pipe and posts (configuration 3, Figure 6.37) tests. The force data recorded from these experiments were time series representing the total force on all 4 support posts and the central pipe. In order to fit coefficients that would specifically represent the posts, the forcing on the pipe needed to be subtracted from the forcing acting on the entire pipe and posts configuration. Time series force data from tests on configuration 2 (central pipe only) was imported and subtracted from the forces recorded during tests on configuration 3. This was done by aligning the peaks in force data of the two experimental time series prior to subtraction. The result was an experimental force time series representing forcing on the 4 posts. A MOJS equation could then be fitted to this support posts force series using the weighted least squares method in order to determine the force coefficients for the 4 posts.

$$F(t)_{posts} = F(t)_{pipe+posts\ (conf.3)} - F(t)_{pipe\ (conf.2)} \quad [6.10]$$

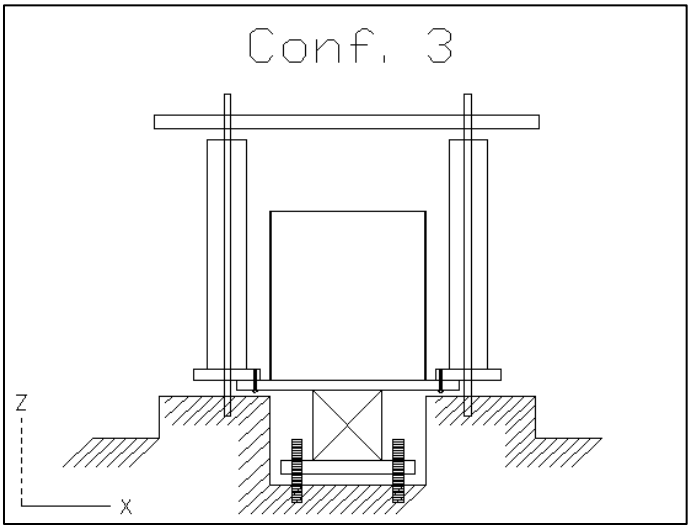

Figure 6.37: Configuration (3) for isolating forces on pipe and posts while maintaining presence of cap

Forcing predicted using the Morison equation was once again fitted with force coefficients using the weighted least squares method. Figure 6.38 displays experimental forces on configuration 3 and the MOJS predicted forces for test 4 (H = 3m, d = 7.5m).

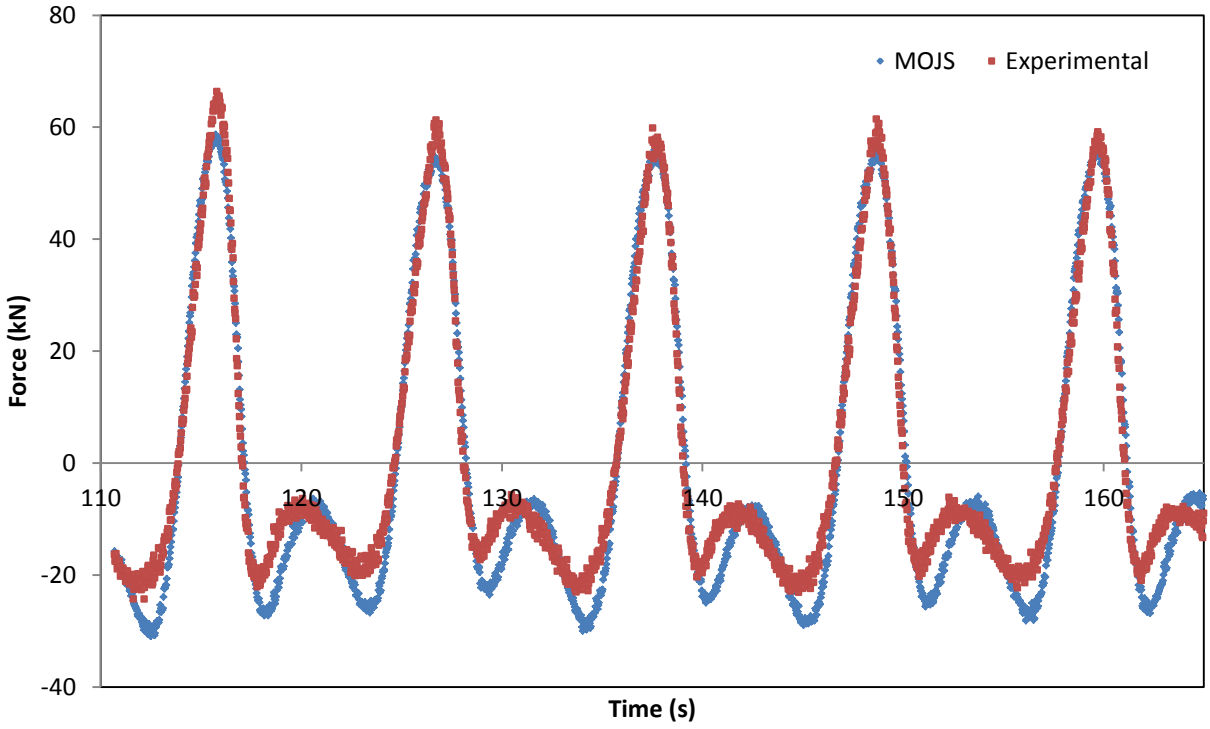

Figure 6.38: MOJS fitted to peaks of total force on posts and central pipe; C_M = 4.95 and C_D= 1.31

Figure 6.38 displays the time series of experimental force data measured on the pipe and support posts (configuration 3). The Morison equation force plotted is the sum of the experimental force time series of forces on the pipe alone (configuration 2) and that of the MOJS force time series for the 4 support posts:

$$F(t)_{MOJS} = F(t)_{Exp-Conf\ (2)} + F(t)_{MOJS-Posts} \quad [6.11]$$

The Morison equation time series plotted in Figure 6.38 shows an excellent fit. This is due to the experimental forces on the central pipe being included in the MOJS force time series, which carries the same negative force behaviour during the wave trough that isn't accurately predicted by the Morison equation (Figure 6.34). MOJS predicted forces were fitted similarly for all regular wave tests on configuration and the force coefficients for the posts were determined.

6.2.7 Velocity Cap Force Coefficients

Drag and inertia coefficients were determined for the velocity cap in both the X and Z directions from regular wave testing. These coefficients were fitted using force data from wave tests on structural configuration 1; experiments where all forces on the structure were transferred to the force dynamometer at the base (Figure 6.39). The current meter during these tests was raised to the elevation of the velocity cap, providing water particle velocity and acceleration information at the elevation of the portion of the structure of interest. For the X direction, a MOJS force time series was fitted and coefficients were determined for the cap using the method of weighted least squares similarly to what was done for determining the force coefficients on the support posts of the structure.

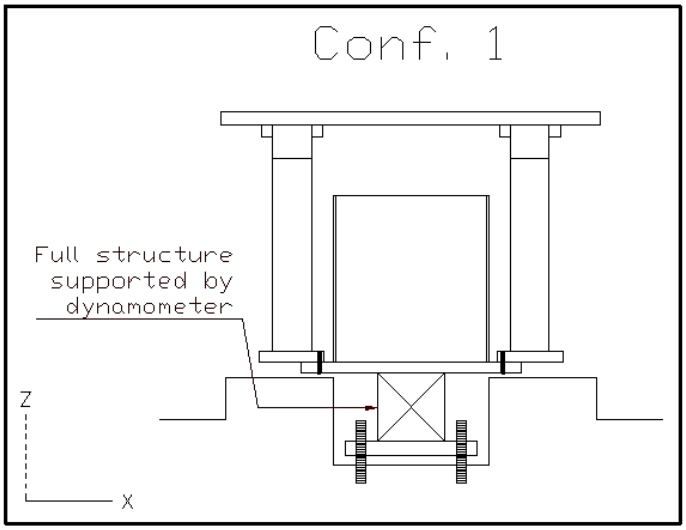

Figure 6.39: Configuration for measuring forces on entire structure

To determine the force coefficients representing the horizontal forces on the velocity cap, an experimental force time series for horizontal forces on the cap had to be obtained. Experimental force time series from test series E, which represent forces on the central pipe and posts, was imported and subtracted from test series B (full structure), by aligning the peaks in force data of the 2 experimental time series. The remainder was an experimental force time series for forcing on just the velocity cap.

$$F(t)_{cap} = F(t)_{total\ force} - F(t)_{pipe+posts} \quad [6.12]$$

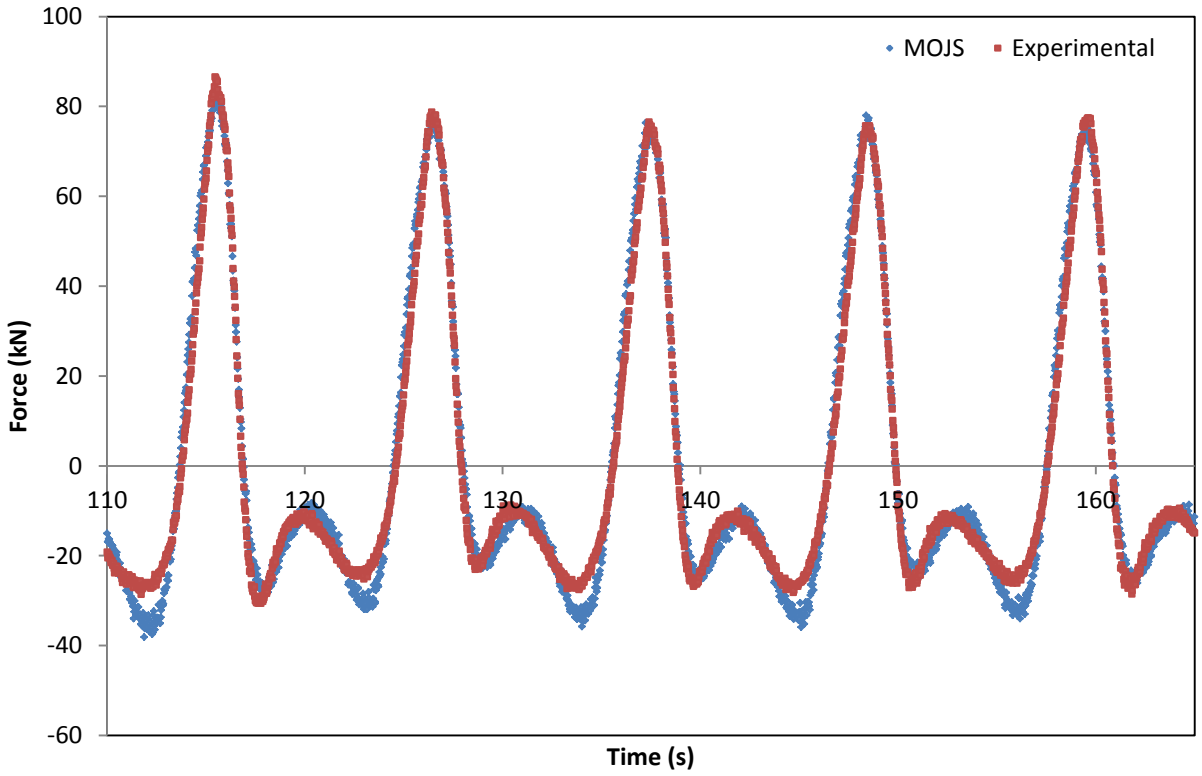

Figure 6.40: MOJS fitted to peaks of forces on total structure for determining cap coefficients; C_M = 1.55 and C_D = 4.74

Figure 6.40 displays time series of force data recorded on the full structure and the experimental time series of forces on the pipe and posts (configuration 3) plus a MOJS time series of horizontal forces on the velocity cap:

$$F(t)_{MOJS} = F(t)_{Exp-Conf\ (3)} + F(t)_{MOJS-Cap} \quad [6.13]$$

The Morison equation plotted above Figure 6.40 again provides an excellent fit, with an even larger portion of the MOJS time series being experimental forces, as the pipe and posts account for approximately 80% of the horizontal forces measured on the total structure.

Force coefficients for the vertical forces on the velocity cap were investigated similarly to the method used to find the force coefficients for the horizontal forces on the central pipe. The time series for vertical forcing, current velocity, and current acceleration in the vertical direction were imported to create a MOJS expression for vertical forces on the velocity cap. Inertia and drag coefficients were fitted using the caps geometry, with the value for area being in the direction of flow (vertical), and fitted using the method of weighted least squares. Measured vertical forcing and the MOJS equation are plotted below for test case 16 (0 m MWL, H = 3 m).

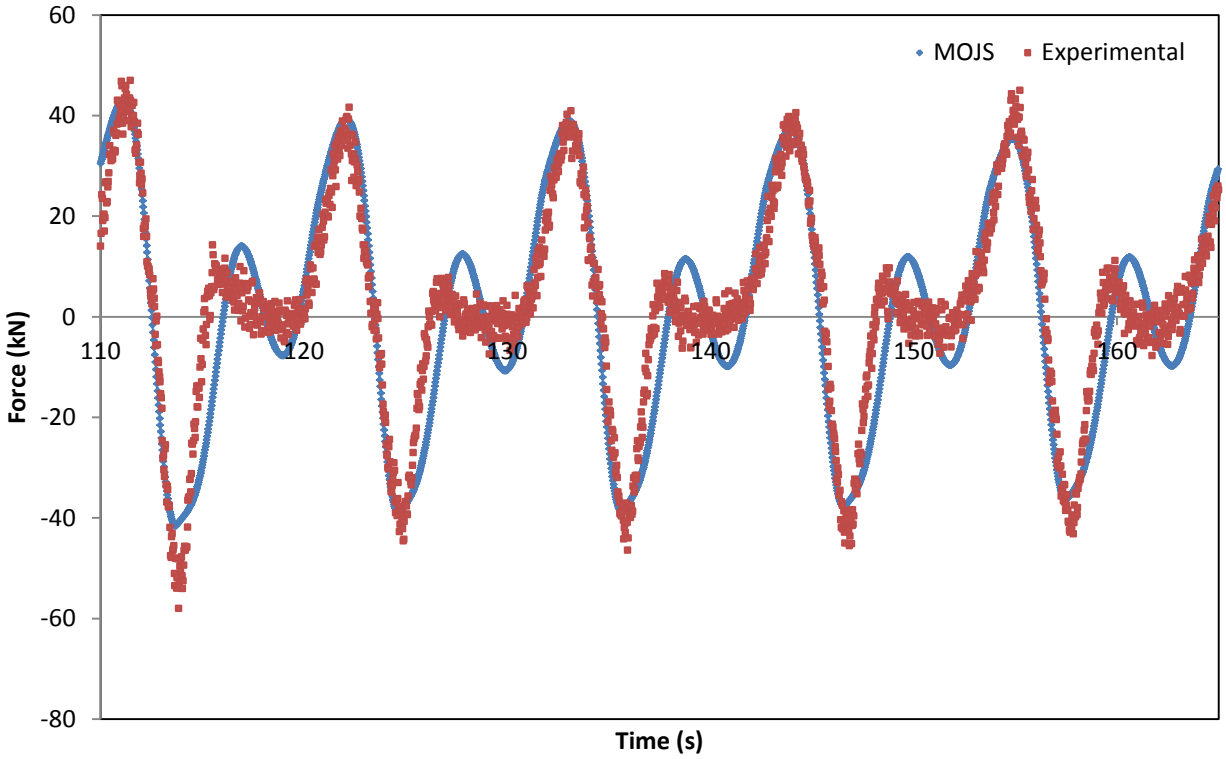

Figure 6.41: MOJS fitted to peaks of vertical forces on cap; C_M = 13.62 and C_D = 7.40

6.2.8 Structure Configuration 1 & 3 - Force Coefficients

Once force coefficients from each regular wave test were determined for each separate component of the structure, force coefficients representing each structural configuration were then determined for the full structure (conf. 1) as well as the central pipe and posts configuration (conf. 3). Force coefficients for configuration 2, where only the central pipe is connected to the force dynamometer, have been previously determined. For configuration 1, coefficients were fitted to the recorded force and plotted using the following expression for MOJS forces on the full structure.

$$F(t)_{MOJS} = C_M * \left(\frac{du}{dt}\right) * \left(V_{pipe} + 4 * V_{post}\right) + \frac{1}{2} * C_D * u|u| * \left(A_{pipe} + 4 * A_{post}\right) \quad [6.14]$$

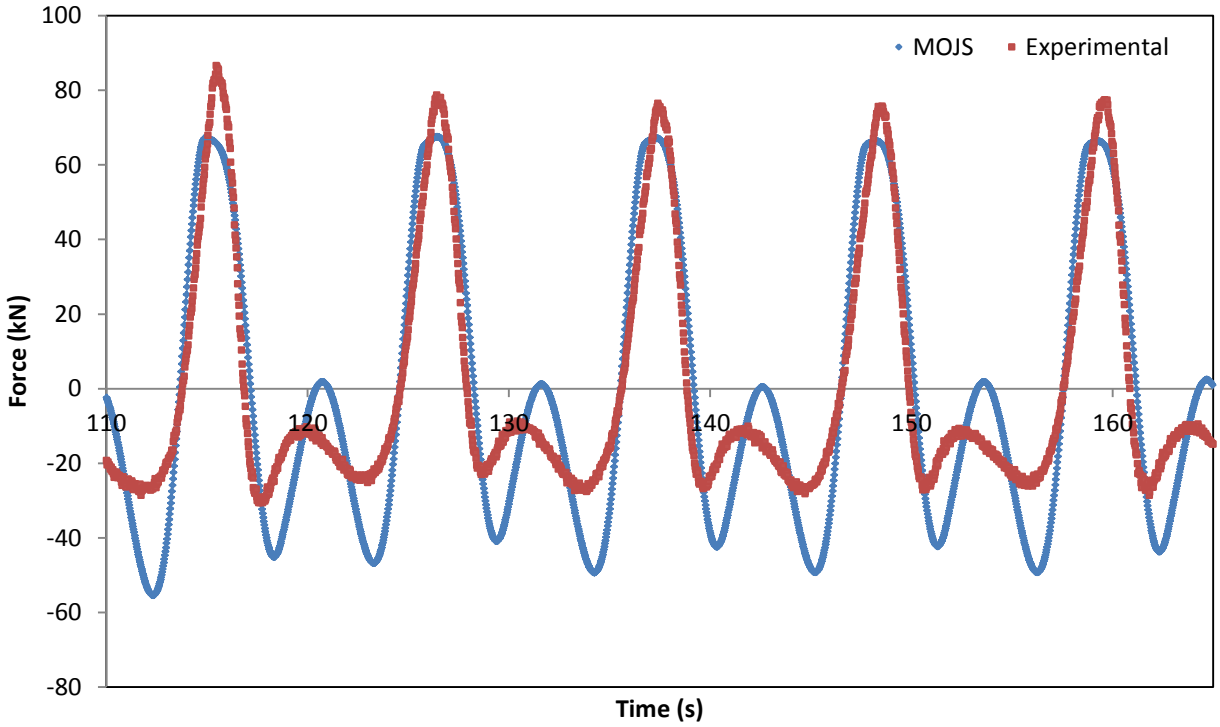

Figure 6.42: MOJS fitted to peaks of vertical forces on configuration 3 (pipe and posts); C_M = 4.09 and C_D = 1.91

The geometry of the velocity cap was excluded from the Morison expression (6.14) for simplicity and due to its minimal influence on horizontal forces. The same process was repeated for configuration 3, where forcing on the central pipe and support posts (cap excluded) was recorded. The same MOJS expression used to fit coefficients from configuration 1 was used. This means the structural geometry in the MOJS expression again only accounts for the central pipe and posts. The result was slightly smaller drag and inertia coefficients for each regular wave test.

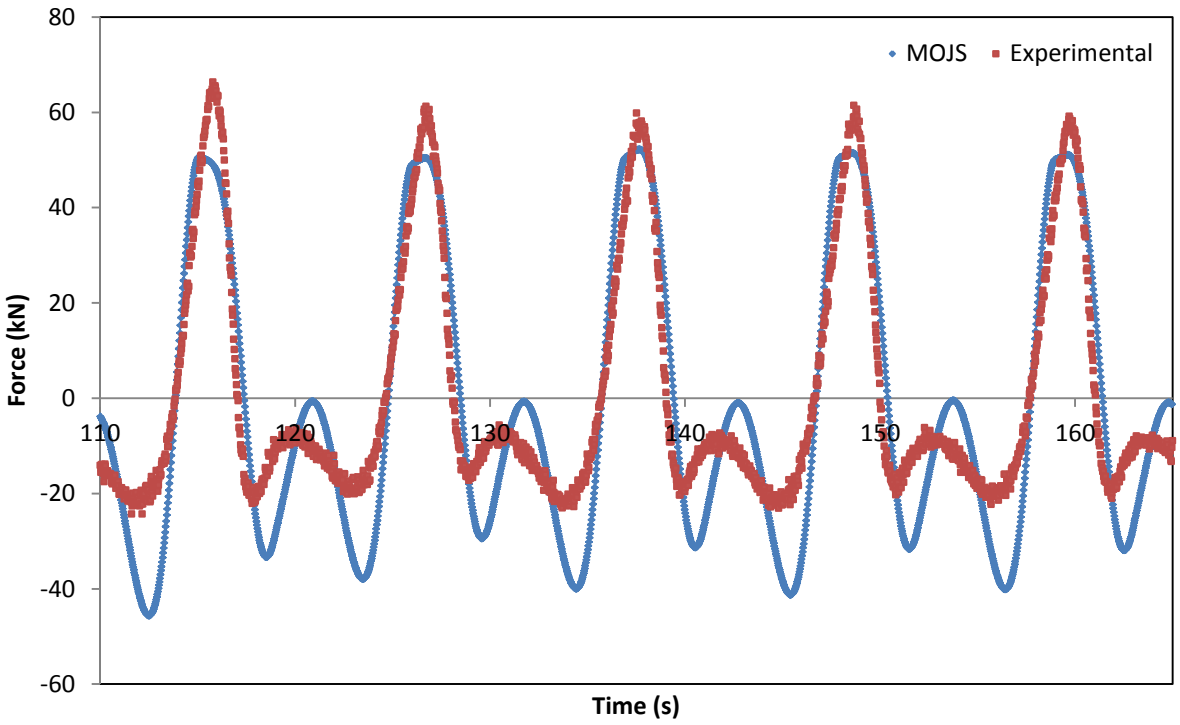

Figure 6.43: MOJS fitted to peaks of vertical forces on configuration 1 (full structure); C_M = 3.19 and C_D = 1.68

In this section, force coefficients have been determined for each regular wave condition tested in Table 4.1 and for each separate component of the intake structure such that current data could be used to create a MOJS predicted force time series on each of the central pipe, 4 surrounding posts, and the velocity cap. Force coefficients have also been determined for each structural configuration, representing the total force recorded during testing of that configuration. Finally, a set of Z-direction force coefficients for the velocity cap have been fitted. Next, these coefficients were analyzed to investigate a possible relation with the varying wave and current conditions. In the coefficient fitting section, the MOJS equations with fitted coefficients were plotted to show examples of the quality of fit for forcing on each structural component and configuration. The complete set of plots for each regular wave condition can be seen in the appendix (page 158).

6.3 Force Coefficient Analysis

6.3.1 Force Coefficients with Keulegan-Carpenter Number

The previous section showed that inertia and drag force coefficients could be determined for each structural component and configuration with acceptable accuracy for each regular wave condition tested. These coefficients were then plotted against varying wave properties and their respective Keulegan-Carpenter (KC) numbers to demonstrate how force coefficients change in highly nonlinear wave conditions and with separated flows around multiple cylinders in close proximity.

This KC number is the ratio of water particle horizontal displacement per wave cycle to cylinder diameter. The KC number has been proven useful for comparing forces on different cylinders in different wave tests, as a KC number may represent any different combination of wave characteristics and cylinder diameters with complex and obstructed flow fields. Coefficients determined for both the central pipe and support posts from regular wave tests were plotted versus the average KC number from their respective cycle of 10 waves (Figure 6.44). The group of data points with low KC values represent the central pipe (larger diameter), and the group with KC values in the 30-60 range represent the support posts (smaller diameter).

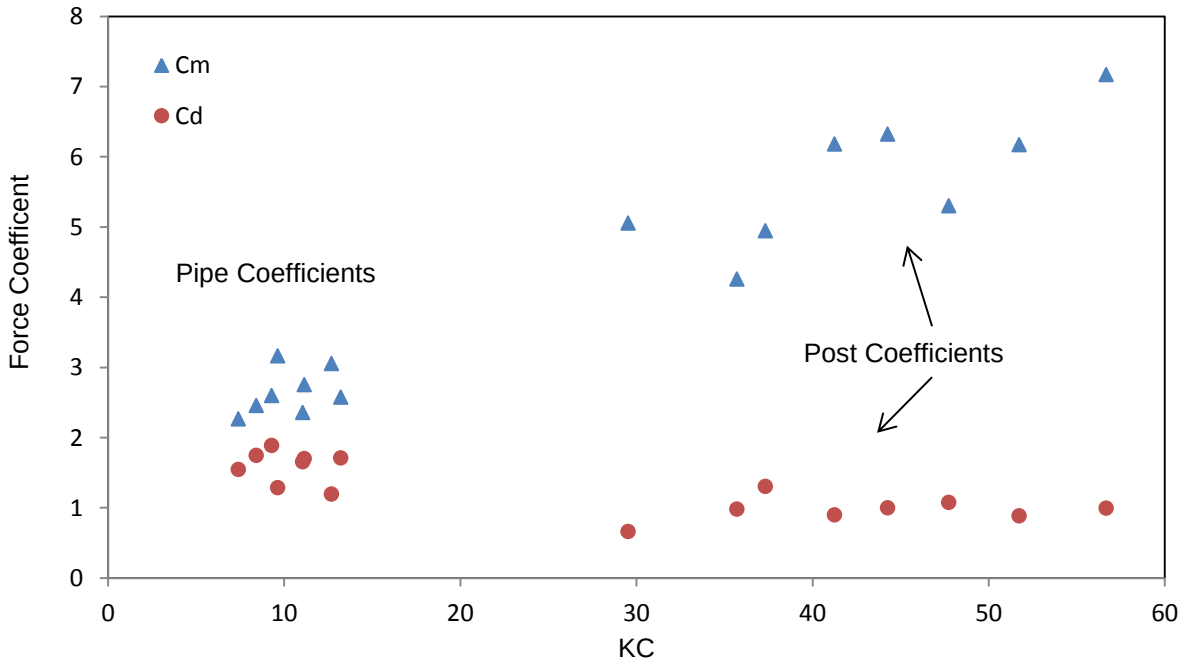

Figure 6.44: Force coefficients for the central pipe and support posts determined from cycles of 10 waves

A single pair of force coefficients for each structural component from each of the 9 regular wave tests did not provide a wealth of data from which analyze for correlations with wave properties and draw conclusions. Therefore a wave-by-wave coefficient analysis was performed for each test series. A wave-by-wave analysis is simply applying the same weighted least squares method employed to a single wave cycle. Each wave is defined by the up-crossing of the horizontal velocity of the water particle data (Davies et al., 1990). A set of force coefficients and respective KC number (using the maximum recorded velocity value from the specific wave) is then calculated for each wave. The force coefficients determined using a wave-by-wave analysis are plotted (Figure 6.45) again to compare with the results from a 10 wave cycle. A similar pattern seen in Figure 6.44 is noted, with more scatter in the vertical direction. There is a linear upward trend for the added mass coefficients, but fairly constant values for drag coefficients.

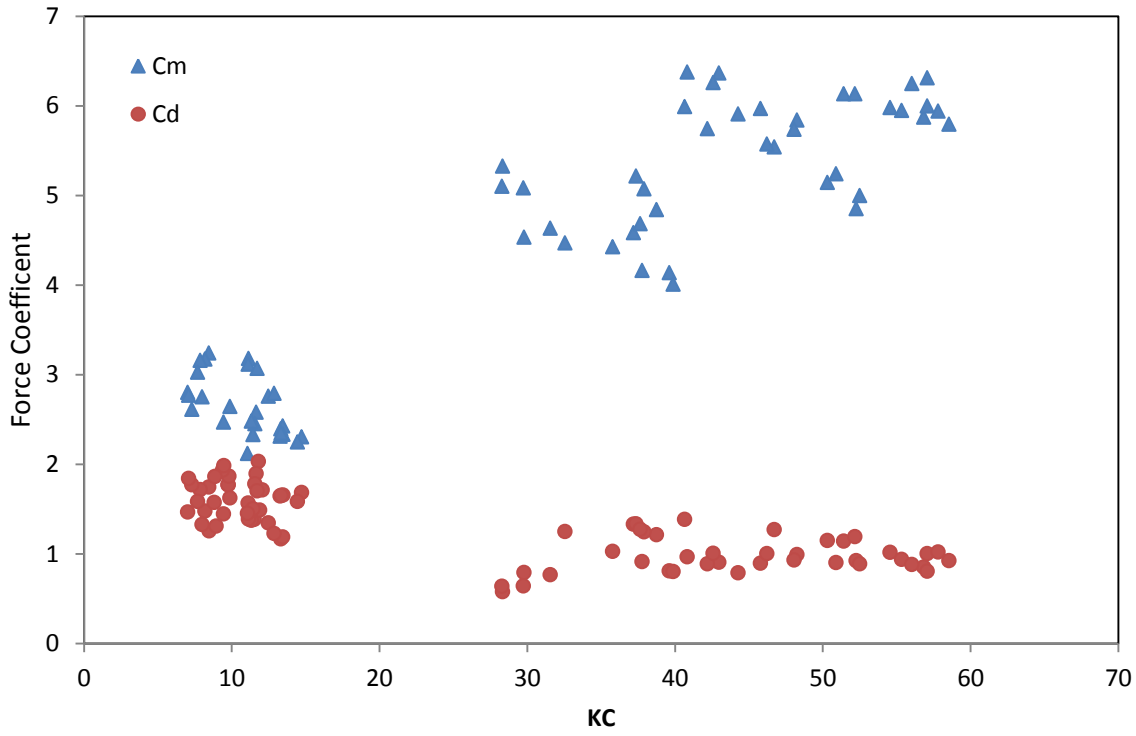

Figure 6.45: Force coefficients on the central pipe and support posts determined from single wave cycles

To add validity to these force coefficient findings, the results were compared to those of a similar study published by Sarpkaya (1979). The study, which determined force coefficients for a large central pipe surrounded by smaller diameter tubes, is detailed in the Literature Review. Below are the results of the study, with inertia and drag coefficients plotted for 2 separate structural configurations (Figure 6.46).

The KC values on the abscissa are of similar scale to those tested in this study. The inertia and drag coefficients in Figure 6.46 show similar values and trends with KC as the results of this study (Figure 6.44).

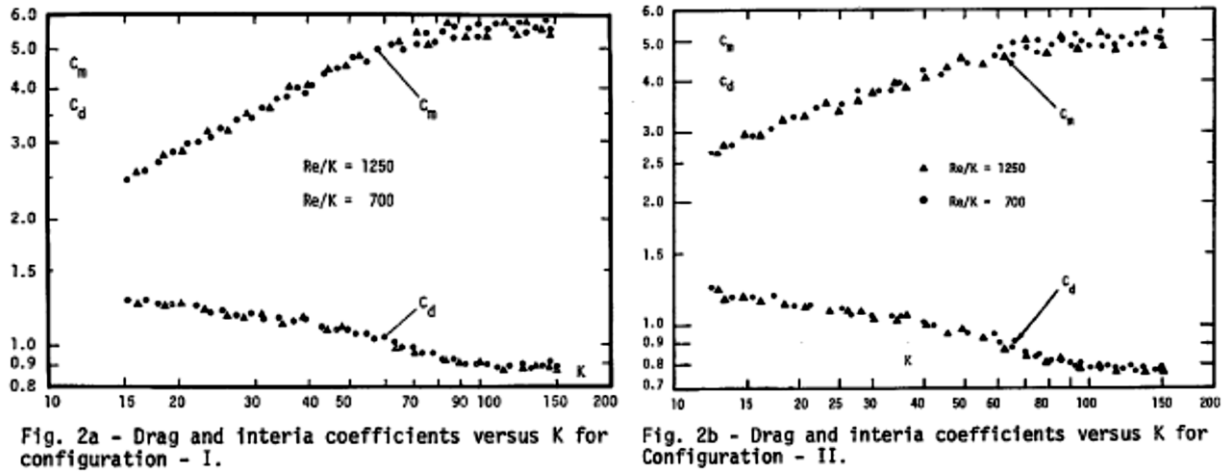

Fig. 2a - Drag and interia coefficients versus K for configuration - I.

Fig. 2b - Drag and interia coefficients versus K for Configuration - II.

Figure 6.46: Force coefficient data for 2 configurations of circular tube arrays with central pipe

The 2 main parameters varied during regular wave tests were water level and wave height, with period remaining constant at 11s for each test. Force coefficients were plotted versus KC separately each water level and wave height to observe correlation and sensitivity to these changing parameters. Water level is an important factor for wave forces on a structure in a fairly shallow location, as the water depth at structure will affect wave shoaling and breaking. For water level sensitivity, inertia and drag coefficients are plotted for separate water levels in Figures 6.47 & 6.48 respectively.

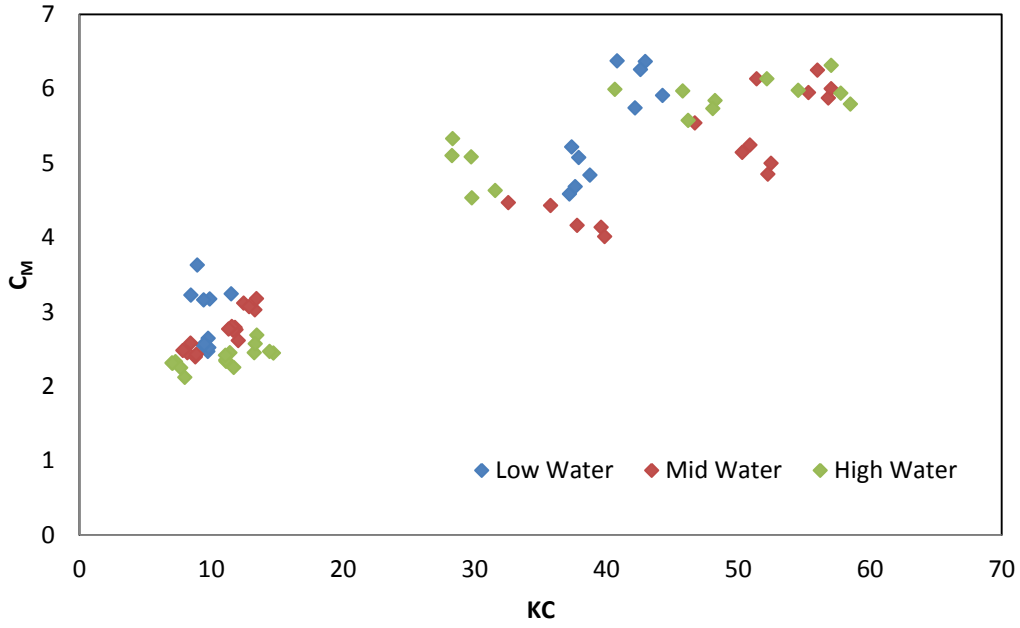

Figure 6.47: Inertia coefficient versus KC for various water levels

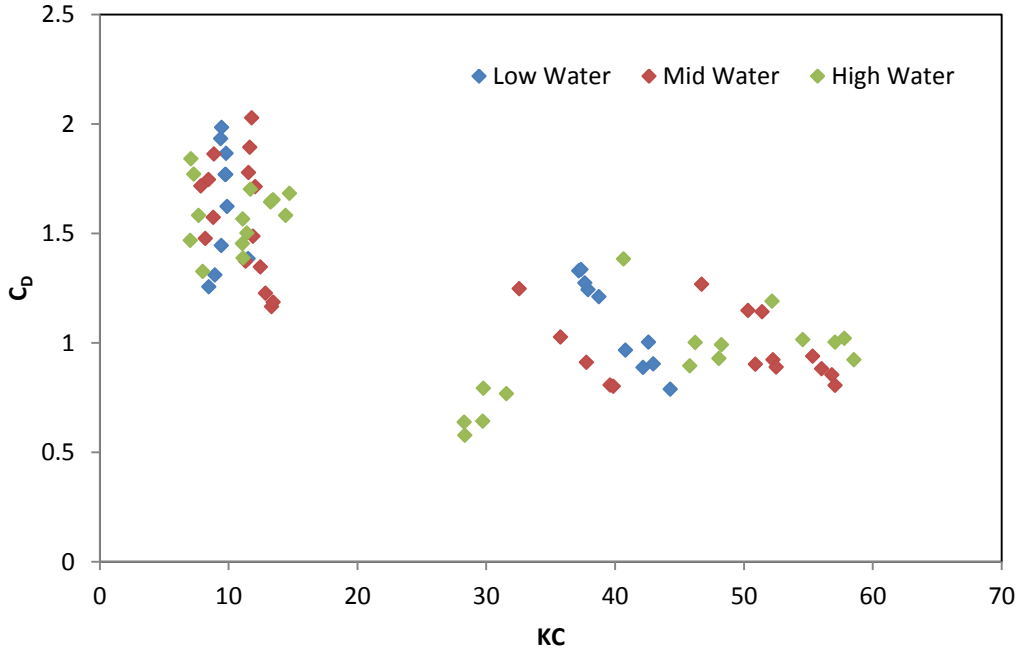

Figure 6.48: Drag coefficient versus KC for various water levels

Similar to Figure 6.44, Figure 6.48 shows a linear trend in values for inertia coefficient increasing with KC. Water level does not appear to have an effect on the inertia coefficient as the values from the 3 different water levels tested are found randomly throughout the plot. Drag coefficients in Figure 6.48

show independence from water level and similar scatter as in Figure 6.47. Force coefficients were then plotted separately by wave height, which has been noted earlier in the Peak Force Analysis to have a significant effect.

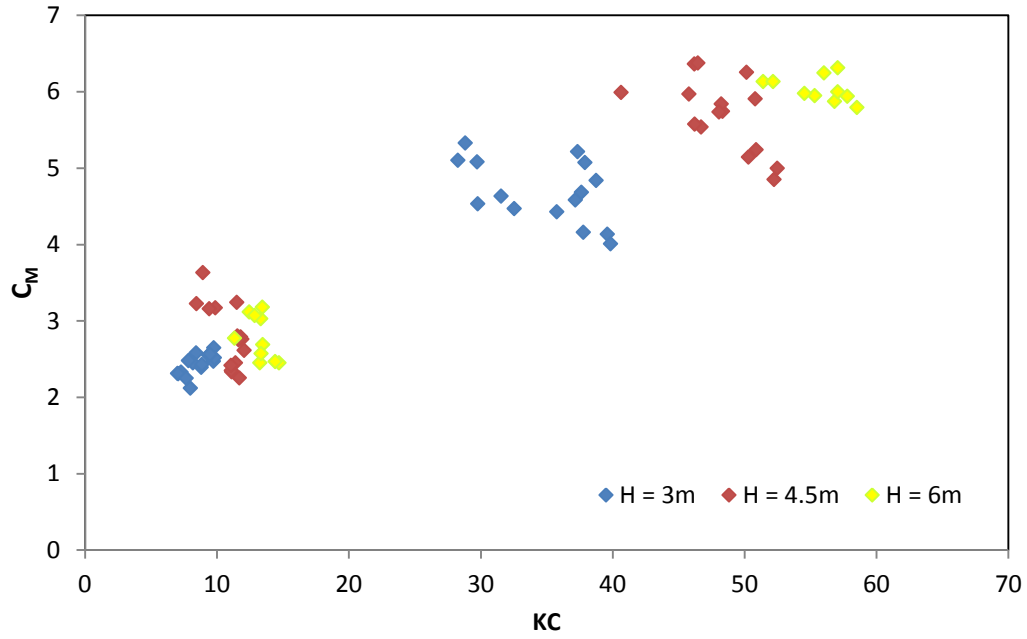

Figure 6.49: Inertia coefficient versus KC for various wave heights

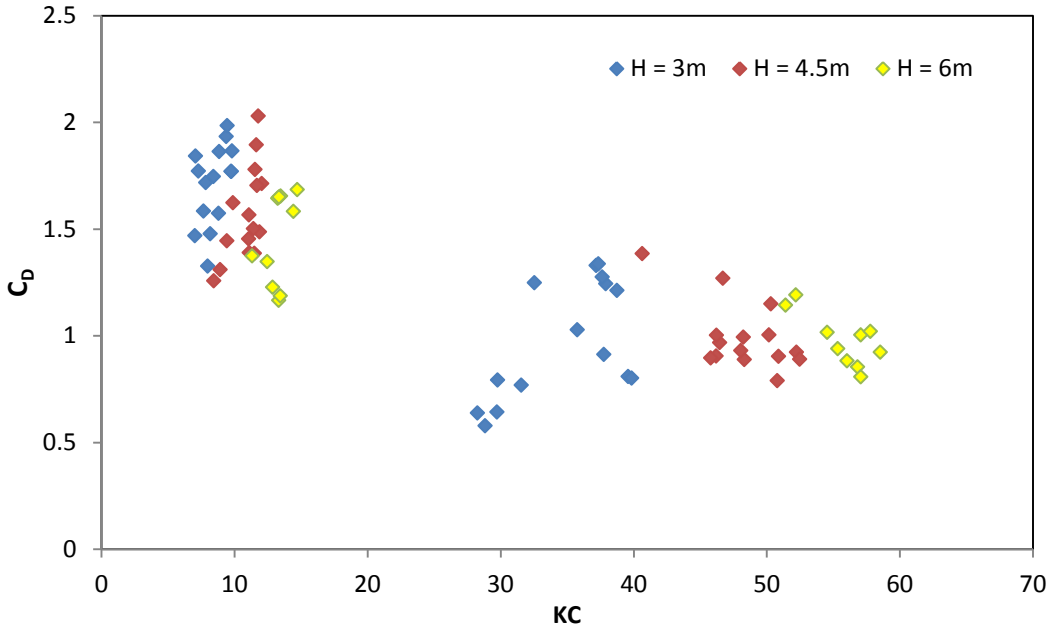

Figure 6.50: Drag coefficient versus KC for various wave heights

When inertia coefficients are plotted by wave height versus KC, it can be seen that the larger waves generate larger KC values (due to larger water particle orbit diameters). Following the linear trend noticed in inertia coefficients (Figure 6.49), it is observed that the larger wave heights require larger inertia coefficients to fit the force data due to the larger range of water particle orbits. Similar to what was observed before when plotting drag coefficients, there is no noticeable trend between wave heights and drag coefficients (Figure 6.50), other than the fact that larger waves at the same depth and waver period generate larger KC values.

6.3.2 Force Coefficients with Wave Steepness

For the forcing recorded on the central pipe, no trend could be observed for the force coefficients when plotted against to KC (Figure 6.51). This is likely due to the small range of KC values of the wave conditions the pipe is tested in, with the larger diameter of the pipe compared to the posts leading to a smaller range of KC values. It was observed that larger added mass coefficients were fitted from regular waves that were breaking shortly after or directly on top of the structure. Therefore, force coefficients for the pipe were plotted versus wave steepness at the structure (Figure 6.52). Wave steepness (H/L) was calculated using wave height data recorded from the gauge positioned beside the structure, and wave length data from linear wave theory. The force coefficients for the central pipe are plotted first to illustrate the lack of correlation with KC (Figure 6.51).

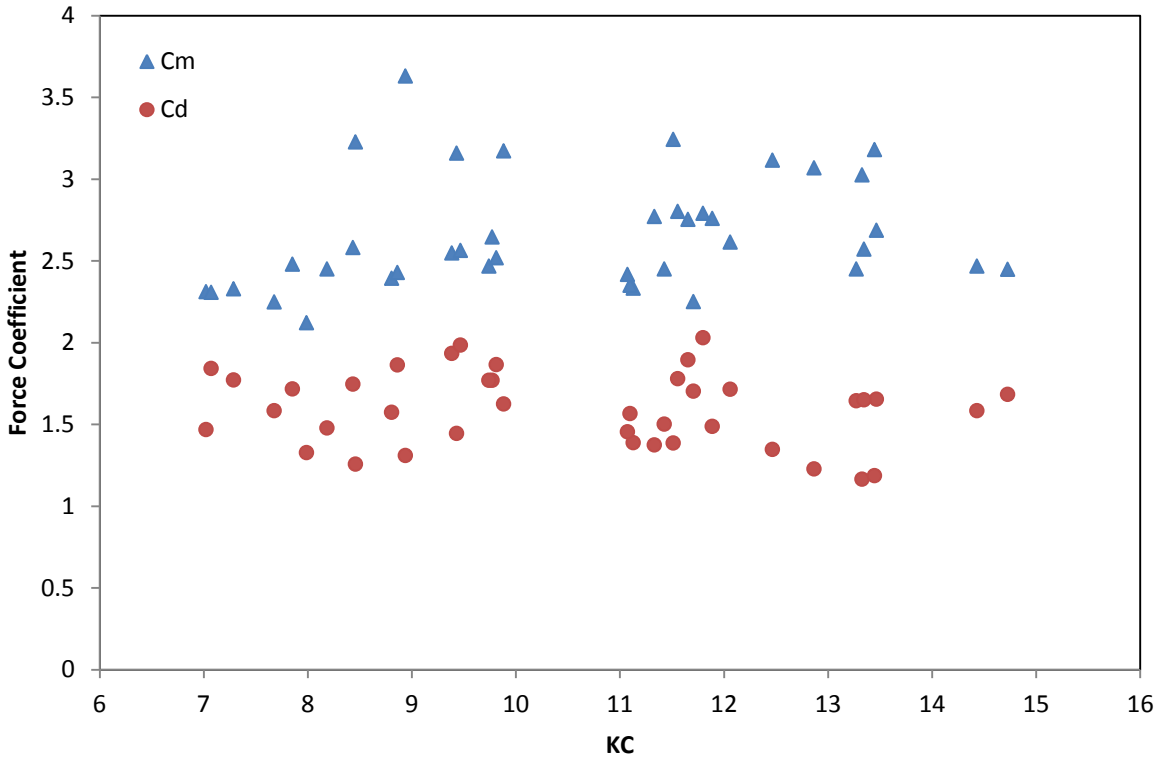

Figure 6.51: Force coefficients for central pipe versus KC

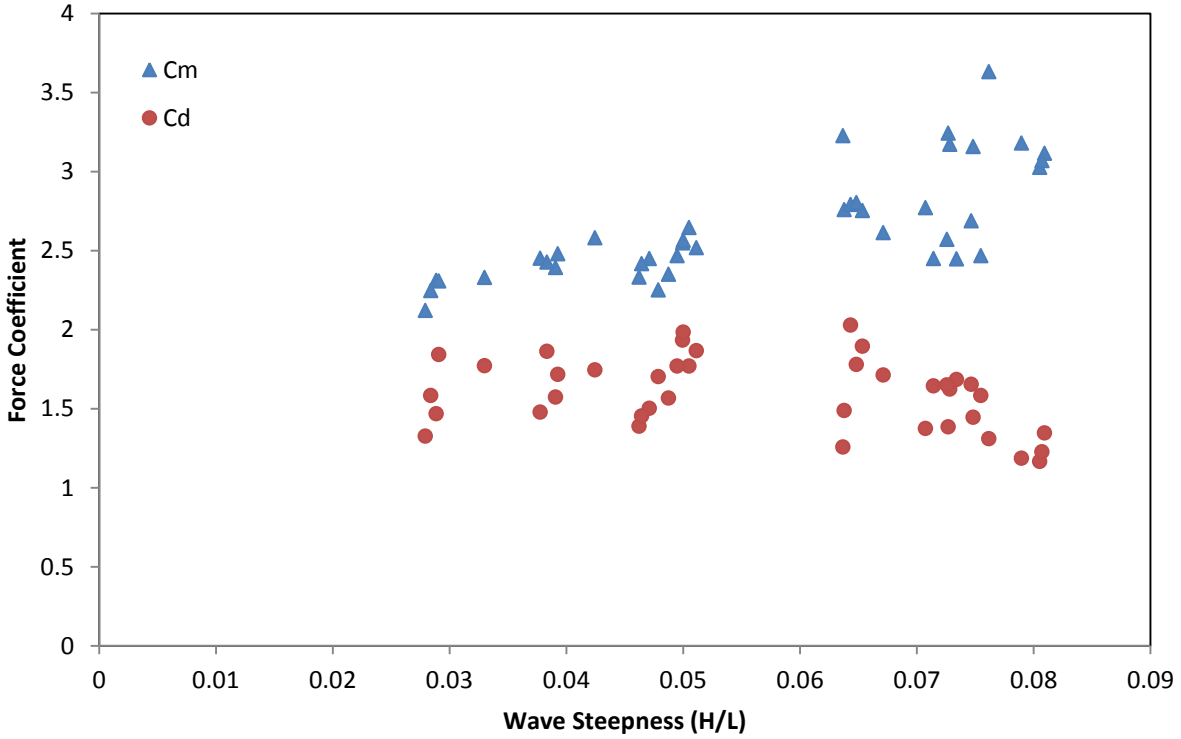

Figure 6.52: Force coefficients plotted versus wave steepness at the structure

In Figure 6.52, an increasing trend can be seen between added mass coefficients and wave steepness at the structure. However, there is very significant scatter, particularly at larger steepness values. Similar to other results, there is no clear trend in the drag coefficient data. Coefficient data was plotted separately for varying water level and wave heights against wave steepness, but no correlations were noted.

6.3.3 Force Coefficients with Wave Height

The relationships between wave height and force coefficients were further investigated. Using methods employed in peak force analysis, the wave height parameter was normalized by dividing by the water depth for that test at the location of the structure. First, Inertia coefficients (C_M) for the support posts and central pipe were plotted versus H/d in Figures 6.53.

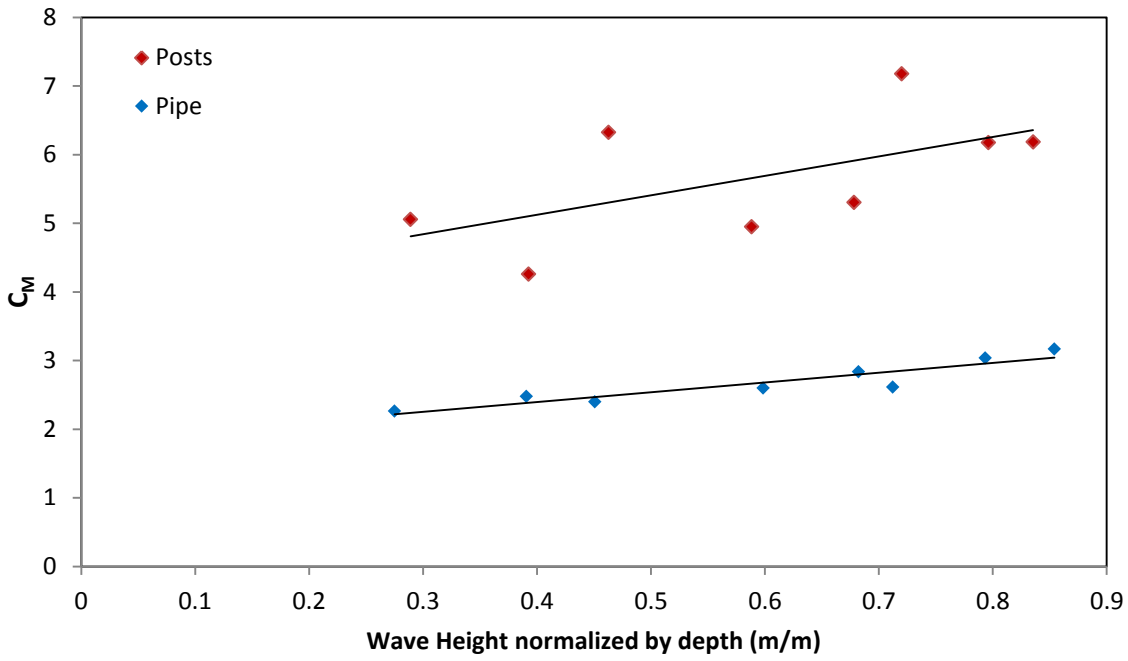

Figure 6.53: Inertia coefficients for central pipe and support posts plotted versus normalized wave height

In the above plot, pipe and post inertia coefficients are easier to compare with each other now that the abscissa values are in a similar range since KC is not used. The inertia coefficients for the central pipe displays a uniform linear trend increasing with H/d, with very little deviation or scatter. Larger water particle orbits accompany larger waves and therefore larger KC values, so a slight linear increase agrees with observations from Figure 6.49.

Support post inertia coefficients display significant scatter. Previous studies conducted for researching force coefficients for multiple cylinders have shown that the proximity effects from other cylinders tend

to increase the inertia coefficient and decrease the drag coefficient of an individual cylinder. The separated flow around one of the cylindrical components of the intake structure is affected by the separated flow field around another cylinder in proximity. Table 6.1 from Peak Force Analysis shows the spacing ratios for the central pipe and support posts. The spacing criterions for interference established by Zdravkovich (1977) state that the central pipe is close enough to the posts to interfere with their flow fields and likely amplify the forces on these cylinders. The posts are small enough in diameter and sufficiently far away to have minimal or no effect on the flow field and subsequent forcing of the central pipe.

These critical spacing ratios are intended to be applied to proximity effects on drag force and drag coefficients. If these principles of proximity effects from spacing are applied to the inertia forces and coefficients, the results in Figure 6.53 are justified. The proximity effects of the central pipe on the posts increase the inertia coefficients on the posts to values larger than the theoretical inertia coefficient value for a single cylinder in isolation ($C_M \approx 2$). The unpredictable nature of proximity effects also explains the scatter in inertia coefficients for the posts from the trend line. Finally, the conformity of the pipe's coefficients to the linear trends, as well as their lower values, prove here that the spacing ratios from Zdravkovich can be used to explain the lack of proximity effects from the support posts on the central pipe, with values being much closer to $C_M \approx 2$.

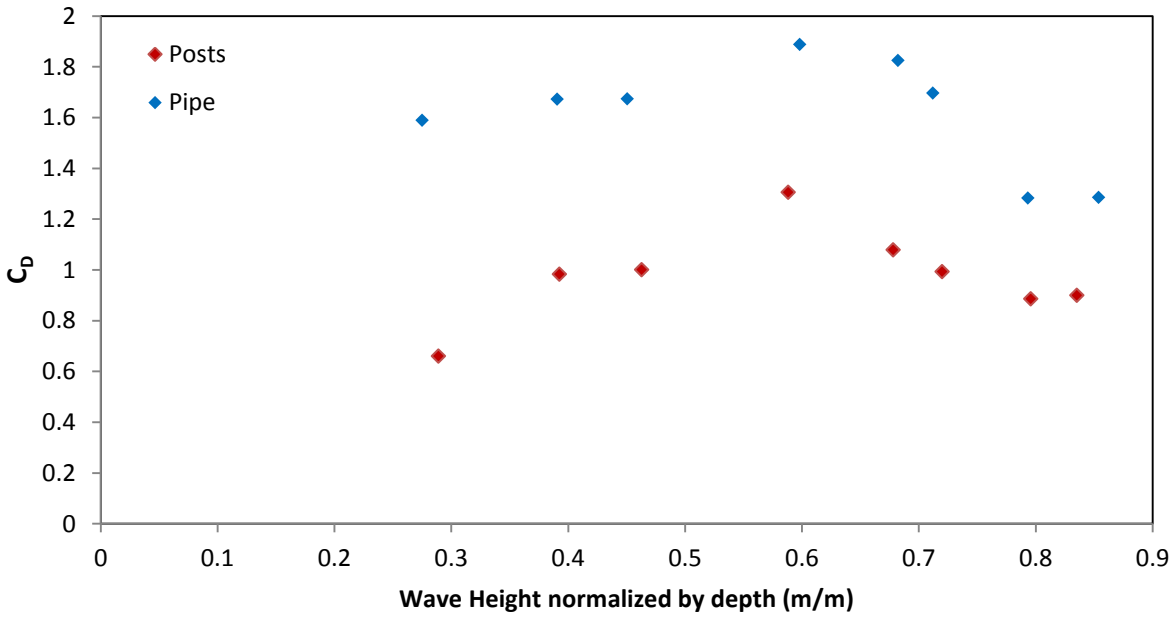

Figure 6.54: Drag coefficients for central pipe and support posts plotted versus normalized wave height

Figure 6.54 shows results for drag coefficients that align with the principles of interference effects on drag coefficients from Zdravkovich. The central pipe has the larger drag coefficients due to minimal flow interference from the support posts. The posts are subject to proximity effects and have their respective ambient flow fields altered by the presence of the central pipe. As a result, drag coefficients for the support posts are smaller than for the central pipe. It is interesting to note that drag coefficients for the posts and pipe display similar conformity to the trend when plotted against H/d, while inertia coefficients do not (Figure 6.53). This demonstrates that interference effects on force coefficients, due to proximity of other cylinders, manifest themselves more in the inertia forces and coefficients. While flow interference decreases drag coefficients, it typically increases inertia coefficients.

6.3.4 Velocity Cap Force Coefficients

Force coefficients were determined for both the horizontal and vertical directions for the velocity cap. The experimental horizontal forcing on the cap was isolated in a similar manner as the forcing on the support posts was; the forcing recorded from tests on the pipe and posts configuration was subtracted from the forcing on the entire structure. Force coefficients could then be determined by fitting a MOJS expression to the force time series using the weighted least squares method. The results for each wave condition are plotted below.

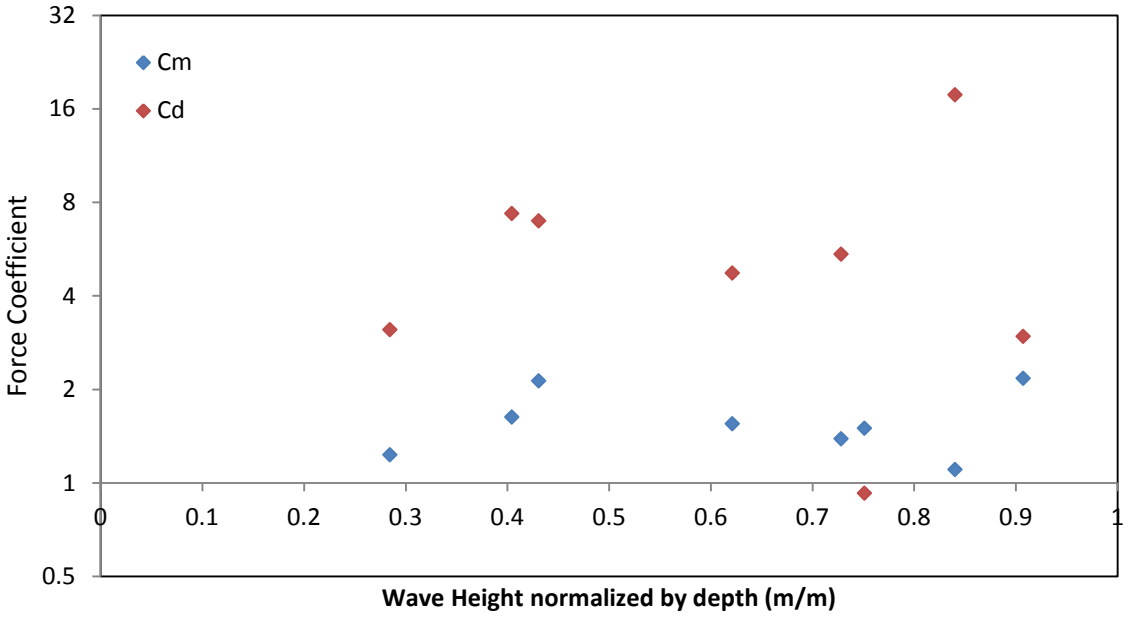

Figure 6.55: Force coefficients for velocity cap in the horizontal direction

The magnitude of horizontal forcing on the velocity cap is quite small and largely inertia dominated due to the very small area of the cap normal to the flow direction. Inertia coefficients have values between 1.1 and 2.2 but do not display any trend with H/d. Drag coefficient values range dramatically and display no trend at all with H/d. This is likely due to the low influence of drag on total horizontal forcing on the velocity cap.

For the vertical direction, the Z-direction forcing from tests on the full structure configuration was used. This requires the assumption that all the vertical forcing recorded is on the velocity cap. This is a valid assumption, as it is noted that vertical force values from both irregular and regular wave tests on the other structural configurations (2 & 3) that do not include the velocity cap are very small. This conservative approach will estimate vertical forces on the entire structure and overestimate the actual vertical forcing on the velocity cap. The same value for volume of the cap is used for creating a MOJS expression for forces on the cap in the X & Z directions. In the calculation of drag forces in the vertical direction, the much larger area normal to z-direction flow is used. The results of Z-direction force coefficients on the velocity cap are plotted below.

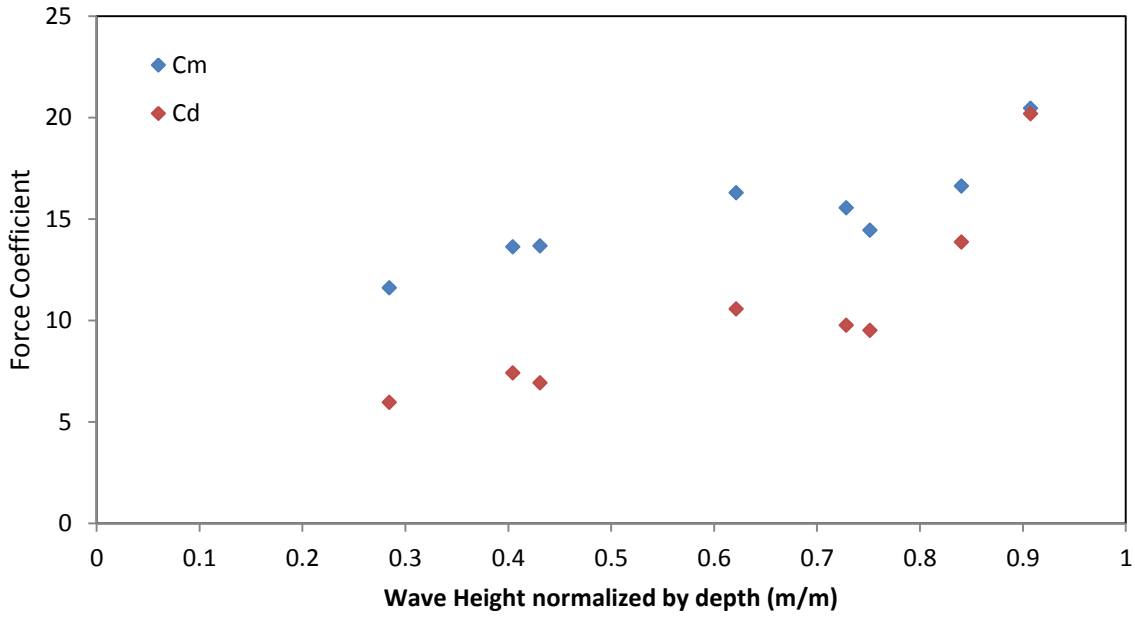

Figure 6.56: Force coefficients for velocity cap in the vertical direction

There is better correlation between force coefficients and H/d in the z-direction (Figure 6.56), likely because forces on the cap are of much larger magnitude in the vertical direction than in the horizontal. It is worth noting that the values here for inertia and drag coefficients are significantly larger than the

coefficient values determined for the pipe and support posts. Peak vertical forces on the structure are larger than peak horizontal forces for some irregular wave conditions, yet the components of the structure experiencing forces in the horizontal direction (pipe and posts) are larger than the velocity cap. Water particle velocity and acceleration are also greater in the horizontal direction, shown by the elliptical orbit of water particles in shallow waves. The coefficients increase with H/d at a similar rate for both inertia and drag coefficients.

The Z direction force coefficients for the cap were compared to results of previous studies. Results from the numerical study of 2-D flow interacting with a single submerged plate by Lian (1988) are presented below (Figure 6.57). Results of experimental studies are included. For the inertia coefficients (C_M), results of this study trend in the same direction as those from Lian, but are of large magnitude. For the drag coefficients (C_D), the results from this study are of similar magnitude but trend in the opposite direction.

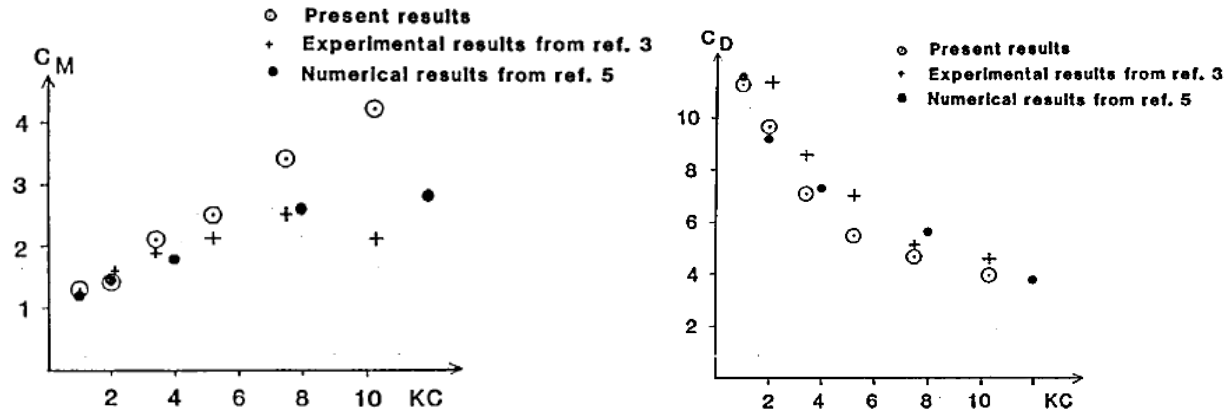

Figure 6.57: Force coefficients from numerical and physical studies on a submerged plate

6.3.5 Structural Configurations Force Coefficients

The inertia and drag coefficients determined to represent each structural configuration are analyzed separately from the coefficients that represent the posts and central pipe, due to the more complex geometry of the full intake structure compared to the individual cylindrical components. The Keulegan Carpenter number was not used in analysis of each configuration coefficients due to the presence of various cylinder diameters in the intake structure, as well as poor correlations between force coefficients and KC noted in the pipe and posts section of the analysis. Instead, H/d was used to plot coefficients, as was done successfully for each structural component. Presented below are the inertia and drag coefficients from each structural configuration. It should be noted that the results for

configuration 2 (central pipe) are the same values from the previous analysis section on pipe coefficients.

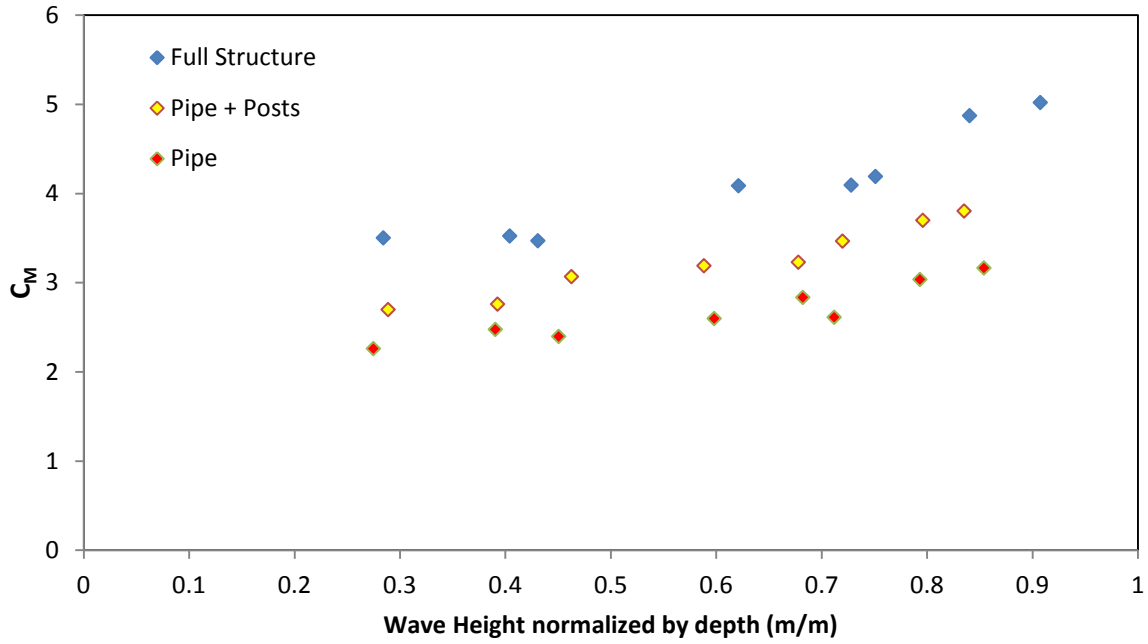

Figure 6.58: Inertia coefficients for the 3 structural configurations

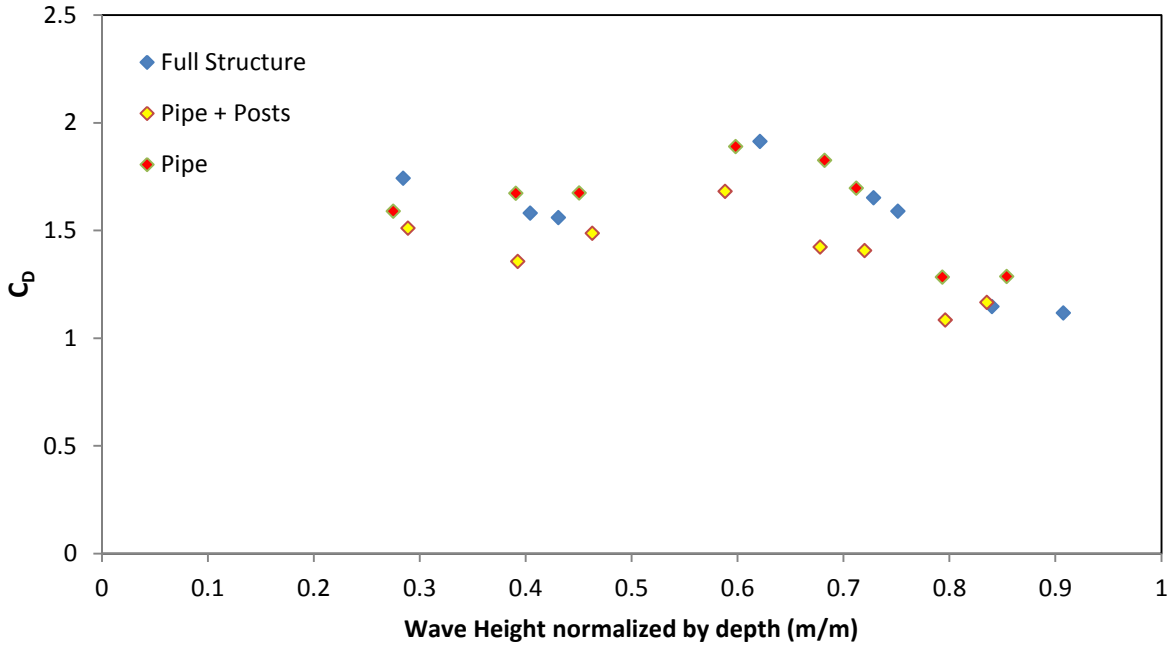

Figure 6.59: Drag coefficients for the 3 structural configurations

The inertia coefficients plotted in Figure 6.58 increase slightly with H/d, similarly to the inertia coefficients for the pipe and posts (Figure 6.53). The value of the inertia coefficient at each H/d increases as the structural configuration becomes more complex. Inertial force increases with other structural members in proximity, as water mass is trapped within the area under the cap intake structure. This bundle effect has been noted to increase inertia coefficients (Sarpkaya, 1979). The coefficients for the full structure configuration will be slightly higher than for the pipe and posts configuration regardless of this bundle effect, as the same structural geometry was used in calculation of force coefficients between the 2 test series (i.e. the geometry of the cap was omitted for calculating MOJS forces in the horizontal direction on the entire structure).

Drag coefficients for all 3 structural configurations plotted in Figure 6.59 also demonstrate similar trends noted in the drag coefficients of the pipe and posts (Figure 6.54). Once again the drag coefficients for the pipe are larger than those for the pipe and posts, due to the flow interference effects on lowering drag force from the central pipe on the flow fields of the 4 surrounding posts. In the pipe and posts structural configuration, the drag forces on the central pipe are included, so the discrepancy between drag coefficients isn't as large as in Figure 6.54. The drag coefficients for the full structure are larger than for the pipe and posts configuration, approximately the same values as the coefficients for the central pipe at each value of H/d recorded. This is merely a coincidence, as the drag coefficients for the full structure will be larger than those for the pipe and posts because the same geometrical values are used in the force calculation of both test series despite the velocity cap portion of the full structure slightly contributing to horizontal forces.

It is interesting to note that drag coefficients for all 3 structural configurations and for the support posts all follow the same pattern when plotted against H/d. The drag coefficients increase slightly and peak at $H/d \approx 0.6$. Following this point, drag coefficients decrease. As H/d increases, the waves become increasing steeper and non-linear. Inertia coefficients increase past $H/d \approx 0.6$; possibly indicating that forcing from waves breaking or beginning to break on the intake structure is inertia dominated.

6.3.6 Discussion

All force coefficients determined for each structural component and configuration are presented in Table 6.4 (page 130) according to the regular wave test that the coefficients were determined from. The analysis of force coefficients for varying wave and current conditions led the author to draw several conclusions:

1. Force coefficients for cylindrical components follow the same trend as the KC numbers and that is to be expected due to proximity effects.

Force coefficients derived from fitting the Morison equation to peak forces from regular waves on the submerged cylinders of the intake structure have been proven to be larger than coefficients for a single cylinder in isolation ($C_M = 2$, $C_D = 1.2$) due to proximity effects. The analysis of the force coefficients for cylindrical components (central pipe and support posts) shows an upward linear trend between the inertia coefficients (C_M) and the Keulegan-Carpenter number (KC). Drag coefficients (C_D) tended to decrease with the KC number. These results, which were recoded for both the central pipe and posts, prove that there is a significant effect due to proximity between structural members. Zdravkovich (1977) proved that proximity of cylinders would have a significant effect on the force coefficients if the inline space ratio L/D < 3.5, and side-by-side L/D < 2.2. All 4 posts are spaced evenly from the central pipe, with L/D = 4.6 (using post diameter). This indicates that the presence posts do not have a significant effect on the flow field and subsequent forcing on the central pipe. However, the flow field is still disturbed and vorticity behind the front post is only dissipated approximately 30% over this distance (Bloor and Gerrard, 1966). This leads to scatter of the drag coefficient plot and a slight increase of the central pipe drag coefficients with KC (Figure 6.54). Sarpkaya (1979) stated that a “bundle effect” of fluid trapped in a cylinder array increases the inertia coefficient. Due to fairly large spacing between the support posts, the inertia coefficients for the central pipe are close to that of the theoretical single cylinder value of $C_M = 2$ (Figure 6.51), although slightly larger due to this bundle effect. The inertia coefficients for the central pipe and posts are comparable to the values recorded by Sarpkaya (1979) on a circular pipe array with central pipe experiments (Figure 6.46).

The interference effects stemming from the proximity of the central pipe to the support posts are more significant. Using the central pipe diameter to evaluate its proximity to the support posts, the space ratio (L/D) in all directions is 0.65. This is significantly less than the critical space ratio for in-line and side-by-side cylinders of 3.5 and 2.2, respectively (Zdravkovich 1977), indicating that the flow field

around the central pipe significantly alters the flow around the 4 posts. This leads to increased turbulence around the structure, and to the altering of the force coefficients for the posts. The force coefficients determined for the posts follow the principles of proximity effects: the inertia coefficients are larger than those for the pipe, and the drag coefficients are smaller (Figures 6.44). The effects listed above, generated by the proximity between cylindrical members on force coefficients is observed when coefficients are plotted against shallow water wave height normalized by water depth (H/d) in Figures 6.53 and 6.54.

2. For all wave and current properties, force coefficients correlate best with H/d

Force coefficient results for all structural components (central pipe, support posts, velocity cap) and configurations (full structure, pipe + posts) show a strong linear correlation with the shallow water wave height normalized by the structure water depth (H/d). The complete set of inertia and drag coefficients for all structural components and configurations are plotted versus H/d on separate pages in Figures 6.60 and 6.61, respectively. The same principles of proximity between cylindrical structural components noted in the discussion on coefficients versus KC are observed when force coefficients are plotted against H/d: the drag coefficients are lower for the posts, and the inertia coefficients are lower for the central pipe. All four sets of inertia coefficients that were fitted to an experimental force time series (configurations 1-3, cap in Z direction) increase linearly, with minimal scatter, with H/d,. Inertia coefficients fitted to a force time series that was not recorded experimentally but created from the subtraction of 2 force time series (posts, cap in X direction), show considerable scatter when plotted against H/d.

Drag coefficients for all cylindrical components and structural configurations display similar trends when plotted against H/d. There is a linear increase that peaks at $H/d \approx 0.6$, followed by a decrease in the drag coefficient values. This may indicate that forcing from larger, breaking waves ($H/d > 0.7$) is more inertia-dominated as C_M values increase beyond $H/d \approx 0.6$ (Figure 6.60). It was noted in the analysis of the peak wave forces from the random wave tests that maximum waves recorded have H/d values of up to 1.2 and this correlated well when plotted versus the 95% peak horizontal force. The regular wave conditions in which forces were recorded and used to calculated inertia coefficients does not exceed H/d values of 0.9. Therefore, a MOJS model for random wave forces on the intake structure may fail to predict the peak forces from extreme waves.

3. Force coefficients for velocity cap in Z direction are very large

Figure 6.57 shows force coefficients for a single plate. When comparing with results from this study (Figure 6.56), the inertia coefficients (C_M) in the results of Lian (1988) are smaller than the inertia coefficient results in this study. It has been noted by Sarpkaya (1979, 2010) that proximity to other submerged bodies can increase the inertia coefficient. The flow field accelerating against the bottom of the plate used calculate the inertial force is interfered with by the proximity of the support posts and central pipe. During a wave trough, the separated turbulent flow and vortices created behind the support posts and central pipe and swept back against the intake structure and up against the velocity cap. This has a direct effect on drag coefficients (C_D) leading to different results from those in Figure 6.57. Force coefficients for the cap in the X direction were not investigated due to their low impact on total force.

Table 6.4: Drag and Inertia coefficients for all structural components and configurations, as determined from regular wave tests

Test Signal	Wave Height (m)	Water Level	Conf. 1 Full Structure		Conf. 2 Pipe only		Conf. 3 Pipe + Posts		Posts		Cap X direction		Cap Z direction	
			C_D	C_M	C_D	C_M	C_D	C_M	C_D	C_M	C_D	C_M	C_D	C_M
4	3	-2 MWL	1.91	4.09	1.89	2.60	1.68	3.19	1.31	4.95	4.74	1.55	10.55	16.28
8	4.5	-2 MWL	1.12	5.02	1.29	3.16	1.17	3.80	0.90	6.18	2.96	2.17	20.18	20.45
16	3	+0 MWL	1.58	3.52	1.75	2.46	1.35	2.76	0.98	4.26	7.35	1.63	7.40	13.62
20	4.5	+0 MWL	1.65	4.09	1.70	2.76	1.42	3.23	1.08	5.30	5.44	1.39	9.76	15.55
24	6	+0 MWL	1.15	4.87	1.19	3.06	1.08	3.70	0.89	6.17	17.75	1.10	13.85	16.61
28	3	+2 MWL	1.74	3.50	1.55	2.26	1.51	2.70	0.66	5.06	3.11	1.23	5.96	11.60
32	4.5	+2 MWL	1.56	3.47	1.66	2.36	1.49	3.07	1.00	6.32	6.97	2.13	6.91	13.66
36	6	+2 MWL	1.59	4.19	1.71	2.58	1.41	3.47	0.99	7.17	0.93	1.50	9.49	14.43

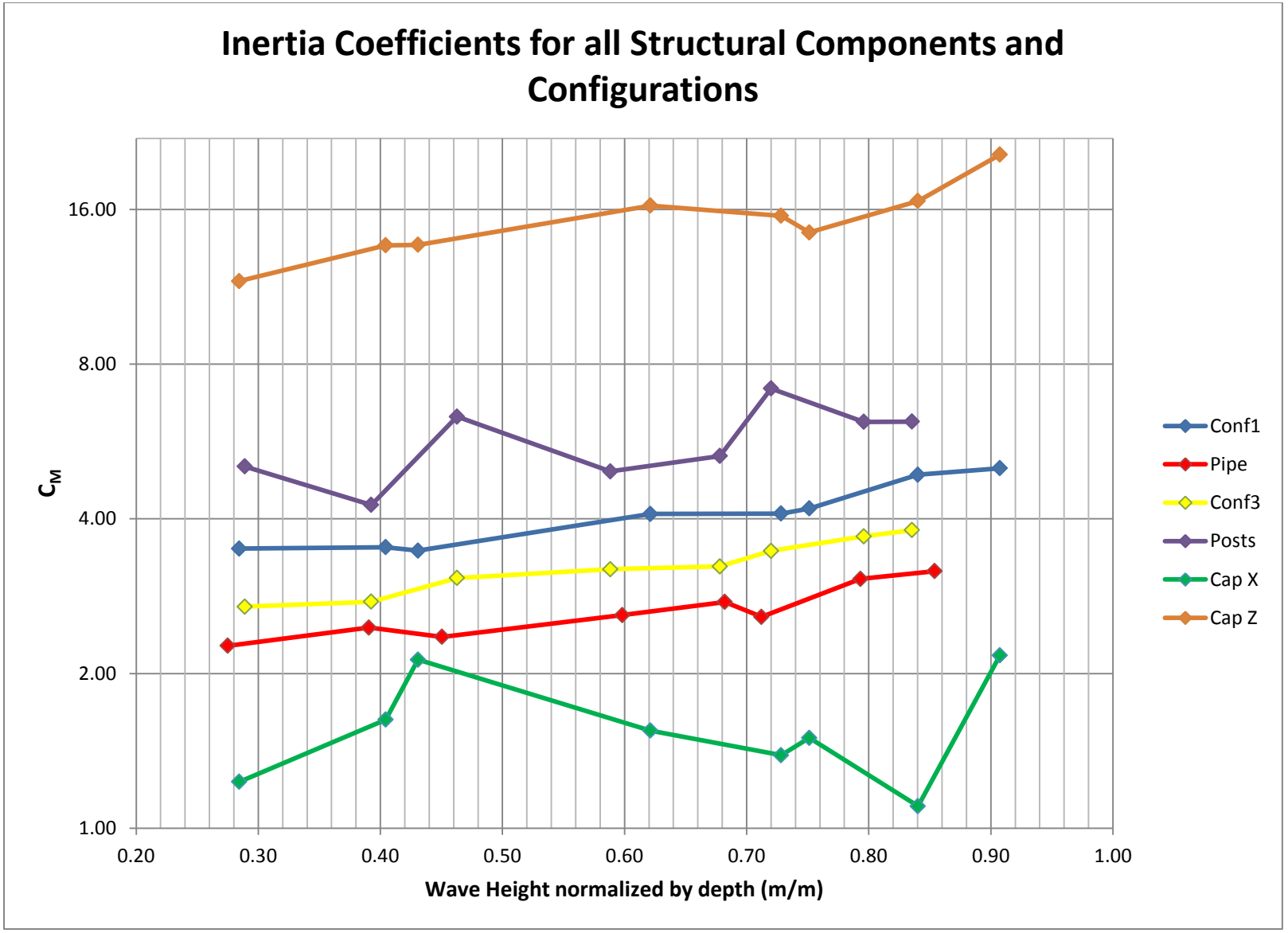

Figure 6.60: Inertia coefficients for all structural components and configurations

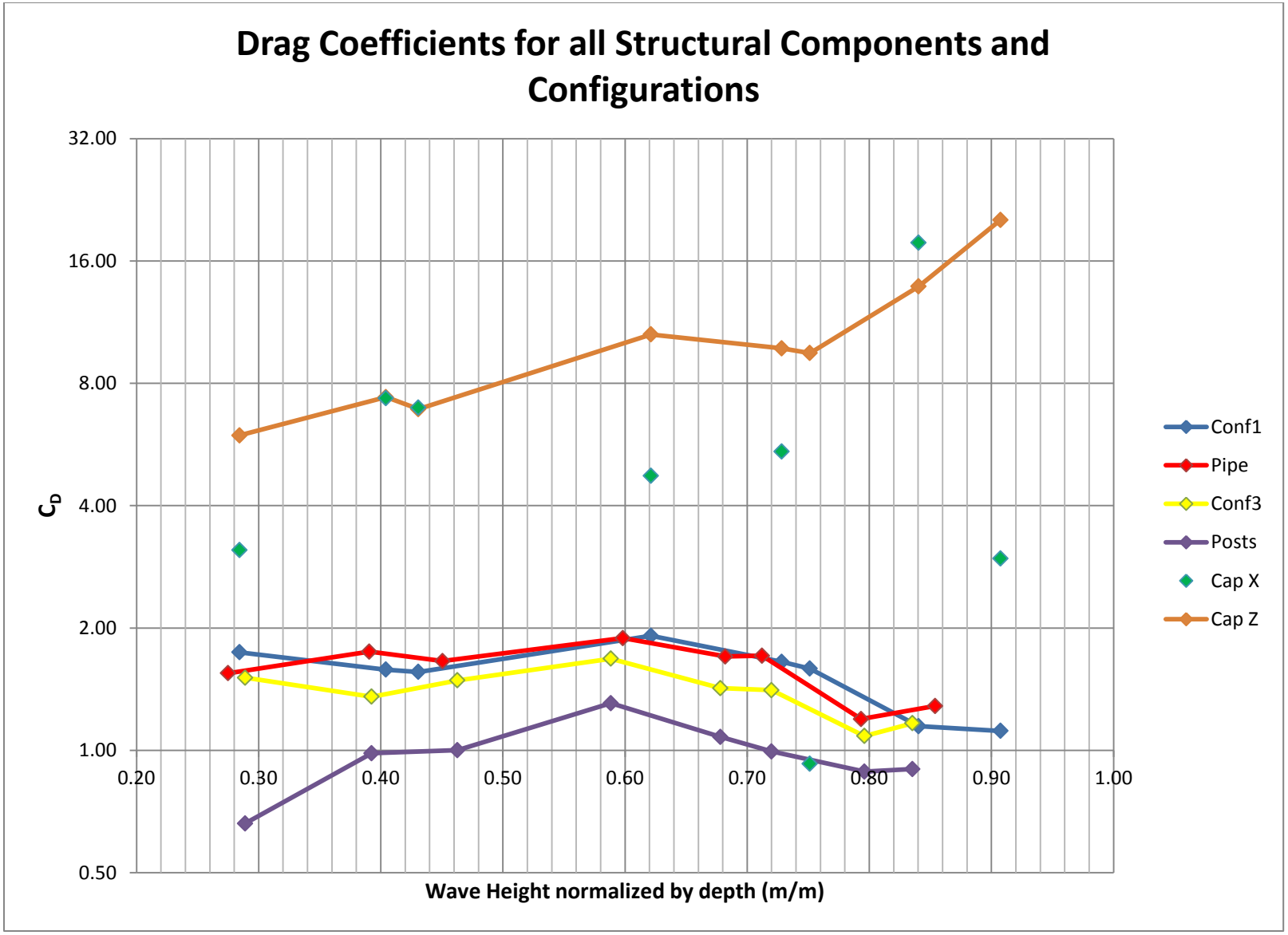

Figure 6.61: Drag coefficients for all structural components and configurations

6.4 Predicting Forcing from Irregular Waves

The force coefficients determined by fitting the Morison equation to results of nonlinear regular wave forcing on the structure were used to create mathematical expressions for modelling nonlinear irregular wave forcing on the intake structure. The current data recorded during the irregular wave tests was used in a series of Morison equation expressions to predict the force time series of irregular wave forcing on the total structure, pipe and posts configuration, and central pipe alone. The wave forcing on the total structure configuration was predicted in both the horizontal (X) and vertical (Z) directions, and in the horizontal direction for all other configurations. These predictive models were evaluated by how well the Morison equation fit the experimental force time series, and by how well peak forces were predicted.

6.4.1 Morison Equation Model

An irregular wave force prediction model was made in GEDAP using the Morison equation, drag and inertia coefficients determined from regular wave tests, and the current data from irregular wave testing. The model, referred to in this section as MOJS (an acronym for the 4 authors on the original Morison equation paper, 1950), was used to predict forcing on from irregular waves on each specific structural configuration, zero-moment wave height (H_{m0}), peak period (T_P), and water level tested (Table 4.1). Forcing was modelled for irregular wave tests of all 3 peak periods (T_P = 8, 11, 14s) despite the fact that all drag and inertia coefficients were determined from regular wave tests using a period of 11s.

MOJS predictive models were constructed in 2 ways: a series of equations representing forcing on each structural component added together, using their respective force coefficients; and force time series for each structural configuration, using the coefficients determined to represent each configuration and the specified wave condition. The Table (6.5) below describes each type of predictive model used.

Table 6.5: Structural configurations for which a model was used to predict forcing are tabulated. Configuration indicates from which test series current data was used.

Predictive Model	Definition
Conf. 1	The full structure configuration. One set of coefficients is used to calculate forcing on all 3 components of the structure.
Conf. 2	The pipe only configuration. One set of coefficients is used to calculate forcing on the central pipe.
Conf. 3	The pipe + posts configuration. One set of coefficients is used to calculate forcing on the central pipe and 4 support posts.

Full – Comp.	The full structure configuration. A separate set of coefficients corresponding to each of the 3 components of the structure is used calculate total forcing.
Full – Conf. 3	The full structure configuration. A separate set of coefficients corresponding to each of the velocity cap and pipe + posts components is used to calculate total forcing.
Conf. 3 – Comp.	The pipe only configuration. A separate set of coefficients corresponding to each of the central pipe and support posts components is used to calculate total forcing.
Z	The full structure configuration. One set of coefficients is used to calculate forcing on velocity cap in the vertical direction.

The following series of equations were used with experimental current data to create a time series predicting forcing on the structure for the entire 31 minute wave test being modelled. For forces on the full structure, a MOJS expression was created in 3 separate ways: an expression using coefficients that represent the whole structure (Conf. 1), an expression for the forcing on each component of the structure (cap, posts, central pipe) summed together (Full – Comp.), and a similar composite expression using a time series for horizontal forcing on the velocity cap added to a series for forcing on the central pipe and posts together (Full - Conf. 3). A similar process was used when modelling the forces on the central pipe and posts structural configuration (3), where coefficients calculated for the configuration (Conf. 3) as well as for the pipe and posts separately (Conf.3 – Comp). Unless otherwise stipulated, all vector values (force, velocity, acceleration) are in the direction of wave propagation (X direction). The forcing on the full structure configuration (1) was calculated in the following 3 ways:

$$F(t)_{Conf1} = \left[C_{M-Conf1} * \left(\frac{du}{dt}\right) * \left(V_{pipe} + 4V_{post}\right) + \frac{1}{2} * C_{D-Conf1} * u|u| * \left(A_{pipe} + 4A_{post}\right)\right] \quad [6.15]$$

$$\begin{aligned} F(t)_{Full-Comp} = & \left[C_{M-Pipe} * V_{pipe} * \left(\frac{du}{dt}\right)\right] + \left[\frac{1}{2} * C_{D-Pipe} * A_{pipe} * u|u|\right] \\ & + \left[C_{M-CapX} * V_{Cap} * \left(\frac{du}{dt}\right)\right] + \left[\frac{1}{2} * C_{D-CapX} * A_{CapX} * u|u|\right] \\ & + \left[C_{M-Posts} * (4V_{post}) * \left(\frac{du}{dt}\right)\right] + \left[\frac{1}{2} * C_{D-Posts} * (4A_{post}) * u|u|\right] \end{aligned} \quad [6.16]$$

$$\begin{aligned} F(t)_{Full-Conf3} = & \left[C_{M-Conf3} * \left(\frac{du}{dt}\right) * \left(V_{pipe} + 4V_{post}\right) + \frac{1}{2} * C_{D-Conf3} * u|u| * \left(A_{pipe} + 4A_{post}\right)\right] \\ & + \left[C_{M-CapX} * V_{Cap} * \left(\frac{du}{dt}\right)\right] + \left[\frac{1}{2} * C_{D-CapX} * A_{Cap} * u|u|\right] \end{aligned} \quad [6.17]$$

The forcing on the pipe and posts configuration (3) was calculated in the following 2 ways:

$$F(t)_{Conf3} = \left[C_{M-Conf3} * \left(\frac{du}{dt}\right) * \left(V_{pipe} + 4V_{post}\right) + \frac{1}{2} * C_{D-Conf3} * u|u| * \left(A_{pipe} + 4A_{post}\right)\right] \quad [6.18]$$

$$F(t)_{Conf3Comp} = \left[C_{M-Pipe} * V_{pipe} * \left(\frac{du}{dt}\right)\right] + \left[\frac{1}{2} * C_{D-Pipe} * A_{pipe} * u|u|\right] + \left[C_{M-Posts} * (4V_{post}) * \left(\frac{du}{dt}\right)\right] + \left[\frac{1}{2} * C_{D-Posts} * (4A_{post}) * u|u|\right] \quad [6.19]$$

Finally, the forcing on the central pipe configuration and vertical forcing on the velocity cap were calculated using the following expressions:

$$F(t)_{Conf2} = \left[C_{M-Pipe} * V_{pipe} * \left(\frac{du}{dt}\right)\right] + \left[\frac{1}{2} * C_{D-Pipe} * A_{pipe} * u|u|\right] \quad [6.20]$$

$$F(t)_{Z} = \left[C_{M-CapZ} * V_{Cap} * \left(\frac{du_Z}{dt}\right)\right] + \left[\frac{1}{2} * C_{D-CapZ} * A_{CapZ} * u_Z|u_Z|\right] \quad [6.21]$$

The entire force time series in the direction of interest from each irregular wave test was simulated in GEDAP using these MOJS expressions. The force time series was calculated using force coefficients from regular wave testing (Table 6.4) and using experimental current data measured beside the structure. This process was repeated for each structural configuration tested. Irregular wave forcing from tests (9, 10, 11) with low water (-2 MWL) and zero-moment wave height of H_{m0} = 6m was not calculated. The regular wave test (12) corresponding to these conditions featured waves that all broke before arriving at the location of the structure, and therefore no force coefficients were calculated for these conditions. Examples of the predicted forcing on the full structure configuration are plotted on the following 5 pages (Figures 6.62 – 6.66). Within each Figure, the top time series plot and energy density spectrum are the experimental force results from the irregular wave test. The predicted force results from the MOJS model used are in the middle. The bottom plot is a specific 150s period from the top plot chosen due to larger forces on the structure, with the MOJS results superimposed for comparison. The first 2 Figures are results from test 1: Figure 6.62 is the forcing simulated using Full-Comp MOJS expression, and Figure 6.63 is the forcing simulated using Conf. 1 MOJS expression. The next 2 Figures are the same format, but using results from test 23. The final plot (Figure 6.66) is the Z direction force results from test 23. Information about these tests, as well as the peak force values, is tabulated below. Similar plots for MOJS modelling results for Conf. 2, Conf. 3, Full - Conf. 3, and Conf. 3 – Comp for test 23 can be seen in the Appendix.

Table 6.6: Description of tests used to provide examples of MOJS predicted forcing

Figure	Test	MOJS model	Water Level	H_{m0} (m)	T_P (s)	Experimental Peak Force (kN)	MOJS Predicted Peak Force (kN)
6.62	1	Full - Comp	-2 MWL	3	11	69	57
6.63	1	Conf. 1	-2 MWL	3	11	69	56
6.64	23	Full - Comp	+0 MWL	6	14	171	215
6.65	23	Conf. 1	+0 MWL	6	14	171	114
6.67	23	Z	+0 MWL	6	14	262	286

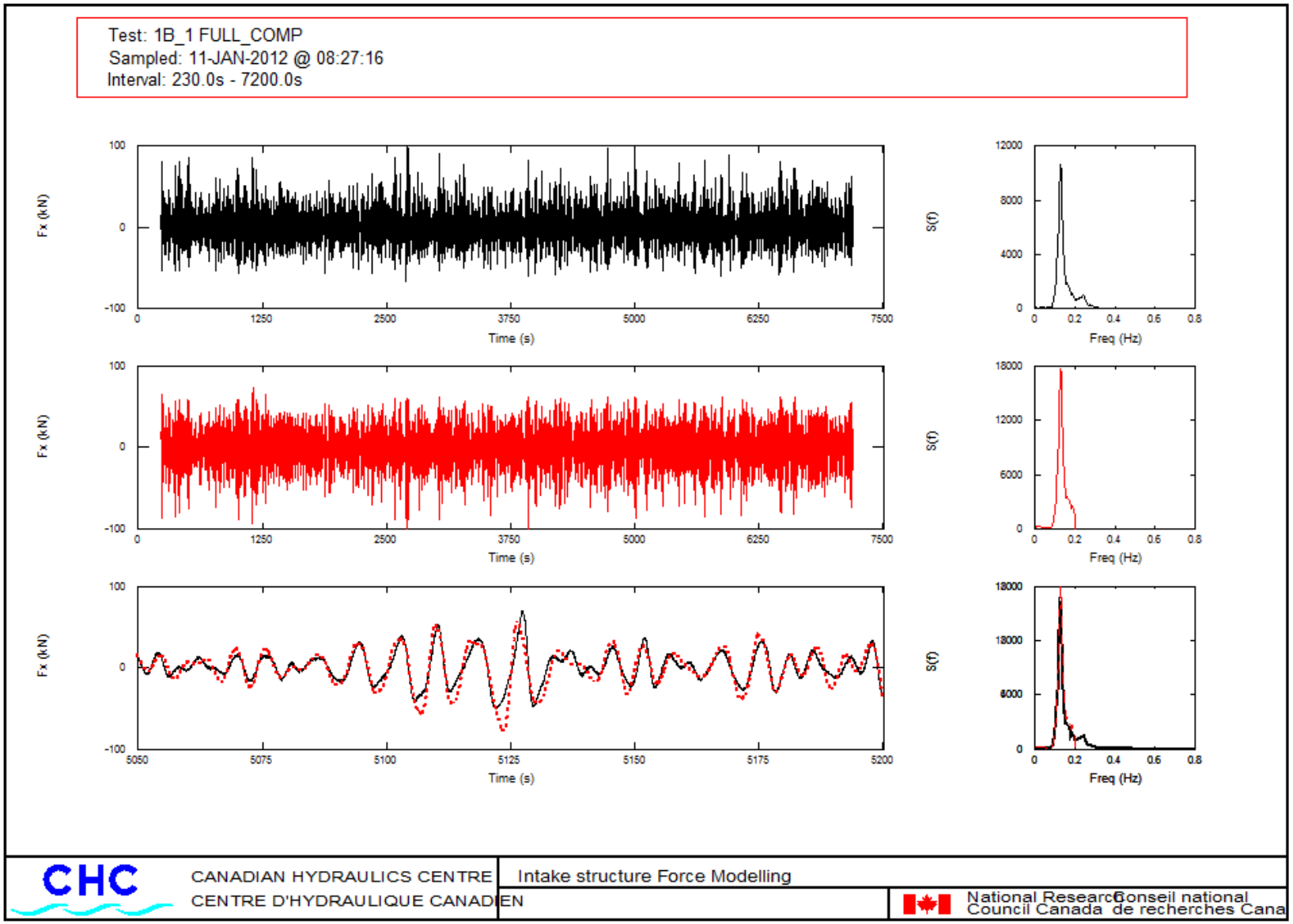

Figure 6.62: Experimental forcing (top), Morison equation predicted forcing (middle), and both (bottom) for an irregular wave test

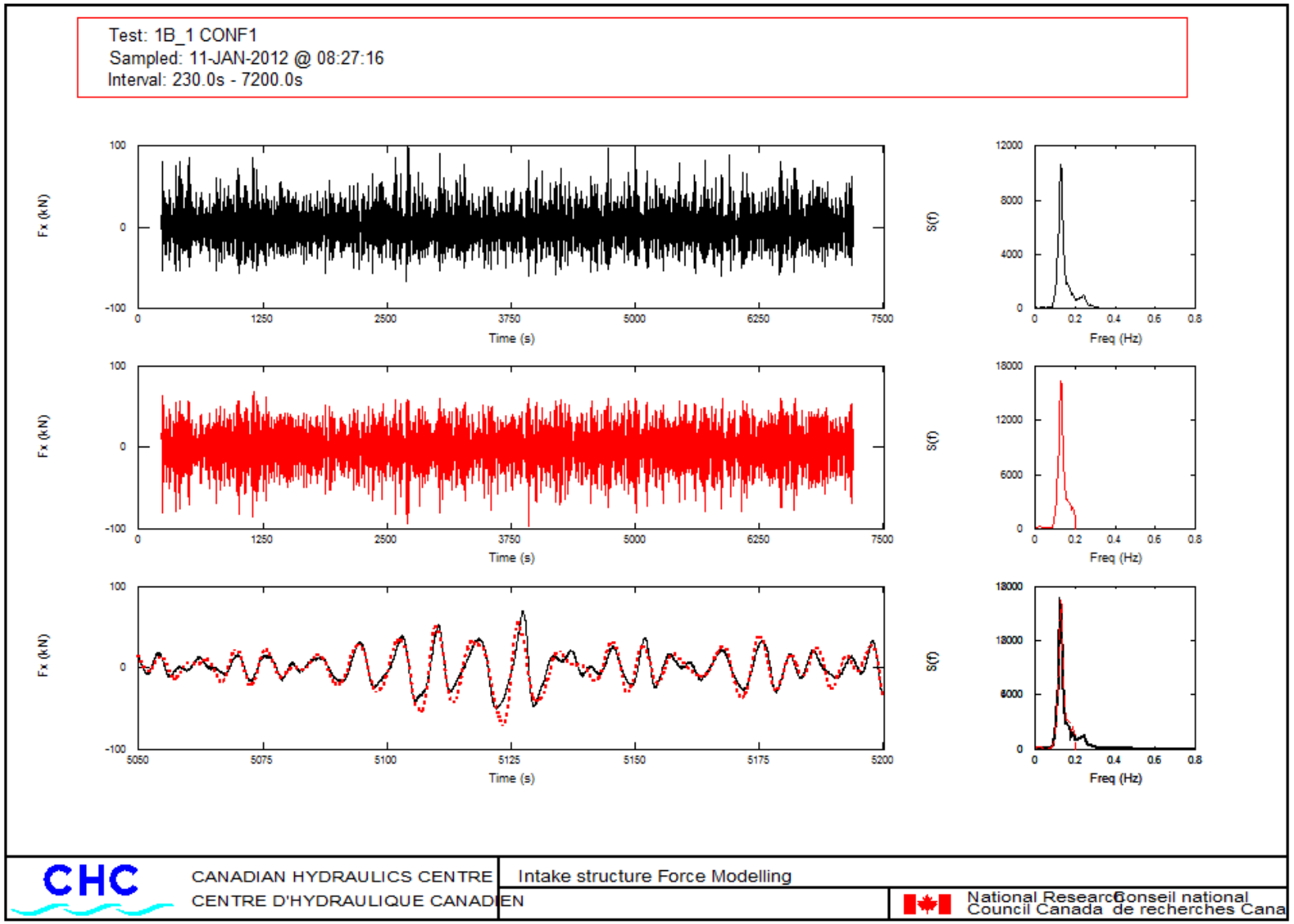

Figure 6.63: Experimental forcing (top), Morison equation predicted forcing (middle), and both (bottom) for an irregular wave test

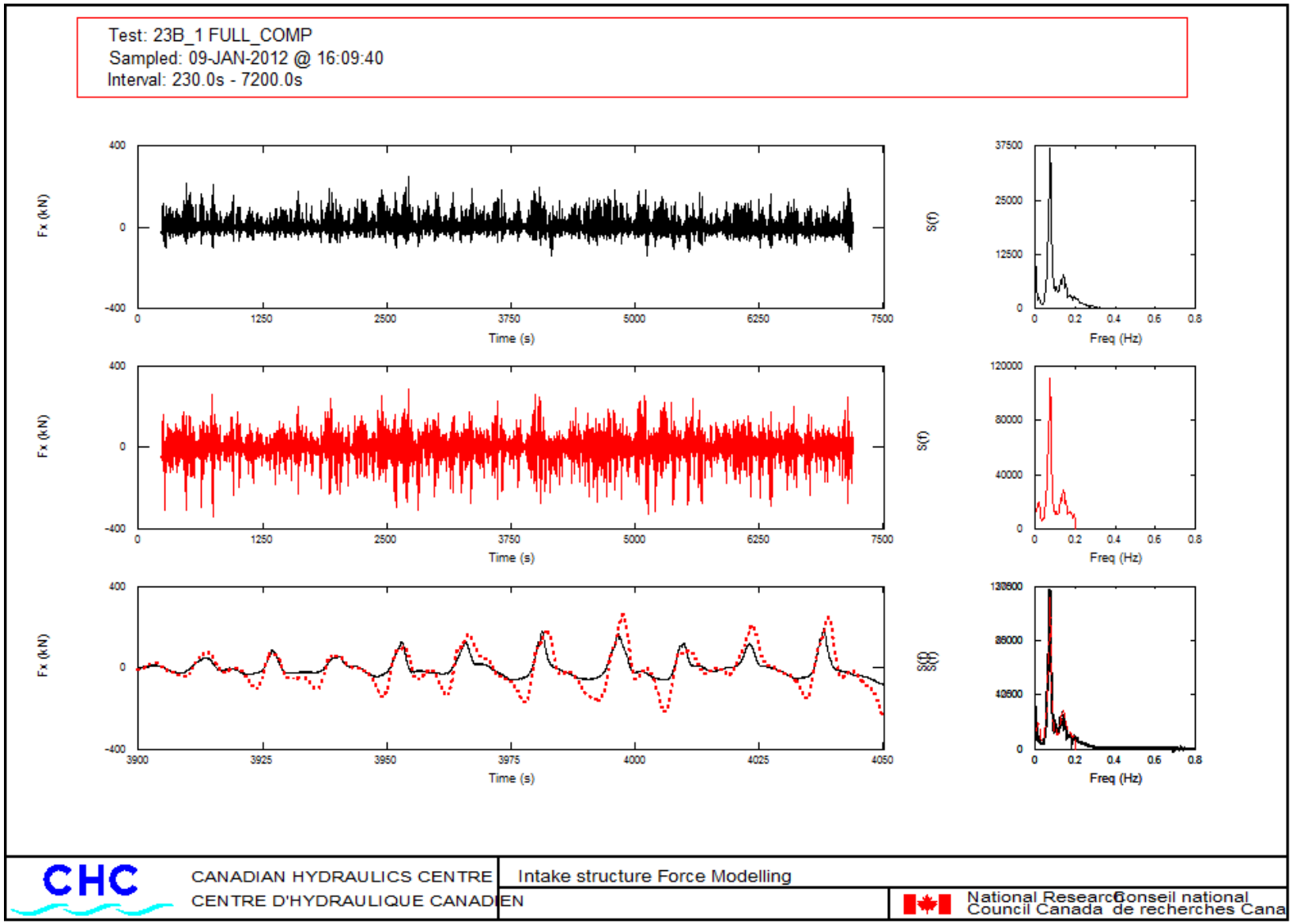

Figure 6.64: Experimental forcing (top), Morison equation predicted forcing (middle), and both (bottom) for an irregular wave test

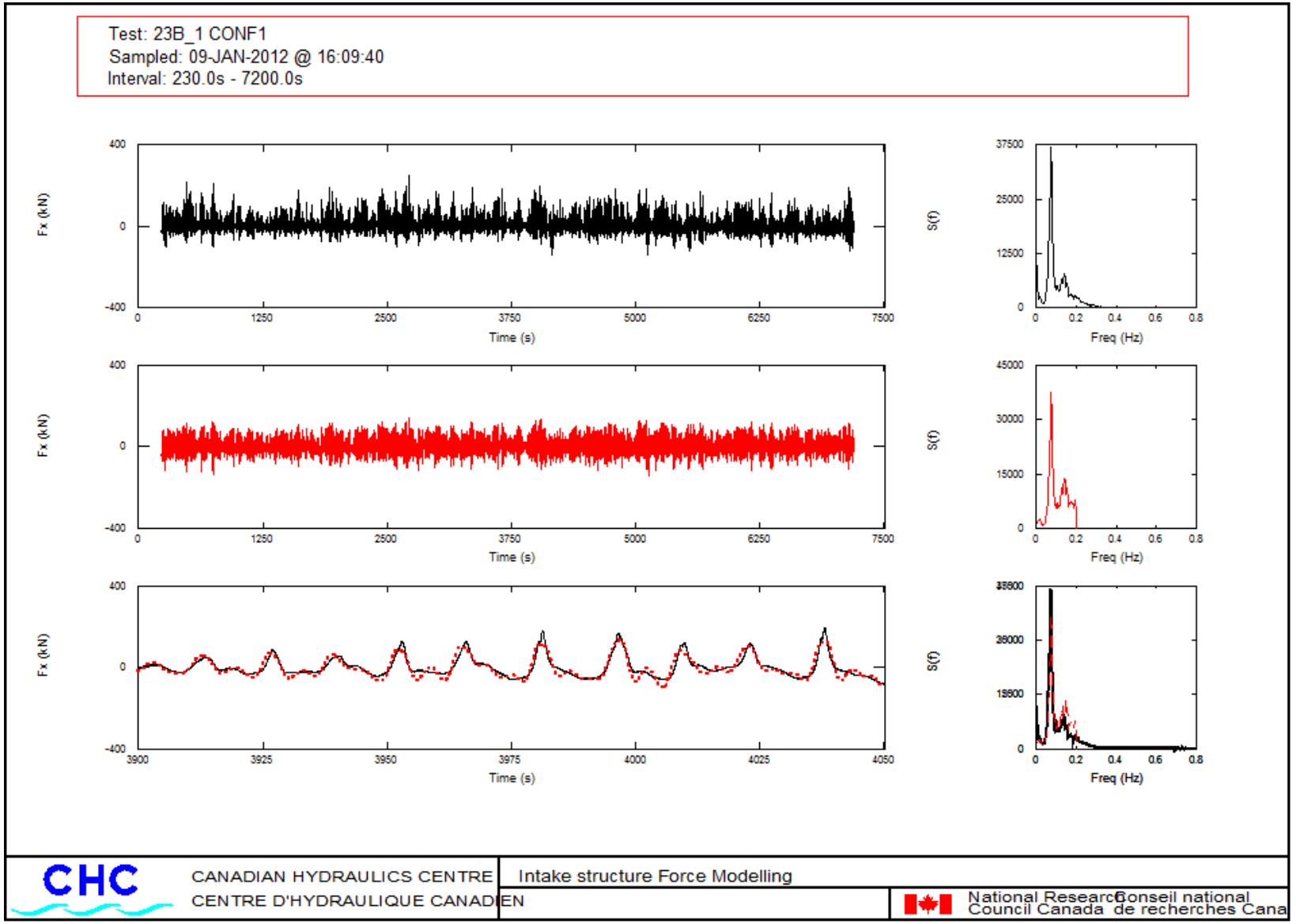

Figure 6.65: Experimental forcing (top), Morison equation predicted forcing (middle), and both (bottom) for an irregular wave test

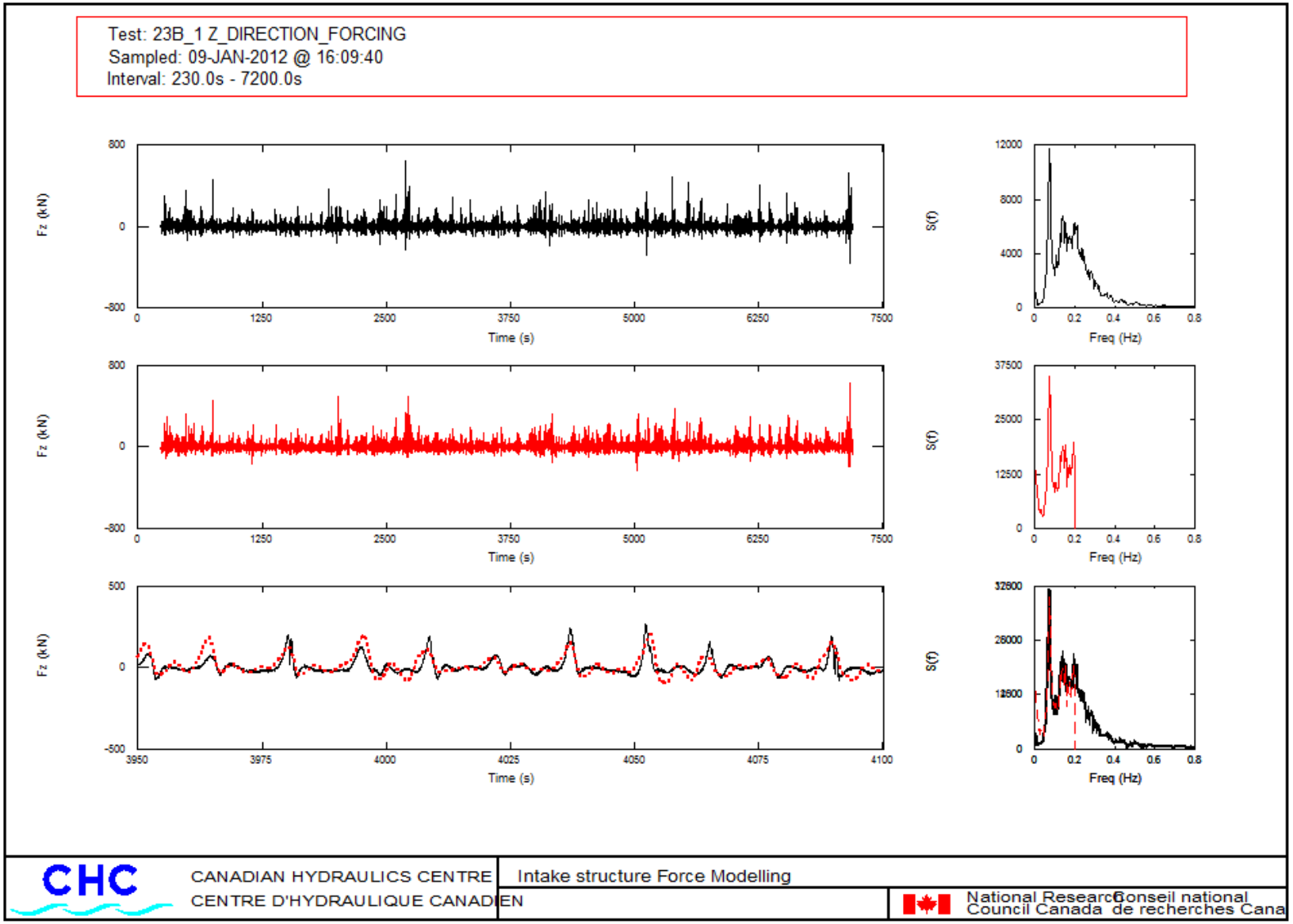

Figure 6.66: Experimental forcing (top), Morison equation predicted forcing (middle), and both (bottom) for an irregular wave test

In Figure 6.62, it can be seen that the MOJS Full-Composite expression predicts random wave forces very accurately. The 2 time series are in near perfect phase, and most peaks in force during wave crests and troughs are predicted well, with some overestimation of peak negative forces. Figure 6.63, which is the same test but using the MOJS Conf. 1 expression to predict forcing, demonstrates nearly identical results. This indicates that in relatively calm wave conditions (H_{m0} = 3m), the Morison equation is very accurate at predicting horizontal forcing. It also shows that there is not a large discrepancy between using one set of force coefficients and a set of coefficients for each component of the structure in relatively calm conditions. Figures 6.64-6.65 show the results of the MOJS model for more severe wave conditions (H_{m0} = 6m). Here the discrepancy between the two MOJS expressions for predicting total force on the structure is more pronounced. The MOJS Full-Composite expression over predicts force values for large peaks and troughs, while the MOJS Conf. 1 expression is a much better fit. However, Table 6.6 shows that by over predicting forces, the peak (95^{th} percentile) in-line force was more closely estimated by the full-comp model than the Conf.1 model.

A simulation of vertical (Z) direction forcing was presented with experimental results in Figure 6.66. Despite a reasonable prediction of peak force in Table 6.6, the bottom plot of Figure 6.66 shows that peaks in force were not predicted very accurately by the MOJS Z model. This may be due to the discrepancy in the energy density spectra of the experimental and MOJS forces. Current data used to determine force coefficients from regular wave tests was filtered with an upper limited of 0.2 Hz, the value necessary to eliminate noise and false readings during large waves. Since coefficients were determined with these current conditions, current data from irregular wave tests was filtered in a similar manner before used to calculate the MOJS expressions. For forcing in the vertical direction, there is a significant amount of force energy in frequencies greater than 0.2 Hz, which was not recreated by the MOJS expression. The peak force values from experimental and MOJS results in Figures 6.62-6.66 were presented in Table 6.6. The analysis between experimental and predicted peak forces for all irregular wave tests is discussed in the following section.

6.4.2 Prediction of Peak Forces

The same force analysis procedure in GEDAP used to determine peak experimental forces was used to determine peak MOJS predicted forces. To observe the accuracy of this model for its ability to predict peak forces on the structure, the difference (%) between experimental and MOJS peak force for each structural configuration are tabulated below. Each column is a different MOJS expression used to predict forcing. Each row is a statistic of the predicted results of all irregular wave conditions tested in this

study. A positive percentage value indicates the model overestimated the experimental results, and a negative value indicates the experimental peak force was underestimated by the model. The top half of the table is results from all 24 irregular wave tests. The bottom half is the results from the 8 irregular wave tests on that had a peak period of 11s, the period used in tests the force coefficient were derived from.

$$\% \, Error = \frac{(F_{95\ Predicted} - F_{95\ Experimental})}{F_{95\ Experimental}} \, x \, 100 \qquad [6.22]$$

Table 6.7: Statistics for accuracy of MOJS models when attempting to predict peak force from irregular wave tests

	Conf. 1	Conf. 2	Conf. 3	Full - Conf. 3	Full - Comp	Conf. 3 Comp	Z Direction	Average
	All Tests							
	Error	Error	Error	Error	Error	Error	Error	Error
MAX	-38.10%	-34.46%	-40.04%	-33.37%	42.79%	-41.14%	-43.53%	39.06%
MIN	- 0.67%	-3.75%	-4.32%	3.81%	-0.34%	-0.93%	0.95%	2.11%
AVERAGE	-20.54%	-17.77%	-21.87%	-9.15%	-7.71%	-19.20%	-5.94%	-14.60%
STDEV	10.55%	7.59%	9.65%	16.35%	17.15%	12.36%	19.48%	13.30%
|AVERAGE|	20.87%	17.77%	21.87%	16.89%	15.69%	19.85%	17.44%	18.63%
|STDEV|	9.88%	7.59%	9.65%	8.10%	10.36%	11.29%	10.52%	9.63%
	Tp = 11s							
	Error	Error	Error	Error	Error	Error	Error	Error
MAX	-35.01%	-21.23%	-22.60%	17.39%	-16.57%	-21.21%	-24.28%	22.61%
MIN	-12.92%	-10.44%	-16.44%	-8.58%	-6.11%	-13.10%	0.95%	9.79%
AVERAGE	-19.83%	-15.71%	-20.59%	-9.25%	-7.53%	-17.50%	-1.80%	-13.17%
STDEV	6.19%	3.39%	1.79%	10.33%	9.33%	2.53%	14.03%	6.80%
|AVERAGE|	19.83%	15.71%	20.59%	13.60%	11.54%	17.50%	12.51%	15.90%
|STDEV|	6.19%	3.39%	1.79%	2.72%	3.22%	2.53%	6.62%	3.78%

The MAX value represents the irregular wave test with that largest discrepancy between experimental and MOJS peak force, while MIN refers to the test where the MOJS model was closest to predicting the peak force. The average and standard deviations values are calculated based on all the differences in experimental and MOJS peak forces from all the tests on that structural configuration. The absolute value averages and standard deviations were also calculated from these values for a more accurate value of discrepancy between the model and experimental forces, regardless if the force was over or underestimated. All forces are in the direction of wave propagation (X - horizontal), with the exception of the Z forces (vertical).

6.4.3 Discussion

It can be seen from the table above that in almost every case the MOJS model failed to predict the 95th percentile force on the structure or portion of the structure forces were predicted for. In almost all cases, the MOJS model underestimated the peak force, with the average discrepancy of forces on a structural configuration always being negative. The composite MOJS models, where the forces on the full structure were modelled by summing force time series on each separate component together, proved to be more accurate than using one set of coefficients to represent the full structure. While the peak force values of some tests were closely predicted (see MIN, Table 6.7), nearly each structural configuration featured a test with a gross underestimation of the peak force (~-40%), making this MOJS model a poor predictor of peak force. There was no correlation at all between varying wave conditions and predictive accuracy of the MOJS model. Irregular wave tests featuring a peak period of 11s, the same period used when determining the force coefficients, provided more accurate results. The average of absolute discrepancy between experimental and MOJS peak forces for irregular wave tests with a peak period of 11s was 15.9%, compared to 18.73% for all irregular wave tests.

There are multiple reasons why peak forces on the intake structure from irregular waves were not predicted using a Morison equation model and force coefficients determined from regular wave forces. Regular waves with same height as the zero-moment wave height can give erroneous results in the analysis of actions and forcing of waves (Goda, 1985). The close correlation between wave height and peak force noted in the Peak Force Analysis section (Figure 6.13), as well as trends in force coefficients with normalized wave height (H/d) noted in the Force Coefficient Analysis section, indicates that force coefficients derived from a regular wave test with a given H/d value will accurately predict forcing from an irregular wave with the same H/d value. It was noted in the Peak Force Analysis section that large wave events from irregular wave tests have larger H/d values than their corresponding regular wave

tests. Since force coefficients were noted to trend closely with H/d, it is understandable that peaks in force were not predicted. MOJS results that predict or over predict peak force values are simply over predicting the entire force record.

7.0 Conclusions

In this section, conclusions discussed in this study are summarized and recommendations are made for future work on this topic, followed by concluding thoughts by the author.

7.1 Conclusions

Throughout the Peak Force Analysis, Force Coefficient Analysis, and Predicting Forcing from Irregular Waves sections of this study, several conclusions connecting wave properties, force coefficients, and subsequent forcing on the intake structure can be drawn.

Peak Force Analysis:

- Peak horizontal force on the intake structure and structural components increases linearly with the normalized zero-moment wave height (H_{m0}/d) recorded at the location of the structure and with the peak period (T_P) of an irregular wave series. As H_{m0}/d values approach 0.7, the increase in the peak force values ceases, as the largest waves will have broken due to water depth limitations prior to reaching the location of the structure.
- The peak forces on the intake structure are induced by the largest waves recorded at the structure location. Wave records aligned with horizontal force records show a direct correlation between the wave height and amplitude of horizontal forcing on the structure. A steep increase of peak force with H_{MAX}/d occurs when was identified when plotting the peak force value recorded from a wave test versus the normalized maximum wave from the respective irregular wave test shows
- Vertical and horizontal forces recorded on the velocity cap have higher absolute magnitudes in low water conditions (-2m MWL). In shallower water, the velocity cap is closer to the free surface where the flow field exhibits significant magnitude of the vertical components of velocity and acceleration. Hence, shallower water particle kinematics near the free surface of passing waves lead to larger forcing on the velocity cap.
- Forces on central pipe and support post are close in magnitude. Despite different lengths, diameter, volume, and area normal to the direction of flow, for each peak period tested, the peak force values recorded from irregular wave tests on the pipe and posts were close in magnitude. The peak force values on the central pipe, which has a volume approximately 3 times larger than the combined volume of the 4 support posts, are notably larger for irregular wave tests of with a peak period of 14s.

Force Coefficient Analysis:

- Force coefficients for the cylindrical structural components of the intake follows trends similar to the KC number, something to be expected due to proximity effects. Principles established by Zdravkovich (1977) and tested with similar configurations (Sarpkaya, 1979) are observed in the drag and inertia coefficients determined in this study. A notable effect of the proximity of cylindrical structural components on force coefficients includes lower drag coefficients of the support posts relative to those of the central pipe.
- For all wave and current properties, force coefficients correlate best with the normalized wave height (H/d) of the regular wave test that the coefficients were determined from. A linear increase and decrease is noted in the inertia and drag coefficients, respectively, for force coefficients determined for all structural configurations and components.
- Force coefficients for the velocity cap in Z direction are very large. Though the coefficients determined provided a very good fit when used to predict the vertical forcing from regular waves using the Morison equation, the values of the force coefficients do not compare well with other values published for force coefficients on a submerged plate. This is due to the structural complexity of the intake structure which induces significant vorticity/turbulence in the flow field that pushes against the bottom of the velocity cap.

Predicting Forcing from Irregular Waves:

- Forcing on the structure in the horizontal (X) and vertical (Z) directions was successfully modelled for all irregular wave tests (each with a minimum of 500 waves) using current data recorded at the location of the structure, the empirically determined force coefficients, and the Morison equation. The magnitude of the predicted force series for irregular waves as well as their phase were shown to be very similar to those of the experimental data.
- The analysis of peak forces from the predicted force series showed that nearly each tested structural configuration featured a test with a major underestimation of the peak force (~-40%), making these MOJS models a poor predictor of peak force from an irregular wave series.
- The peak forces from irregular wave tests featuring a peak period of 11s - the same wave period used in regular wave tests and force coefficient determination - were predicted slightly more

accurately than for the case of irregular wave tests of all 3 peak periods (15.9% error compared to 18.73%).

The MOJS predictive models developed in this study are capable of modelling forcing from irregular waves with the same H/d values as the regular wave test from which the force coefficients were determined from. Maximum wave events recorded during irregular wave tests have H/d values that exceed those recorded in the test employing regular waves. Since force coefficients were noted to correlate closely with H/d, peaks in force induced by the maximum waves were not predicted accurately. Proximity effects between the cylindrical components of the intake structure cause force coefficients to change with H/d, with the inertia coefficient values increasing and the drag coefficient values decreasing. Inertia forces have been shown to dominate peaks in forcing. Inertia coefficients increase linearly with H/d, as does the induced current, causing the steep increase of peak horizontal forcing on the structure with H/d corresponding to maximum waves.

8.0 Recommendations

Further research is needed with respect to wave-induced forcing on structures and on determining relationships between wave properties and force coefficients from large breaking waves in shallow water. The majority of studies detailed in the literature review in this thesis employ various wave theories to simulate water particle kinematics. However, accurate measurements of water particle kinematics under large breaking wave conditions are a difficult enterprise. The acoustic velocimeter used in this study had to be filtered at a fairly low frequency (Hz) to eliminate noise during these wave events. This may have led to the inability of the MOJS force prediction models to confidently and accurately predict peak forces on the structure. Easson and Greated (1984) used fibre-optic probes to measure water particle velocities and accelerations in large breaking waves. A speckle photography system was also used to photograph water particles at various instances within one wave period and calculate the kinematics using laser measurement techniques. Such experimental methods are necessary to accurately measure currents induced by large breaking waves.

To further the understanding of wave induced forcing on a submerged intake structure, it is the belief of the author that more research and data accumulation is needed to study force coefficients. It has been shown in this thesis that wave properties and corresponding current velocities alone cannot be confidently used to predict forcing on a complex structure, as force coefficients for such a structure

differ from those of simpler geometry (for instance, those of a single cylinder) and depend highly on the local wave conditions. A single set of force coefficients may not suffice to model forcing on such a complex structure under various wave conditions. It is also the belief of the author that numerical models capable of reproducing the turbulent flow field and forcing on submerged structures may benefit from using the data generated from this study to further validate their theoretical and numerical formulation.

8.1 Concluding Thoughts

The topic of turbulent flow induced by waves around a submerged cylinder and the subsequent forcing is very complex due to the several factors such as flow separation and generated turbulence and associated vorticity. Estimating forces on a submerged structure composed of multiple cylinders of different geometries in close proximity under breaking wave conditions further complicates the issue. Relatively accurate solutions for estimating forces on a submerged cylinder are available through analytical and numerical models for a single cylinder in controlled flow and wave conditions. However, due to the many variables influencing the flow field around the cylinders in the physical model presented in this study, simplification of the solution was required. An application of Morison's equation, using force coefficients empirically derived from wave tests conducted in this study, provided a good solution for wave-induced forcing on a submerged intake structure under breaking waves. With suitable force coefficients for a structure of this nature, it was proven that the Morison equation can be used an acceptable engineering design tool for a submerged intake structures in a realistic ocean environment.

References

Agarwal, P., & Manuel, L. (2011). Incorporating irregular nonlinear waves in coupled simulation and reliability studies of offshore wind turbines. *Applied Ocean Research*, 33(3), 215-227.

Agerschou, H. A., & Edens, J. J. (1965, October). Fifth and first order wave-force coefficients for cylindrical piles. In *Coastal Engineering: Santa Barbara Specialty Conference* (pp. 219-241).

Apelt, C. J., & Piorewicz, J. (1986). Interference Effects on Breaking Wave Forces on Rows of Vertical Cylinders. In *First Australasian Port, Harbour & Offshore Engineering Conference 1986,* Sydney, 29 September-2 October 1986: Preprints of Papers (p. 191). Institution of Engineers, Australia.

Apelt, C. J., & Piorewicz, J. (1987). Laboratory studies of breaking wave forces acting on vertical cylinders in shallow water. *Coastal engineering*, *11*(3), 263-282.Bloor, M. S. and Gerrard J. H. 1966. Measurements on turbulent vortices in a cylinder wake. Proc. R. Soc. London Ser. A 294, 319–342.

Borgman, L. E. (1967). Spectral analysis of ocean wave forces on piling. *Journal of the Waterways and Harbors Division, Proceedings of ASCE*, *2*, 129-156.

Bostroem, T., & Overvik, T. (1986). Hydrodynamic force coefficients in random wave conditions. In *Proceedings 5th Int. Offshore Mech. and Arctic Eng. Symp.*, Tokyo, Japan 1986, pp. 236-143.

Boussinesq, J. (1872). Théorie des ondes et des remous qui se propagent le long d'un canal rectangulaire horizontal, en communiquant au liquide contenu dans ce canal des vitesses sensiblement pareilles de la surface au fond. *J. Math. Pures Appl.*, *17*(2), 55-108.

Bullock, G. N., Stansby, P. K., & Warren, J. G. (2011, June). Loading and response of cylinders in waves. In *Proceedings of the International Conference on Coastal Engineering* (Vol. 1, No. 16).

Burrows, R., Tickell R.G., Hames D., Najafian G. (1997). Morison wave force coefficients for application to random seas. *Applied Ocean Research*, 19, 183-199.

CERC (Coastal Engineering Research Centre) (1984). Shore Protection Manual Vol. 1, Army Corps of Engineers, Washington D.C.

CHC, (2009). Large Scale Wave Flume (LWF) NRC, Web. 09 May 2012. <http://www.nrc-cnrc.gc.ca/eng/facilities/chc/lab-wave.html>.

Davies, M. J. S., Graham, J. M. R., & Bearman, P. W. (1990, November). In-Line Forces On Fixed Cylinders In Regular And Random Waves. In *Environmental Forces on Offshore Structures and Their Predictions*: Advances in Underwater Technology, Vol. 26 Kluwer Academic Publishers (1990), pp. 113–136

Davies, M.H., Laurich, P.H., Mansard, E.P.D., & Miles, M.D. (1992). A New Wave Research Flume at NRC. Tech. Ottawa. Print.

DNV (2011). Recommended Practice DNV-RP-H103. Modelling and Analysis of Marine Operations.

Easson, W. J., & Greated, C. A. (1984). Breaking wave forces and velocity fields. *Coastal Engineering*, 8(3), 233-241.

Gran, S. (1973). Wave forces on submerged cylinders. In *Offshore Technology Conference*. Houston, Paper No. OTC 1817, April-May, 1973, pp. 801-812.

Goda, Y. (1973). Wave forces on circular cylinders erected upon reefs. *Coastal engineering in Japan*, *16*, 137-146.

Goda, Y., 1985: Random Sea and Design of Maritime Structures. University of Tokyo Press

Hildebrandt, A., Sparboom, U., & Oumeraci, H. (2008). Wave Forces on Groups of Slender Cylinders in Comparison to an Isolated Cylinder Due to Nonbreaking Waves. In *Proceedings of the International Conference on Coastal Engineering*. Hamburg, Germany. 3770-3781.

Hoerner, S. F. (1965). *Fluid-dynamic drag: practical information on aerodynamic drag and hydrodynamic resistance*. Hoerner Fluid Dynamics.

Hughes, S. A. (1993). *Physical models and laboratory techniques in coastal engineering* (Vol. 7). World Scientific Publishing Company Incorporated.

Hur, D. S., & Mizutani, N. (2003). Numerical estimation of the wave forces acting on a three-dimensional body on submerged breakwater. *Coastal Engineering*, *47*(3), 329-345.

Isaacson, M. (1979). Wave induced forces in the diffraction regime. *Mechanics of Wave-Induced Forces on Cylinders.* Ed. By TJ Shaw, Pitman, San Francisco.

Isaacson, M., Baldwin, J., & Niwinski, C. (1991). Estimation of drag and inertia coefficients from random wave data. *Journal of Offshore Mechanics and Arctic Engineering*, *113*, 128.

Jonkman, .J.M., Buhl, M.L. Jr. (2005). FAST user's guide. Tech. rep. NREL/EL-500-38230; Golden (CO): National Renewable Energy Laboratory.

Kakuno, S., Nakata, Y., & Liu, P. L. F. (1996). Wave forces on an array of vertical cylinders. *Journal of waterway, port, coastal, and ocean engineering*, 122 (3), 147-149.

Kenyon, K. E., & Sheres, D. (1990). Stable gravity wave of arbitrary amplitude in finite depth. *International Journal of Theoretical Physics*, 29(1), 101-108.

Keulegan, G.H., Carpenter, L.H. (1956), Forces on cylinders and plates in an oscillating fluid, NBS Report No. 4821*, National Bureau of Standards*, Washington, D.C.

Kudeih, M., Cornett, A., & Nistor, I. (2010). An Experimental Study of Wave and Current-Induced Forces on a Compact Linear Array of Vertical Cylinders in Shallow Water. In *Proceedings of the International Conference on Coastal Engineering*. Shanghai, China, 2010.

Kyte, A., & Tørum, A. (1996). Wave forces on vertical cylinders upon shoals. *Coastal Engineering*, *27*(3), 263-286.

Larson, L.E., Dallas, I. Downs., Southern California Edison Company (1975). *Water Intake Structure*. Rosemead, Calif., assignee. Patent 3927534.

Lian, W. (1988). A numerical study of two-dimensional separated flow past bluff bodies at moderate KC-numbers. *Applied Ocean Research*, *10*(3), 114-119.

Marino, E., Borri, C., & Peil, U. (2011). A fully nonlinear wave model to account for breaking wave impact loads on offshore wind turbines. *Journal of Wind Engineering and Industrial Aerodynamics*, *99*(4), 483-490.

McCowan, J. (1894). XXXIX. On the highest wave of permanent type. *The London, Edinburgh, and Dublin Philosophical Magazine and Journal of Science*, *38*(233), 351-358.

Mogridge, G., Jamieson, W., (1978). Non-Breaking and Breaking Wave Loads on a Cooling Water Outfall. *Proceedings of the International Conference on Coastal Engineering*. Hamburg, Germany, 1978. 2461-2480.

Morison, J. R., O'Brien, M. P., Johnson, J. W., Schaaf, S. A. (1950). The force exerted by surface waves on piles. *Petroleum Transactions (American Institute of Mining Engineers)*, 189, 149–154.

Parkinson, G. V. (1974). Mathematical models of flow-induced vibrations of bluff bodies. *Flow-induced structural vibrations*.(A 75-15253 04-39) Berlin, Springer-Verlag, 1974,, 81-127.

Rance, P.J. (1969, March). The Influence of Reynolds Number on Wave Forces. Conference Proceedings Hosted by TU Delft Library. *Symposium "Research on Wave Action*. Delft, The Netherlands, March 24-26, 1969, Delft.

Sarpkaya, T. (1979). Hydrodynamic forces on various multiple tube riser configurations. In *Eleventh Offshore Technology Conference*. Houston, USA. Houston: OTC. 1603-1606.

Sarpkaya, T. (2006). Structures of separation on a circular cylinder in periodic flow. *Journal of Fluid Mechanics*, *567*, 281-297.

Sarpkaya, T. (2010). Wave Forces on Offshore Structures. Cambridge University Press.

Sarpkaya, T., & Shoaff, R. L. (1979). An inviscid model of two dimensional vortex shedding for transient and asymptotically steady separated flow over a cylinder. In *American Institute of Aeronautics and Astronautics, Aerospace Sciences Meeting,* 17 th, New Orleans, La (p. 1979).

Sarpkaya, T., & Tuter, O. (1974). Periodic flow about bluff bodies. Part 1: Forces on cylinders and spheres in a sinusoidally oscillating fluid. *Technical Report, Sep. 1973-1974 Naval Postgraduate School*, Monterey, CA., 1.

Schlichting, H., & Shapiro, A. H. (1968). Boundary layer theory. *Journal of Applied Mechanics*, *35*, 846.

Schmidt, D. W. von & Tilmann, P. M., (1972). Uber die zirkulationsentwicklung in nachlaufen von rundstaben. *Acoustics* 27, 14–22.

Sparboom, U., Oumeraci, H., Schmidt-Koppenhagen, R., Grüne, J. (2005). Large-Scale Model Study on Cylinder Groups Subject to Breaking and Nonbreaking Waves. *Proceedings of Fifth International Symposium WAVES 2005*. Madrid, Spain. 106.

Sumer, B. M., & Fredsøe, J. (1997). *Hydrodynamics around cylindrical structures* (Vol. 12). World Scientific Publishing Company Incorporated.

Wolfram, J., Naghipour, M. (1999). On the estimation of Morison force coefficients and their predictive accuracy for very rough circular cylinders. *Applied Ocean Research*, 21, 311-328.

Zdravkovich, M. M. (1977). Review of Flow Interference between Two Circular Cylinders in Various Arrangements. *Journal of Fluids Engineering, Trans. ASME*, 99, 618-633.

Appendix

Force Coefficient Fitting Plots

All plots of the Morison equation fitted to regular wave forcing on the structure for purposes of force coefficient determination are presented in this appendix. The force coefficients corresponding to each plot are available in Table 6.4 of the Force Coefficient Analysis section. The test number in the title of each plot corresponds to a regular wave test in Table 4.1 of the Experimental Methodology section. These plots displayed the quality of fit for each set of force coefficients used in the Predicting Forcing from Irregular Waves section.

Central Pipe Force Coefficients

The following plots are of the Morison equation fitted to forcing on the central pipe (configuration 2) from all regular wave tests.

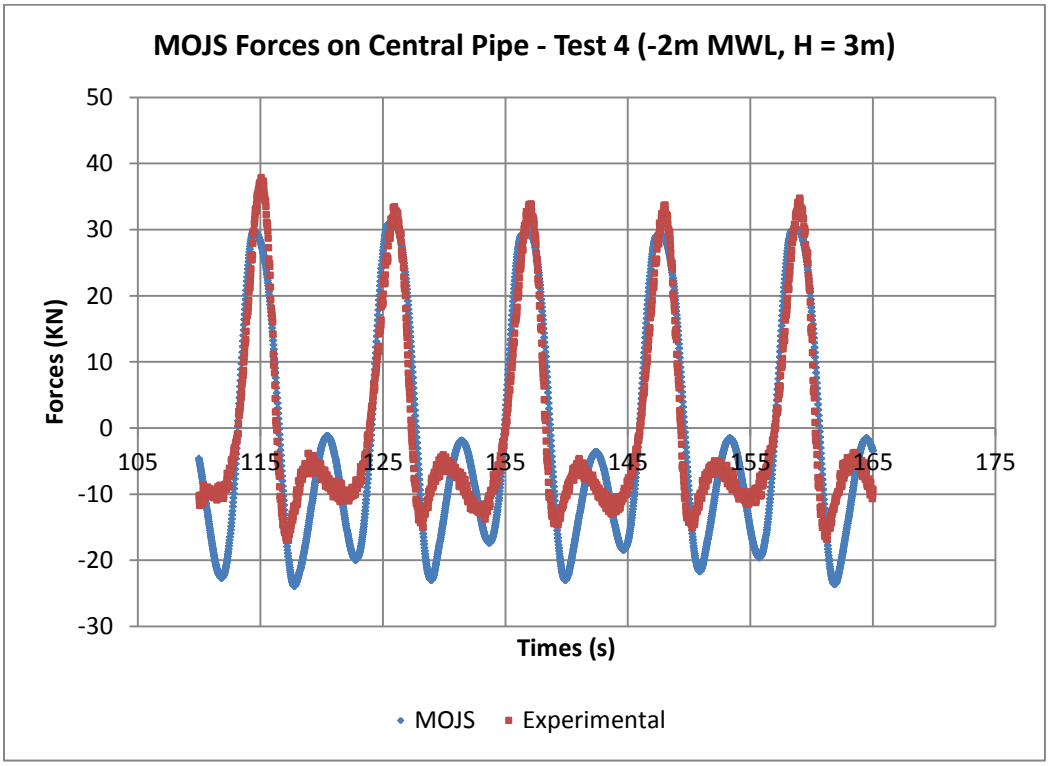

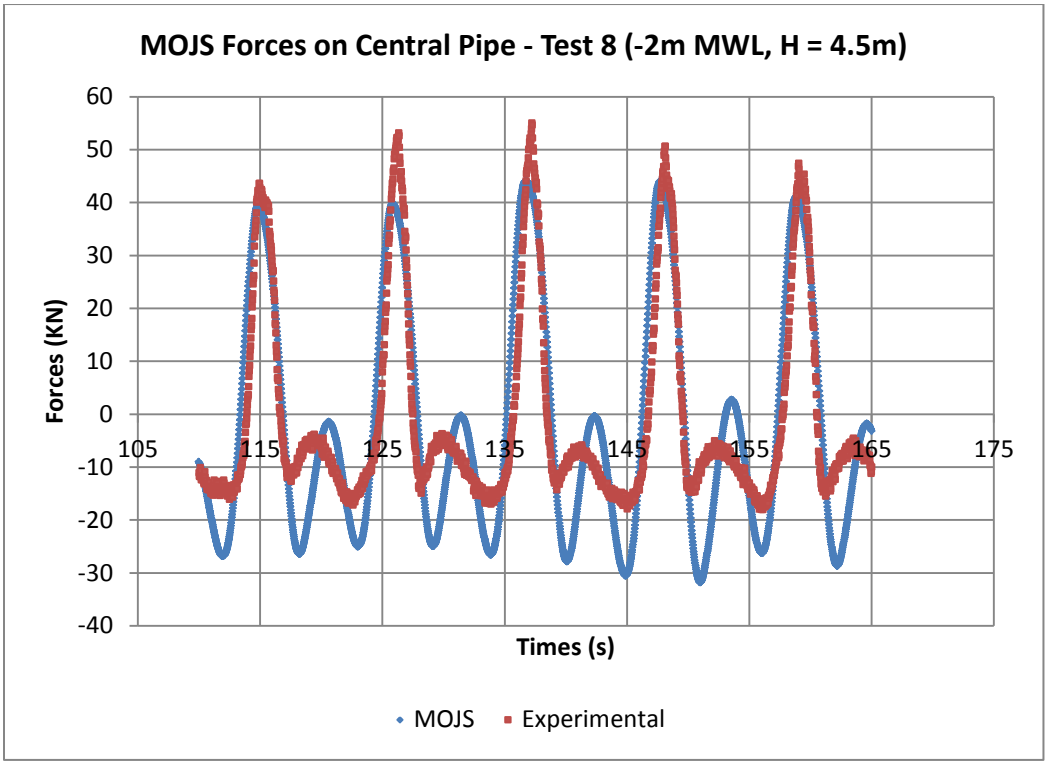
MOJS Forces on Central Pipe - Test 8 (-2m MWL, H = 4.5m)
Forces (KN)
60
50
40
30
20
10
0
-10
-20
-30
-40
105
115
125
135
145
155
165
175
Times (s)
MOJS
Experimental

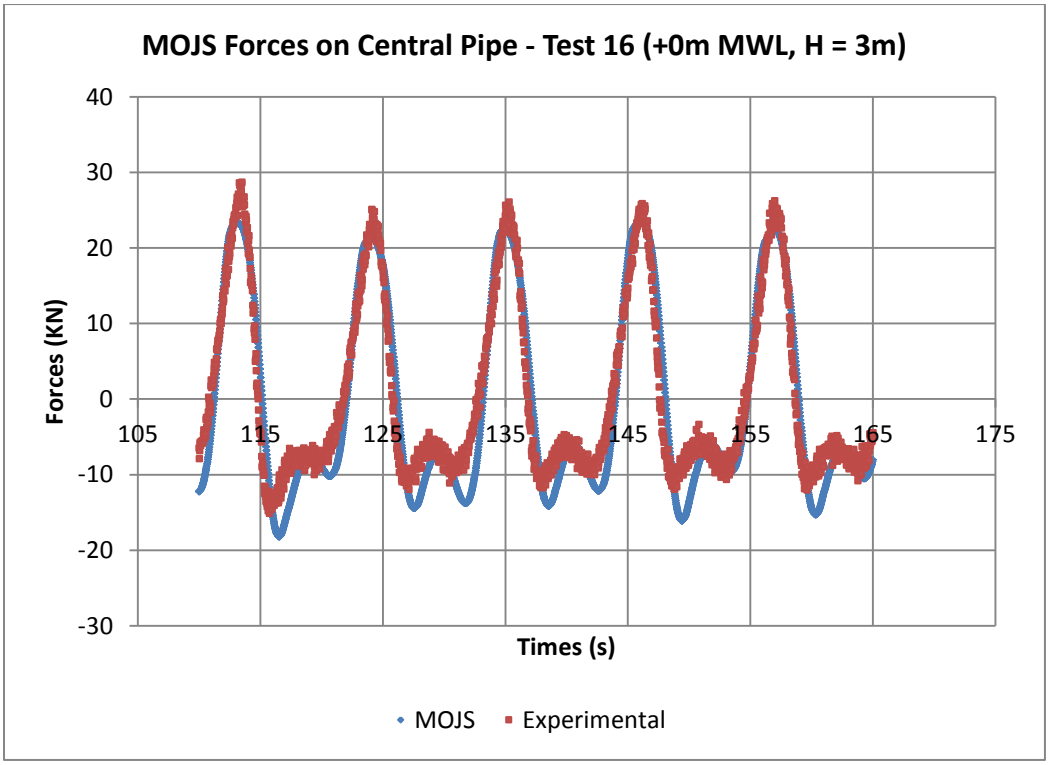
MOJS Forces on Central Pipe - Test 16 (+0m MWL, H = 3m)
Forces (KN)
40
30
20
10
0
-10
-20
-30
105
115
125
135
145
155
165
175
Times (s)
MOJS
Experimental

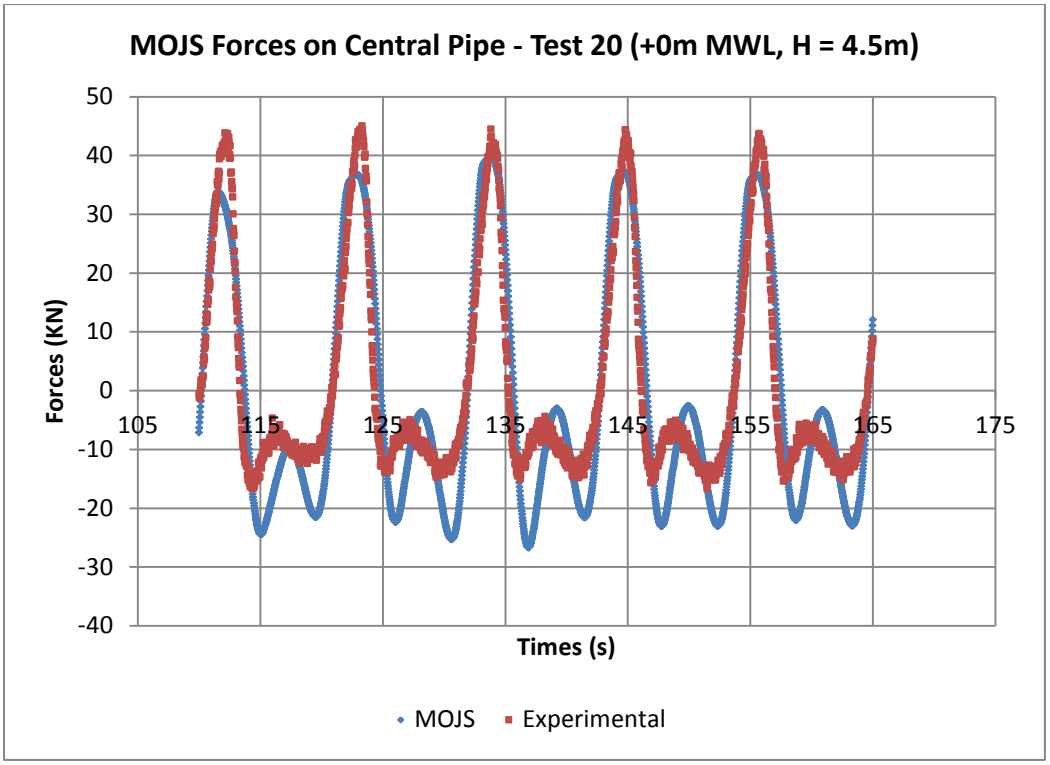
MOJS Forces on Central Pipe - Test 20 (+0m MWL, H = 4.5m)
Forces (KN)
50
40
30
20
10
0
-10
-20
-30
-40
105
115
125
135
145
155
165
175
Times (s)
MOJS
Experimental

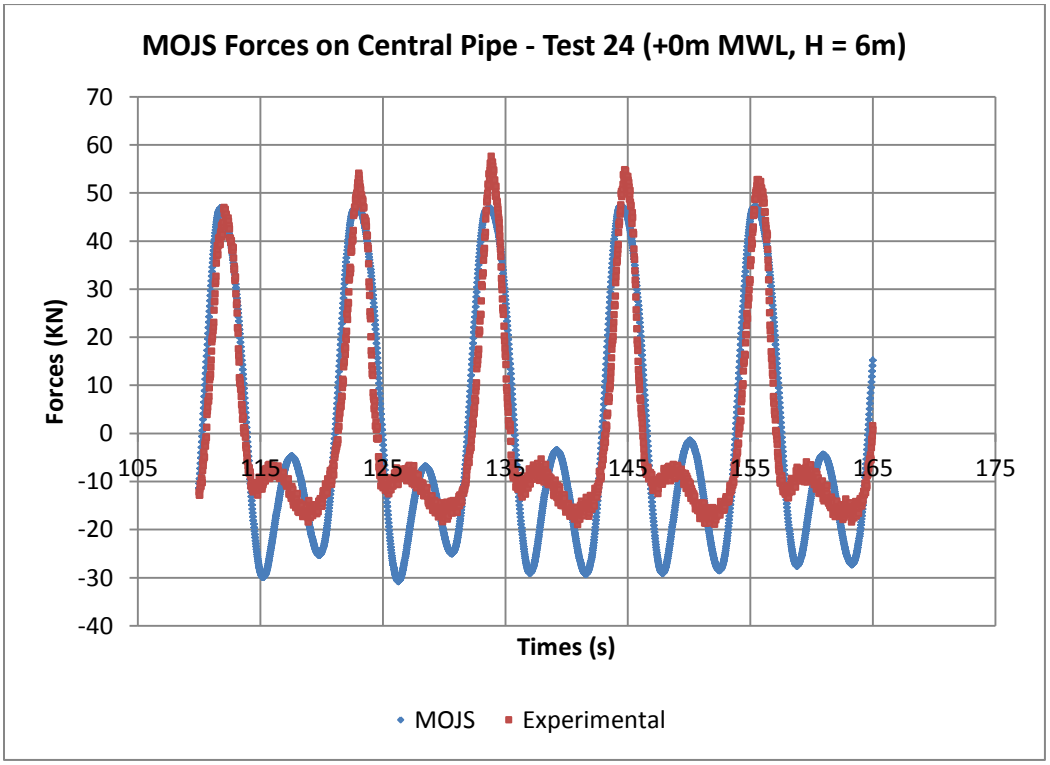
MOJS Forces on Central Pipe - Test 24 (+0m MWL, H = 6m)
Forces (KN)
70
60
50
40
30
20
10
0
-10
-20
-30
-40
105
115
125
135
145
155
165
175
Times (s)
MOJS
Experimental

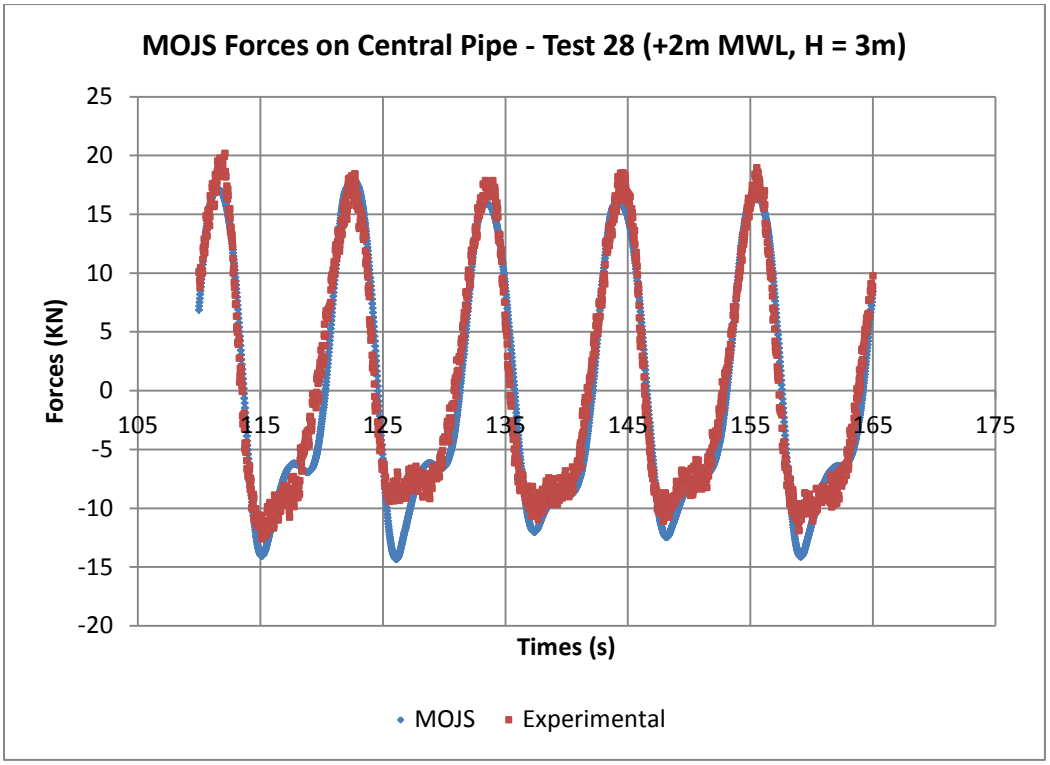
MOJS Forces on Central Pipe - Test 28 (+2m MWL, H = 3m)
Forces (KN)
25
20
15
10
5
0
-5
-10
-15
-20
105
115
125
135
145
155
165
175
Times (s)
MOJS
Experimental

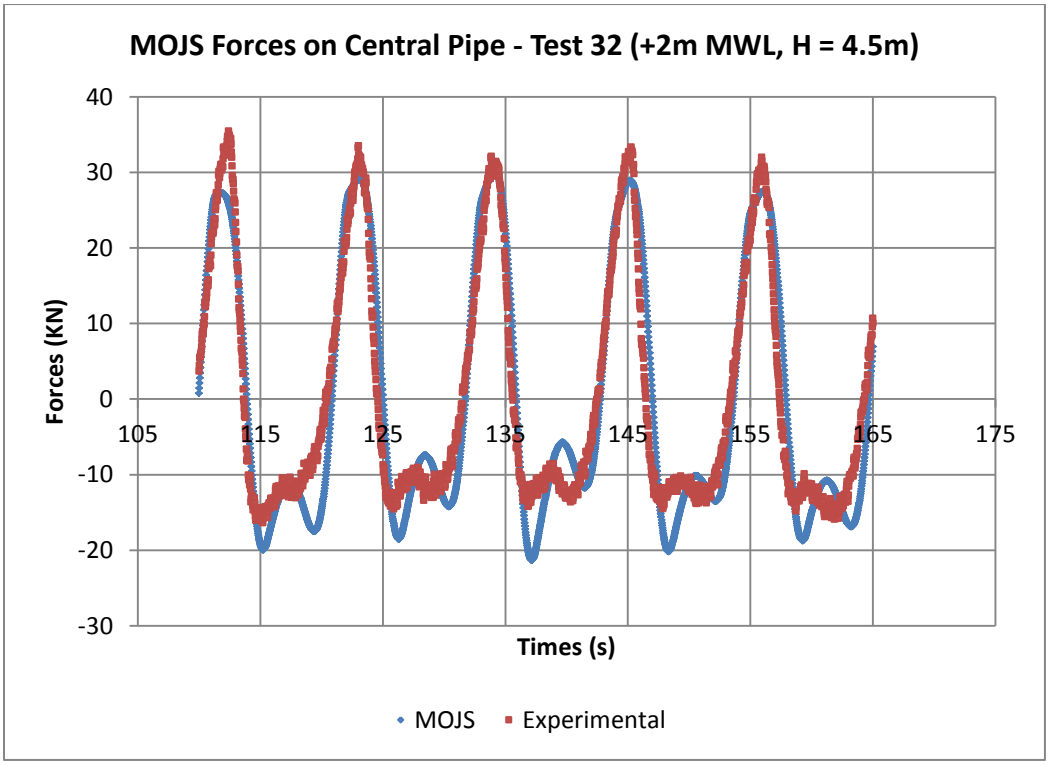
MOJS Forces on Central Pipe - Test 32 (+2m MWL, H = 4.5m)
Forces (KN)
40
30
20
10
0
-10
-20
-30
105
115
125
135
145
155
165
175
Times (s)
MOJS
Experimental

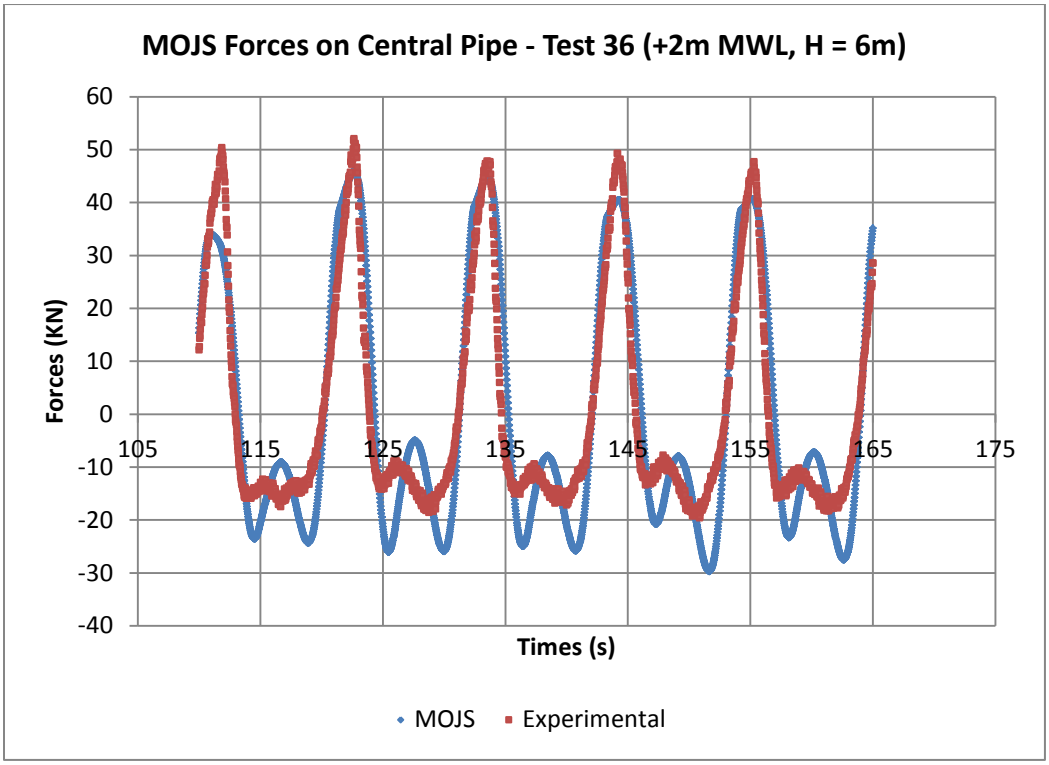

Support Posts Force Coefficients

The following plots are of the Morison equation fitted to forcing on the support posts from all regular wave tests. The values plotted are of forcing on the pipe + posts configuration (3), with the pipe forcing component of the MOJS series being experimental values and the support posts component predicted by the Morison equation using fitted coefficients.

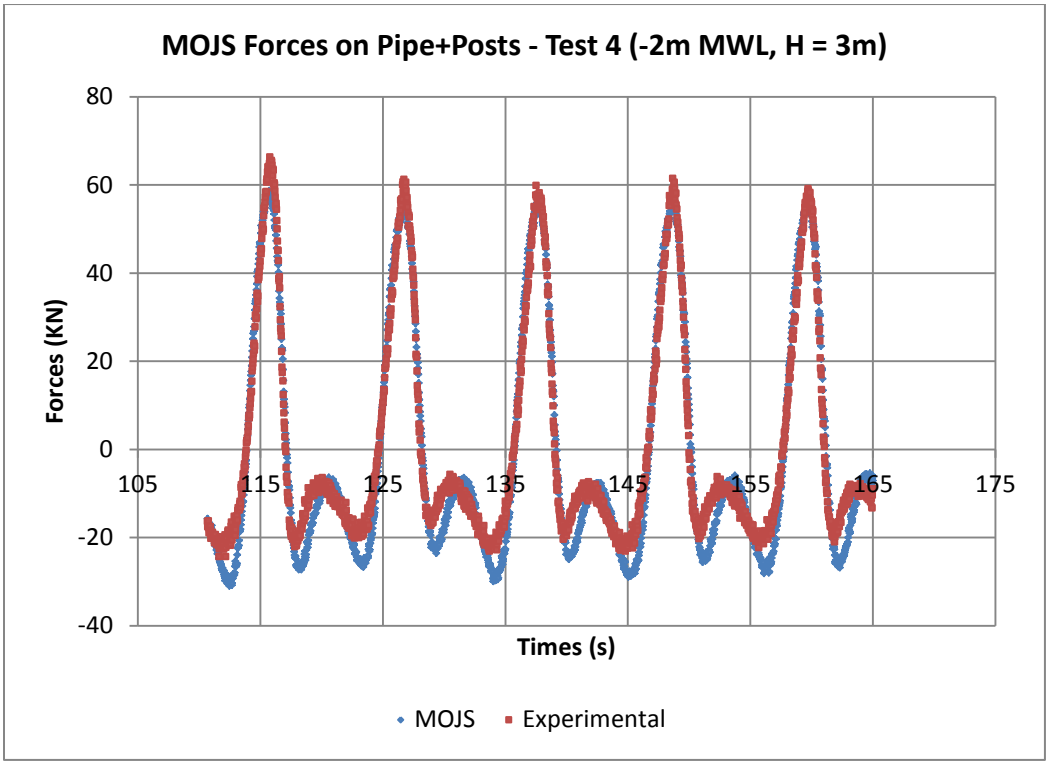
MOJS Forces on Pipe+Posts - Test 4 (-2m MWL, H = 3m)
80
60
40
20
0
-20
-40
105
115
125
135
145
155
165
175
Forces (KN)
Times (s)
MOJS
Experimental

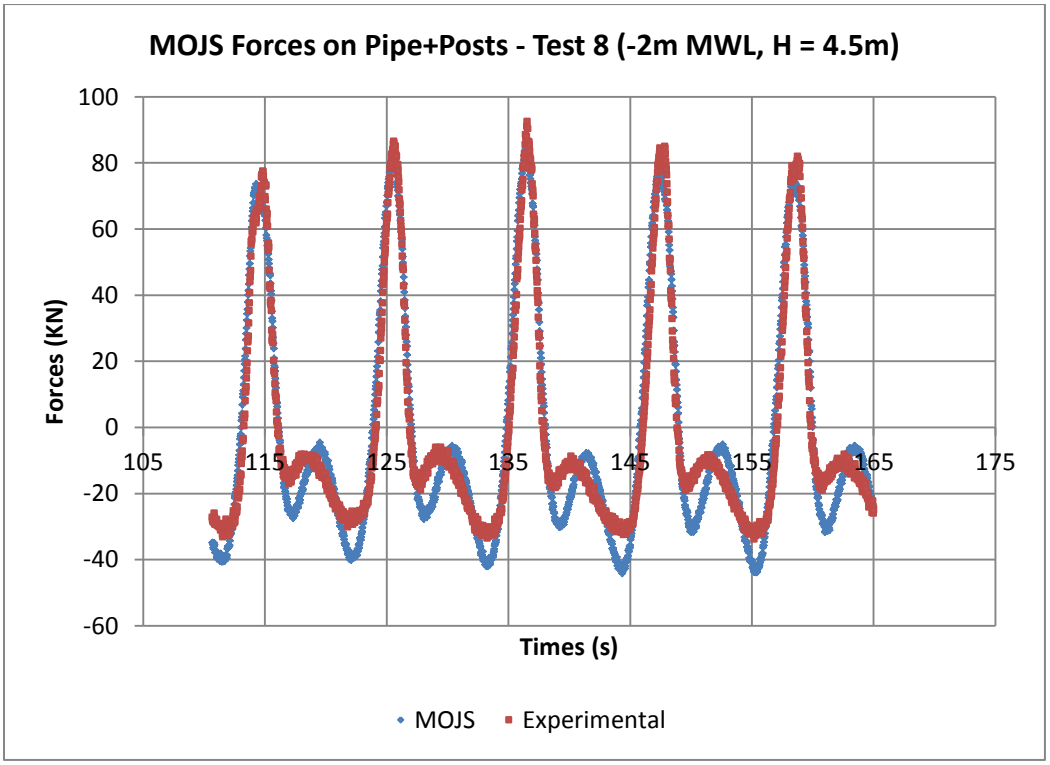
MOJS Forces on Pipe+Posts - Test 8 (-2m MWL, H = 4.5m)
100
80
60
40
20
0
-20
-40
-60
105
115
125
135
145
155
165
175
Forces (KN)
Times (s)
MOJS
Experimental

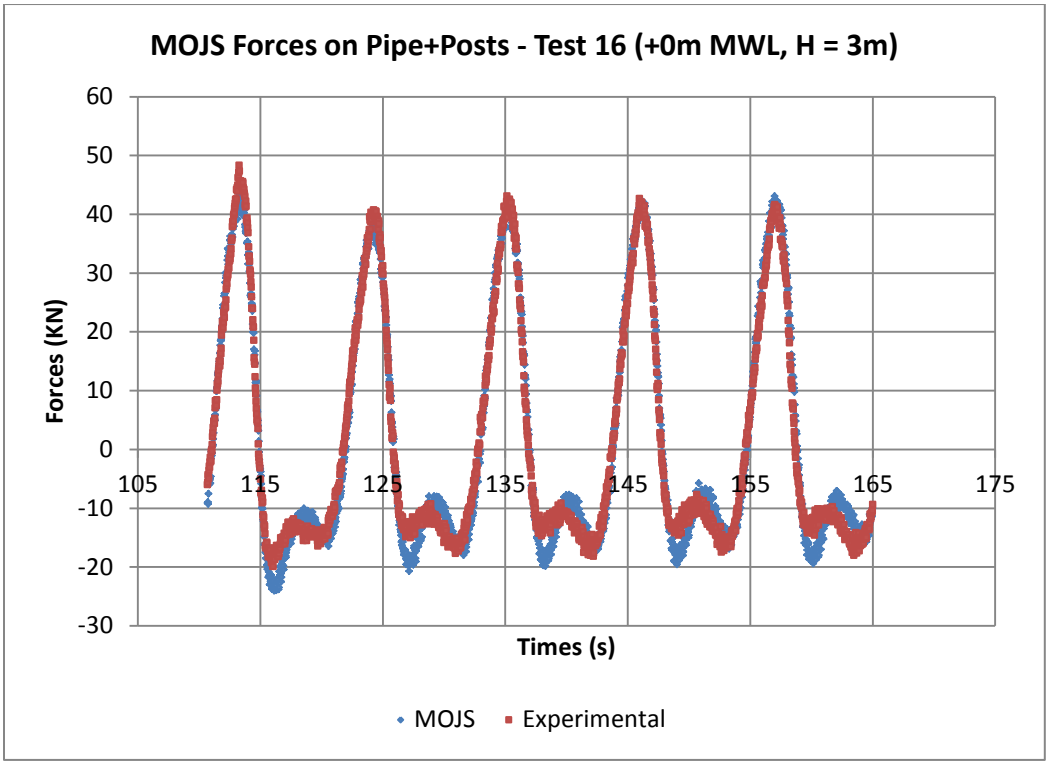
MOJS Forces on Pipe+Posts - Test 16 (+0m MWL, H = 3m)
Forces (KN)
60
50
40
30
20
10
0
-10
-20
-30
105
115
125
135
145
155
165
175
Times (s)
MOJS
Experimental

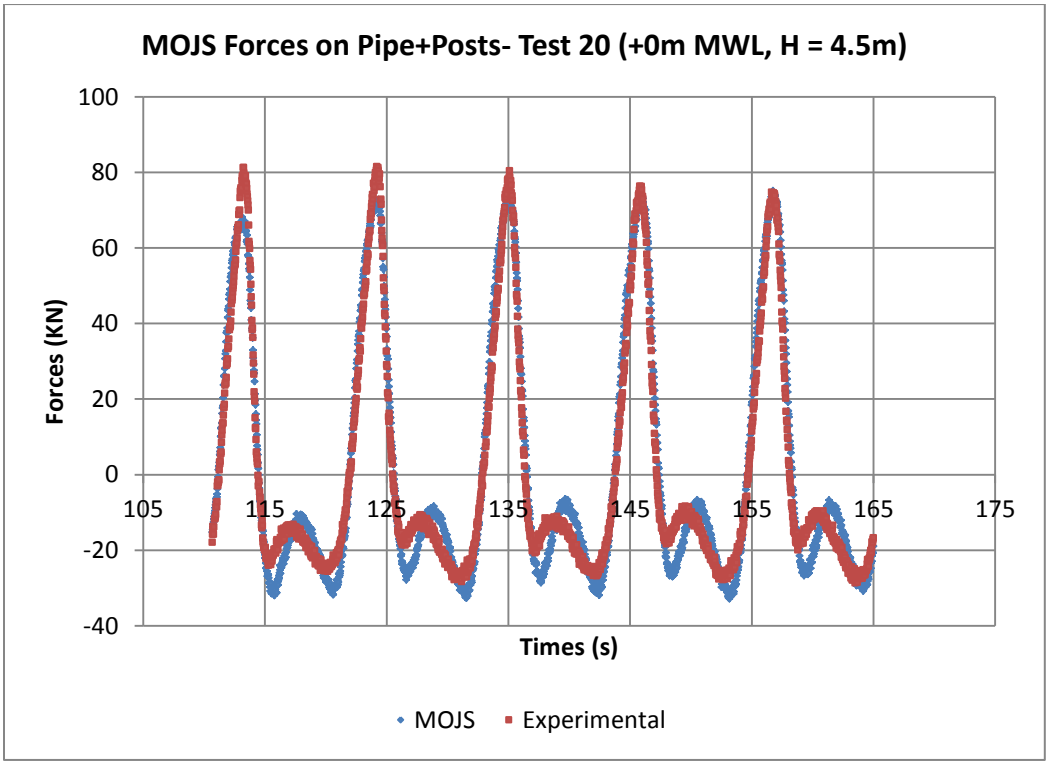
MOJS Forces on Pipe+Posts- Test 20 (+0m MWL, H = 4.5m)
Forces (KN)
100
80
60
40
20
0
-20
-40
105
115
125
135
145
155
165
175
Times (s)
MOJS
Experimental

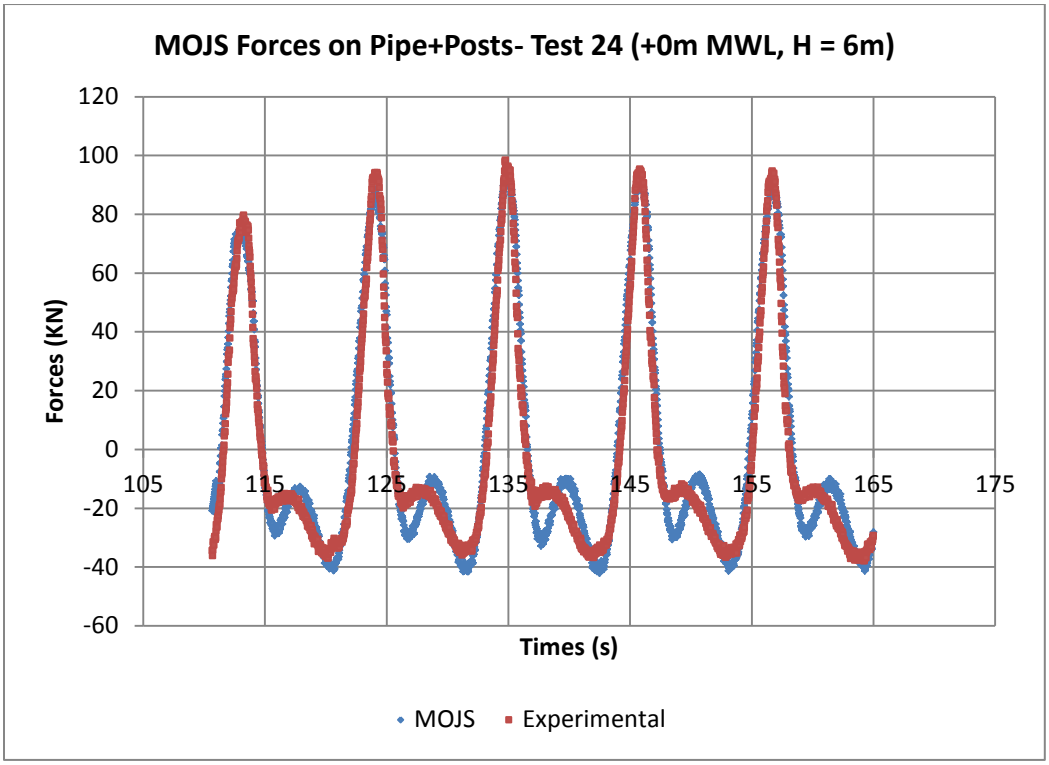
MOJS Forces on Pipe+Posts- Test 24 (+0m MWL, H = 6m)
Forces (KN)
120
100
80
60
40
20
0
-20
-40
-60
105
115
125
135
145
155
165
175
Times (s)
MOJS
Experimental

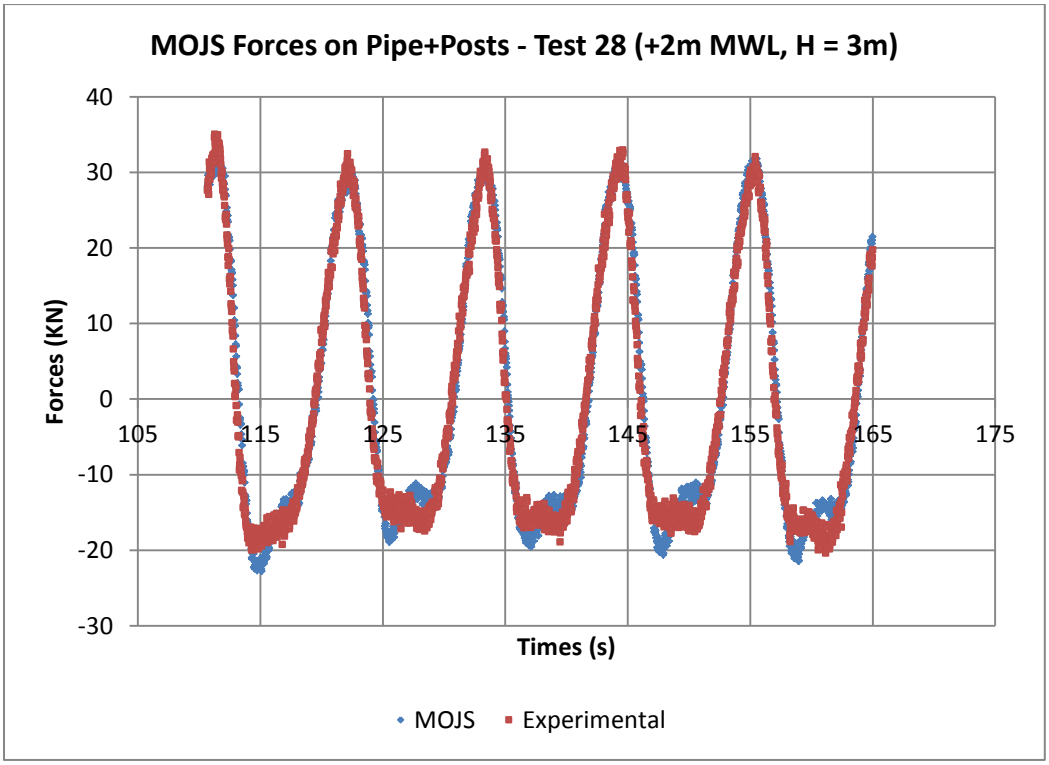
MOJS Forces on Pipe+Posts - Test 28 (+2m MWL, H = 3m)
Forces (KN)
40
30
20
10
0
-10
-20
-30
105
115
125
135
145
155
165
175
Times (s)
MOJS
Experimental

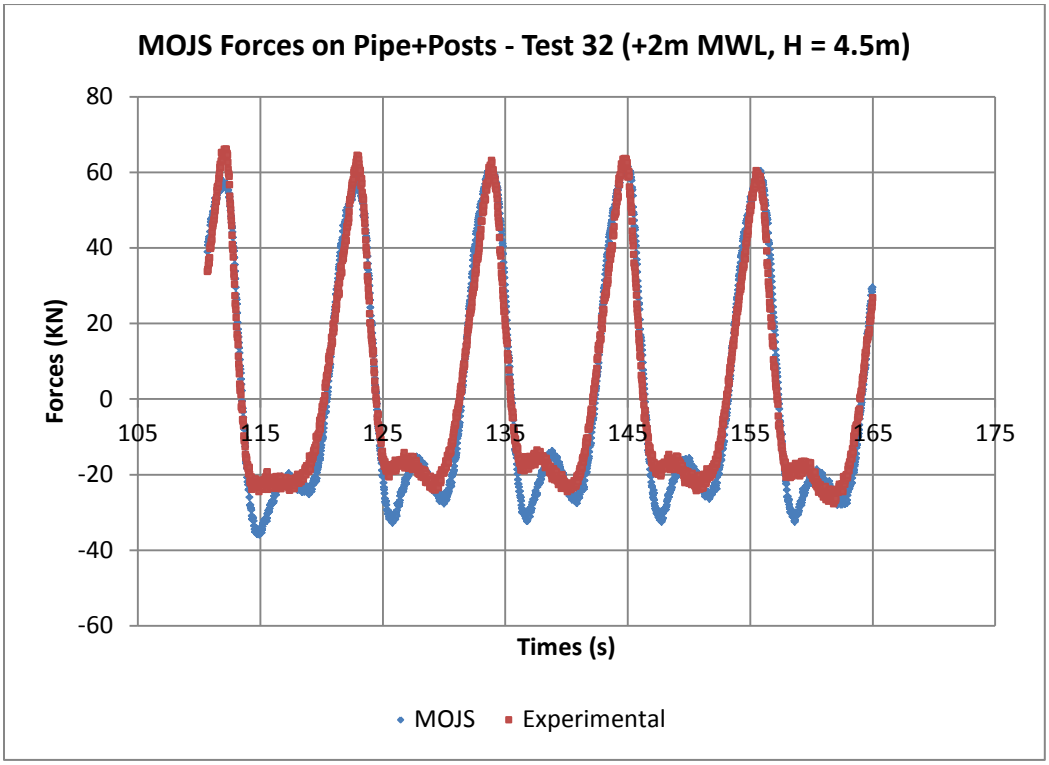
MOJS Forces on Pipe+Posts - Test 32 (+2m MWL, H = 4.5m)
Forces (KN)
80
60
40
20
0
-20
-40
-60
105
115
125
135
145
155
165
175
Times (s)
MOJS
Experimental

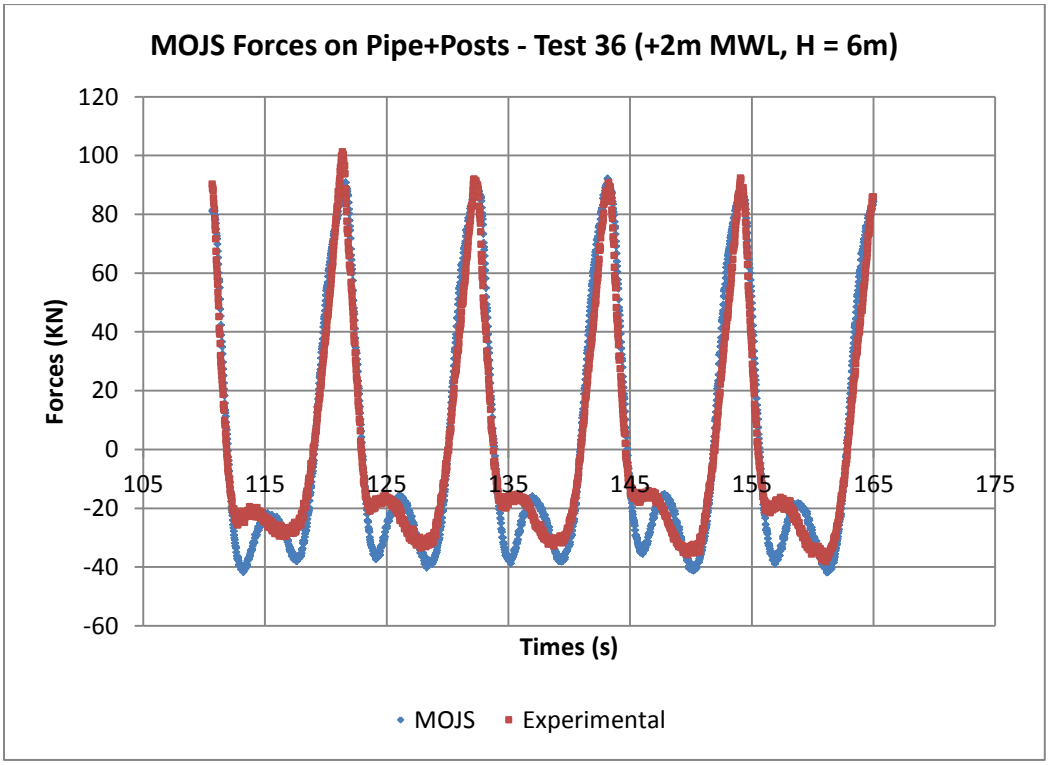
MOJS Forces on Pipe+Posts - Test 36 (+2m MWL, H = 6m)
Forces (KN)
120
100
80
60
40
20
0
-20
-40
-60
105
115
125
135
145
155
165
175
Times (s)
MOJS
Experimental

Full Structure (Configuration 1) Force Coefficients

The following plots are of the Morison equation fitted to forcing on the full structure configuration (1) from all regular wave tests.

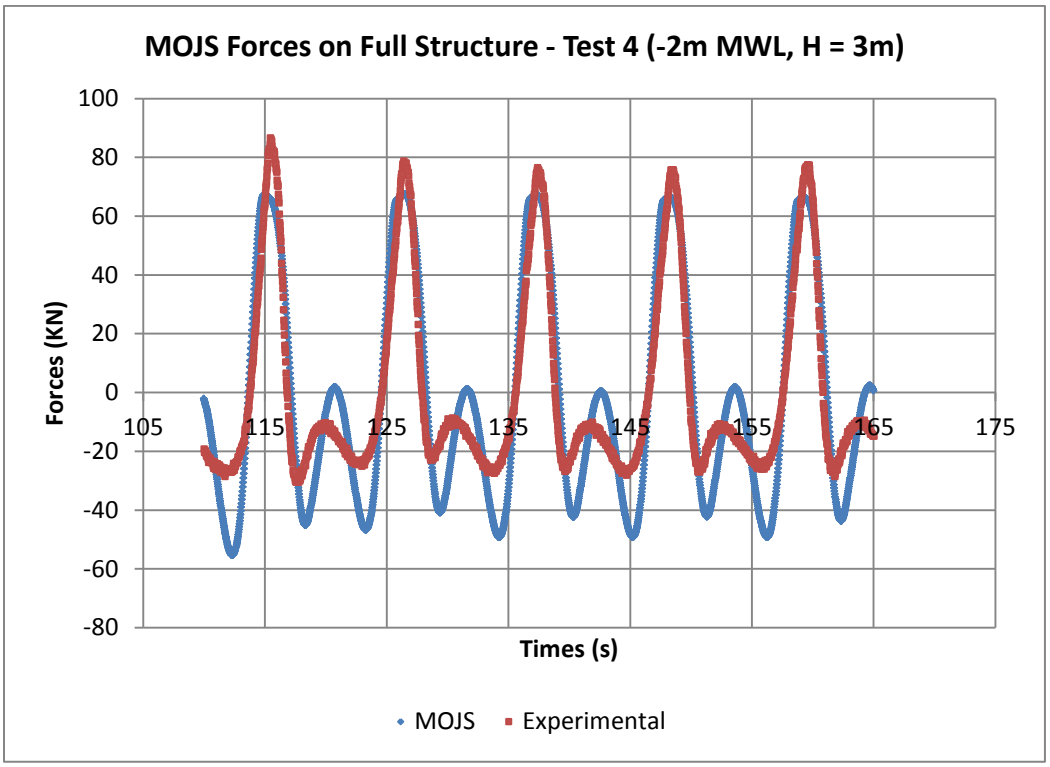

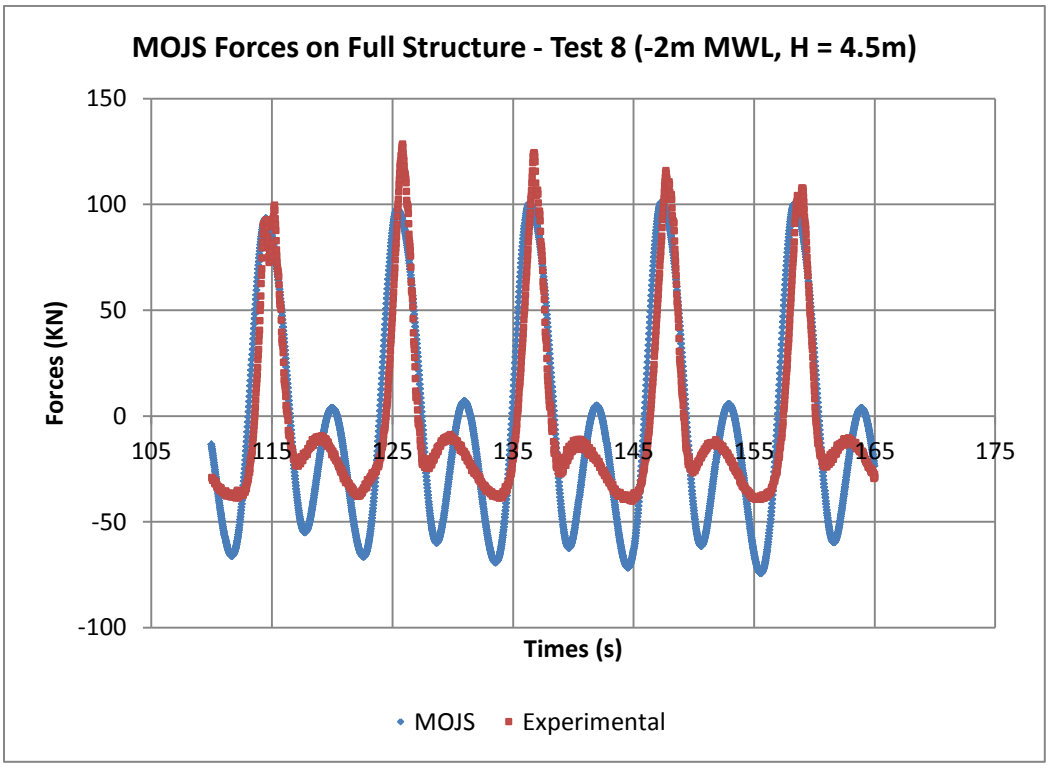

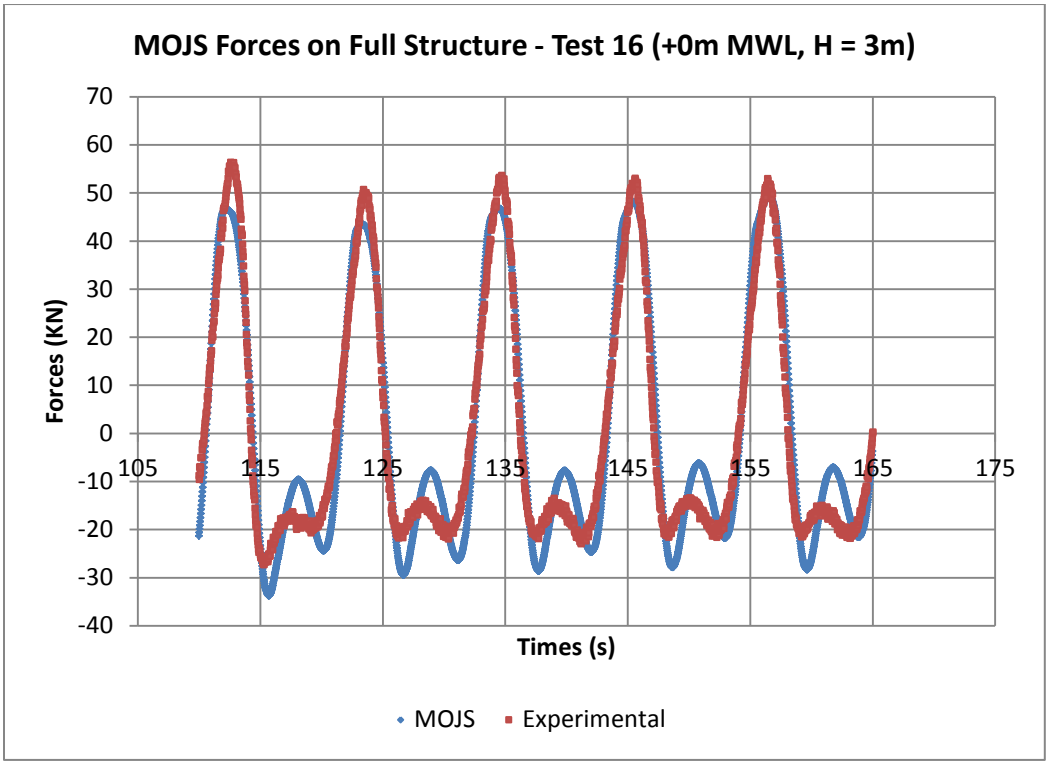
MOJS Forces on Full Structure - Test 16 (+0m MWL, H = 3m)
Forces (KN)
70
60
50
40
30
20
10
0
-10
-20
-30
-40
105
115
125
135
145
155
165
175
Times (s)
MOJS
Experimental

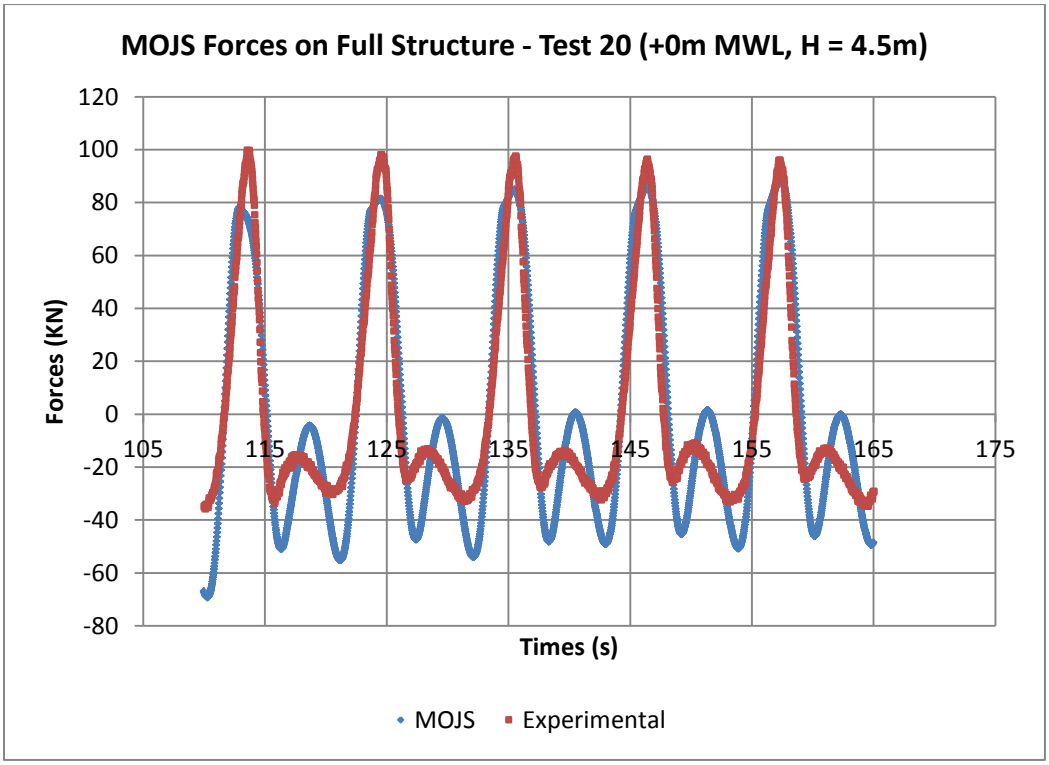
MOJS Forces on Full Structure - Test 20 (+0m MWL, H = 4.5m)
Forces (KN)
120
100
80
60
40
20
0
-20
-40
-60
-80
105
115
125
135
145
155
165
175
Times (s)
MOJS
Experimental

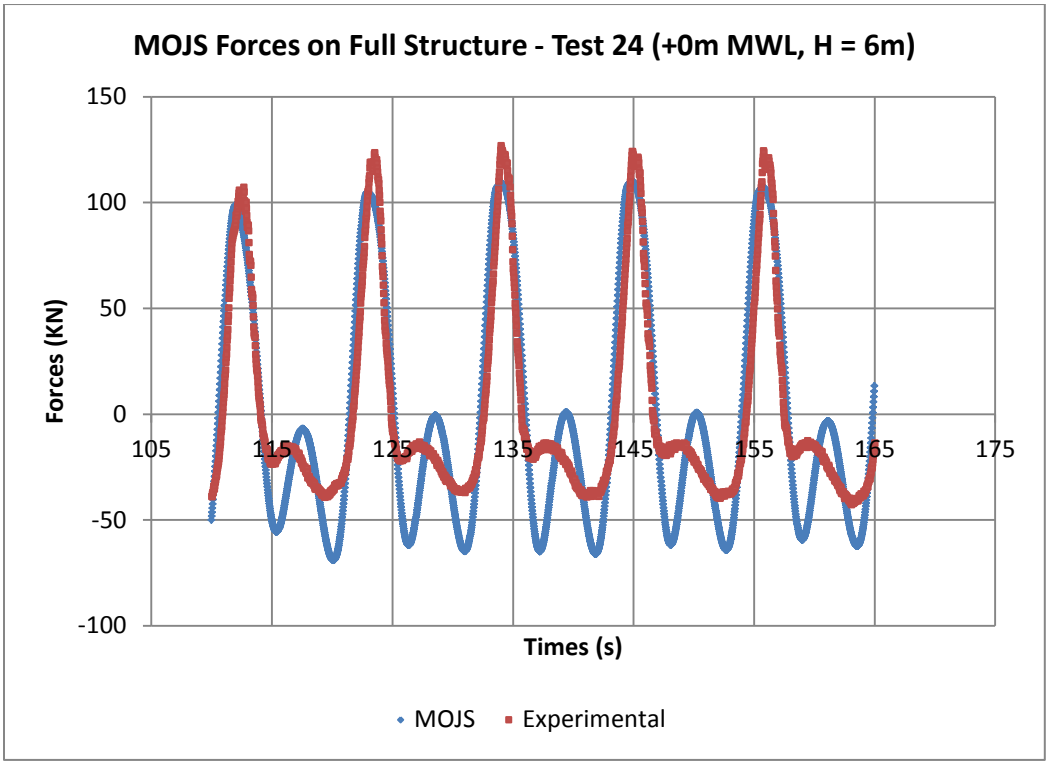
MOJS Forces on Full Structure - Test 24 (+0m MWL, H = 6m)
150
100
50
0
-50
-100
105
115
125
135
145
155
165
175
Forces (KN)
Times (s)
MOJS
Experimental

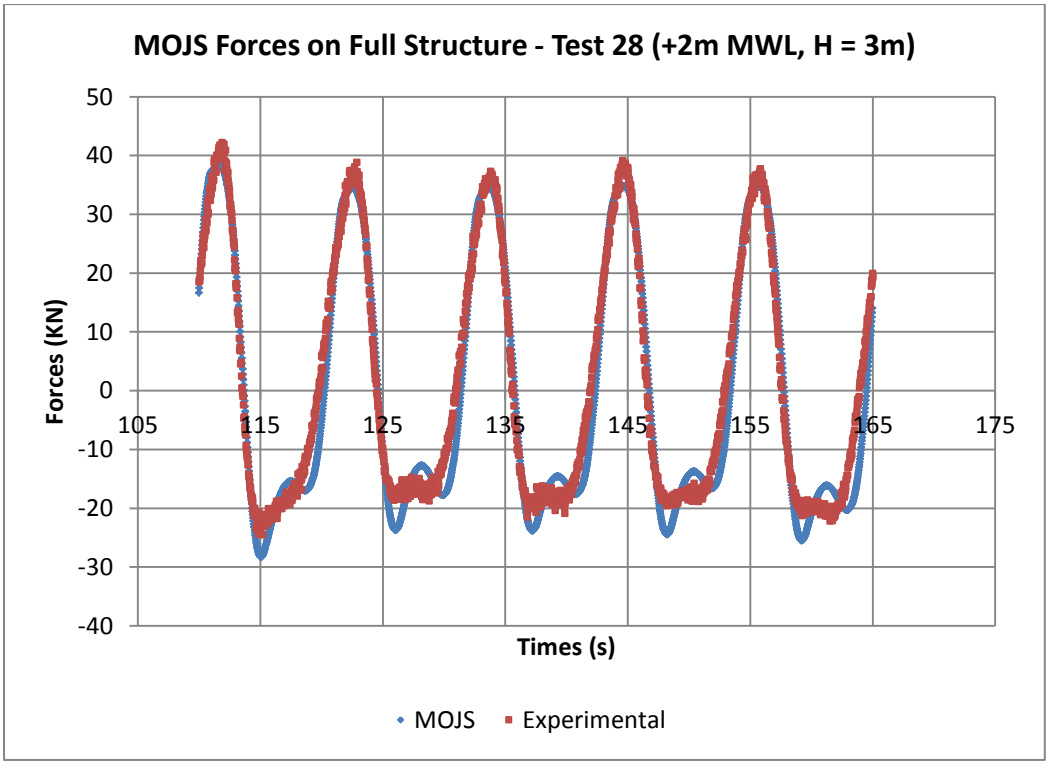
MOJS Forces on Full Structure - Test 28 (+2m MWL, H = 3m)
50
40
30
20
10
0
-10
-20
-30
-40
105
115
125
135
145
155
165
175
Forces (KN)
Times (s)
MOJS
Experimental

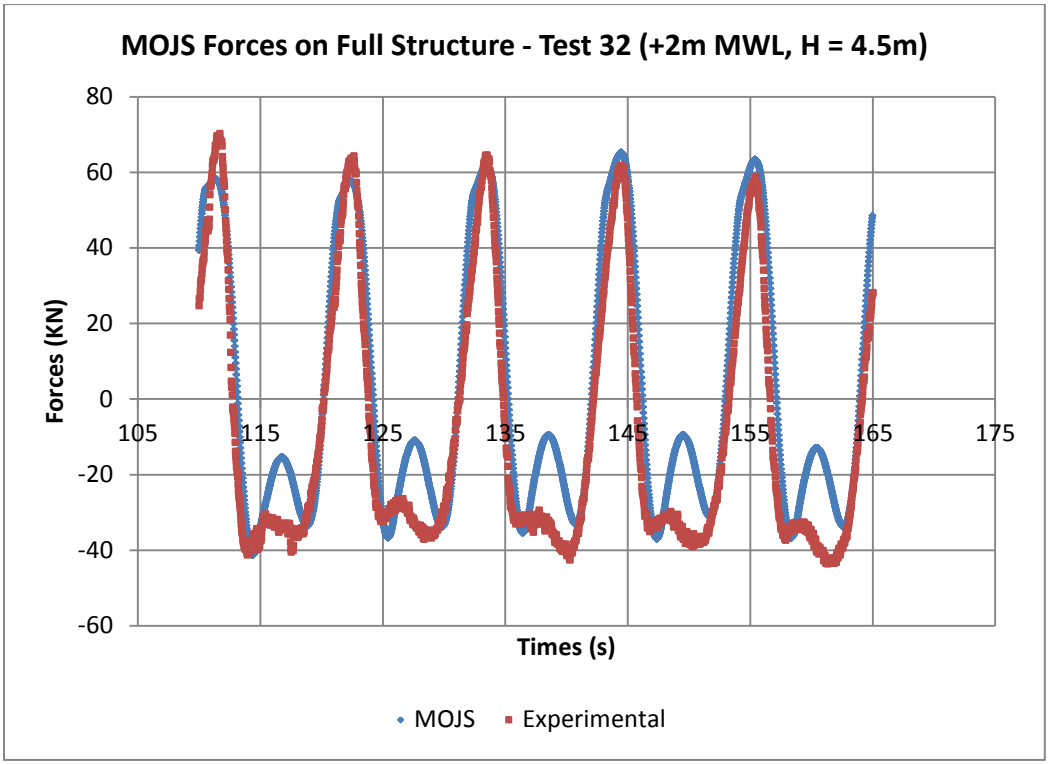
MOJS Forces on Full Structure - Test 32 (+2m MWL, H = 4.5m)
Forces (KN)
80
60
40
20
0
-20
-40
-60
105
115
125
135
145
155
165
175
Times (s)
MOJS
Experimental

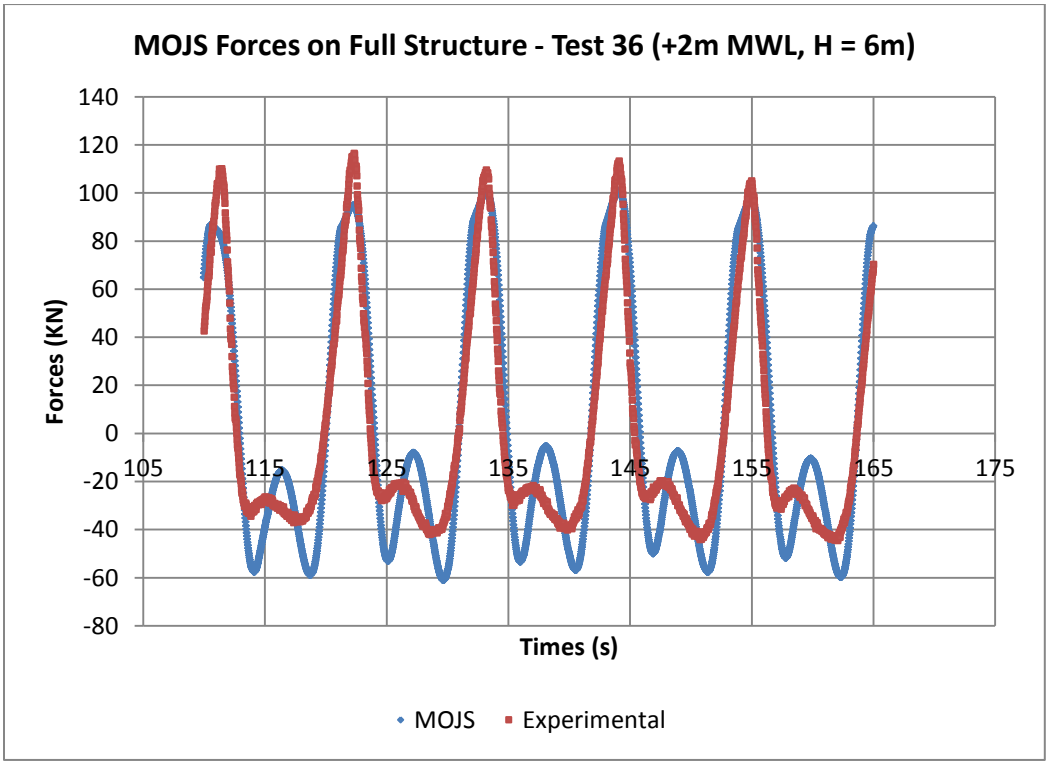
MOJS Forces on Full Structure - Test 36 (+2m MWL, H = 6m)
Forces (KN)
140
120
100
80
60
40
20
0
-20
-40
-60
-80
105
115
125
135
145
155
165
175
Times (s)
MOJS
Experimental

Pipe and Posts (Configuration 3) Force Coefficients

The following plots are of the Morison equation fitted to forcing on the pipe and posts configuration (3) from all regular wave tests.

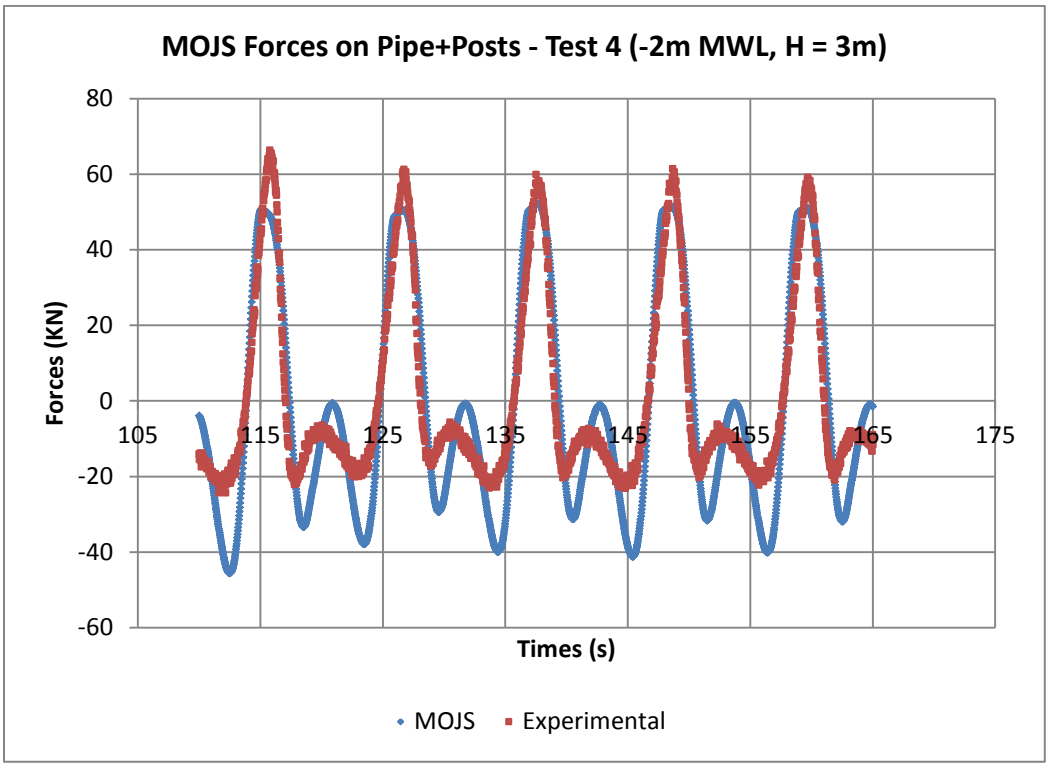

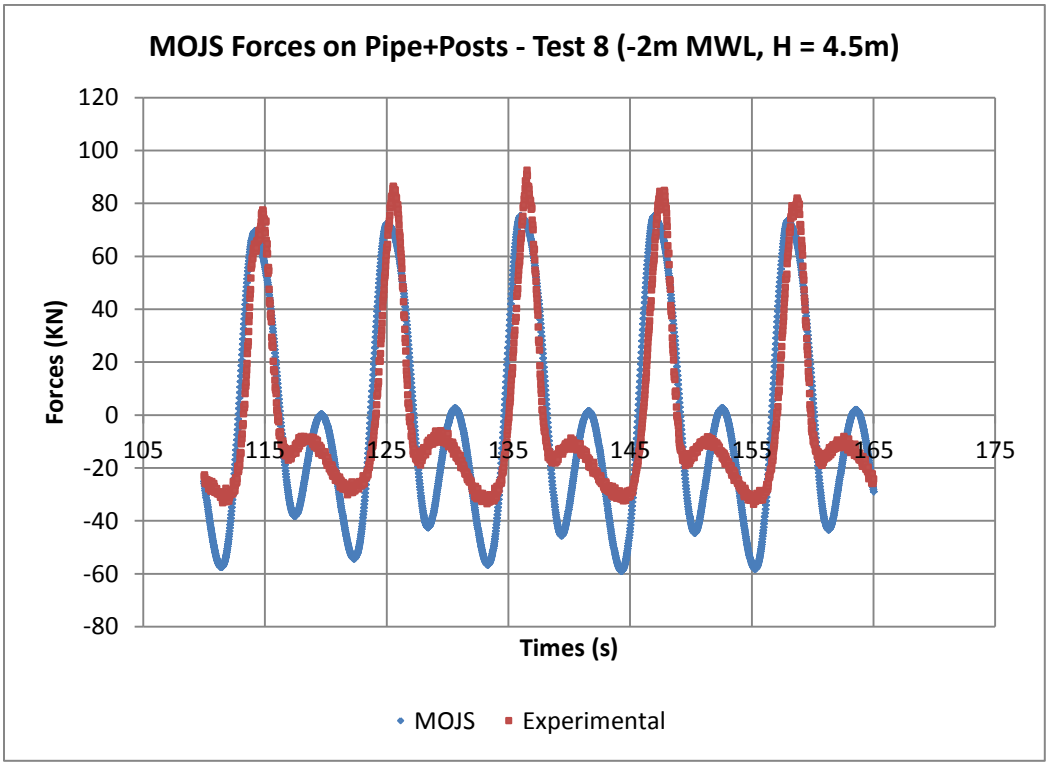

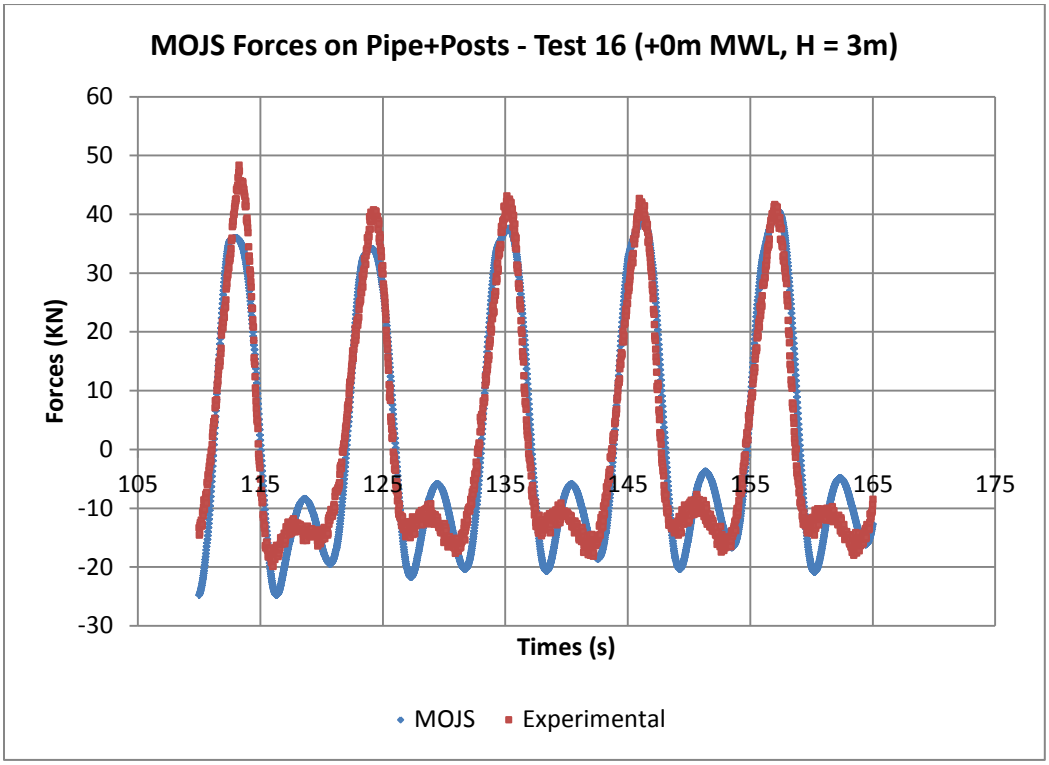
MOJS Forces on Pipe+Posts - Test 16 (+0m MWL, H = 3m)
Forces (KN)
60
50
40
30
20
10
0
-10
-20
-30
105
115
125
135
145
155
165
175
Times (s)
MOJS
Experimental

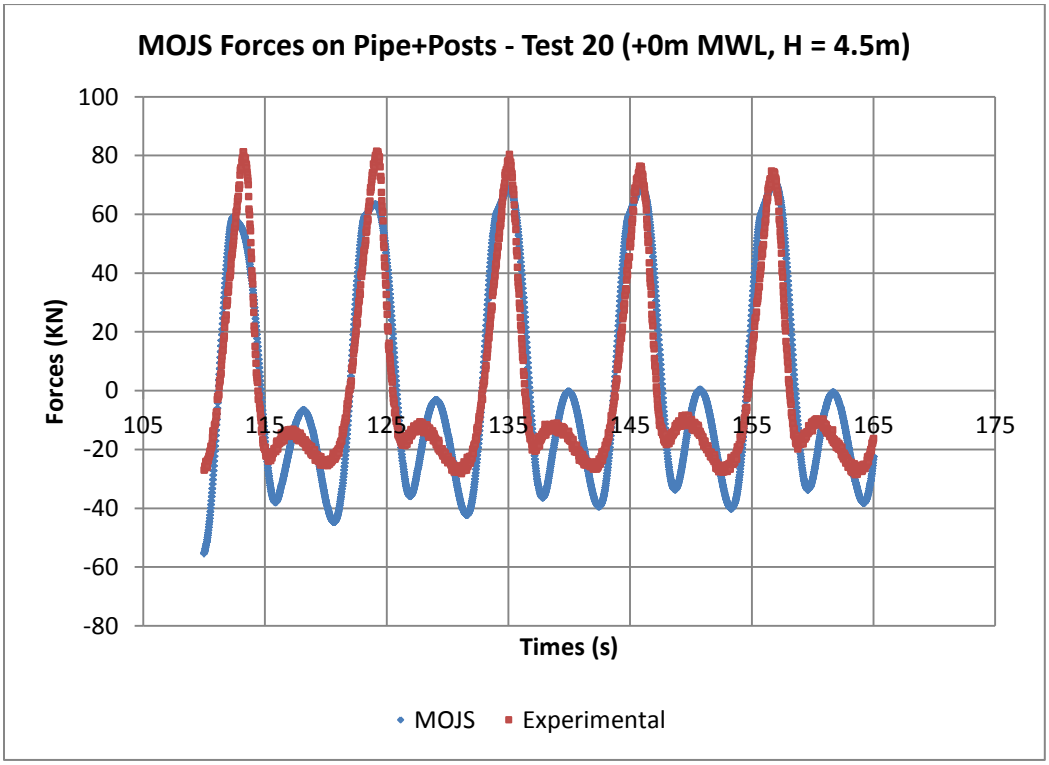
MOJS Forces on Pipe+Posts - Test 20 (+0m MWL, H = 4.5m)
Forces (KN)
100
80
60
40
20
0
-20
-40
-60
-80
105
115
125
135
145
155
165
175
Times (s)
MOJS
Experimental

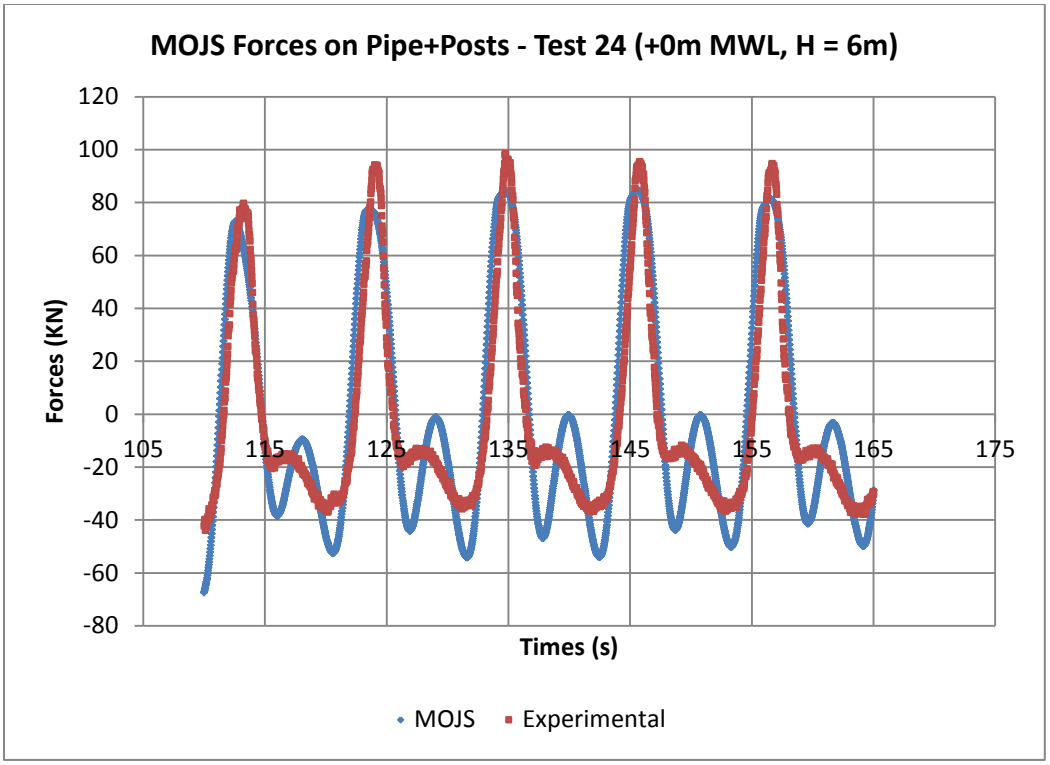
MOJS Forces on Pipe+Posts - Test 24 (+0m MWL, H = 6m)
120
100
80
60
40
20
0
-20
-40
-60
-80
Forces (KN)
105
115
125
135
145
155
165
175
Times (s)
MOJS
Experimental

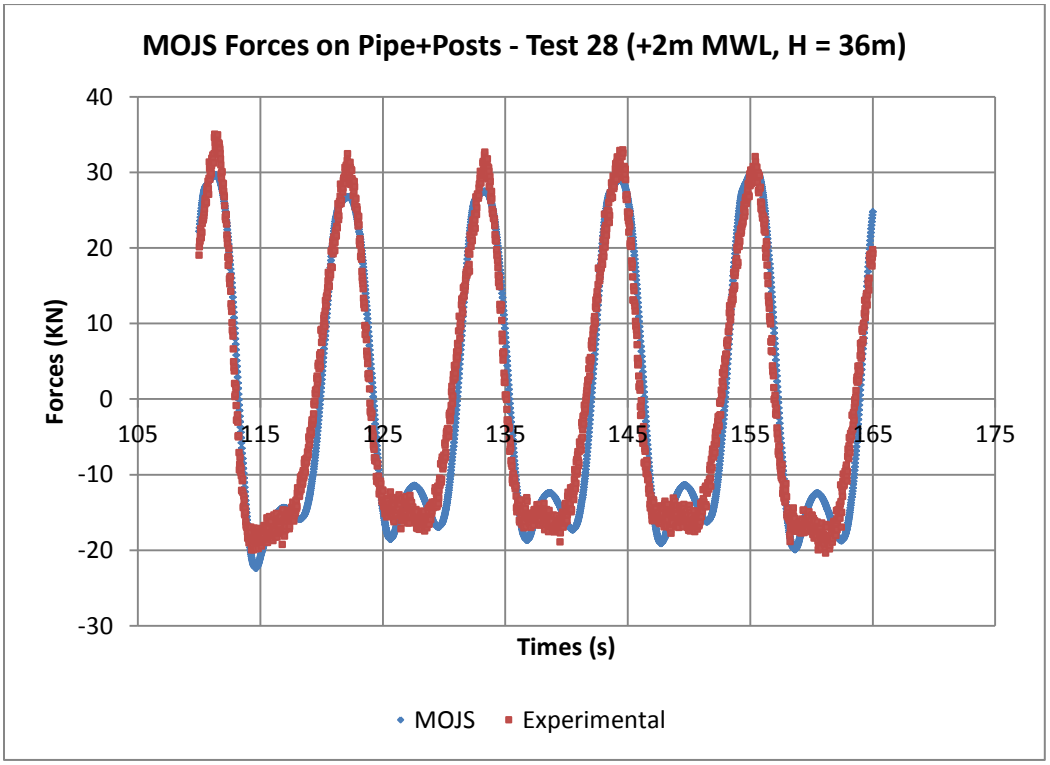
MOJS Forces on Pipe+Posts - Test 28 (+2m MWL, H = 36m)
40
30
20
10
0
-10
-20
-30
Forces (KN)
105
115
125
135
145
155
165
175
Times (s)
MOJS
Experimental

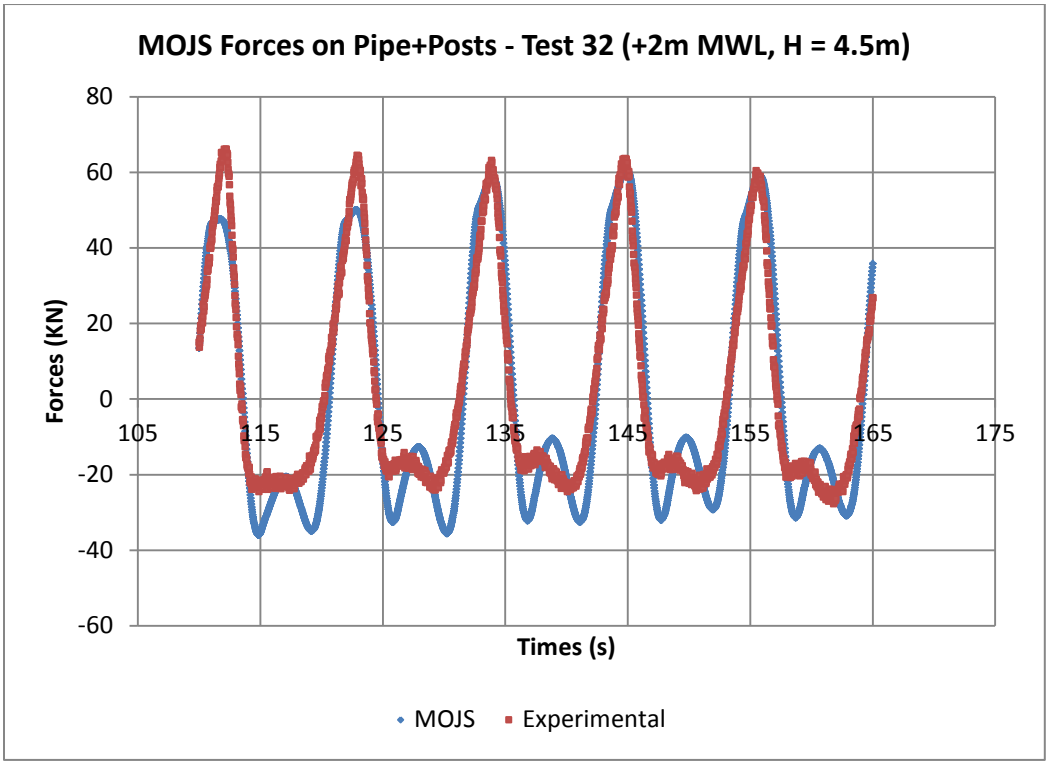
MOJS Forces on Pipe+Posts - Test 32 (+2m MWL, H = 4.5m)
Forces (KN)
80
60
40
20
0
-20
-40
-60
105
115
125
135
145
155
165
175
Times (s)
MOJS
Experimental

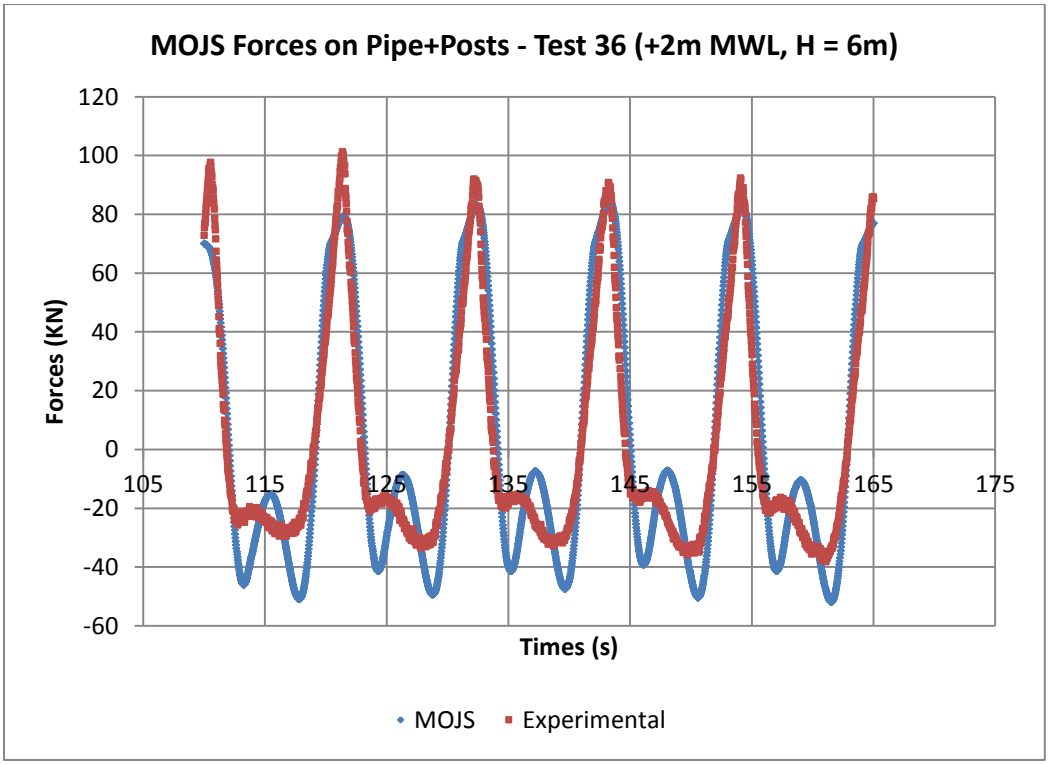
MOJS Forces on Pipe+Posts - Test 36 (+2m MWL, H = 6m)
Forces (KN)
120
100
80
60
40
20
0
-20
-40
-60
105
115
125
135
145
155
165
175
Times (s)
MOJS
Experimental

Velocity Cap Force Coefficients – Z direction

The following plots are of the Morison equation fitted to forcing on velocity cap in the vertical direction (configuration 1) from all regular wave tests.

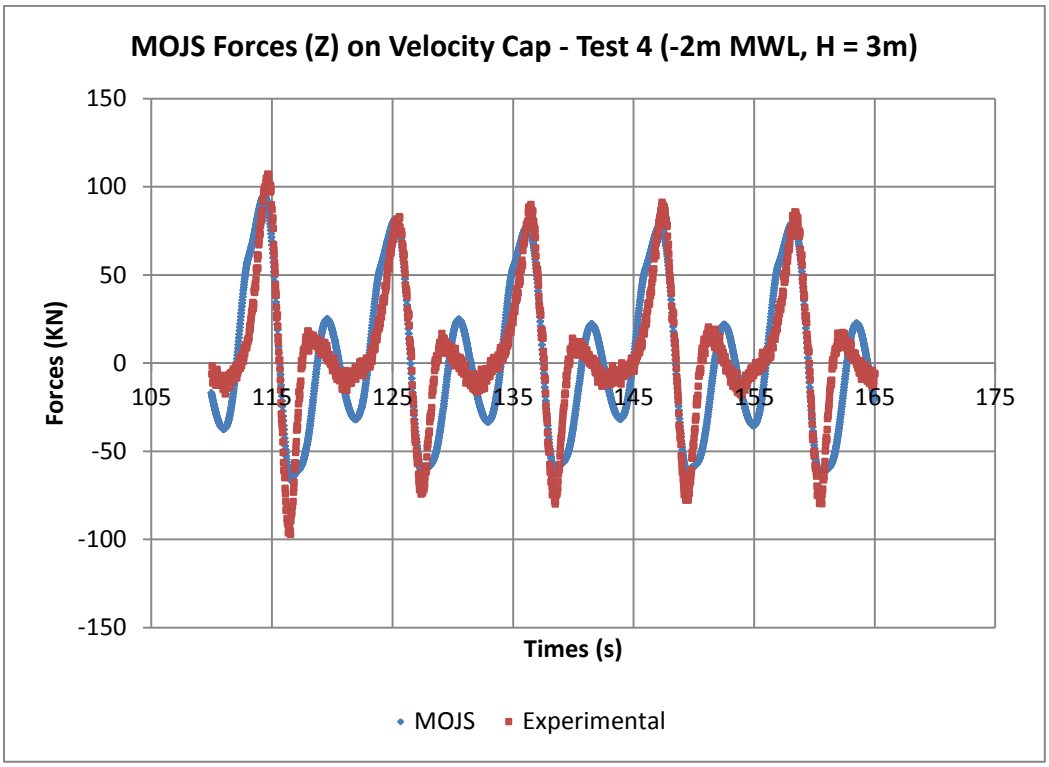

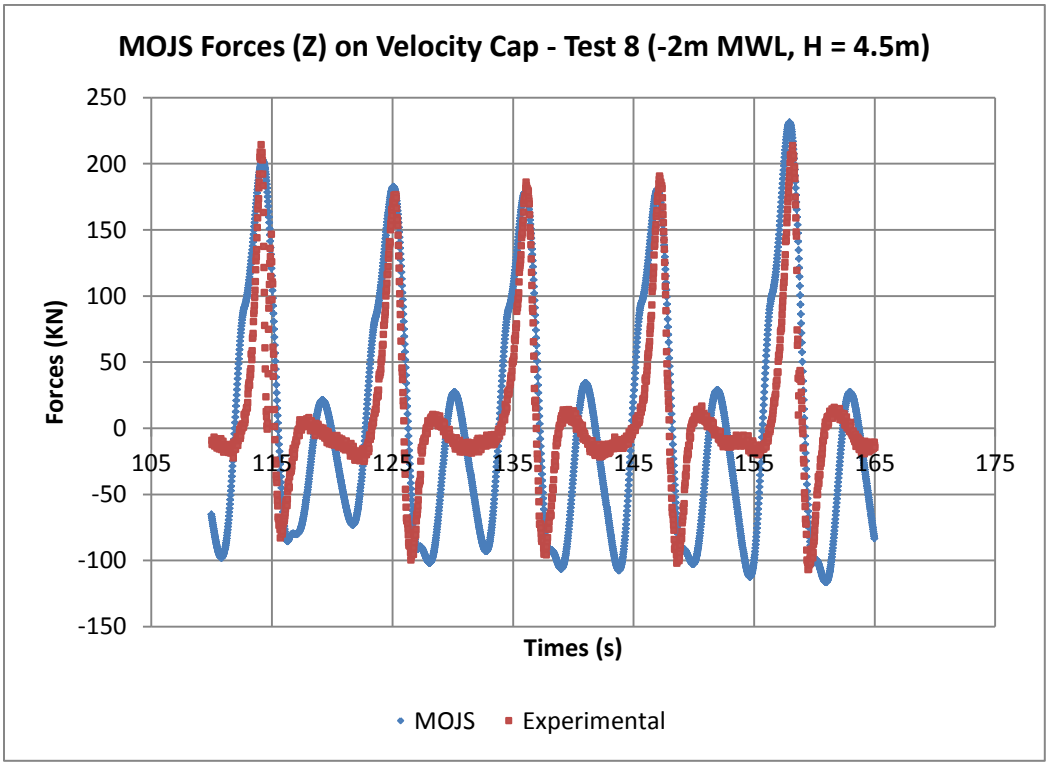

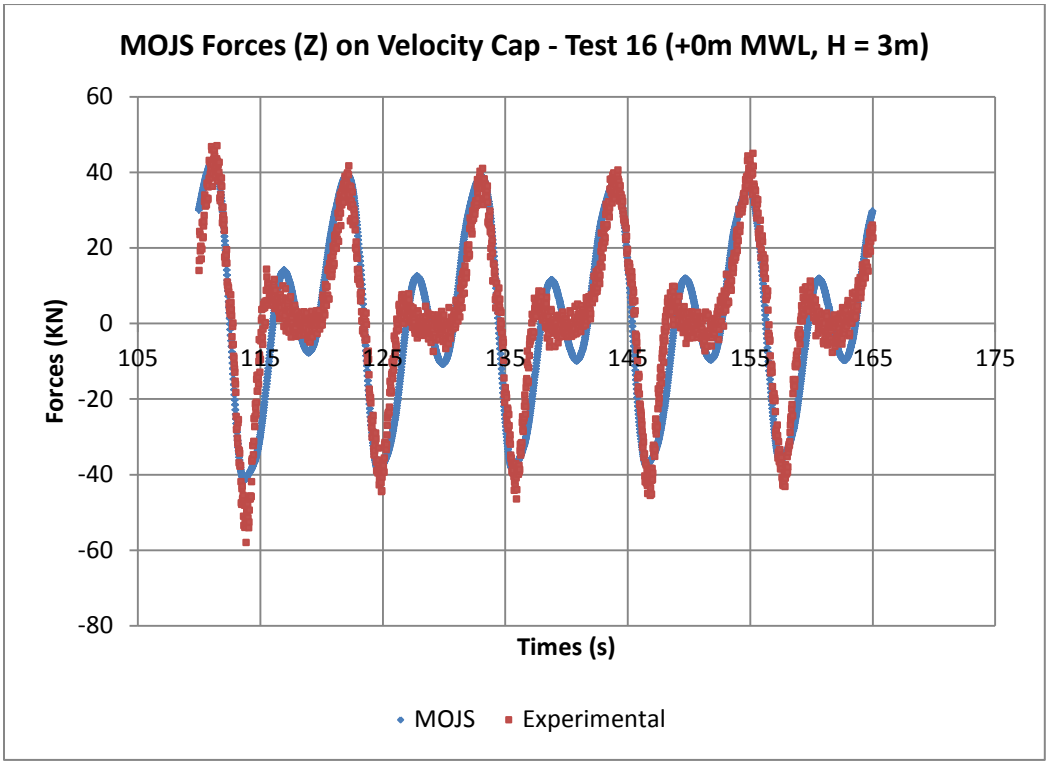
MOJS Forces (Z) on Velocity Cap - Test 16 (+0m MWL, H = 3m)
60
40
20
0
-20
-40
-60
-80
105
115
125
135
145
155
165
175
Forces (KN)
Times (s)
MOJS
Experimental

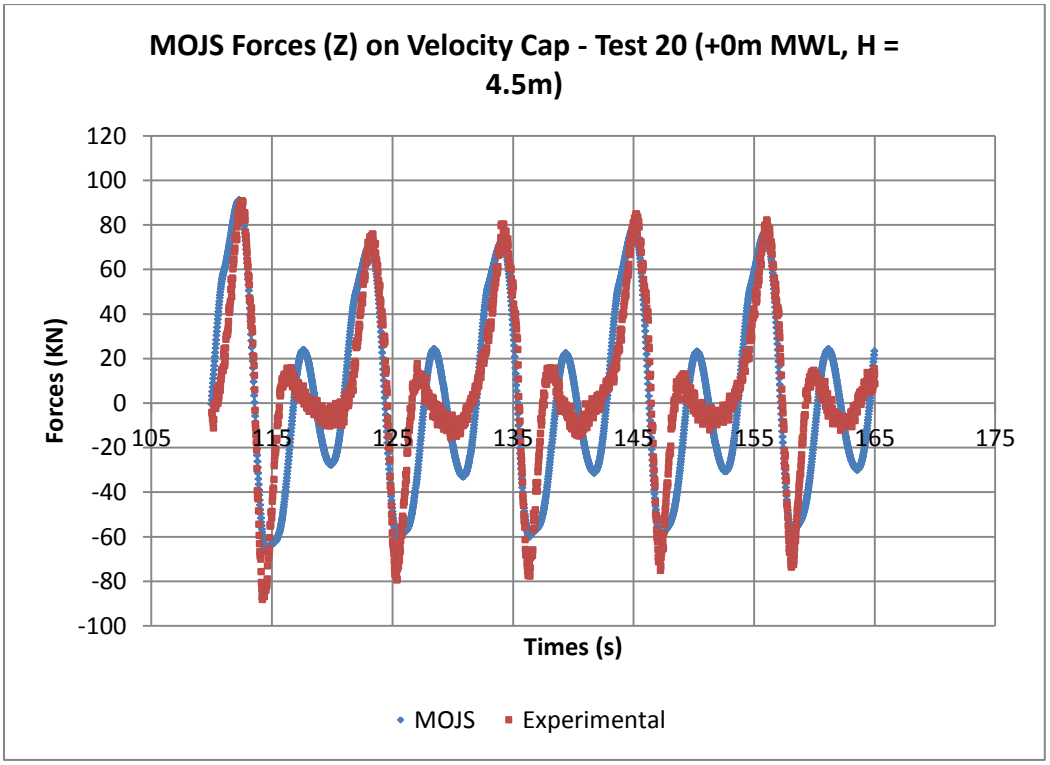
MOJS Forces (Z) on Velocity Cap - Test 20 (+0m MWL, H = 4.5m)
120
100
80
60
40
20
0
-20
-40
-60
-80
-100
105
115
125
135
145
155
165
175
Forces (KN)
Times (s)
MOJS
Experimental

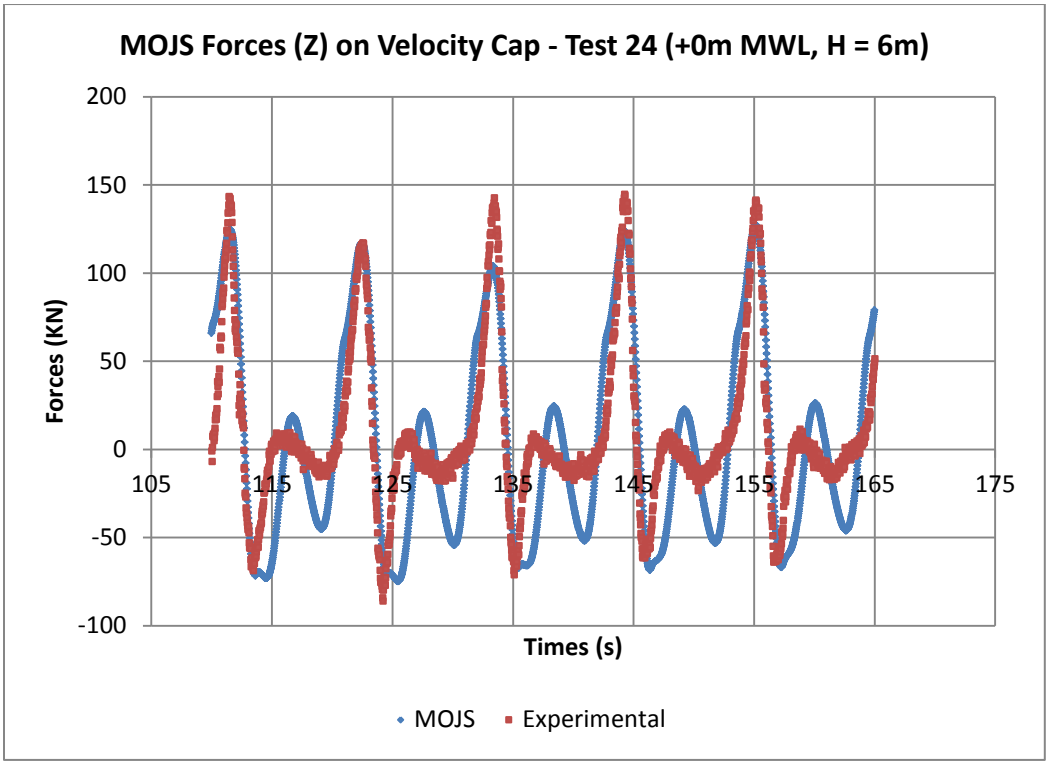
MOJS Forces (Z) on Velocity Cap - Test 24 (+0m MWL, H = 6m)
Forces (KN)
200
150
100
50
0
-50
-100
105
115
125
135
145
155
165
175
Times (s)
MOJS
Experimental

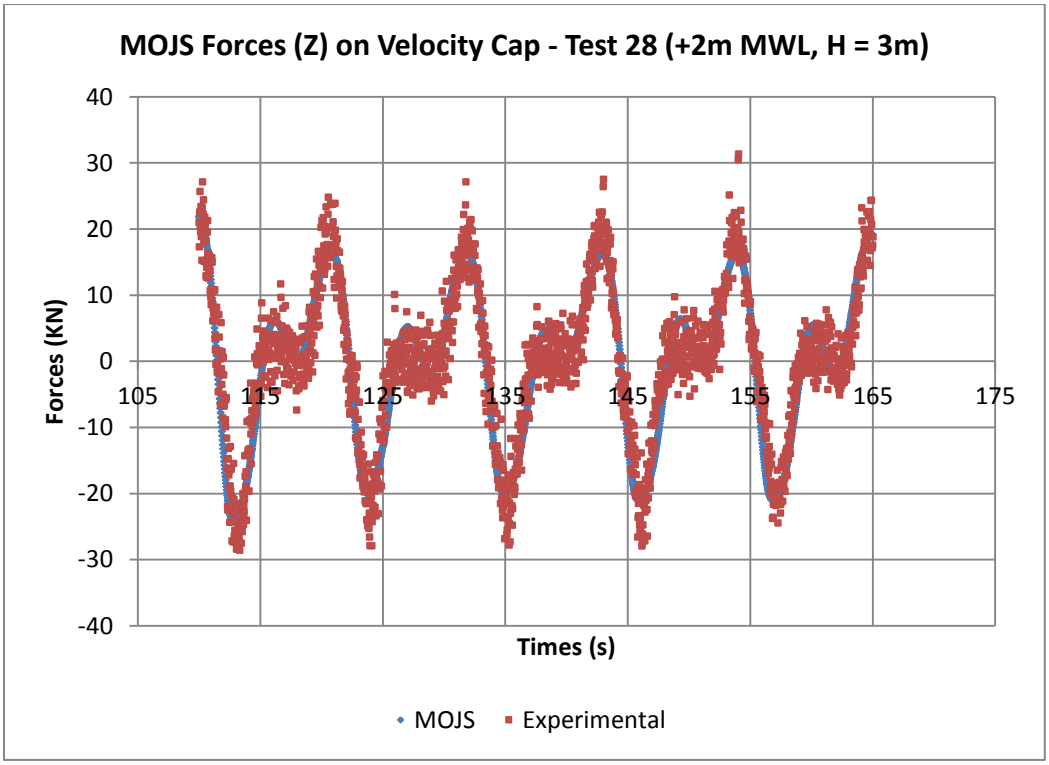
MOJS Forces (Z) on Velocity Cap - Test 28 (+2m MWL, H = 3m)
Forces (KN)
40
30
20
10
0
-10
-20
-30
-40
105
115
125
135
145
155
165
175
Times (s)
MOJS
Experimental

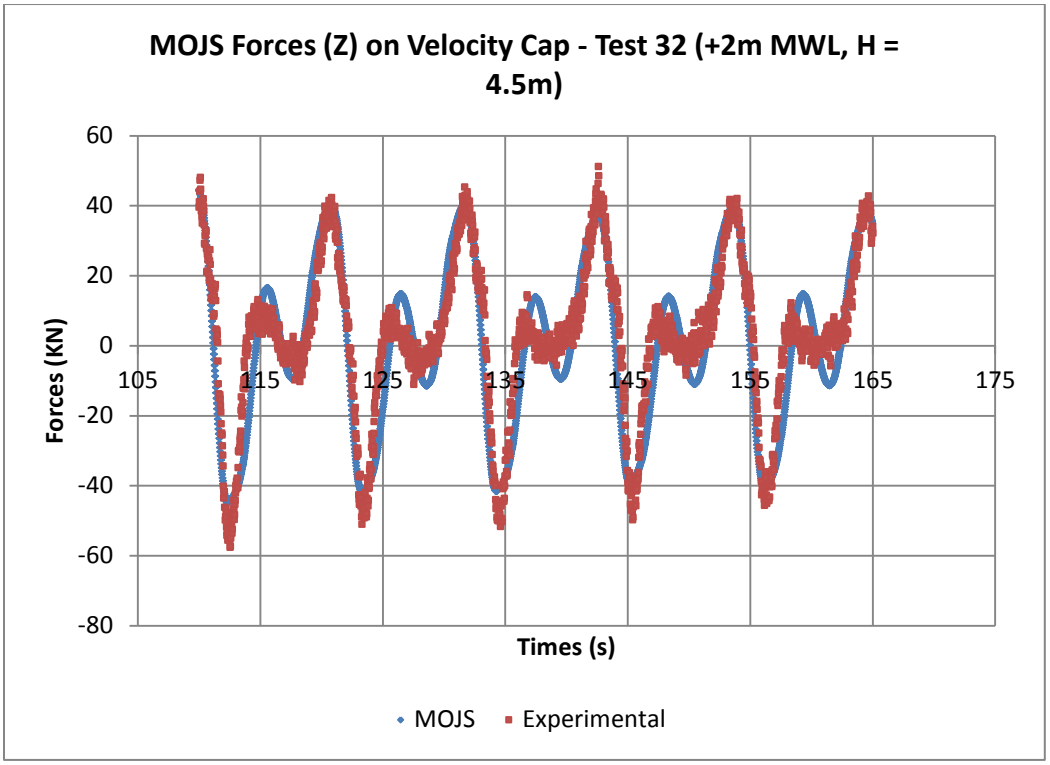
MOJS Forces (Z) on Velocity Cap - Test 32 (+2m MWL, H = 4.5m)
Forces (KN)
60
40
20
0
-20
-40
-60
-80
105
115
125
135
145
155
165
175
Times (s)
MOJS
Experimental

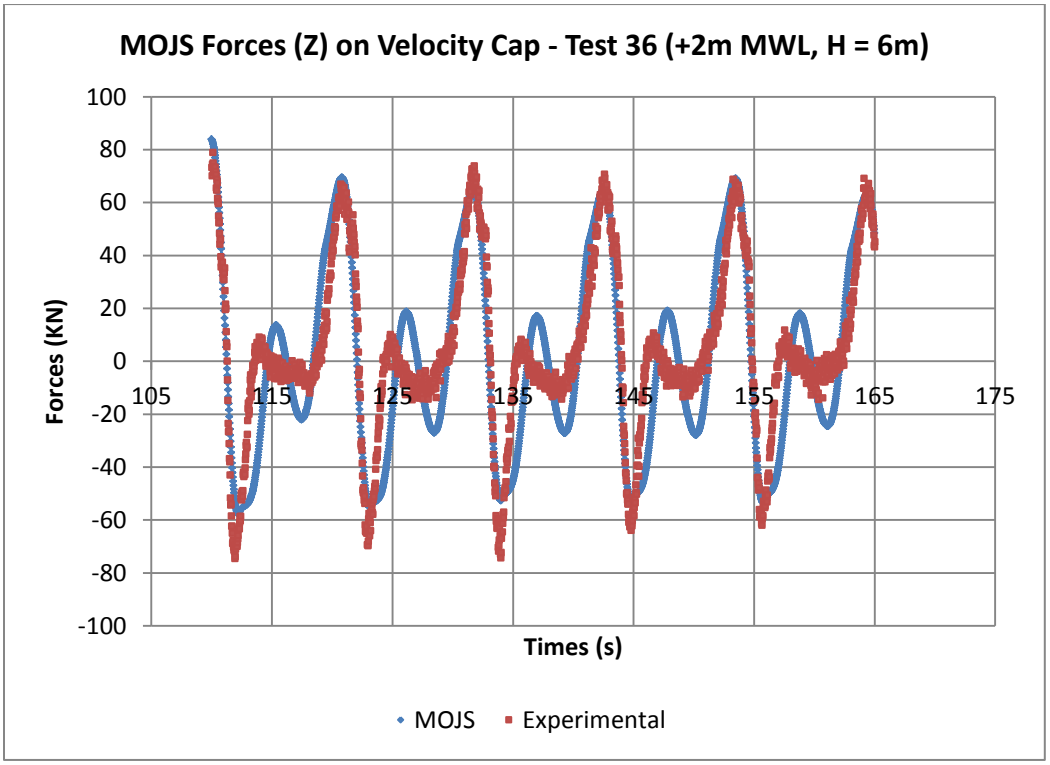
MOJS Forces (Z) on Velocity Cap - Test 36 (+2m MWL, H = 6m)
Forces (KN)
100
80
60
40
20
0
-20
-40
-60
-80
-100
105
115
125
135
145
155
165
175
Times (s)
MOJS
Experimental

MOJS Plots

In the Predicting Forcing from Irregular Waves section, MOJS Full-Comp., Conf. 1, and Z direction modelling results were presented for test 23 (Table 4.1) in Figures 6.64, 6.65, and 6.66 respectively. The results of the rest of the MOJS models (Pipe, Conf. 3, Conf. 3 – Comp, Full - Conf.3) for test 23 are displayed below.

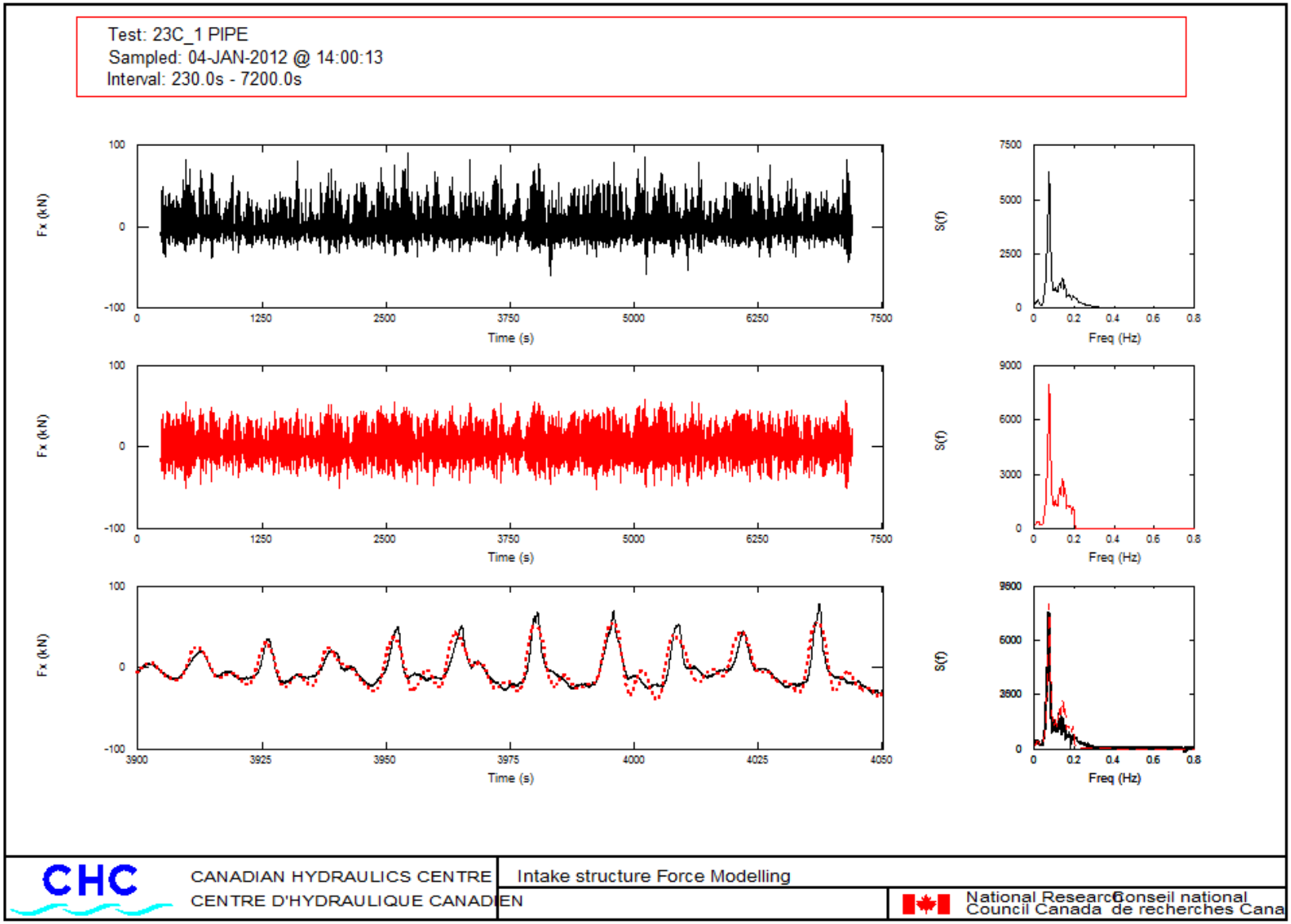
Test: 23C_1 PIPE
Sampled: 04-JAN-2012 @ 14:00:13
Interval: 230.0s - 7200.0s
Fx (kN)
Time (s)
S(f)
Freq (Hz)
CHC
CANADIAN HYDRAULICS CENTRE
CENTRE D'HYDRAULIQUE CANADIEN
Intake structure Force Modelling
National Research Council Canada
Conseil national de recherches Cana

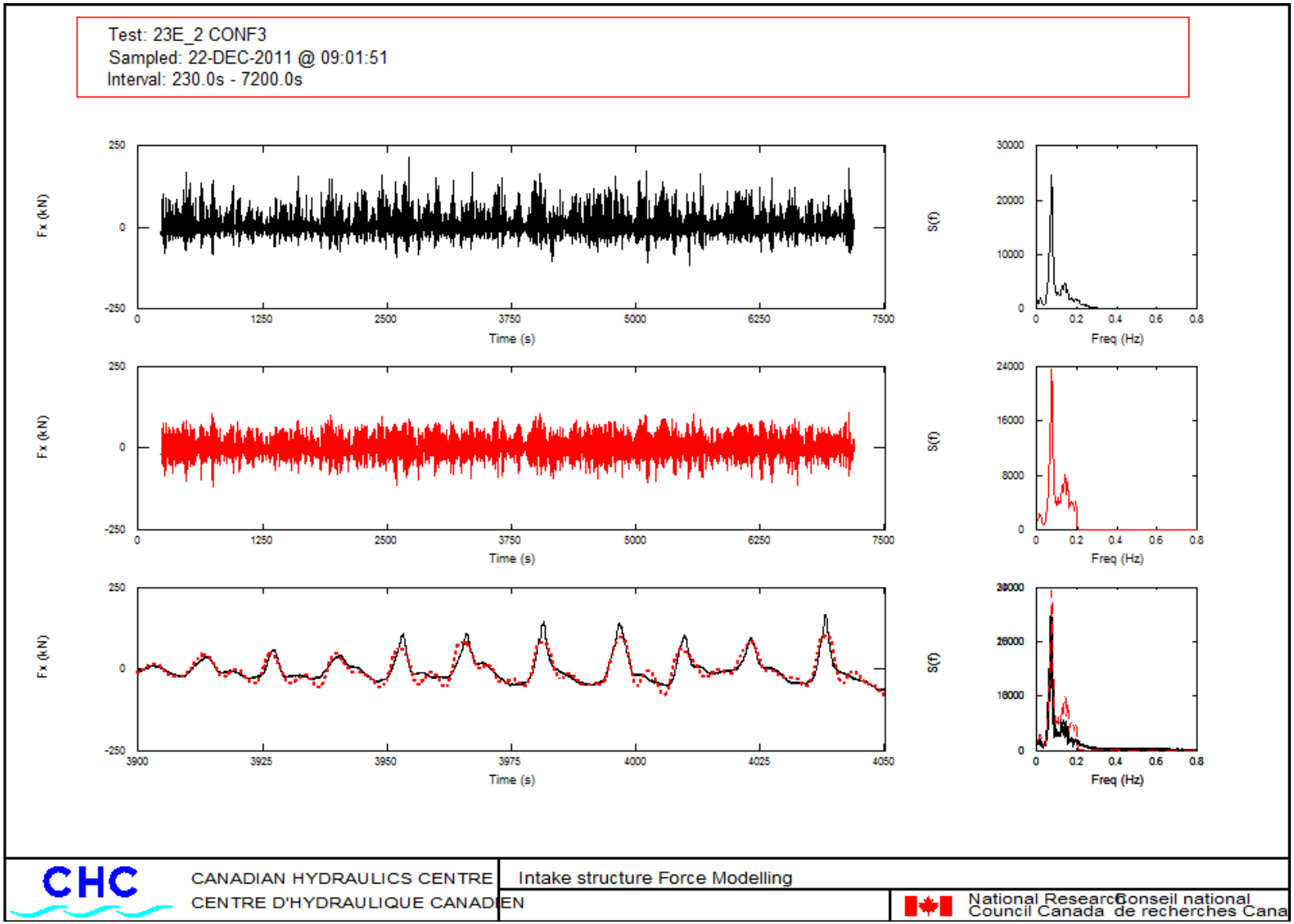
Test: 23E_2 CONF3
Sampled: 22-DEC-2011 @ 09:01:51
Interval: 230.0s - 7200.0s
Fx (kN)
Time (s)
S(f)
Freq (Hz)
CHC
CANADIAN HYDRAULICS CENTRE
CENTRE D'HYDRAULIQUE CANADIEN
Intake structure Force Modelling
National Research Council Canada
Conseil national de recherches Cana

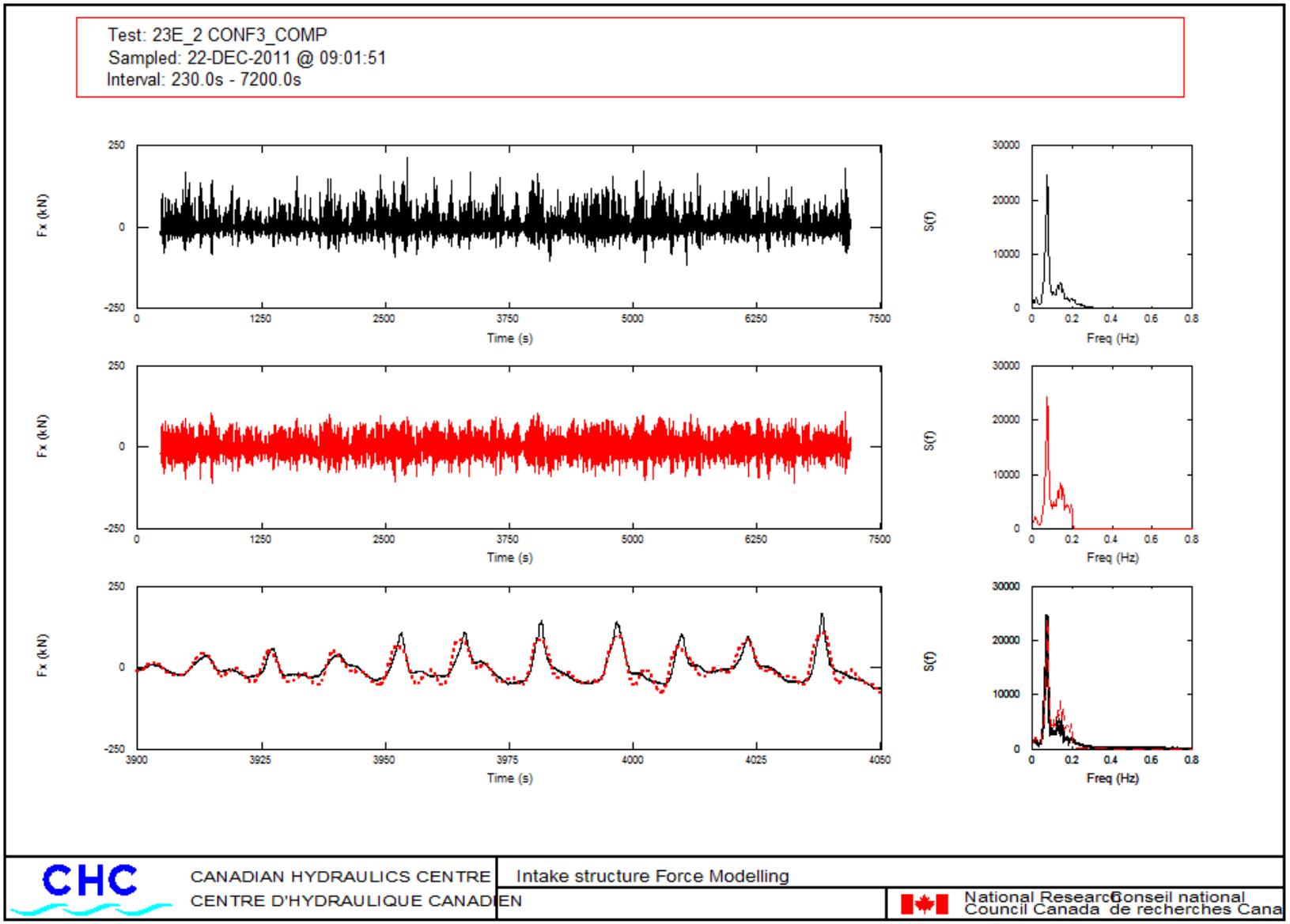
Test: 23E_2 CONF3_COMP
Sampled: 22-DEC-2011 @ 09:01:51
Interval: 230.0s - 7200.0s
Fx (kN)
Time (s)
S(f)
Freq (Hz)
CHC
CANADIAN HYDRAULICS CENTRE
CENTRE D'HYDRAULIQUE CANADIEN
Intake structure Force Modelling
National Research Council Canada
Conseil national de recherches Cana

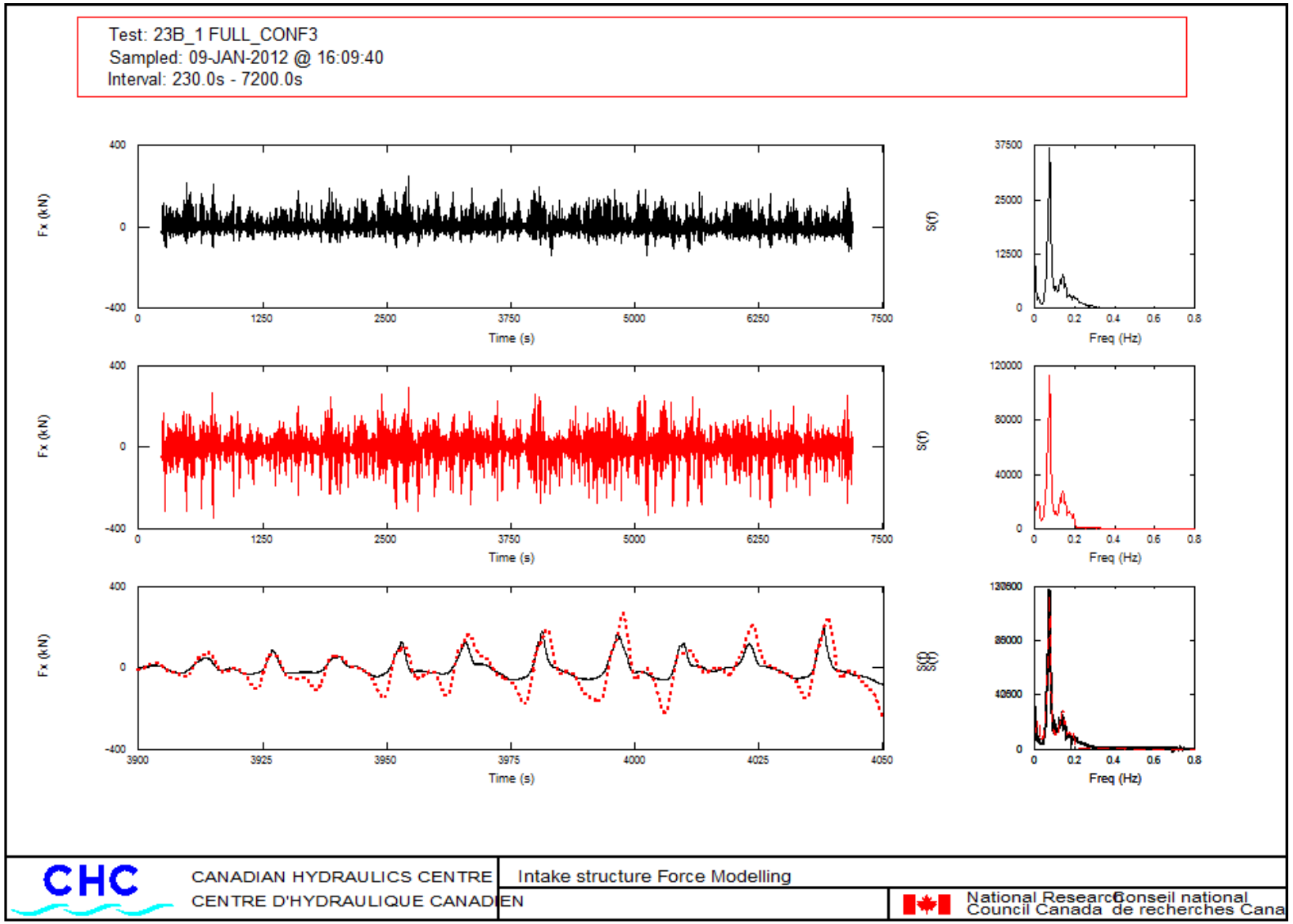
Test: 23B_1 FULL_CONF3
Sampled: 09-JAN-2012 @ 16:09:40
Interval: 230.0s - 7200.0s
Fx (kN)
Time (s)
S(f)
Freq (Hz)
CHC
CANADIAN HYDRAULICS CENTRE
CENTRE D'HYDRAULIQUE CANADIEN
Intake structure Force Modelling
National Research Council Canada
Conseil national de recherches Cana